LA-13670-SR

Approved for public release;
distribution is unlimited.

Busted Butte Unsaturated Zone Transport Test: Fiscal Year 1998 Status Report

Yucca Mountain Site Characterization Program
Deliverable SPU85M4

Los Alamos
NATIONAL LABORATORY

Los Alamos National Laboratory is operated by the University of California for the United States Department of Energy under contract W-7405-ENG-36.

This work was supported by the Yucca Mountain Site Characterization Project Office as part of the Civilian Radioactive Waste Management Program of the U.S. Department of Energy. The Site Characterization Office manages the Yucca Mountain Project.

Edited by Gilles Y. Bussod, Kay Coen, and Roger Eckhardt

An Affirmative Action/Equal Opportunity Employer

LA-13670-SR

Issued: November 1999

Busted Butte Unsaturated Zone Transport Test: Fiscal Year 1998 Status Report

Yucca Mountain Site Characterization Program
Deliverable SPU85M4

Gilles Y. Bussod
H. Jake Turin
*William E. Lowry**

Contributors:
David E. Broxton
H. Mike Buettner
Veraun Chipman
William D. Daily
Sandra Dalvit Dunn
Carl W. Gable
Schon S. Levy
Neva Gray Mason
John E. Peterson
Abe Ramirez
Thomas E. Ricketts
Bruce A. Robinson
Wendy E. Soll
E. Joe Sponeman
Jerry Stockton
David T. Vaniman
Hari S. Viswanathan
Kenneth H. Williams
Laura E. Wolfsberg
David S. Wykoff
Dong Xiao Zhang

* *Consultant at Los Alamos. Science and Engineering Associates, Inc., 1570 Pacheco, Santa Fe, NM 87505*

Los Alamos
NATIONAL LABORATORY
Los Alamos, New Mexico 87545

Busted Butte web site: www.ees.lanl.gov/EES5/bbutte

TABLE OF CONTENTS

LIST OF FIGURES

LIST OF TABLES

ACKNOWLEDGEMENTS

The principal investigators of this work would like to give special thanks to Chuck Harrington, Tom Hirons, Dick Kovach, Orlando Lujan, Dick McDonald, Alyssa Olsen, Tom Ricketts, and Joe Sponeman, and other members of the Test Coordination Office (TCO), Kewit, and the Construction Management Organization (CMO). This test would not have been possible without the efforts of Ned Elkins, formerly of the TCO and now at Sandia National Laboratories, Chris Breeds, and Ross Webb from Subterra, Inc., and many others throughout the YMP organization. The technical review of this document by George A. Zyvoloski was greatly appreciated. Finally, we would like to thank Paul Dixon of the YMP M&O and Dennis Williams, Russ Patterson, and Debbie Bryan of the DOE for their support and exceptional management of this test.

G. B. and J. T.

BUSTED BUTTE UNSATURATED ZONE TRANSPORT TEST: FISCAL YEAR 1998 STATUS REPORT

Yucca Mountain Site Characterization Program Deliverable SPU85M4

by
Gilles Y. Bussod, H. Jake Turin, and William E. Lowry

Contributers:
David E. Broxton, H. Mike Buettner, Veraun Chipman, William D. Daily, Sandra Dalvit Dunn, Carl W. Gable, Schon S. Levy, Neva Gray Mason, John E. Peterson, Abe Ramirez, Thomas E. Ricketts, Bruce A. Robinson, Wendy E. Soll, E. Joe Sponeman, Jerry Stockton, David T. Vaniman, Hari S. Viswanathan, Kenneth H. Williams, Laura E. Wolfsberg, David S. Wykoff, and Dong Xiao Zhang.

ABSTRACT

This report is an update on the unsaturated-zone transport test at Busted Butte initiated on April 2, 1998. The report describes the status of the testing program and documents the progress of construction activities and site and laboratory characterization activities undertaken in fiscal year 1998. Also presented are "blind" predictive flow-and-transport simulations for Test Phases 1 and 2 and the preliminary results and status of the test phases. Future anticipated results obtained from unsaturated-zone transport testing in the Calico Hills at Busted Butte are also discussed in view of their importance to performance assessment needs. The results can be used to build confidence in and reduce the uncertainty of site-scale flow-and-transport models and their abstractions for performance for the license application of the proposed Yucca Mountain nuclear waste repository.

Although flow-and-transport field data collected to date are limited, observations of the available data collected so far, and the modeling of these data, lead to several key conclusions of relevance to performance assessment. These conclusions are summarized in this report.

Initial results from the Phase-1B experiment are now under investigation. The transport times observed immediately below the injection point in the lower section of the Topopah Spring basal vitrophyre (Tptpv2) are relatively longer than expected for pure fracture flow. Tracer injected immediately adjacent to a fracture appears to be imbibed quickly into the surrounding matrix, suggesting that fracture matrix interactions are important in the unsaturated zone beneath the potential repository site at Yucca Mountain. Site-scale models will be evaluated in light of this and future observations at Busted Butte, as models that predict significant fracture flow at percolation rates low enough for the matrix to transmit the flow may be inconsistent with Phase-1B experimental results.

1. INTRODUCTION

This report describes the status of the Busted Butte Unsaturated Zone Transport Test (UZTT) and documents the progress of construction activities and site and laboratory characterization activities undertaken in fiscal year 1998. Also presented are predictive flow-and-transport simulations for Test Phases 1 and 2 of testing and the preliminary results and status of these test phases.

Future anticipated results obtained from unsaturated-zone (UZ) transport testing in the Calico Hills Formation at Busted Butte are also discussed in view of their importance to performance assessment (PA) needs to build confidence in and reduce the uncertainty of site-scale flow-and-transport models and their abstractions for performance for license application.

1.1 Test Objectives

The principal objectives of the test are to address uncertainties associated with flow and transport in the UZ site-process models for Yucca Mountain, as identified by the PA working group in February 1997. These include but are not restricted to:

1. The effect of heterogeneities on flow and transport in unsaturated and partially saturated conditions in the Calico Hills Formation. In particular, the test aims to address issues relevant to fracture-matrix interactions and permeability contrast boundaries.

2. The migration behavior of colloids in fractured and unfractured Calico Hills rocks.

3. The validation through field testing of laboratory sorption experiments in unsaturated Calico Hills rocks.

4. The evaluation of the 3-D site-scale flow-and-transport process model (i.e., equivalent-continuum/dual-permeability/discrete-fracture-fault representations of flow and transport) used in the PA abstractions for license application.

5. The effect of scaling from lab scale to field scale and site scale.

1.2 Location of Test

The Busted Butte test facility is located in Area 25 of the Nevada Test Site (NTS) approximately 160 km northwest of Las Vegas, Nevada, and 8 km southeast of the potential Yucca Mountain repository area. The site was chosen based on the presence of a readily accessible exposure of Topopah Spring Tuff and Calico Hills Formation and the similarity of these units to those beneath the potential repository horizon.

1.3 Scope

The scope of work in fiscal year 1998 included site-permitting applications, facility design and construction, test design, scoping calculations and test implementation, laboratory experimentation, and laboratory and field analyses. Details of the design and construction criteria can be found elsewhere (see *Design Report for the Unsaturated Zone Transport Test, Busted Butte Test Facility* (Sub Terra, Inc. 1998, p. 48)). With the exception of construction activity updates, this report will be limited to the scientific scope of work for fiscal year 1998.

2. OVERVIEW OF FISCAL YEAR 1998 ACTIVITIES

2.1 Chronology of Fiscal Year 1998 Activities

With the exception of permit-application and safety-related concerns, the fiscal year 1998 effort began with the characterization of the Busted Butte site for purposes of test design and construction. Details of fiscal year 1998 activities are listed in Appendix A of this report. This effort included the recovery of samples from outcrops, which were used for the initial laboratory characterization studies of hydrologic properties and mineralogy. The geological context and lithological descriptions of core samples from the test site were used to provide further information on the geometry of the beds at the site so as to guide the construction of the tunnel. Construction and design efforts have proceeded at a remarkable rate through the sustained efforts of the Yucca Mountain Project (YMP) Test Coordination Office (TCO) and the seamless integration of construction, design, and scientific activities. All of this effort has allowed testing to begin on schedule on April 2, 1998 (Phase 1A).

Laboratory measurements of hydrologic, mineralogic, and tracer sorption and matrix diffusion properties of the core samples collected once the tunnel was excavated are now providing needed information for predictive modeling studies.

2.2 Mapping

The Busted Butte site was mapped and sampled for the purposes of test design and construction during the fall of 1997 (see Appendix A). Preliminary results of this activity are described in Section 4.

2.3 Construction

The fiscal year 1998 construction activities in support of the transport studies at Busted Butte involved 1) road improvement activities, completed November 14, 1997; 2) the construction of a pad and highwall, completed December 18, 1997; 3) the excavation of a 75-m main drift, completed January 21, 1998; 4) the excavation of a 19-m test alcove, completed January 30, 1998; and 5) dry drilling 34 test boreholes, completed March 19, 1998.

The primary objective of the underground testing is to, first of all, assure minimal disturbance of the in-situ test block in the initial stages of unsaturated tracer transport testing. Design, construction, and scientific teams were all involved in insuring that the test block itself remained undisturbed by construction activities. Shotcrete and NaSi glass applications to the tunnel walls were coordinated so as to optimize safety concerns and testing requirements.

All of these activities were crucial to the implementation of the test program, and TCO construction and design support are ongoing at this time to allow for mineback, auger, and overcoring activities scheduled for fiscal year 1999.

2.4 Underground Testing Activities

The first testing activity for the first year (fiscal year 1998) involved collecting “Q” samples from the dry drilling of the boreholes from the Main Drift and the Test Adit to provide core samples for geologic, hydrologic, and geochemical laboratory investigations and scoping calculations. Following this activity, the boreholes were surveyed and instrumented for injection tests.

2.4.1 Test Phase 1

Test Phase 1 was instrumented sequentially in the hydrologic Calico Hills lithologies, Phase 1A (Tac and Tptpv1), and in the Topopah Spring Tuff, Phase 1B (Tptpv2). Phase-1A installation was completed on April 2, 1998, the same day as the initial injection testing. Phase 1A involves two injection rates: 1ml/hr in Boreholes 2 and 4 and 10 ml/hr in Boreholes 1 and 3. This “blind” testing phase is expected to be complete in early fiscal year 1999, after which time, a “mini-mineback” will expose the ingress of the tracer into the rock mass. Auger samples will be used to collect sam-

ples from this test to be analyzed at Los Alamos National Laboratory (LANL) for the presence of conservative, reactive tracers and of microspheres. Test predictions are included in this report.

Phase-1B installation involved both injection and collection membranes and was instrumented on May 12, 1998. Injection started on the same day in the lower section of the Topopah Spring basal vitrophyre (Tptpv2). Phase 1B involves two injection rates: 1 ml/hr in Borehole 7 and 10 ml/hr in Borehole 5. Because of the paucity of data on fracture-matrix interactions in these lithologies, this test is not associated with predictive modeling but serves as a "calibration" test for fracture-matrix interactions to be used in Phase-2 simulations. Because Phase 1B involves two 2-m collection membranes located immediately below the injection boreholes, arrival of tracer in the higher injection-rate experiment (Borehole 5, 10 ml/hr) has been detected by ultraviolet (UV) fluorescence on June 16, 1998, in Collection Borehole 6. No tracer has been detected from the 1-ml/hr injection experiment in Collection Borehole 8. The analysis of collection pads from this test are ongoing, and some preliminary results are documented in this report. This test is expected to be completed in early fiscal year 1999, after which time, either a "mini-mineback" or overcoring will provide samples for further analysis of the test results for use in Phase-2 predictions.

2.4.2 Test Phase 2

As in Phase 1, this test was instrumented sequentially as Phases 2A, 2B, and 2C. Phase 2A consists of a single borehole instrumented with 10 injection points and 10 moisture sensors, one at each injection point. The injection rate is 1 ml/hr per injection point, which corresponds to an overall infiltration rate of 30 mm/yr. This borehole is restricted to the Tptpv2 lithology, which consists of fractured, moderately welded tuff from the basal vitrophyre. Phase-2A instrumentation was completed on July 23, 1998, and injection was started the same day. To date, no tracer has been detected in the collection boreholes located at right angles to the injection boreholes.

Phase 2B consists of four injection boreholes, each instrumented with 10 injection points and 10 moisture sensors, one at each injection point. The injection rate is 10 ml/hr per injection point, which corresponds to an overall infiltration rate of 380 mm/yr. This injection plane is restricted to the Calico Hills Formation (Tac) and is meant to activate the lower section of the test block simultaneously with the upper section (Phases 2A and 2C). Phase-2B instrumentation was completed July 30, 1998, the same day that injection was initiated. Tracer breakthrough has been visually detected on August 6, 1998, by UV fluorescence in Collection Borehole 46, and on August 13, in Collection Borehole 48, both located in the same plane approximately 17 cm from the injection plane. Analyses of these results are underway.

Phase 2C consists of three injection boreholes, each instrumented with 9 injection points and 12 moisture sensors, one at each injection point and two additional sensors located toward the borehole collar to detect tracer movement towards the front of the borehole. The injection rate is 50 ml/hr per injection point, which corresponds to an overall infiltration rate of 1550 mm/yr. As in Phase 2A, this injection system is restricted to a horizontal plane in the Tptpv2 lithology. Phase-2C instrumentation was completed on August 4, 1998. Phase-2C injection was initiated on August 5, 1998. To date, no tracer breakthrough has been observed on any of the collection membranes.

2.5 Scoping Calculations and Test Design

The site characterization of the potential test block in fiscal year 1998 involved the mapping of the main drift wall, core sampling for mineralogy/petrology (Min/Pet), and hydrologic characterization of the reconnaissance geochemical laboratory tests. For scoping calculations, test design, and Phase-1 predictions, a high-resolution unstructured grid was completed. These predictions are described in Section 6. For Phase 2, the mapped tunnel walls were subsequently incorporated into a three-dimensional (3-D) computational grid using the software

GEOMESH for subsequent FEHM code scoping calculations. A series of numerical simulations were carried out in support of the design of the unsaturated-zone transport tests at Busted Butte. These calculations are presented in Section 7.

2.6 Laboratory Activities

2.6.1 Mineralogy/petrology

Along with mapping of the site for purposes of test design and construction, samples from outcrops were collected at the Busted Butte site on October 8, October 20, October 28, and November 6 and 7 (see Appendix A) for Min/Pet analyses and site-characterization activities. Some of these samples were also used for hydrologic properties determinations (i.e., SPC 7047, 7048, 7049, and 7050). Other samples from the test-block walls were also collected throughout the year for the study, and descriptions of the lithologies present in the test area were gathered. Details of this work are included in this report, Sections 3 and 4.

2.6.2 Hydrology

Samples of Calico Hills Formation and Topopah Spring Tuff rocks from Busted Butte outcrops collected in Fall 1997 were used to determine the hydrologic properties of the formations in the test block. Results from these analyses are included in Section 4 and Appendix C. Six samples, four whole-rock cores, and two recomposites, were used to measure the unsaturated hydraulic conductivity, $K(\theta)$, the matric potential, $\Psi(\theta)$, or water retention, using the UFA method (centrifuge-induced flow). The Calico Hills (Tac) sample (SPC 7048) has a total porosity of 50 to 56% and a saturated conductivity K of approximately 2×10^{-3} cm/s. The Topopah Springs Tptpv1 sample (SPC 7049) has a total porosity of 64% and a saturated conductivity K of approximately 6×10^{-4} cm/s. Both of these samples represent the hydrologic Calico Hills (CHn). Conversely, samples from the base of the basal vitrophyre (Tptpv2), representing the top of the test block, Phases 1 and 2, exhibited lower saturated conductivities K varying from 4×10^{-4} to less than 4×10^{-10} cm/s (SPC 7050 and 7047, respectively). These results are used in conjunction with YMP database parameters to run the model simulations presented in the report.

2.6.3 Geochemistry

Preliminary results on the geochemistry of the test block are presented in this report. Field-scale transport behavior is primarily a function of the ambient flow field and the interactions between the geologic host and the material being transported. Secondary influences include details of the pore-water chemistry, including pH, Eh, ionic strength, and chemical composition. Changes in any of these variables may affect solute sorption behavior and colloid stability and may lead to dissolution or precipitation of minerals resulting in permeability changes. These considerations lead to a fundamental conflict in field-tracer studies: on the one hand, alteration of the in-situ water chemistry should be limited to minimize the artificial perturbations introduced by chemistry variations; on the other hand, introduction of any artificial tracer will inherently alter water chemistry. (One exception might be the use of miniscule amounts of isotopic tracers; not a practical alternative at this phase of the Busted Butte studies.) Our plan at Busted Butte was to introduce our artificial tracers in a matrix designed to mimic natural pore-water chemistry as closely as practical, acknowledging that some alterations were inevitable. Accordingly, we collected and analyzed pore-water samples from rock cores collected in the adit, developed a recipe for "synthetic" Busted Butte water that closely resembled the in-situ chemistry, and used this synthetic water as our injection matrix. Results of the chemical analyses are presented in Section 4, and details of the synthetic water recipe are presented in Section 3. (The issue of matching in-situ water chemistry is not unique to Busted Butte; a similar approach is taken at the C-Wells facility. There, however, no "synthetic" water is needed because the pumping well provides an ample supply of authentic C-Wells water.)

2.6.4 Tracer evaluation

To predict the performance of the Calico Hills bar-

rier to radioactive waste migration at Yucca Mountain under different percolation flux scenarios, a series of process models in flow and transport have been developed by the Project based on theory and on field and laboratory studies. For viability assessment, site suitability, and licensing, the effectiveness and reliability of the geologic barriers will be determined using modeling predictions of radionuclide migration to the accessible environment. Measurements on a small scale can be conducted in the laboratory, but validating the extrapolation of these data in the presence of larger-scale heterogeneities requires field-tracer tests. Unfortunately, although the behavior of actual radionuclides of concern has been extensively studied in the laboratory, regulatory and environmental concerns prevent the use of these materials in the field. Efforts are being made to determine possible low-level short-lived radionuclides and analog tracers to be used for performance-confirmation testing in Phase 3. For the Busted Butte field tests, analog conservative and reactive tracers are used as surrogates for radionuclides. To validate the use of these tracers and the site-scale use of the minimum-K_d approach for sorption and the processes of matrix diffusion and colloid migration, laboratory batch-sorption and column studies are underway. These tests are run in parallel with the field tests. Samples collected from the boreholes at Busted Butte are used to conduct these geochemical tests in the laboratory. Preliminary results are presented in this report.

3. TEST DESIGN

3.1 Concept

The Unsaturated Zone Transport Test (UZZT) at Busted Butte is designed to validate and continuously improve the Yucca Mountain Project's flow-and-transport site-scale model for the unsaturated zone (Bussod et al. 1998, pp. 165–192). In terms of transport, the principal barrier to radionuclide migration in the unsaturated-zone (UZ) barrier at Yucca Mountain is the Calico Hills Formation. For this purpose, the test block was located at Busted Butte where the exposure of Calico Hills rocks represents a distal extension of the formation located immediately beneath the potential repository horizon. This location means that the site is not an analog site but, to the best of our knowledge, represents both the Calico Hills Formation and the Topopah Spring Tuff as they exist beneath the potential repository horizon west of the Ghost Dance fault.

Due to the proximity of the deadline for total-site-performance assessment–license application (TSPA-LA), the activities at Busted Butte have been designed to meet an accelerated testing schedule. This schedule has been rigorously adhered to in fiscal year 1998 (see Appendix A) so that the continuation of this testing program during fiscal year 1999 should result in tangible improvements for TSPA-LA. To meet this goal, the test has been subdivided into three phases. Phases 1 and 2 are designed to provide input to TSPA-LA for the license application in 2002. Phase 3 supports performance-confirmation UZ transport testing and may include the use of radionuclide tracers.

In addition to field testing, parallel laboratory analytical and testing programs in geochemistry, tracer evaluation, hydrology, and mineralogy are designed to help interpret the field results. The geochemistry program includes measurement of in-situ pore-water chemistry and development of a synthetic injection matrix. The tracer evaluation program includes batch-sorption studies on Busted Butte samples using Phase-1 and Phase-2 conservative and reactive analog and radioactive tracers, as well as modeling of the geochemical behavior of those tracers in the ambient water chemistry. The hydrology program involves the measurement of the matric potentials and conductivities as a function of saturation for core samples from Busted Butte. The porosity of each sample is also characterized. The Min/Pet program involves the mineralogic characterization of the Busted Butte samples from Q cores from Phases 1 and 2. When possible, splits from the Q-core samples are used in all three characterization programs.

Because the principal objective of the test is to evaluate the validity of the flow-and-transport site-scale process models used in PA abstractions, a flow-and-transport modeling program has also been implemented. This effort will allow us to update the site-scale flow-and-transport model by simulating and predicting experimental field results and by addressing the effects of scaling from laboratory to field scales. Initial predictions of the field tests are included below.

3.2 Experimental Design

As described previously, the Busted Butte test is subdivided into three phases (Fig. 1). Phases 1 and 2 are meant to provide tangible results for TSPA-LA, and Phase 3 is planned for performance confirmation. Details of the test plan can be found in Bussod et al. (1997, p. 155).

3.2.1 Phase 1

Phase 1 represents a simple test program that serves both as a precursor or scoping phase to Phase 2 and as a short-term (6-month duration) experiment aimed at providing initial transport data for early fiscal year 1999 model updates. Phase 1 involves six single-point injection boreholes and two inverted-membrane collection boreholes. All Phase-1 boreholes are 2 m in length and 10 cm in diameter. A mixture of conservative tracers (bromide, fluorescein, pyridone, and fluorinated benzoic acids), a reactive tracer (lithium), and fluorescent polystyrene microspheres are being used to

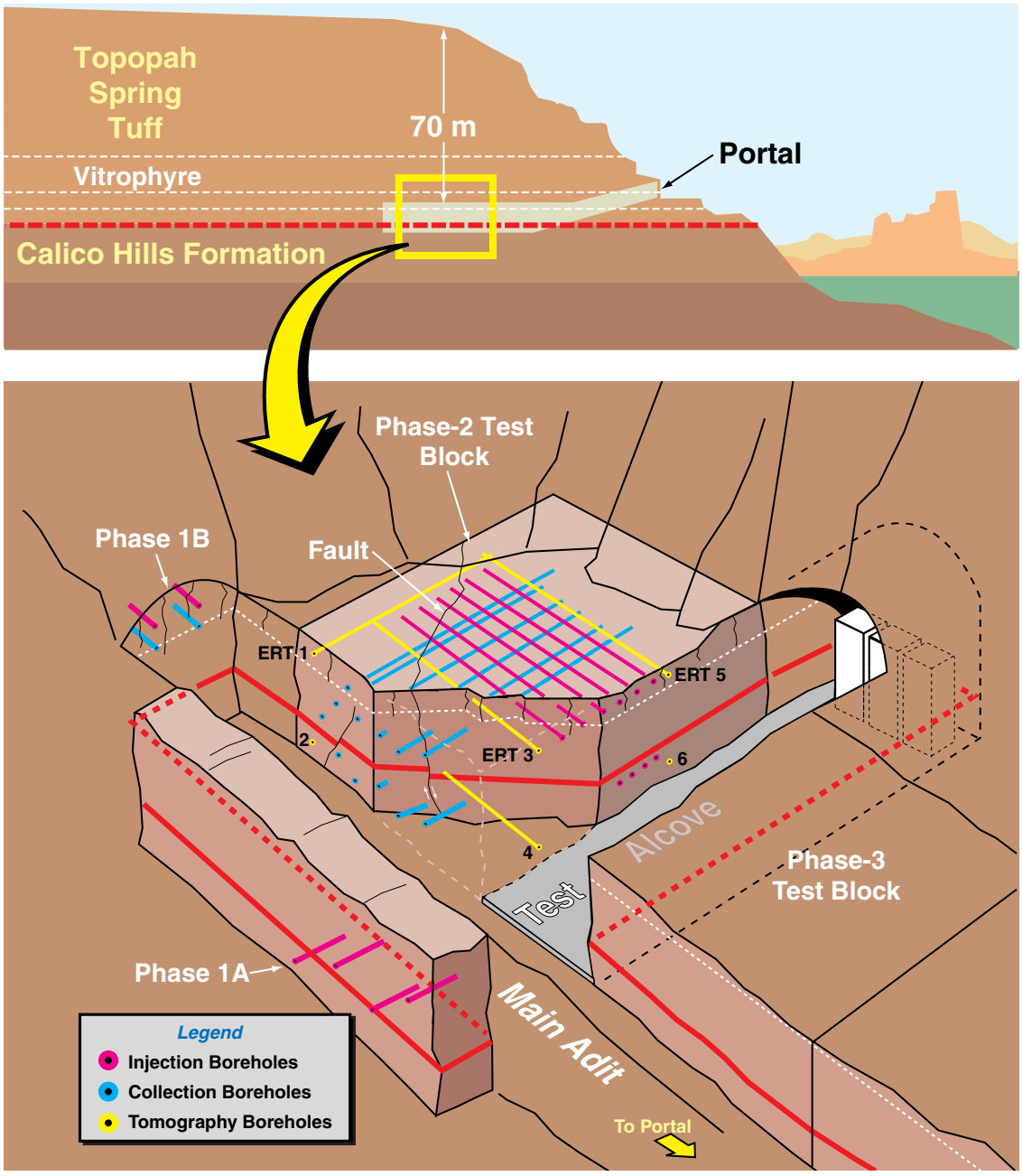

Figure 1. Busted Butte Unsaturated Zone Transport Test. This schematic of the Busted Butte test area shows the relative locations of the boreholes and the test blocks for the different experimental phases of the Unsaturated Zone Transport Test (UZTT).

track flow, reactive transport, and colloid migration, respectively.

Phase 1A, located in the hydrologic Calico Hills (CHn), is a noninstrumented or "blind" test consisting of four single-point injection boreholes, which are to be excavated by "mini-mineback" and auger sampling in early fiscal year 1999. Model predictions associated with Phase 1A (presented below in Section 6) are, therefore, also "blind" and

are meant to test our ability to predict the flow-and-transport results given present YMP databases and modeling capabilities. Continuous injection was started on April 2, 1998. Injection rates vary from 1 ml/hr (Boreholes 2 and 4) to 10 ml/hr (Boreholes 1 and 3).

Phase 1B, located at the base of the Topopah Spring Tuff basal vitrophyre (Tptpv2), involves two single-point injection holes and two collection boreholes located directly below the injection holes, each occupied by an inverted membrane with nine collection pads. Because this test is located in a relatively low-permeability fractured rock, its principal goal is to provide data on fracture-matrix interactions for use in improving Phase-2 predictions. The paucity of data on the properties of fractured rocks precludes the use of this test for predictive simulations. Continuous injection was started on May 12, 1998. Injection rates vary from 1 ml/hr (Borehole 7) to 10 ml/hr (Borehole 5).

3.2.2 Phase 2

Phase-2 testing involves a large, 7-m high, 10-m wide, and 10-m deep block comprising all the lithologies of Phase 1 (Fig. 1). Unlike the single-point injection geometries in Phase 1, the injection systems in Phase 2 are designed to activate large surfaces of the block. Due to the short time frame available for testing, both high and low injection planes are used for testing in Phase 2. The injection points for this phase are distributed in two horizontal, subparallel planes arranged to test the properties of the lower Topopah Spring basal vitrophyre and the hydrologic Calico Hills. Phase-2 mixed-tracer solutions include those used in Phase 1 but also include a mixture of new reactive tracers (Ni^{2+}, Co^{2+}, Mn^{2+}, Sm^{3+}, Ce^{3+}, and Rhodamine WT).

Phase 2 is subdivided into three subphases according to location and the injection rates used. Phase 2A consists of a single high borehole with 10 injection points and an injection rate of 1 ml/hr per point. Phase 2B consists of four low boreholes with 10 injection points each and an injection rate of 10 ml/hr per injection point. Finally, Phase 2C consists of three high boreholes with 9 injection points each and an injection rate of 50 ml/hr per injection point. Injection rates of 1, 10, and 50 ml/hr correspond to infiltration rates of 30, 380, and 1550 mm/yr, respectively. Natural infiltration rates at Yucca Mountain vary between 0.01 and 250 mm/yr with an average of 5 mm/yr (Flint et al. 1996, p. 174). Phase 2A falls within the range of natural present-day infiltration rates at Yucca Mountain, whereas Phase 2B lies at the high end of predicted values for a pluvial climate scenario. Phase-2C infiltration rates are artificially higher than expected natural infiltration rates for the region but provide for the best testing conditions given the short duration of the experiment. Model simulations indicate that even at these high injection rates, the system is expected to remain unsaturated. The validity of this assumption and the relevance of the highest injection-rate experiments (i.e., Phase 2C) will be evaluated using the results from the other two injection-rate experiments (i.e., Phases 2A and 2B).

The high injection plane consists of fractured Topopah Spring Tuff Tptpv2. As in Phase 1B, this unit represents the base of the TSw basal vitrophyre and is characterized by subvertical fractured surfaces representing columnar joints. Thirty-seven injection points distributed along 4 injection holes approximately 8 m deep each are used for tracer injection along a horizontal surface. The natural fracture pattern present in this unit serves as the conduit for tracer migration into the CHn. The lower horizontal injection plane is located in the Calico Hills formation (Tac) and involves 40 injection points distributed in 4 horizontal and subparallel boreholes. This test (Phase 2B) is meant to activate the lower part of the block in the event that the top injection system does not activate the entire block in the short duration of the testing program (2 yr maximum).

Whereas all injection boreholes are located in the Test Alcove, the 12 collection boreholes associated with Phase 2 are located in the Main Adit. These boreholes are 8.5 to 10.0 m in length, and each con-

tains 15 to 20 collection pads evenly distributed on inverted membranes. Because of the complexity of the flow fields expected in this block, several tomographic techniques (i.e., electrical-resistance tomography, ground-penetrating radar, and neutron logging) are used to image the 2-D and 3-D saturation state of the block in monthly to bi-monthly intervals.

Injections for Phases 2A, 2B, and 2C started in 1998 on July 23, July 30, and August 5, respectively.

3.3 Conservative and Reactive Tracers and Microspheres

The tracers were chosen so that conservative, reactive, and colloid-like behaviors could be monitored in a single continuous injection scenario. The tracers were mixed together so as to normalize the hydrologic conditions of the injection. The tracer matrix was synthetic pore water, based on the measured composition of Busted Butte pore waters collected from the test area on January 30, 1998. Analytic results are presented in Section 4; the recipe for the synthetic water is provided below.

3.3.1 Phase-1 tracers

Phase-1 tracers were chosen based on the list of tracers permitted for use in the C-wells tests. Analog conservative and reactive tracers and colloids are mixed together so as to normalize the hydrologic conditions they experience and provide for higher accuracy of the results. The tracers used in the Busted Butte experiments of Phase 1 include:

lithium bromide,
potassium iodide,
fluorescent polystyrene latex microspheres,
fluorescein sodium,
"pyridone" (3-carbomoyl-2(1H)-pyridone),
2,4-difluorobenzoic acid,
2,6-difluorobenzoic acid,
2,4,5-trifluorobenzoic acid,
2,3,4,5-tetrafluorobenzoic acid, and
pentafluorobenzoic acid.

The reactive tracer used is lithium ($K_d \leq 1.0$), and the colloid analogs are fluorescent polystyrene latex microspheres of two sizes: 0.2 and 1 μm diameter. Di- and penta-fluorobenzoic acids (FBA's) are conservative tracers used to tag the various injection boreholes according to injection rates (i.e., 1 and 10 ml/hr rates). Fluorescein sodium and pyridone are UV fluorescent and are used as conservative tracer markers that can be detected in the field at a concentration level of approximately 10 ppm using UV illumination.

Phase 1A—10 ml/hr Injection Rate; Boreholes 1 and 3:
500 mg/L lithium bromide
500 mg/L sodium fluorescein
100 mg/L 2,6 di-FBA
1 ml/L fluorescent polystyrene microspheres

Phase 1A—1 ml/hr Injection Rate; Boreholes 2 and 4:
500 mg/L lithium bromide
500 mg/L sodium fluorescein
100 mg/L penta-FBA
1 ml/L fluorescent polystyrene microspheres

Phase 1B—10 ml/hr Injection Rate; Borehole 5:
500 mg/L lithium bromide
500 mg/L sodium fluorescein
100 mg/L 2,6 di-FBA
100 mg/L pyridone
1 ml/L fluorescent polystyrene microspheres

Phase 1B—1 ml/hr Injection Rate; Borehole 7:
500 mg/L lithium bromide
500 mg/L sodium fluorescein
100 mg/L penta-FBA
100 mg/L pyridone
1 ml/L fluorescent polystyrene microspheres

3.3.2 Phase-2 tracers

Phase-2 tracers include those used in Phase 1 but with the addition of a fluorescent reactive tracer (Rhodamine WT) and additional reactive ions that are proposed as better analogs for neptunium, plu-

tonium, and americium:

Neptunium Analogs (NpO^{2+}, Np(V)):
- nickel (Ni^{2+})
- cobalt (Co^{2+})
- manganese (Mn^{2+})

Plutonium Analog (Pu^{3+}):
- samarium (Sm^{3+})

Plutonium Analogs (colloidal form):
- charged (+/-) and neutral polystyrene microspheres

Americium Analog (Am^{3+}):
- cerium (Ce^{3+})

Of the proposed analogs listed above, the tracers used in Phase-2 testing at Busted Butte are:

Phase 2A—1 ml/hr Injection Rate; Borehole 23:
- 1000 mg/L lithium bromide
- 10 mg/L sodium fluorescein
- 100 mg/L 2,4,5 tri-FBA
- 10 mg/L pyridone
- 1 ml/L microspheres

Phase 2B—10 ml/hr Injection Rate; Boreholes 24, 25, 26, 27:
- 1000 mg/L lithium bromide
- 10 mg/L sodium fluorescein
- 100 mg/L 2,6 di-FBA (BH-26, BH-27)
- 100 mg/L 2,3,4,5 tetra-FBA (BH-24, BH-25)
- 10 mg/L pyridone
- 10 mg/L rhodamine WT
- 1 ml/L microspheres

and, starting 9/2/98:
- 10 mg/kg $NiCl_2 \cdot 6H_2O$ (2.47 mg/kg of Ni^{2+})
- 10 mg/kg $MnCl_2 \cdot 4H_2O$ (2.78 mg/kg of Mn^{2+})
- 10 mg/kg $CoCl_2 \cdot 6H_2O$ (2.48 mg/kg of Co^{2+})
- 5 mg/kg $SmCl_3 \cdot 6H_2O$ (2.06 mg/kg of Sm^{3+})
- 5 mg/kg $CeCl_3 \cdot 7H_2O$ (1.88 mg/kg of Ce^{3+})

Phase 2C—50 ml/hr Injection Rate; Boreholes 18, 20, 21:
- 1000 mg/L lithium bromide
- 10 mg/L sodium fluorescein
- 100 mg/L 2,6 di-FBA (BH 18)
- 100 mg/L penta-FBA (BH 20)
- 100 mg/L 2,4 di-FBA (BH 21)
- 10 mg/L pyridone
- 10 mg/L rhodamine WT
- 1 ml/L microspheres

and, starting 9/2/98:
- 10 mg/kg $NiCl_2 \cdot 6H_2O$ (2.47 mg/kg of Ni^{2+})
- 10 mg/kg $MnCl_2 \cdot 4H_2O$ (2.78 mg/kg of Mn^{2+})
- 10 mg/kg $CoCl_2 \cdot 6H_2O$ (2.48 mg/kg of Co^{2+})
- 5 mg/kg $SmCl_3 \cdot 6H_2O$ (2.06 mg/kg of Sm^{3+})
- 5 mg/kg $CeCl_3 \cdot 7H_2O$ (1.88 mg/kg of Ce^{3+})

Note: The use of short-lived radionulide tracers are under consideration for use in Phase-3 testing for performance confirmation.

3.3.3 Synthetic pore-water recipe

To minimize the reactivity of the tracer solution with the country rock, a synthetic pore water, based on measured in-situ composition (Section 4), is used as a matrix for the tracers in solution.

Phase-1 Synthetic Pore Water:
- 76.8 mg/kg $SiO_2 \cdot nH_2O$ (amorphous silica)
- 36.8 mg/kg $CaCl_2 \cdot 2H_2O$ (calcium chloride dihydrate)
- 44.8 mg/kg $Ca(NO_3)_2 \cdot 4H_2O$ (calcium nitrate tetrahydrate)
- 3.8 mg/kg NaF (sodium fluoride)
- 10.7 mg/kg Na_2SO_4 (sodium sulfate)
- 51.2 mg/kg $NaHCO_3$ (sodium bicarbonate)
- 9.0 mg/kg $KHCO_3$ (potassium bicarbonate)
- 36.9 mg/kg $MgSO_4 \cdot 7H_2O$ (magnesium sulfate heptahydrate)
- 7.8 mg/kg $Ca(OH)_2$ (calcium hydroxide)

Phase-2 Synthetic Pore Water:

Phase 2 is identical to Phase 1 with the exception that, due to the large quantities required, the source of water is J-13 water that has been deionized (DI) using resin cartridges. This results in a DI water with approximately 30 ppm Si so that no additional silica is added.

3.4 Injection and Sampling Borehole Systems

Injection and sampling of the liquid tracers was

accomplished by two pneumatically inflated borehole sealing and measurement systems (Fig. 2). To allow visual inspection of the injection points under both standard and UV illumination, a transparent packer system was developed for the injection holes. To accomplish moisture sampling in the collection boreholes, inverting membranes were fabricated with mesh pockets to retain absorptive sample pads. The inverting membranes are removed from the boreholes regularly (as frequently as weekly) for sample-pad removal and replacement, whereas the injection packers remain in the holes for the duration of the test program. Each system is maintained at slight overpressure (1.7 to 3.5 kPa) to maintain contact between the sampling/injection pads and the tuff and, also, to prevent circulation of air within the borehole.

A special transparent packer design was developed for use in the tracer-injection systems (Fig. 3). Modular units, approximately 2.5 m long and 10 cm in diameter, were assembled to both seal the borehole and support the injection pads and moisture sensors. The design incorporates moisture sensors mounted to the outside of the packers to monitor both ambient soil moisture and injection moisture. The packers were sized to the length of each borehole. In boreholes exceeding 2 m in length, multiple packers were coupled together to achieve the correct borehole depth. Each packer or set of packers was inflated, and the pressure maintained, via a pressurization manifold supplied by a small, DC-operated diaphragm pump. A pressure range of 1.7 to 3.5 dPa (0.25 to 0.50 psi) is sufficient to maintain packer/moisture sensor contact with the inside of the borehole. The transparent nature of the packer allows viewing of the interior of the test borehole at any desired depth using a

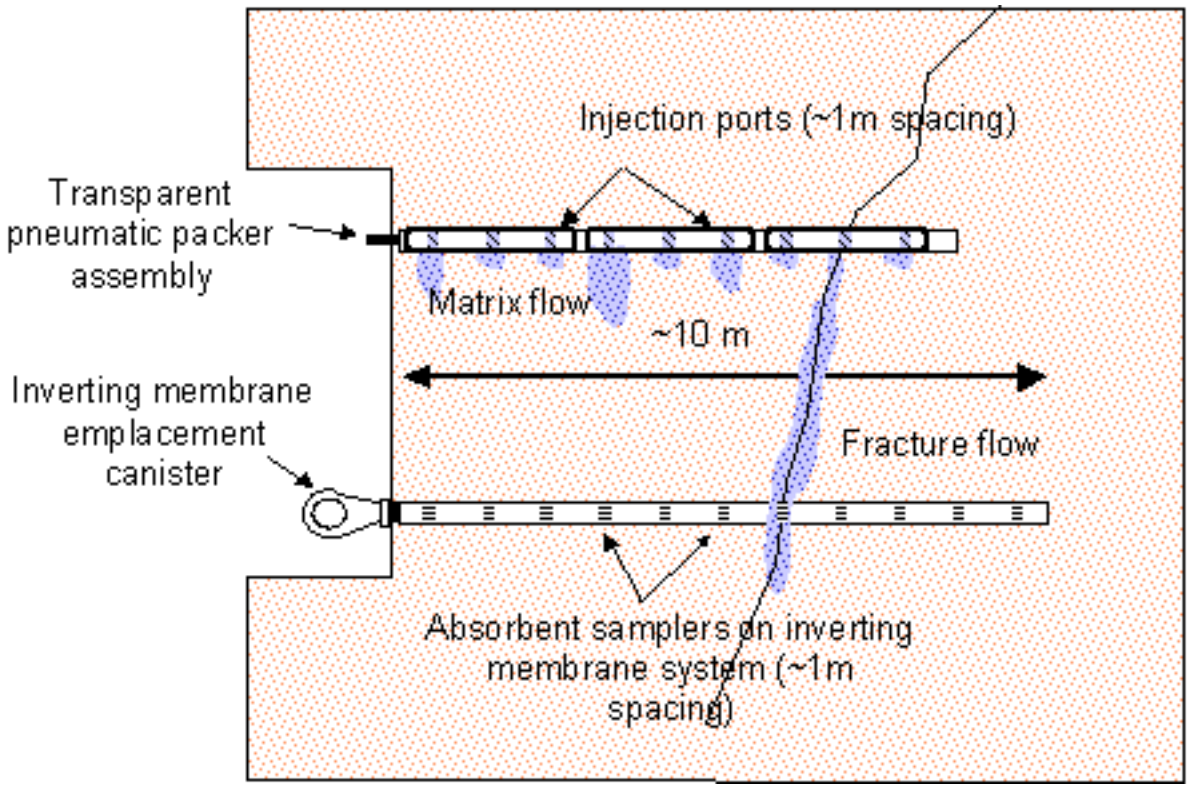

Figure 2. Injection and Collection Systems. The light blue areas above show hypothetical movement of tracer, including rapid transport along a fracture, between the upper layer of injection ports and the lower collection system.

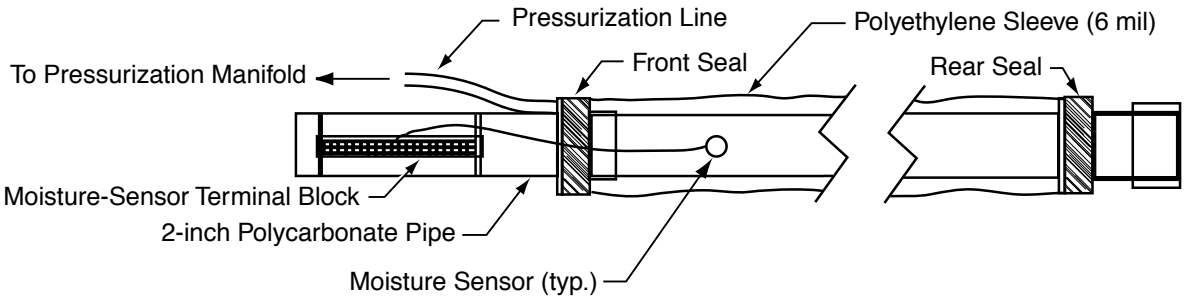

Figure 3. Injection System. The schematic diagram above shows the polyethylene sleeve that acts as an inflatable, transparent packer in the injection system. A moisture sensor, built by Science and Engineering Associates (SEA), is attached to the outside.

1-in diameter color video camera moved in and out of the packer center tube under both visible and UV illumination. Both the exterior polyethylene membrane and the inner polycarbonate center tube of the packer are transparent to UV light, allowing visualization of any fluorescent tracer present in injection lines, injection pads, or anywhere in the test borehole. The borehole can also be viewed with the video camera and incandescent light, which allows inspection of packers or borehole geology.

Moisture sensing and sampling were accomplished using pneumatically emplaced inverting membranes. These membranes are constructed of double-coated polyester fabric welded into tubular form nominally 10 cm in diameter. On one side of the membrane, a mesh is fabricated to form a pocket for absorbent sample pads. The pocket runs the length of the membrane and allows emplacement of sampling pads (stacks of filter paper) at any desired spatial frequency (Fig. 4). The membrane is deployed and retrieved from a pressurized canister (Fig. 5).

3.5 Moisture Sensors

Simple resistive moisture sensors were installed to diagnose the relative moisture state of the injection pads and the arrival of liquid tracer at the sampling-pad membranes. These sensors, built by Science and Engineering Associates (SEA), consisted of two wires separated a fixed distance embedded in an absorbent-pad assembly. Their signal level was sensed by the Campbell Scientific dataloggers, using an alternating polarity resistance measurement technique to avoid charge polarization. Although the sensor output is not quantitative, the values successfully indicated the general state of the sensing location: dry pads before installation tended to be in the range of 300 to 500 kohm, pads equilibrated with the tuff moisture showed a resistance of 80 to 100 kohm, and pads sensing the arrival of tracer (fluorescene dye being conductive) were distinctly lower in resistance at 10 to 30 kohms. These moisture indications were meant to guide the inverting-membrane sampling operations (indicating tracer arrival) and diagnose the injection-pad moisture state, indicating loss of injection or over-injection.

Approximately 250 moisture sensors were built and installed in both the tracer-injection and collection systems for all phases of the field test. These sensors are composed of two strands of 30-gauge wire, a 2.5-cm by 2.5-cm strip of chemically pure cotton, bonding web, and a bead of epoxy. To build a sensor, two strands of wire were cut to a desired length, one end of each wire was stripped 1 cm, and the exposed wire was bent and placed on

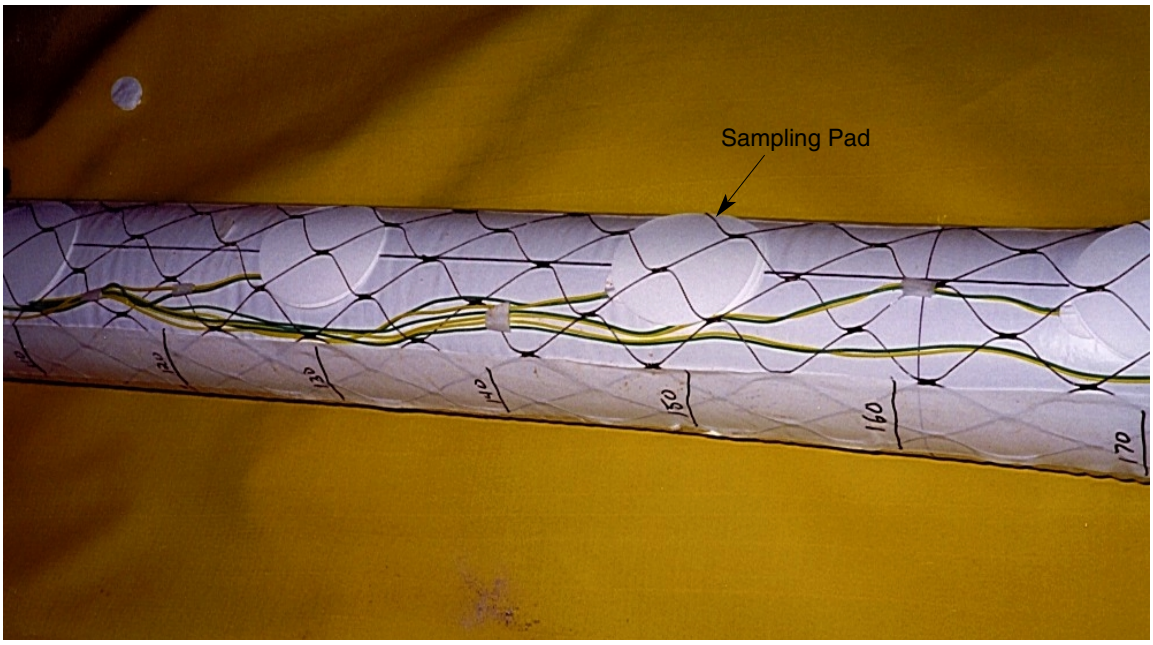

Figure 4. Collection Membrane. The photo shows details of the collection membrane, including sampling pads (stacks of filter paper) placed along the mesh pocket and the electrical leads to the SEA moisture sensors, which are under the sampling pads.

Figure 5. Emplacement Canister. The photo shows the pressurized emplacement canister and the collection membrane during initial installation of sampling pads.

the square of fabric such that two exposed wires were 1 cm apart (Fig. 6). Next, a piece of bonding fabric was inserted, the fabric was folded on top of the assembly, and a warm iron pressed the fabric, thus activating the bonding web. The final steps included knotting the wire just beneath the sensor and applying a thin layer of epoxy for strength.

The sensors operate by measuring resistance across the exposed leads of the wires. Moisture

absorbed by the fabric reduces the resistance between the two exposed wires. The wetter the fabric, the lower the resistance. If the sensor is dry, the circuit is open, and therefore, infinite resistance is produced.

The moisture sensors were installed on the injection packers by taping the wire just below the knot to the membrane and running the wire extension towards the exit end of the membrane. A different approach was used for the sensor installation in the inverting-membrane collection system, because these membranes were to be pulled in and out of the borehole multiple times over the duration of the unsaturated-zone transport test. The sensors were woven through the netting on the outside of the membrane and then tied onto the webbing at a desired location. This installation process prevents the sensors from being pulled from the fabric square when there is stress on the wires (Fig. 7).

3.6 Configuration Files Used for Phase-1 and Phase-2 Data Collection

Campbell Scientific dataloggers are being used to collect measurement data from sensors and instrumentation that can be used to either help understand or validate the collected experimental chemical data or aid in ongoing decisions in conducting the Busted Butte saturated-flow tracer experiments. Environmental and experimental control data are measured and collected with two dataloggers. The data are stored in the dataloggers at user-defined intervals. A computer outside the tunnel portal connects to the dataloggers periodically via a short-haul modem and downloads the data. The data can then be transferred to a remote computer using a phone link and modem. Figure 8 shows a schematic of the data-collection setup.

3.6.1 Phase 1

There were three operating programs written for the Phase-1 Busted Butte tests. Each was written for a Campbell Scientific 21X datalogger. The first operating program measured the pressure in the injection/sampling manifold, output from 14 moisture sensors, the panel temperature and battery voltage of the 21X datalogger, and the number of times the syringe pumps cycled in a given period of time. This operating program was used for the Phase-1A injection tests.

The second operating program measured the relative humidity, air temperature, and atmospheric pressure in the experimental area, output from 12 moisture sensors, the battery voltage of the 21X datalogger, and the number of times the syringe pumps cycled in a given period of time. Prior to the beginning of Phase 1B, it was decided that the two programs could be combined to run on a single 21X datalogger if a Campbell Scientific AM416 Relay Multiplexer was used. Eliminating a datalogger reduced the complexity of the wiring from

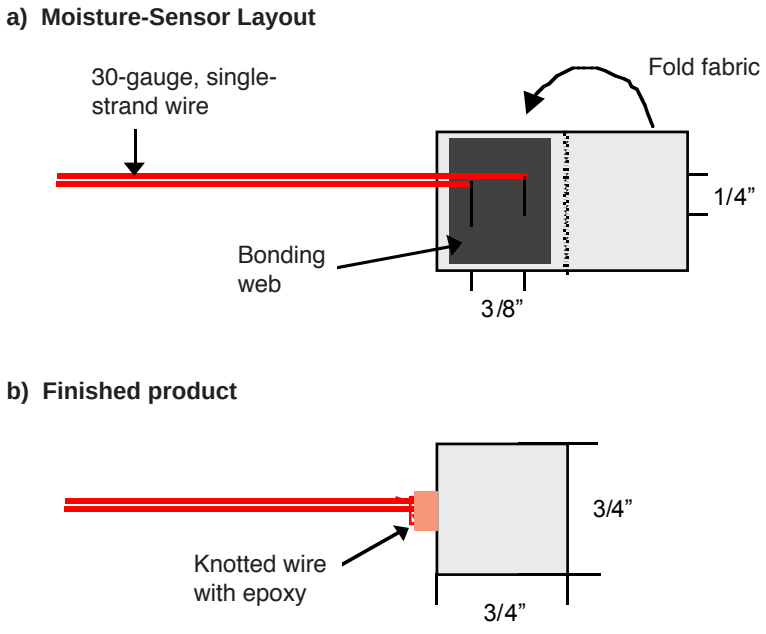

Figure 6. Design of Moisture Sensor. Part a) shows the layout of a moisture sensor and wire before the fabric has been folded over and then b) after folding and bonding has taken place.

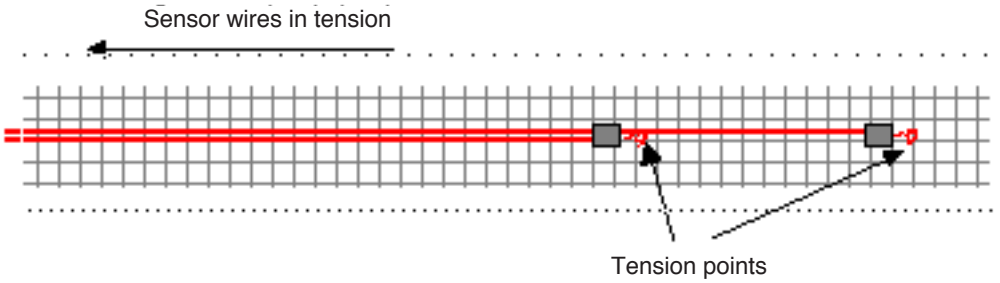

Figure 7. Collection-Sensor Installation. The wire leads to the moisture sensors in the collection system were woven through the webbing on the outside of the collection membrane opposite to the direction of the leads. This technique keeps the sensors from being torn from their fabric squares during periodic removal and replacement of the membranes.

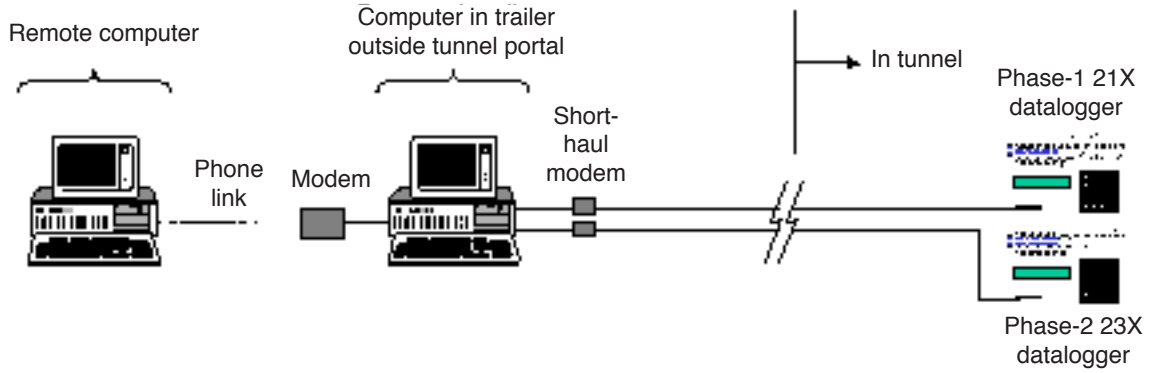

Figure 8. Data Collection. This schematic shows the setup for collection of data from the Busted Butte transport experiments.

the tunnel to the control computer outside the tunnel. The combined code measures everything that the other two codes measured plus the output from additional moisture sensors (a total of 32) and from an anemometer.

3.6.2 Phase 2

The operating program for the Phase-2 experiment is complex. It measures over 200 different sensors, controls the injection of the tracer (by turning the syringe pumps on and off via a Campbell Scientific REL6 relay board), and performs a number of system checks. The code allows the user to define the interval that data will be stored and to define two separate injection intervals for the tracer. In addition, it was designed so that the environmental sensors (relative humidity, air temperature, atmospheric pressure, and wind speed in the vent system) presently being collected with the 21X datalogger can be measured with a 23X datalogger once the Phase-1 tests are completed.

The following data are (or can be) collected with the 23X datalogger:

- environmental control information,
- ambient pressure,
- ambient temperature,
- relative humidity,
- wind speed in the vent system,
- experimental control information,
- pressure in the injection/sampling membrane manifolds,
- weight recorded by each load cell (total of 7 cells),

number of times banks of pumps have been activated,
relative saturation at all injection points (via 100 moisture sensors),
relative saturation at the face of the 3 boreholes that will have tracer fluid injected at a rate of 50 ml/hr (via 3 moisture sensors), and
relative saturation along sampling membranes (via 88 moisture sensors).

Additional miscellaneous control information concerning the Campbell Scientific dataloggers is presented in Appendix B.

3.7 Use of Numerical Simulations in Scoping Calculations for Test Design

Prior to starting Phase 1A, scoping simulations were run to help design Phase-1A and subsequent tests. These scoping simulations were used to identify how the planned injection system would work and to estimate reasonable injection rates for the test. For these preliminary simulations, the same single-borehole model system was used with a few modifications. The most significant modification was to use Bandelier Tuff Unit-1a properties (Krier et al. 1997) for the rock matrix. Bandelier Tuff properties were used to try to compare simulation results with preliminary experiments that SEA were running in their lab (below). SEA's experiments were used to test the injection system and to make preliminary estimates of water and tracer travel distance in Phase 1A.

The experimental setup differed from that of the UZTT single-borehole configuration primarily in borehole diameter and system size. The sample itself was approximately 0.7 m in diameter, whereas the model system was much larger. The only difference between model and experiment expected to arise from difference in domain size was an influence of boundary conditions. Tracer distribution in the experiment was more likely to be affected by its boundaries than was the model.

The difference in borehole diameter was slight, with the experiment's borehole slightly larger: 0.108 m as opposed to 0.1 m. In the experiments, the tracer solution was injected into a pad with dimensions of 0.051 m by 0.51 m. The model injection-pad dimensions were reduced to 0.046 m by 0.051 m to correct proportionally for the smaller model borehole.

Initial conditions in the model were set up to mimic those of the experiment. The system was allowed to equilibrate from an initial rock-matrix saturation of 60%, initial pad saturation of 25%, side boundary conditions with saturation fixed at 60%, and air pressure fixed at atmospheric.

The experiment was stopped at 1.8 days, and measurements of the spread of the fluorescing tracer were made. The concentration of the observable fluorescein from the experiments was estimated to be 50%. Output from the numerical model showed that the average apparent radius of the 50%-concentration isosurface was 0.09 to 0.10 m. The values from the experiment were only slightly larger. The comparison was considered a reasonable match.

For the Tac and Bandelier matrix materials used in these simulations, the size and shape of the pad does not influence the fluid movement due to the overwhelming capillarity of the porous rock and the similar basic material parameters between the polypropylene and the rock. In all of the simulations in these two materials, the pad wets only locally to the injection point.

3.7.1 Tracer-injection system test

(This section is from William E. Lowry, Science and Engineering Associates, Santa Fe, NM.)

The purpose of the tracer-injection system test was to validate the methodology and experimental setup in preparation for the Phase-1 field-scale test at the Busted Butte site. The objectives of the lab-scale test were to:

- operationally test all the system components,
- determine an appropriate liquid-tracer injection rate, and

- check the FEHM simulations on a laboratory scale.

The rock used in the test was a sample of Bandelier tuff, unit 1v, just above the vapor-phase notch, taken from the Los Alamos Truck Route roadside just outside the Los Alamos National Laboratory. The sample of Bandelier tuff was used because its material properties were very similar to the Calico Hills formation and because of the difficulty in obtaining a large-enough off-site sample of the Calico Hills formation from the Nevada Environmental Park.

The sample of Bandelier tuff was cored using a 4-in masonry drill bit. It was then placed in front of a fan for three days to dry. The rock was weighed, placed in a water bath for two days to saturate, weighed again to determine the water uptake required to reach 100% saturation, and finally allowed to dry for approximately 24 hr until a 60% saturation was reached. A 60% saturation was used to coincide with the in-situ saturation found in the Calico Hills formation at the Busted Butte site. The sample of Bandelier tuff was then placed in a double-lined plastic bag to allow the moisture to uniformly distribute itself prior to the test, and it was kept covered during the test to prevent drying.

The injection membrane consists of moisture sensors, small polyethylene tubing, and a polypropylene absorbent pad, all attached to a urethane-coated polyester clear membrane. The membrane itself is attached to the ends of a clear polycarbonate, 2-in diameter tube. The clear polycarbonate tube allows access for video surveys in the borehole. Moisture sensors, composed of two wires sandwiched between Whatman 42 filter paper, were secured to the membrane at 0, 90, 180, and 270 degrees on the equator with respect to the injection point and at 0 degrees and 6 in from either side of the injection point. The moisture-sensor leads were connected to a terminal strip attached to the end of the clear polycarbonate tube. A 2-in square piece of absorbent pad was taped to the membrane over the top of a moisture sensor, exposing approximately 1 in^2 of pad material. The end of the 1/8-in OD, 1/16-in ID polyethylene tubing was placed in the middle of the square pad and taped to the membrane. Finally, an 8-in wide strip of absorbent material, with the ends sewn together to create a 4-in diameter cylinder, was slid over the top of the clear membrane and injection tubing. The absorbent pad was taped to the clear membrane leaving a 6-in wide exposed pad area.

Equipment used in the experiment consisted of an air pump to maintain the clear membrane pressure, a syringe pump used to deliver a prescribed volume of tracer to the injection pad, and a Campbell Scientific 21X data logger connected to a laptop computer to collect and analyze data.

The pump maintained the clear packer pressure to nominally 0.25 to 1 psi. This pressure allowed intimate contact between the borehole wall and the injection pad without significantly compressing the pad and causing a reduction in effective pad porosity.

A syringe pump, manufactured by Soil Measurement Systems, was used to deliver tracer to the injection pad on the clear membrane. This multichannel syringe pump uses replaceable plastic syringes to maintain constant flow rates over long periods of time. The pump is capable of both continuous and intermittent pumping. The intermittent mode allows precise flow control over long periods of time. Pump intervals and pump stroke length are adjustable to deliver a wide range of flows. In addition, the flow rate can be varied using multiple syringes and different sized syringes. The multichannel syringe pump was calibrated by SEA in the laboratory using 5 different syringes (1, 3, 5, 10, and 20 ml) as well as variable stroke lengths.

A single-channel, 3-ml syringe was used to deliver a fluorescein and rhodamine tracer through the polyethylene tubing to the injection pad. Tracer was drawn from a graduated cylinder mounted on top of a triple-beam scale. The tracer concentration was 25 ml of dye and 2000 ml of distilled

water. The syringe pump was set to deliver 10 ml of tracer every hour for the duration of the test. Tracer volume delivered to the injection pad was also calculated using a mass-difference approach and the triple-beam scale.

The 21X datalogger measured resistivity from the six moisture sensors, as well as resistivity for two control resistors, temperature, membrane packer pressure, and syringe pump strokes.

The moisture sensor in the injection pad sensed tracer arrival with the first stroke of the syringe pump. A decrease in resistivity is associated with each injection of the syringe pump, and a subsequent rise in resistivity is associated with the sensor drying as tracer is transported away from the injection pad and into the rock.

After approximately 40 hr of testing and 400 ml of fluorescein tracer delivered, the injection system was shut down, and the clear packer was removed to examine the tracer transport to the rock. Examination of the rock hole with UV light showed a spherical pattern of tracer on the wall. No tracer was found on the outside surface of the rock. The packer injection pad was then replaced, the packer was reinserted into the rock, and injection of rhodamine tracer at 10 ml/hr was initiated. The second test lasted for 18 hr and delivered approximately 180 ml of rhodamine tracer. Results of the second injection showed a similar but smaller-diameter spherical pattern of tracer on the rock hole wall as the first test. After observing the tracer patterns on the rock walls, the rock was split roughly perpendicular to the axis of the rock hole using a hammer and chisel. Splitting the rock facilitated observation of the depth of tracer transport in the rock. Figures 9 through 11 show the size and distribution of the fluorescein (yellow-green) tracer and the rhodamine (pink) tracer.

3.7.2 Numerical simulations for test design

As noted above, for both Phases 1 and 2, numerical simulations are performed for test design purposes. Unstructured 2-D and 3-D grids matching the injection-system configuration are created with the GEOMESH software, and predictive simulations of flow effects and tracer migration are performed with FEHM (Fig. 12). The test design completed for Phase-1 and Phase-2 testing involves the use of laboratory measurements of hydrologic properties as well as the comparison between results obtained from laboratory tests and the scoping calculations. Due to the time requirements for obtaining data and the necessity for rapid turn-around times associated with the test design, the pretest modeling activities were limited to scoping calculations used in the design of the injection and collection. The simulations are designed to represent the experimental configuration as closely as possible and are used to scope the injection rates and travel distances for the tracer solution. The 82,000-node, 3-D unstructured grid used in the scoping calculations contains the full representation of the injection borehole, the 25-cm^2 injection pad, and 54 m^3 of the surrounding rock mass (Fig. 12). The FEHM simulations using this grid compare favorably with the two-day laboratory tests (Fig. 13). The code is presently used for test design by extending predictions to the one- to two-year duration of the tests (i.e., Phases 1 and 2).

Due to time constraints, injection of Phase-2 tracers overlaps Phase-1 testing. However, improvements from the comparison of Phase-1 results with Phase-1 numerical simulations will be used in improving the predictions on the behavior of the Phase-2 test block. Notably, the results on fracture-matrix interactions from Phase 1B will be used as input to the predictions in Phase 2, which may involve the transition from fracture-dominated to matrix-dominated flow and transport (i.e., Topopah Springs to Calico Hills transition).

3.8 Use of Numerical Simulations as Performance Measures

Determining the validity of current concepts for unsaturated-zone flow and transport, and simultaneously demonstrating and documenting the improvement of the model as new data are incor-

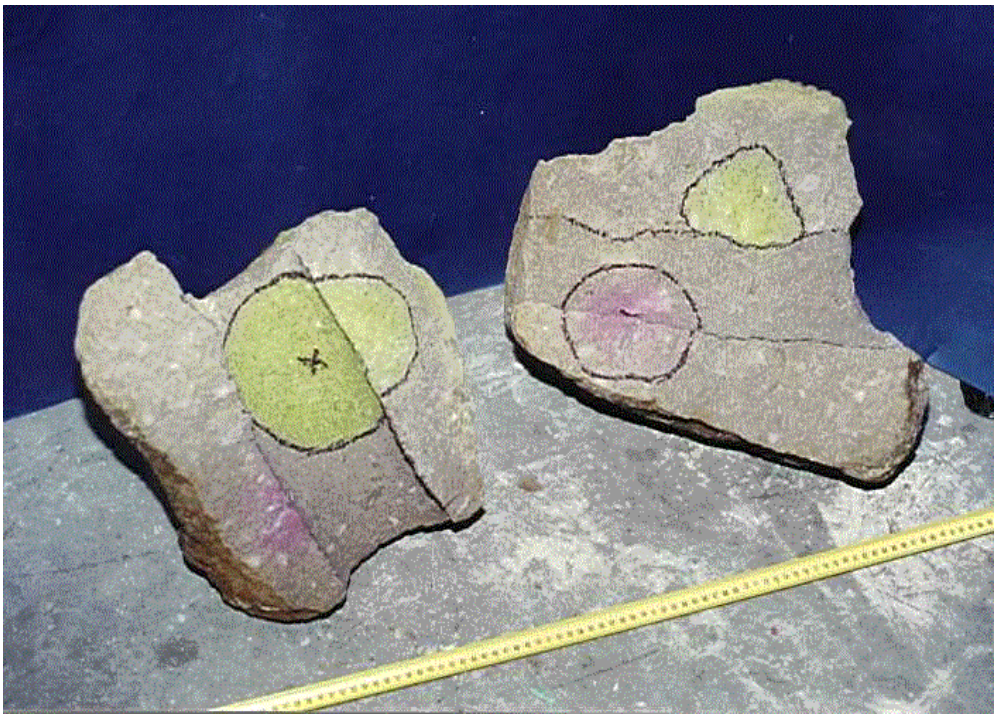

Figure 9. Block of Bandelier Tuff Used in SEA Laboratory Test. The block is broken in two along the axis of the injection hole. Traces of fluorescein dye (yellow-green) and rhodamine dye (pink) are visible and outlined in black.

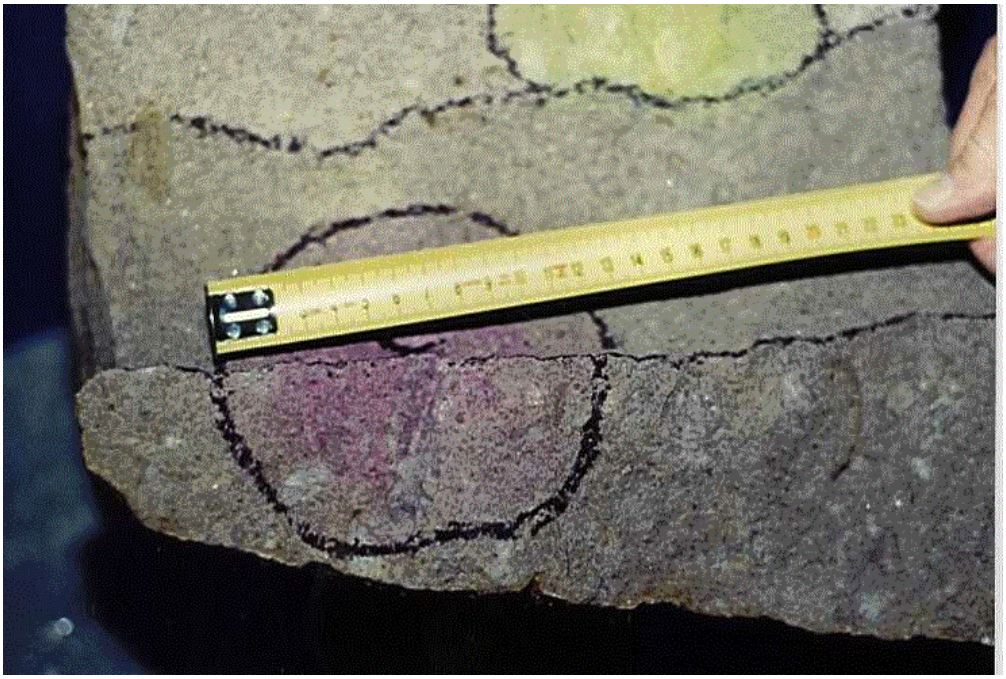

Figure 10. Rhodamine Dye Trace. Close-up of rhodamine dye trace (pink) on inside of borehole and penetrating into the Bandelier tuff sample.

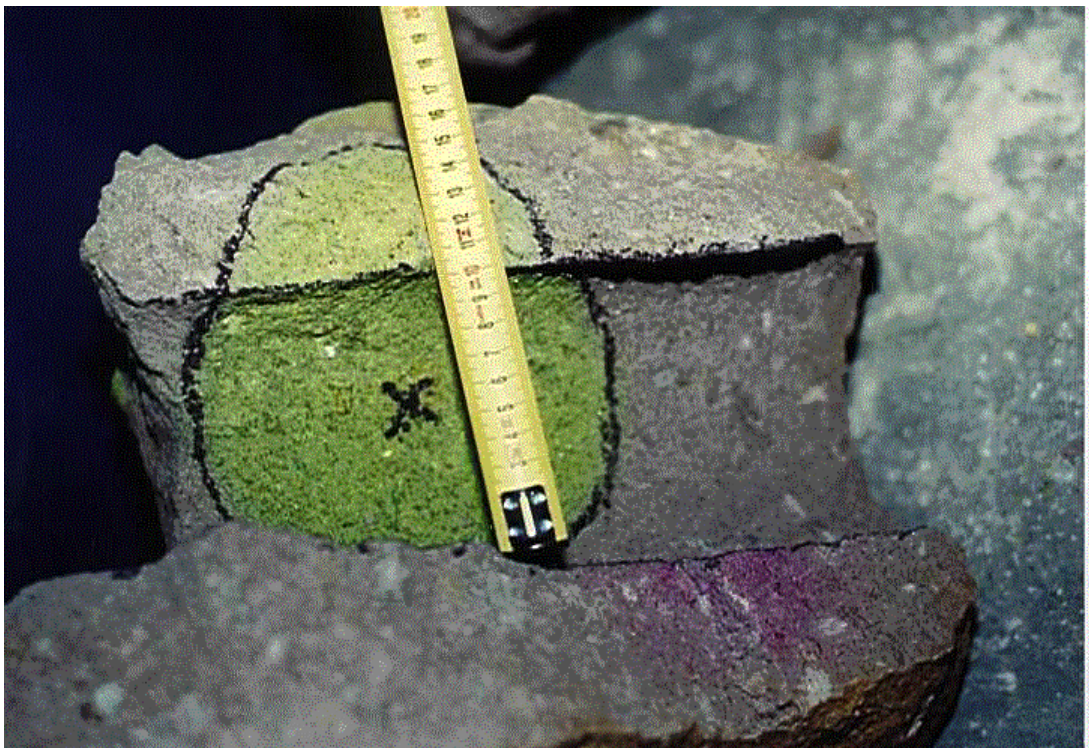

Figure 11. Fluorescein Dye Trace. Close-up of fluorescein dye trace (yellow-green) on inside of borehole and penetrating into the Bandelier tuff sample.

porated, requires making predictions throughout the different stages of the testing program. The cyclic process of prediction, measurement, and model refinement adopted in this work will result in increased confidence in the site-scale unsaturated-zone model. The predictive simulations will serve to document our ability to forecast the experimental results using current YMP databases and models.

Numerical simulations are, therefore, intimately involved in the prediction and analysis of the test phases as well as the scaling of parameters for the site-scale models. In support of the numerical models, hydrologic, geologic, mineralogic, and geochemical parameters from the test block are being measured. Furthermore, the physical state of the block (e.g., saturation and pore-water chemistry) and the boundary conditions are being measured for incorporation in the numerical models. Due to the time constraints of the field test, these measurements are being collected in conjunction with the test instrumentation rather than prior to it. However, the impacts of this procedure on formal predictions are minimal due to the phased development of the testing program. That is, parameters and boundary conditions necessary for the large block simulations are being measured during the single-borehole testing phase. The construction of a 500,000-node, 3-D computational grid for the test block using GEOMESH software is presently underway.

Because of the paucity of data for the properties of the Calico Hills rocks, the predictions are likely to produce erroneous results. However, this exercise serves to document the full impact of the test at Busted Butte on both YMP databases and models. As more data become available, these predictions will be updated and modified. At the end of the testing period and the concurrent laboratory and modeling activities, the Yucca Mountain Project will be improved, and a more defensible model that describes the flow-and-transport behavior at the

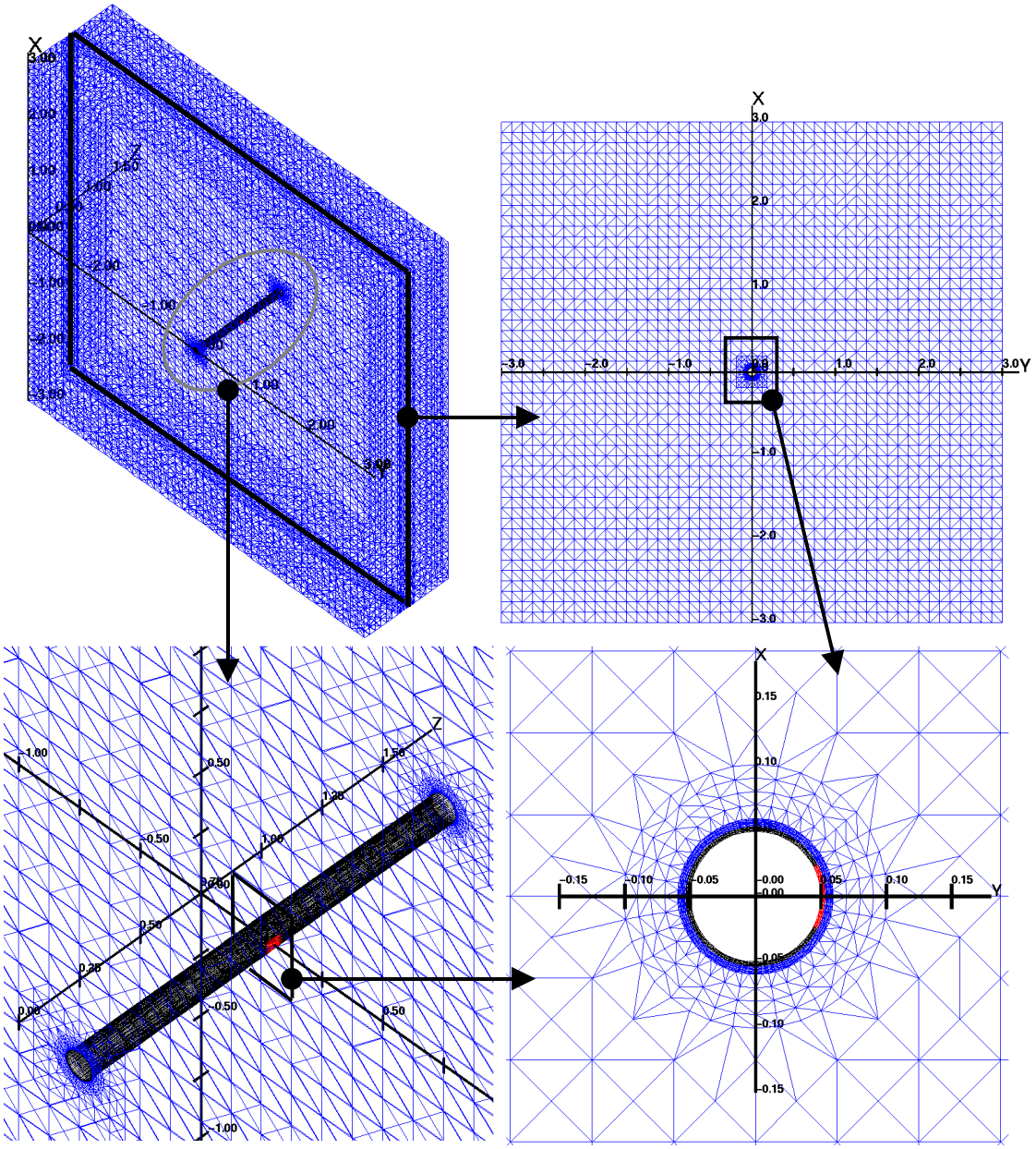

Figure 12. Single-Borehole Computational Grid. The figure shows the GEOMESH-generated computational grid for single-borehole simulations. The grid has 82000 nodes with the porous rock matrix in blue and the injection pad in red. The domain is 6 m × 6 m × 1.5 m.

site will exist. The abstractions based on this model will be incorporated into the Total Systems Performance Assessment for License Application (TSPA-LA) by the end of fiscal year 1999.

In addition to FEHM sensitivity analyses on a 3-D model of the test block, the performance measures for Phase 2 will involve a 2-D and 3-D stochastically derived code (i.e., FEHM-S). The developed stochastic model will give the means and the standard deviations for flow quantities such as pressure, saturation, and velocity. The mean pressure (saturation or velocity) can be used to estimate the pressure (saturation or velocity) field,

a) Front view (slice through borehole)

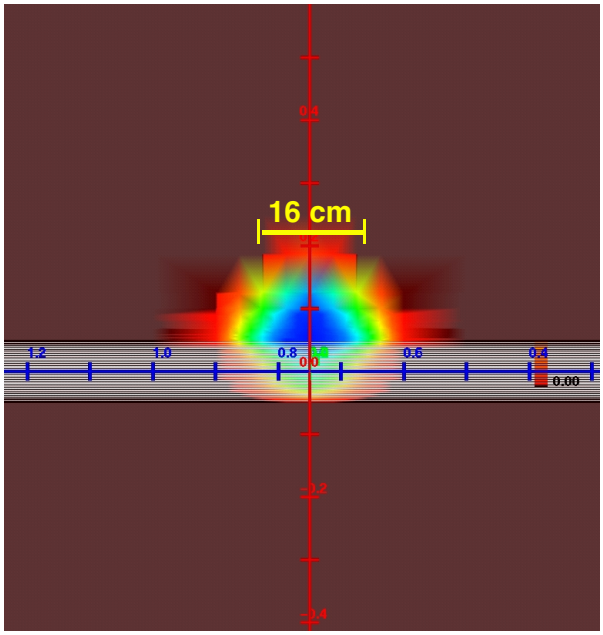

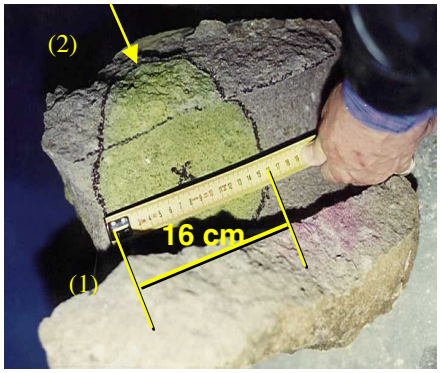

c) Laboratory Experiment (fluorescein dye)

Test Conditions:

Tracer: fluorescein dye
Injection rate: 10 ml/hr
Borehole diameter: 10 cm
Injection pad: 25 cm^2
Rock: Bandelier Tuff
Saturation: 0.6

Comparison of Results:

Infiltration diameter (1):
Experiment: ~ 16 cm
Simulation: 17–19 cm
Tracer migration (2) :
Experiment: ~ 6 cm
Simulation: ~ 7 cm

b) Angle view (behind borehole)

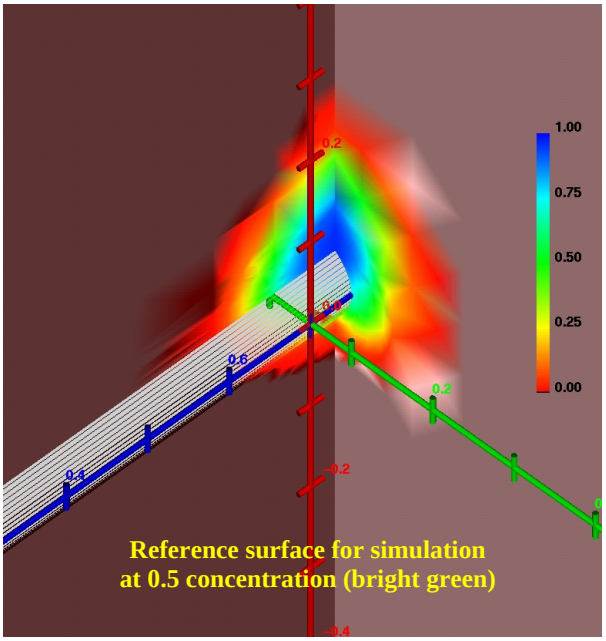

Figure 13. FEHM and SEA Comparison. The above figure compares the results of the scoping calculations using FEHM and of the SEA injection experiment on Bandelier tuff.

and the standard deviation measures the associated uncertainty (error) due to incomplete information about the medium properties. Calculated moment equations will be used to construct confidence intervals for the flow results, and the flow moments will serve as input for stochastic transport predictions. In this way, quantitative comparisons between test results and simulations can be made. Predictions using this methodology will be compared to multiple-realization, Monte Carlo simulations of the heterogeneous system. This work will be completed in fiscal year 1999 prior to Phase-2 test results.

3.9 Geophysical Techniques at the Busted Butte Unsaturated-Zone Test Facility

The original test plan for Busted Butte (Bussod et al. 1997, p. 155) relied on inverting-membrane collection-pad systems to collect UZ water samples for detailed tracer analysis at discrete points in the block and during final destructive mineback of the entire block. Recent successes of combined real-time geophysical monitoring techniques—ground-penetrating-radar tomography (GPR-T) and electrical-resistance tomography (ERT)—at the Large Block Facility and the ESF thermal tests suggest that these techniques may be used to provide real-time data on the advance of the tracer front through the block and enable us to optimize our collection-pad sampling schedule to collect data. Each of the techniques has advantages and drawbacks; by combining them, we obtain detailed, high-resolution, 3-D, calibrated, real-time monitoring of moisture and tracer movement through the unsaturated fractured medium. Specifically, ERT provides 3-D global coverage, GPR-T provides high spatial resolution, and neutron logging enables absolute moisture-content calibration. The techniques are listed below, along with their characteristics and the advantages they bring to the test program at Busted Butte.

ERT (electrical-resistance tomography)

- 3-D snapshot of moisture content and tracer front
- Covers entire test block
- Half-meter spatial resolution
- Measurements on demand (probably weekly or monthly)

GPR-T (ground-penetrating radar tomography)

- 2-D slices of moisture content
- Selected locations through available boreholes
- 1- to 10-cm spatial resolution
- Measurements at opportunistic intervals (tied to collection-borehole sampling frequency)
- Can determine matrix permeabilities

Neutron Logging

- 1-D moisture profiles along existing boreholes
- Provides absolute "ground-truth" moisture measurements to calibrate ERT and GPR-T
- 20-cm spatial resolution
- Measurements at opportunistic intervals

Ongoing geophysical monitoring is presently helping us guide the timing of collection-pad retrieval for detailed tracer analysis. Independent physical measurement techniques (collection pads and block mineback) will ultimately provide field-scale evaluation of geophysical techniques, increasing their applicability and acceptability for other Yucca Mountain Project activities. None of these techniques interfere physically with the test or with the testing schedule.

4. PRELIMINARY RESULTS

4.1 Geology of the Busted Butte Test Facility

Busted Butte is a small (2.5 km by 1 km) north-trending mountain block primarily made up of thick ignimbrite deposits of the Paintbrush Group. This fault-block uplift is bound by northeast- and north-trending normal faults, and it is split by a north-trending down-to-the-west normal fault that gives Busted Butte its distinctive appearance. Tuff units generally have dips less than 10° except where affected by drag near large faults. Small windows of older volcanic units, including the Calico Hills Formation, Wahmonie Formation, and Prow Pass Tuff, are exposed through colluvial deposits on the north and southeast sides of Busted Butte.

The test facility is located within a small horst on the southeast side of Busted Butte. The horst is 300 to 350 m wide and is bound by the down-to-the-west Paintbrush Canyon Fault on the west and by a down-to-the-east splay of the Busted Butte Fault on the east (Scott and Bonk 1984). Geologic units exposed in the vicinity of the test facility include, in ascending order, the Wahmonie Formation, the Calico Hills Formation, and Topopah Spring Tuff (Fig. 14). The test facility is constructed in the Topopah Spring Tuff and the Calico Hills Formation.

A brief description of geologic units in the underground test facility is given below. The Topopah Spring Tuff is described in terms of its thermomechanical subunits because this nomenclature best represents rock properties that control groundwater movement. It should be noted, however, that ignimbrite depositional units in the lower part of the Topopah Spring Tuff cross thermomechanical boundaries. In the lower Topopah Spring Tuff, thermomechanical properties are controlled by compaction and welding features, and these features are superimposed on depositional units whose surfaces have up to a couple of meters of relief.

4.1.1 Calico Hills Formation

Up to a meter of Calico Hills Formation is exposed in the test area of the facility in the lower walls of both the Main Adit and the Test Alcove. The Calico Hills Tuff consists of alternating beds of poorly cemented salmon-pink massive tuff and well-cemented, white ash beds.

The salmon-pink tuffs contain round to slightly elongated white vitric pumices that are generally less than a centimeter in diameter. The matrix is a mixture of fine ash, phenocrysts, and locally abundant fragments of black glass. The salmon-pink tuffs gradually become more deeply colored upsection, suggesting the upper parts of these units are more oxidized and may represent weakly developed paleosols. The clay content in these tuffs appears to be low, based on x-ray diffraction results (see Section 4.2).

There are two well-cemented ash beds intercalated with the salmon-pink tuffs in the Main Adit and Test Alcove. These ash beds are about 130 cm apart on the right rib of the Main Adit. The ash beds are 15 to 20 cm thick and typically form resistant ledges in outcrops outside of the test facility and resistant layers inside the facility. The results of hand augering suggest there may be additional ash beds in unexposed portions of the Calico Hills Formation below the floor of the test facility.

4.1.2. Topopah Spring Tuff

Tptpv1—The lowermost 1 to 1.5 m of the Topopah Spring Tuff is thermomechanical unit Tptpv1. The base of Tptpv1 is locally marked by a 3- to 4-cm coarsely bedded fall (?) deposit. This deposit consists of 0.5- to 3-cm pumice fragments and 0.25-cm black perlitic lava clasts. This thin deposit pinches out laterally and is similar to thin discontinuous beds of fall (?) deposits at the base of the Topopah Spring Tuff in outcrops outside of the test facility. A 4.5-cm-thick, crudely laminated shardy tuff overlies the fall (?) deposit. The shardy tuff is also discontinous laterally.

Above the thin bedded deposits, Tptpv1 consists of

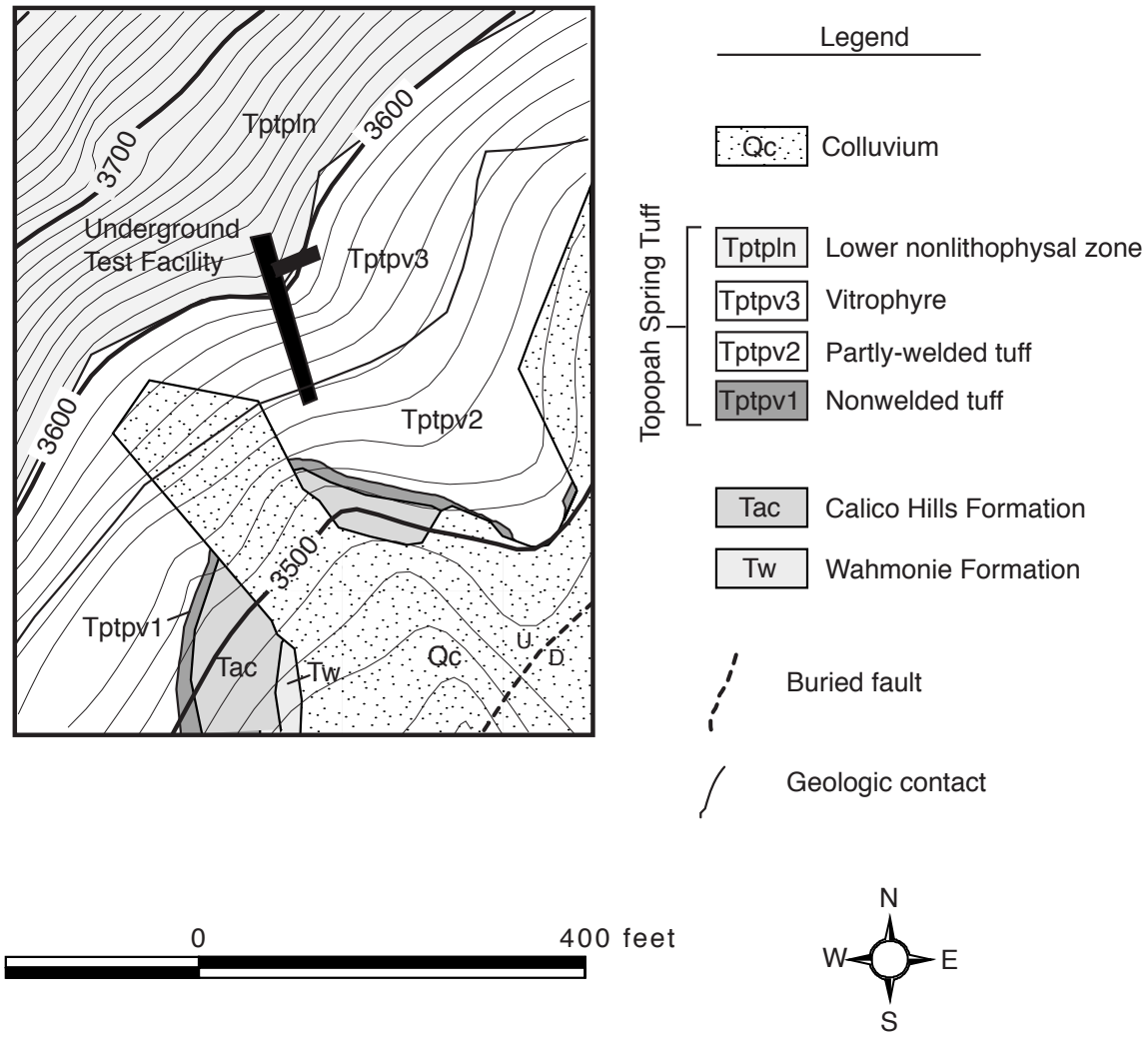

Figure 14. Busted Butte Geologic Map. The plot is a geologic map of the area around the underground test facility in the southeastern part of Busted Butte.

light gray nonwelded ignimbrites. The ignimbrite flow units contain medium-gray pumices in a pink-gray matrix. Near the top of Tptpv1, pumices are tan. Glassy lava fragments and red-brown lithics are common. Pumices increase in size and abundance upsection in individual ignimbrite flow units. The two lowermost ignimbrite flow units are separated by a bedded tuff that is 0.2 to 8 cm thick. The character of these bedded tuffs is variable, consisting of laminated shardy tuff in some places and clast-supported pumiceous deposits in others. Because of relief on the surface that these bedded tuffs were deposited on, they fall within Tptpv1 in the Test Alcove and within Tptpv2 towards the back of the Main Adit.

In the Test Alcove, the upper part of Tptpv1 is characterized by a distinctive zone of clay alteration typically about 70 cm thick. The clay occurs both as rinds around pumice clasts and as complete replacement of the pumices. The clays are typically reddish brown but also include small round bodies of white clay within the reddish-brown clays (giving it a mottled appearance). In some replaced pumices, white clay overlies layers of reddish-brown clay. Clay alteration also occurs in the tuff

matrix and along subhorizontal fractures. One such fracture contains four different layers of clay up to 1.5 cm thick. The lower boundary of clay alteration is undulatory and has up to 0.5 m of relief.

Tptpv2—Thermomechanical unit Tptpv2 is the highest stratigraphic unit exposed in the back of the Main Adit and in the Test Alcove area. It is characterized by tan, partly welded ignimbrite that has well-developed columnar joints. The matrix of these ignimbrites has a distinctive salt and pepper appearance due to the presence of black glass shards in a tan ashy matrix. Pumices are typically 1 to 6 cm in their long dimension and exhibit flattening ratios from 6:1 to 8:1. Welding increases upsection through Tptpv2, and rocks in this unit yield a distinctive clink when hit with a hammer.

4.2 Mineralogy of the Busted Butte Locality

The tables below and on the next page summarize the quantitative x-ray diffraction (XRD) data from surface samples at the Busted Butte test locality. Tables 1 to 3 are for the Tpt samples, and Table 1 provides the stratigraphic descriptions for the samples in Tables 2 and 3. The calcite and gypsum reported in the Tpt samples represent calcrete contamination in the surface samples.

The erionite detected in the altered sample from the Tptpln/Tptpv3 contact zone is the only occurrence of this hazardous mineral found at the site. A survey for erionite occurrence shows no other detectable erionite (detection limits of 250 ppm) in the strata below the Tptpln/Tptpv3 contact, where

Table 1. Descriptions of Samples Collected from Busted Butte for Erionite Survey.

Sample	Lithology
SPC 517960	altered interzone at the top of the lower vitrophyre (Tptpln/Tptpv3)
SPC 517962	upper densely welded perlitic subzone (upper Tptpv3)
SPC 517963	middle densely to moderately welded vitric subzone (mid Tptpv2)
SPC 517964	middle moderately to nonwelded vitric subzone (mid Tptpv1)
LANL #2814	lower densely welded perlitic subzone (lower Tptpv3)
LANL #2815	upper densely to moderately welded vitric subzone (upper Tptpv2)
LANL #2816	middle densely to moderately welded vitric subzone (mid Tptpv2)
LANL #2817	lower densely to moderately welded vitric subzone (lower Tptpv2)
LANL #2818	upper moderately to nonwelded vitric subzone (upper Tptpv1)
LANL #2819	lower moderately to nonwelded vitric subzone (lower Tptpv1)
LANL #2820	vitric pumice swarm at base of the Topopah Spring Tuff (basal Tptpv1)

Table 2. Quantitative X-Ray Diffraction Results for Erionite-Bearing Sample at Top of Lower Vitrophyre, Tpt.*

Sample	Smectite	Erionite	Chabazite	Clinoptilolite	Mordenite	Quartz	Feldspar	Mica/Illite	Total
Tptpln/Tptpv3									
SPC 517960	trace	0.021	2 ± 1	32 ± 5	4 ± 1	28 ± 4	33 ± 8	trace	99 ± 11

*Sample was run using the external standard method.

Table 3. Quantitative X-Ray Diffraction Results for Samples from Lower Tpt Section.

Sample	Smec-tite	Opal-CT/ Cristob.	Quartz	Feld-spar	Glass/ Amorph.	Hema-tite	Mica/ Illite	Cal-cite	Gyp-sum	Kaoli-nite	Total
Tptpv3											
SPC 517962	1 ± 1	2 ± 1	trace	4 ± 1	93 ± 2	—	trace	trace	—	—	100 ± 2
LANL #2814p1	1 ± 1	4 ± 1	trace	3 ± 1	92 ± 2	—	trace	—	—	—	100 ± 2
Tptpv2											
LANL #2815p1	—	4 ± 1	1 ± 1	5 ± 1	90 ± 2	—	—	trace	—	—	100 ± 2
SPC 517963	1 ± 1	—	trace	3 ± 1	95 ± 2	trace	trace	1 ± 1	trace	—	100 ± 2
LANL #2816p1	2 ± 1	4 ± 1	trace	4 ± 1	90 ± 2	—	trace	—	—	—	100 ± 2
LANL #2817p1	3 ± 1	3 ± 1	trace	3 ± 1	91 ± 2	—	trace	—	—	—	100 ± 2
Tptpv1											
SPC 517964	trace	—	trace	2 ± 1	95 ± 1	—	trace	3 ± 1	—	—	100 ± 1
LANL #2818p1	trace	2 ± 1	trace	2 ± 1	96 ± 1	—	trace	trace	—	—	100 ± 1
LANL #2819p1	3 ± 1	1 ± 1	trace	3 ± 1	91 ± 2	—	trace	trace	—	2 ± 1	100 ± 2
LANL #2820p1	2 ± 1	1 ± 1	4 ± 1	8 ± 1	84 ± 2	1 ± 1	trace	trace	—	—	100 ± 2

— = not detected trace = Trace abundance of < 0.5 wt% errors are conservative 2-sigma values

the Busted Butte test facility has been excavated.

The samples from the Tptpv2 and Tptpv3 intervals show that the poorly welded to nonwelded vitric portions of the lower Topopah Spring Tuff at this site are largely unaltered, without zeolites but with modest smectite occurrences.

Table 4a covers the Calico Hills Formation and the Wahmonie surface samples at the Busted Butte site. These samples are arranged in Table 4a by relative depth and show that the lowermost part of the Calico Hills Formation (Tac) contains appreciable amounts of clinoptilolite. The upper part of the Calico Hills Formation at this site, however, is characterized more by smectite than by zeolite alteration. Access to both types of alteration is, therefore, possible at this site. The lowest three samples from an auger hole (AUG-1) into the floor of the Busted Butte Alcove were analyzed (Table 4b) for comparison with the vitric Calico Hills Formation samples from outcrop. Alteration in the alcove samples is generally similar, with smectite greater than clinoptilolite. The mineral constituents in the alcove (especially the low biotite and feldspar components) are characteristic of the Calico Hills Tuff, indicating that any Wahmonie deposits are greater than 396 cm below the present alcove floor.

4.2.1 Comparative data: H-5 and SD-6

The excavated section at Busted Butte is in the lower Topopah Spring Tuff (Tptpv2 and Tptpv1; Tpbt1 poorly represented) and the upper Calico Hills Formation (Tac). The vitric nature of this section and the relatively low abundances of smectite and clinoptilolite alteration are similar to that in drill holes near the crest of Yucca Mountain, such as USW H-5 (Table 5) and USW SD-6 (Table 6). The increase in zeolitization at the base of the Calico Hills Formation, particularly in the Tacbt unit, is comparable to the localized zeolitization in the lower part of the Calico Hills Formation at Busted Butte (Table 4). The more detailed data from SD-6 are unfortunately incomplete because the sample acquisition is too recent for analyses, and the funds to complete these analyses have not been allocated. However, the

Table 4a. Mineral Abundances (weight %) in Calico Hills Formation (Tac) Surface Samples from Busted Butte.

Sample	Smectite	Clinoptilolite	Opal-CT/ Cristob.	Quartz	Feldspar	Glass	Hematite	Biotite	Total
vitric Tac									
DEB 3/90-10	1 ± 1	—	—	2 ± 1	11 ± 1	86 ± 2	—	trace	100 ± 2
DEB 3/90-9	6 ± 2	—	—	4 ± 1	15 ± 2	74 ± 3	—	trace	100 ± 3
DTV-97-2	2 ± 1	—	1 ± 1	1 ± 1	2 ± 1	94 ± 2	—	trace	100 ± 2
DEB 3/90-8a	—	—	1 ± 1	1 ± 1	1 ± 1	97 ± 2	—	trace	100 ± 2
DEB 3/90-8b	1 ± 1	—	1 ± 1	4 ± 1	7 ± 1	86 ± 2	—	trace	100 ± 2
DEB 3/90-7	3 ± 1	1 ± 1	1 ± 1	7 ± 1	12 ± 1	76 ± 2	trace	trace	100 ± 2
zeolitic Tac									
DTV-97-3	—	9 ± 1	1 ± 1	7 ± 1	16 ± 2	64 ± 3	1 ± 1	2 ± 1	100 ± 3
DEB 3/90-6	1 ± 1	12 ± 1	1 ± 1	7 ± 1	16 ± 2	62 ± 3	—	1 ± 1	100 ± 3
Wahmonie									
DEB 3/90-5	5 ± 2	—	—	1 ± 1	26 ± 3	54 ± 5	1 ± 1	9 ± 3	100 ± 5
DEB 3/90-4	4 ± 1	—	—	2 ± 1	24 ± 3	46 ± 6	2 ± 1	17 ± 5	100 ± 6

— = not detected trace = Trace abundance

Table 4b. Mineral Abundances (weight %) in Calico Hills Formation (Tac) Samples from an Auger Hole into the Floor of the Busted Butte Test Alcove.

Sample	Depth (cm)	Smectite	Clinoptilolite	Opal-CT/ Cristob.	Quartz	Feldspar	Glass	Hematite	Biotite	Total
vitric Tac										
AUG-1-P	375–383	3 ± 1	1 ± 1	1 ± 1	8 ± 1	12 ± 2	74 ± 3	trace	1 ± 1	100 ± 3
AUG-1-Q	383–389	6 ± 2	1 ± 1	1 ± 1	8 ± 1	18 ± 3	65 ± 4	trace	1 ± 1	100 ± 4
AUG-1-R	389–396	3 ± 1	1 ± 1	1 ± 1	7 ± 1	11 ± 2	76 ± 3	trace	1 ± 1	100 ± 3

trace = Trace abundance

data that are available indicate a distribution of alteration similar to that at Busted Butte. In considering the SD-6 and H-5 data, however, it is important to bear in mind that both drill holes had only partial core or cuttings recovery, potentially skewing the mineralogic information. A much more accurate picture of these poorly indurated vitric units is obtained by excavation, as was accomplished at Busted Butte.

4.2.2 Influence of partial zeolitization on hydrologic properties: Evidence from the exploration block

The data displayed in Fig. 15 show that zeolite abundances as low as 8% to 2% correlate with the sample porosity. Significant differences in the structure of sample porosity even occur in the transition from 0% zeolite content to 2% zeolite content. Whether such small differences in alteration mineralogy impact transport will be determined by

Table 5. Quantitative XRD Results for USW H-5 Core and Drill Cuttings.

Sample	Depth (m)	Smectite	Clinoptilolite	Mordenite	Tridymite	Cristobalite	Opal-CT	Quartz	Feldspar	Glass	Mica	Hematite	Calcite	Hornblende	Total
Tptpv3 482.2–505.7															
1590/1600	486.2	35 ± 10	10 ± 5	—	—	17 ± 5	—	—	40 ± 10	—	—	—	—	—	102 ± 16
1610 (DC)	490.7	—	—	—	—	2 ± 3	—	1 ± 1	7 ± 3	90 ± 5	—	—	—	—	100 ± 7
1630/1640	498.3	trace	—	—	—	2 ± 1	—	1 ± 1	9 ± 1	88 ± 2	trace	—	—	—	100 ± 2
1650/1660	504.4	—	—	—	—	5 ± 1	—	2 ± 1	4 ± 1	89 ± 2	trace	—	—	—	100 ± 2
Tptpv2 505.7–509.6															
1666 (DC)	507.8	50 ± 10	10 ± 5	—	—	12 ± 3	—	1 ± 1	25 ± 5	—	—	—	—	—	98 ± 13
Tptpv1 509.6–517.9															
Tpbt1 517.9–519.7															
Tac 519.7–573.0															
1710/1720	522.7	3 ± 2	—	—	—	5 ± 3	—	5 ± 3	20 ± 10	70 ± 10	—	—	—	—	103 ± 15
1750 (DC)	533.4	—	trace?	—	—	5 ± 5	—	2 ± 3	5 ± 5	85 ± 5	—	—	—	—	97 ± 9
1762 (SW)	537.1	—	—	—	—	1 ± 1	—	1 ± 1	5 ± 5	95 ± 5	—	—	—	—	102 ± 7
1760/1770	538.0	—	6 ± 1	—	—	—	4 ± 1	3 ± 1	6 ± 1	81 ± 2	—	—	—	—	100 ± 2
1800 (SW)	548.6	—	—	—	—	2 ± 3	—	2 ± 3	10 ± 5	85 ± 5	1 ± 1	—	—	—	100 ± 8
1820/1830	556.3	trace	4 ± 1	—	—	—	2 ± 1	4 ± 1	10 ± 1	80 ± 2	—	—	—	—	100 ± 2
1852 (SW)	564.5	—	—	—	—	—	—	2 ± 3	7 ± 3	90 ± 5	1 ± 1	—	—	—	100 ± 7
1875 (SW)	571.5	—	trace?	—	—	—	trace?	2 ± 3	5 ± 5	92 ± 3	—	—	—	—	99 ± 7
Tacbt 573.0–592.0															
1890/1900	577.6	1 ± 1	11 ± 1	—	—	—	3 ± 1	4 ± 1	6 ± 1	75 ± 2	—	—	—	—	100 ± 2
1900/1910	580.6	trace	10 ± 1	—	—	—	1 ± 1	3 ± 1	8 ± 1	78 ± 2	trace	—	—	—	100 ± 2
1910/1920	583.7	trace	18 ± 1	—	—	—	5 ± 1	5 ± 1	7 ± 1	65 ± 2	trace	—	—	—	100 ± 2
1917 (SW)	584.3	—	25 ± 5	—	—	—	10 ± 5	30 ± 5	35 ± 10	—	trace	—	—	—	100 ± 13
1920/1930	586.7	3 ± 1	52 ± 3	—	—	—	7 ± 2	14 ± 1	16 ± 3	6 ± 5	2 ± 1	—	—	—	100 ± 5
1930 (DC)	588.3	2 ± 3	50 ± 10	—	—	—	—	15 ± 5	30 ± 5	—	1 ± 1	—	—	—	98 ± 13

— = not detected trace = Trace abundance

Table 6. Quantitative XRD Results for Samples from Drill Hole USW SD-6.

Sample	Depth (m)	LANL number	Smectite	Clinoptilolite	Tridymite	Cristobalite	Opal-CT	Quartz	Feldspar	Glass	Hematite	Mica	Hornblende	Calcite	Total
Tptpln 378.0–443.8															
1450.3/1450.5	442.1	2975p1	—	—	—	12 ± 1	—	30 ± 2	56 ± 8	—	trace	trace	—	—	98 ± 8
Tptpv3 443.8–455.7															
1456.0/1456.2	443.8	2976p1	23 ± 7	3 ± 1	—	—	13 ± 4	2 ± 1	23 ± 3	36 ± 8	—	—	—	—	100 ± 9
1473.2/1473.3	449.1	2977p1	1 ± 1	—	—	—	5 ± 1	1 ± 1	4 ± 1	89 ± 2	—	trace	—	—	100 ± 2
1477.0/1477.2	450.3	2978p1	1 ± 1	—	—	—	6 ± 1	2 ± 1	7 ± 1	84 ± 2	—	trace	—	—	100 ± 2
1479.5/1479.7	451.0	2479p1	—	—	—	—	7 ± 2	1 ± 1	5 ± 1	85 ± 2	—	trace	—	2 ± 1	100 ± 3
1482.4/1482.5	451.9	2980p1	—	—	—	—	6 ± 1	1 ± 1	5 ± 1	88 ± 1	—	—	—	—	100 ± 2
1486.8/1486.9	453.2	2981p1	—	—	—	—	7 ± 2	1 ± 1	6 ± 1	86 ± 2	—	trace	—	—	100 ± 2
1489.8/1490.0	454.2	2982p1	—	—	—	—	12 ± 3	1 ± 1	10 ± 1	76 ± 3	—	1 ± 1	—	—	100 ± 3
1493.0/1493.2	455.1	2983p1	—	—	—	—	13 ± 3	1 ± 1	9 ± 1	77 ± 3	—	trace	—	—	100 ± 3
Tptpv2 455.7–461.5															
1496.5/1496.7	456.2	2984p1	—	—	—	—	17 ± 4	1 ± 1	11 ± 2	71 ± 4	—	trace	—	—	100 ± 5
1500.1/1500.2	457.3	2985p1	2 ± 1	—	—	—	17 ± 4	1 ± 1	12 ± 2	68 ± 4	—	trace	—	—	100 ± 5
1503.3/1503.4	458.2	2986p1	2 ± 1	—	—	—	20 ± 6	2 ± 1	16 ± 2	60 ± 6	trace	trace	—	—	100 ± 6
1506.2/1506.3	459.1	2987p1	3 ± 1	—	—	—	18 ± 5	1 ± 1	13 ± 2	65 ± 5	trace	trace	—	—	100 ± 6
1509.2/1509.3	460.0	2988p1	3 ± 1	—	—	—	15 ± 4	1 ± 1	11 ± 2	70 ± 4	trace	—	—	—	100 ± 5
1512.1/1512.2	460.9	2989p1	4 ± 1	—	—	—	14 ± 4	1 ± 1	12 ± 2	69 ± 4	—	trace	—	—	100 ± 5
Tptpv1 461.5–471.7															
1516.9/1517.0	462.4	2990p1	4 ± 1	—	—	—	9 ± 2	1 ± 1	10 ± 1	76 ± 2	trace	trace	—	—	100 ± 3
1521.5/1521.6	463.8	2991p1	5 ± 2	—	—	—	4 ± 1	1 ± 1	5 ± 1	85 ± 2	—	trace	—	—	100 ± 3
1524.9/1525.0	464.8	2992p1	5 ± 2	—	3 ± 1	2 ± 1	—	2 ± 1	11 ± 2	77 ± 3	trace	trace	—	—	100 ± 3
1527.8/1527.9	465.7	2993p1	3 ± 1	—	2 ± 1	4 ± 1	—	5 ± 1	21 ± 3	65 ± 3	trace	trace	—	—	100 ± 4
1546.5/1546.6	471.4	2994p1	1 ± 1	—	—	1 ± 1	—	5 ± 1	10 ± 1	83 ± 2	trace	trace	—	—	100 ± 2
Tpbt1 471.7–473.8															
Tac 473.8–526.5															
1560.8/1560.9	475.8	2995p1*	trace	4 ± 1	6 ± 1	10 ± 1	—	27 ± 2	53 ± 8	—	trace	trace	—	—	100 ± 8
1563.3/1563.4	476.5	2996p2*	—	6 ± 1	5 ± 1	13 ± 1	—	25 ± 2	53 ± 8	—	trace	trace	—	—	102 ± 8
1563.3/1563.4	476.5	2996p1	4 ± 1	4 ± 1	—	2 ± 1	—	2 ± 1	7 ± 1	81 ± 2	—	trace	—	—	100 ± 2
1566.7/1566.8	477.6	2997p1	—	2 ± 1	1 ± 1	2 ± 1	—	4 ± 1	10 ± 1	81 ± 2	trace	trace	—	—	100 ± 2
1570.3/1570.5	478.7	2998p1	—	1 ± 1	1 ± 1	3 ± 1	—	8 ± 1	16 ± 2	71 ± 2	trace	trace	—	—	100 ± 3

Stratigraphy from USW SD-6 Prognosis Update Log, SMF Contacts, dated 5/7/98. — = not detected trace = Trace abundance

*The analyses 2995p1 and 2996p2 are from large (> 5 cm) lithic clasts that occur at these depths.

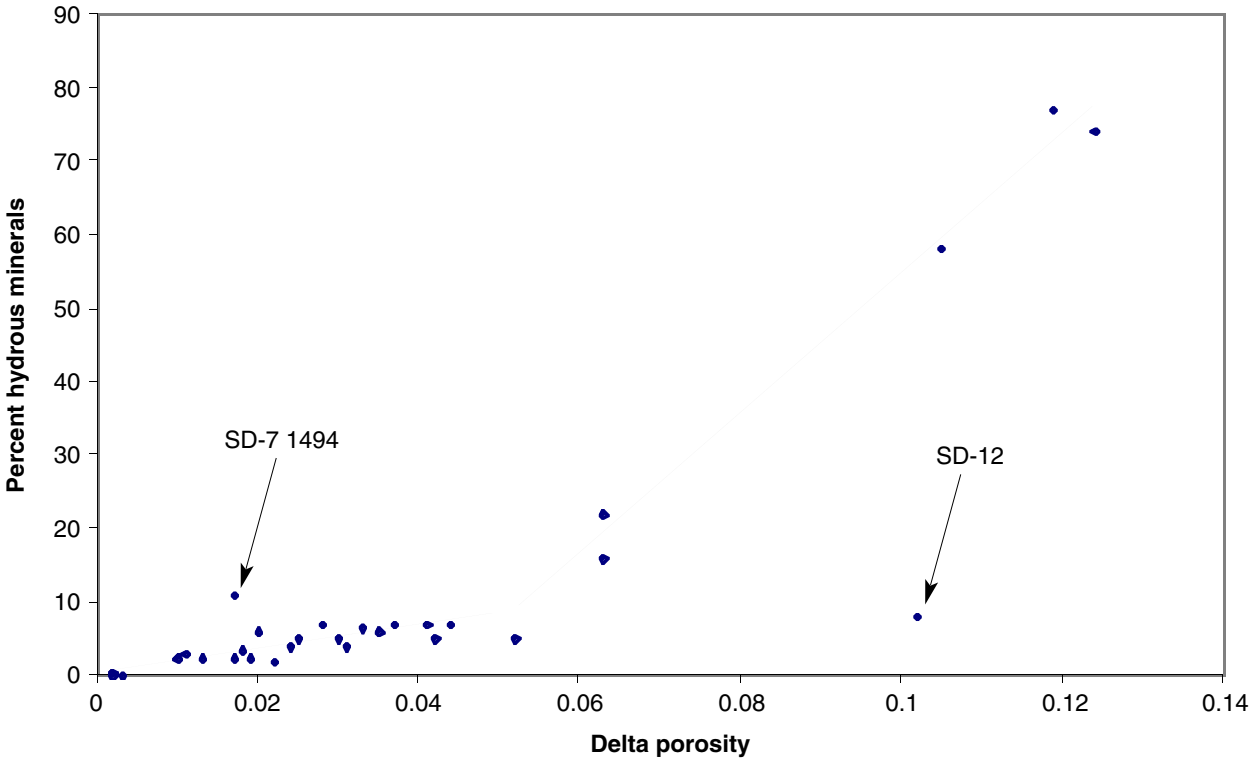

Fig. 15. Vitric/Zeolitic Transition-Zone Samples. The percentage of hydrous minerals is plotted versus delta porosity for samples from the vitric/zeolitic transition zone in drill holes USW SD-7, 9, and 12. Delta porosity is the difference in porosity between the sample oven-dried at 60°C and a relative humidity of 65% and the sample oven-dried at 105°C.

the experiments being conducted at Busted Butte.

As part of a recent revision of the 3-D mineralogic model of Yucca Mountain (Carey et al. 1998, pp. 22 and 24), comparisons were made between hydrologic properties and extent of zeolitization in the lower Topopah Spring Tuff and upper Calico Hills Formation from drill-core samples. Samples that had been analyzed by the U. S. Geological Survey (USGS) for porosity properties were analyzed as subsplits to obtain quantitative XRD mineralogy on exactly the same sample. This approach allows the direct comparison of laboratory-measured matrix properties and the mineralogy. Samples from USW SD-7, 9, and 12 were analyzed in this manner and the results are summarized in Table 7. The columns for mineral or glass abundance and the XRD total report data were collected by standard LANL methods for analyses of Yucca Mountain tuffs. The column for "delta porosity" represents the difference between porosity of the sample oven-dried at 60°C and a relative humidity of 65% and porosity of the sample oven-dried at 105°C, as reported by L. E. Flint of the USGS Hydrologic Research Facility. The data in Table 7 allow direct comparison of not just zeolite abundance but of the total abundance of hydrous minerals (clays and zeolites) versus the laboratory measurement of delta porosity in the unsaturated zone where a vitric-to-zeolitic transition occurs. Outliers may occur for a variety of reasons. Although the anomalously high hydrous mineral content in SD-7 1494 could be a result of differing trends in chabazite-bearing samples, the anomalously low hydrous mineral content and high delta porosity of SD-12 1456.6 occurs in a sample with

Table 7. Quantitative XRD Results (LANL) for Samples with Laboratory Porosity Measurements (Delta porosity: USGS).

Sample	Smectite	Clinoptilolite	Mordenite	Tridymite	Cristobalite	Opal-CT	Quartz	Feldspar	Glass	Hematite	Mica	Hornblende	Chabazite	XRD Total	Delta porosity
SD-7 1494.0	1 ± 1	10 ± 1	—	—	—	5 ± 1	8 ± 1	19 ± 3	53 ± 3	—	trace	trace	4 ± 1	100 ± 4	0.017
SD-9 1430.9	5 ± 2	—	—	—	—	5 ± 1	trace	2 ± 1	88 ± 2	—	trace	—	—	100 ± 2	0.042
SD-9 1433.4	1 ± 1	57 ± 5	—	—	—	29 ± 8	4 ± 1	13 ± 3	—	—	—	—	—	100 ± 10	0.105
SD-9 1437.3	—	—	—	—	—	—	1 ± 1	1 ± 1	98 ± 1	—	trace	—	—	100 ± 1	0.003
SD-9 1440.2	3 ± 1	4 ± 1	—	—	—	6 ± 1	1 ± 1	4 ± 1	82 ± 2	—	—	—	—	100 ± 2	0.041
SD-9 1443.0	19 ± 6	3 ± 1	—	—	—	8 ± 2	1 ± 1	5 ± 1	64 ± 6	—	—	—	—	100 ± 7	0.063
SD-9 1445.2	4 ± 1	1 ± 1	—	—	—	9 ± 2	1 ± 1	4 ± 1	81 ± 2	—	trace	—	—	100 ± 3	0.052
SD-9 1448.5	4 ± 1	3 ± 1	—	—	—	9 ± 2	2 ± 1	6 ± 1	76 ± 2	—	trace	—	—	100 ± 3	0.044
SD-9 1450.9	1 ± 1	5 ± 1	—	—	—	5 ± 1	2 ± 1	6 ± 1	81 ± 2	—	trace	—	—	100 ± 2	0.035
SD-9 1454.2	1 ± 1	15 ± 1	—	—	—	7 ± 2	3 ± 1	7 ± 1	67 ± 2	—	trace	—	—	100 ± 3	0.063
SD-9 1458.2	2 ± 1	71 ± 6	1 ± 1	—	—	20 ± 4	2 ± 1	4 ± 1	—	—	—	—	—	100 ± 7	0.124
SD-9 1460.2	2 ± 1	72 ± 7	3 ± 1	—	—	18 ± 4	2 ± 1	1 ± 1	—	—	—	—	—	98 ± 8	0.119
SD-12 1371.8	—	—	—	—	—	1 ± 1	1 ± 1	2 ± 1	96 ± 1	—	trace	—	—	100 ± 2	0.002
SD-12 1374.8	trace	—	—	—	—	2 ± 1	2 ± 1	4 ± 1	92 ± 1	—	trace	—	—	100 ± 2	0.002
SD-12 1386.6	trace	2 ± 1	—	1 ± 1	—	7 ± 2	3 ± 1	8 ± 1	79 ± 2	trace	trace	—	—	100 ± 3	0.010
SD-12 1389.8	trace	2 ± 1	—	1 ± 1	—	7 ± 2	4 ± 1	12 ± 2	74 ± 3	trace	trace	—	—	100 ± 3	0.013
SD-12 1392.7	trace	2 ± 1	—	trace	—	11 ± 3	5 ± 1	13 ± 2	69 ± 3	—	trace	—	—	100 ± 4	0.017
SD-12 1395.7	trace	2 ± 1	—	1 ± 1	—	6 ± 2	3 ± 1	10 ± 1	78 ± 2	trace	trace	—	—	100 ± 3	0.019
SD-12 1402.2	trace	3 ± 1	—	1 ± 1	—	15 ± 5	8 ± 1	23 ± 3	50 ± 6	—	trace	—	—	100 ± 6	0.018
SD-12 1404.3	1 ± 1	3 ± 1	—	trace	—	7 ± 2	4 ± 1	13 ± 2	72 ± 3	—	trace	—	—	100 ± 3	0.024
SD-12 1407.7	3 ± 1	3 ± 1	—	—	—	3 ± 1	2 ± 1	6 ± 1	83 ± 2	—	trace	—	—	100 ± 2	0.020
SD-12 1410.6	1 ± 1	1 ± 1	—	—	—	3 ± 1	2 ± 1	8 ± 1	85 ± 2	—	trace	—	—	100 ± 2	0.022
SD-12 1440.0	1 ± 1	4 ± 1	—	—	—	7 ± 2	2 ± 1	8 ± 1	78 ± 2	—	trace	—	—	100 ± 3	0.030
SD-12 1440.8	1 ± 1	2 ± 1	—	—	—	1 ± 1	2 ± 1	6 ± 1	88 ± 2	—	trace	—	—	100 ± 2	0.011
SD-12 1447.0	trace	6 ± 1	—	—	—	2 ± 1	2 ± 1	5 ± 1	85 ± 2	—	trace	—	—	100 ± 2	0.033
SD-12 1450.2	1 ± 1	4 ± 1	—	—	—	3 ± 1	2 ± 1	8 ± 1	82 ± 2	—	trace	—	—	100 ± 2	0.025
SD-12 1452.7	1 ± 1	6 ± 1	—	—	—	3 ± 1	3 ± 1	6 ± 1	81 ± 2	—	trace	—	—	100 ± 2	0.037
SD-12 1456.6	1 ± 1	7 ± 1	—	—	—	3 ± 1	2 ± 1	5 ± 1	82 ± 2	—	trace	—	—	100 ± 2	0.102
SD-12 1458.9	1 ± 1	6 ± 1	—	—	—	3 ± 1	3 ± 1	8 ± 1	79 ± 2	—	trace	—	—	100 ± 2	0.028
SD-12 1462.1	1 ± 1	3 ± 1	—	trace	—	4 ± 1	2 ± 1	6 ± 1	84 ± 2	—	trace	—	—	100 ± 2	0.031

— = not detected trace = Trace abundance of < 0.5 wt% errors are conservative 2-sigma values

no mineralogic distinction from neighboring samples that are not anomalous (Table 7). These results suggest that rock texture or fabric may be a significant factor in the ability of samples to retain water within pores. Nevertheless, the data also indicate that a statistically useful relationship between hydrous-mineral abundance and porosity properties might be derived for Yucca Mountain samples, with applicability down to very low abundances of hydrous minerals (Fig. 16).

4.3 Hydrology

Rock samples from Busted Butte outcrops of Calico Hills and Topopah Springs formations were collected on November 11, 1997, and used to determine the preliminary hydrologic properties of the formations in the test block for modeling and test-design purposes. Seven samples, five whole-rock cores, and two recomposites were sent to UFA Ventures, Inc., to measure the unsaturated hydraulic conductivity $K(\theta)$ and the matric potential $\Psi(\theta)$, or water retention, using the UFA method (Table 8). The porosity of the samples was also measured. One of the whole-rock cores was damaged during shipping.

All samples were packaged in bubble wrap as 1.5-in diameter cores and enclosed in 2-in PVC tubes with caps. Sample splits with LANL tracking numbers 2826,X3 and 2827,X2 were simply in plastic bags for use as reconstructed cores. The entire stratigraphic sequence of the test block was represented, that is, from top to bottom: the base of the Topopah Springs (TSw) basal vitrophyre (Tptpv2 and Tptpv2-lower) and the hydrologic Calico Hills (CHn) unit (Tptpv1 and Tac).

The samples and their splits sent to UFA Ventures are described next. These were all collected from Busted Butte on November 7, 1997.

Sample 1. Topopah Springs Tuff, Tptpv2 *SPC 7047, LANL #2825,X1*. This sample (cored vertical to horizontal as measured in field area) is of Topopah Springs Tuff (TSw 2) with a strong fabric as defined by flattened lapilli, low permeability, and moderate fracture density in the field.

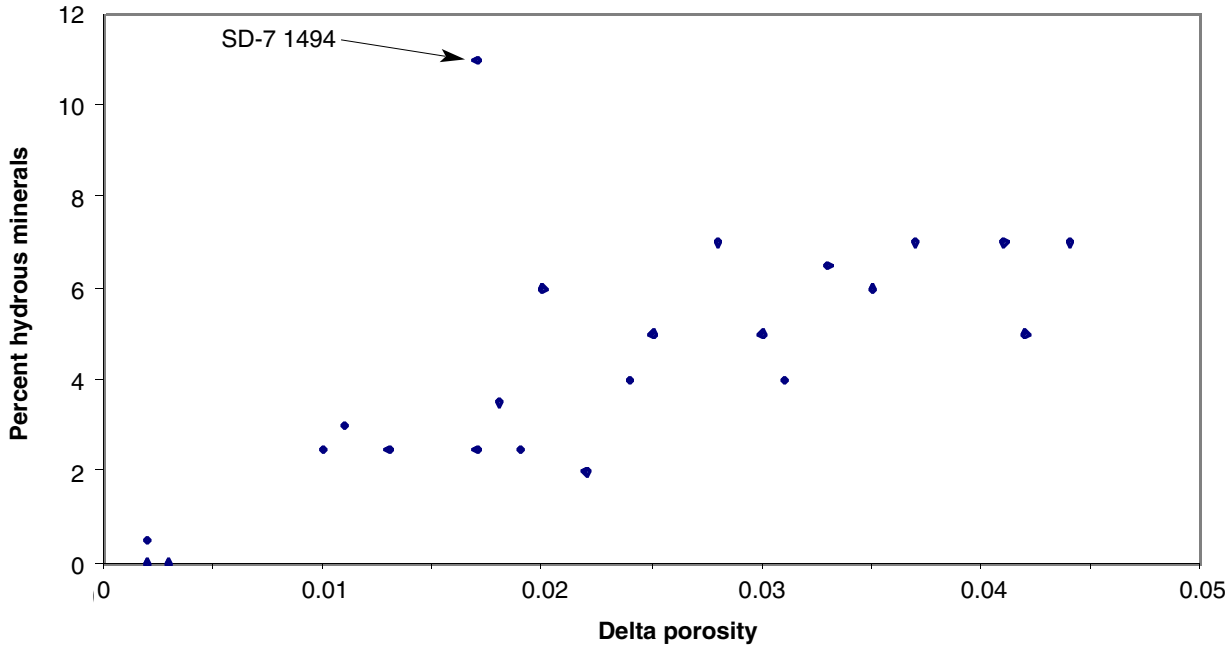

Fig. 16. Low-Porosity Samples. The plot is for samples with delta porosity less than 0.05 from the vitric/zeolitic transition zone in drill holes USW SD-7, 9, and 12.

Table 8. Busted Butte Samples Used for Hydrologic Characterization.

Sample ID	Specimen type	Date collected	Location	LANL #	Comments
Sample 1					
SPC 7047	Tptpv2	11/7/97	Busted Butte	2825,X1	Vertical core
Sample 2					
SPC 7048	Tac	11/7/97	Busted Butte	2826,X1	Vertical core
SPC 7048	Tac	11/7/97	Busted Butte	2826,X2	Horizontal core
SPC 7048	Tac	11/7/97	Busted Butte	2826,X3	Shavings
Sample 3					
SPC 7049	Tptpv1	11/7/97	Busted Butte	2827,X1	Vertical core
SPC 7049	Tptpv1	11/7/97	Busted Butte	2827,X2	Shavings
Sample 4					
SPC 7050	Tptpv2	11/7/97	Busted Butte	2828,X1	Vertical core

This unit is transitional between the basal vitrophyre (Tptpv3) and the base of the Topopah Springs Tptpv2 lower (Sample 3). The unit is a partly welded salt-and-pepper tuff rich in flattened pumice fragments (i.e., lapilli). The core has no visible fractures so that the hydrologic measurements will pertain to the matrix. The core is nearly of perfect dimensions:

Diameter: from 3.790 to 3.795 cm

Usable core length: ~ 5.850 cm

Sample 2. Calico Hills Tuff, Tac

SPC 7048, LANL #2826,X1. This sample (cored vertical to horizontal as measured in field area) is a Calico Hills white ash fall tuff located at the top of the sequence just below Sample 3 (TSw 1, 40 cm below). The unit is ledge forming and approximately 50 cm to 70 cm (2 feet) thick. This sample has no visible fabric and is extremely fragile and friable. The permeability of this sample is expected to be very high (> 100 Darcys?). There are no visible fractures in the field outcrop except in the vicinity of faults, and this sample also has no visible fractures. Core quality is fair to poor as a 2-in core bit was used to core sample. The diameter is consequently highly variable, and the core is somewhat curved with dimensions:

Diameter: from 3.715 to 3.850 cm

Usable core length: ~ 5.000 cm

SPC 7048, LANL #2826,X2. This sample (cored in the horizontal plane as measured in field area and perpendicular to 2826,X1 above) also has no visible fabric but contains at least two fractures at approximately 70° to the core axis and subparallel to each other (subhorizontal). The first fracture extends from one of the core extremities to one-third of the core length, and the other extends through the center of the core. Core quality is fair to poor as a 2-in core bit was used to core sample. Diameter is consequently highly variable, and the core is somewhat curved in addition to containing fractures. The dimensions are:

Diameter: from 3.790 to 3.890 cm

Usable core length: ~ 4.300 cm

SPC 7048, LANL #2826,X3. This sample split is from the sample above but consists of shavings to be used in a reconstruction experiment.

Sample 3. Topopah Springs Tuff, Tptpv1

SPC 7049, LANL #2827,X1. This sample (cored vertical to horizontal as measured in field area) is from the 60-cm to 70-cm thick pumice-rich base of the Topopah Springs formation located 40 cm above Calico Hills Sample 2 and consists of very large (cm

size) pumice fragments defining a moderate fabric. The unit is one of high permeability with little to no throughgoing fractures with the exception of fault zones, and the sample has no visible fractures. Core quality is good considering mechanical heterogeneity of sample. Dimensions are:

Diameter: from 3.720 to 3.605 cm
Usable core length: ~ 4.700 cm

SPC 7049, LANL #2827,X2. This sample is the same as above but consists of shavings to be used in a reconstruction experiment.

Sample 4. Topopah Springs Tptpv2-lower
SPC 7050, LANL #2828,X1. This sample (cored vertical to horizontal as measured in field area) is non- to partly welded Topopah Springs tan ash flow tuff. The unit is approximately 90 cm (3 feet) thick with some fractures and is transitional with that for Sample 1. The sample has weak to moderate fabric, is very fragile and permeable, and contains no visible fractures. Core quality of the sample is good, and its dimensions are:

Diameter: from 3.635 to 3.650 cm
Usable core length: ~ 3.425 cm

Results on the hydrologic properties of these samples can be found in Appendix C. The Calico Hills (Tac) samples (SPC 7048) has a total porosity of 50 to 56% and a saturated conductivity K of approximately 2×10^{-3} cm/s. The Topopah Springs Tptpv1 sample (SPC 7049) has a total porosity of 64% and a saturated conductivity K of approximately 6×10^{-4} cm/s. Both of these samples represent the hydrologic Calico Hills (CHn) unit. Conversely, samples from the base of the basal vitrophyre (Tptpv2), representing the top of the test block, exhibited lower saturated conductivities varying from $K = 4 \times 10^{-4}$ to less than 4×10^{-10} cm/s (SPC 7050 and 7047, respectively). These results are used in conjunction with YMP database parameters to run the model simulations presented in the report.

4.4 Geochemistry

4.4.1 In-situ pore-water chemistry

As discussed previously, tracers were injected in the field in an aqueous matrix designed to mimic the in-situ pore-water chemistry within the test horizons. To determine this chemistry, a set of "Q" rock samples were collected in the Test Alcove on January 30, 1998. These samples were collected from the Tac horizon by hand augering and immediately sealed in accordance with standard YMP procedures by personnel of the Yucca Mountain Sample Management Facility. A series of samples were collected in sequence, starting with sample 3A at the Adit wall, extending to 3U, 1.93 m away from the tunnel into the wall. These samples were transported to Los Alamos and transferred to Laura Wolfsberg (LANL Group CST-7) for analysis.

Pore water was extracted from a subset of these samples by ultracentrifugation, following standard YMP procedures developed for ^{36}Cl studies. Gravimetric moisture contents of the rock samples were determined by weight difference upon drying, and the chemical composition of the extracted pore water was determined using standard ion chromatography (IC) and inductively-coupled-plasma/atomic-emission spectrometry (ICP/AES), all in accordance with YMP QA procedures. (Full QA documentation can be found in LA-CST-NBK-98-002.) Results are presented in Table 9. Note that the IC analyses involve a bicarbonate buffer and, thus, there is no measurement of the bicarbonate alkalinity of the sample. The bicarbonate numbers listed in Table 9 are estimated by charge balance.

The results in Table 9 show that the pore water is a mixed-ion water (Ca-Na-HCO_3-SO_4) with an average total dissolved solids (TDS) of approximately 200 mg/L. Compared to more typical groundwater compositions, the pore water shows high nitrate (probably due to soil biological activity) and high silica (due to relatively rapid equilibration with amorphous silica in the tuff). Sample 3B, from near the Adit wall, differs somewhat from the other samples, perhaps due to the influence of construc-

tion water and atmospheric CO_2 levels. The compositions of the other three pore-water samples were averaged (as shown in the table), and these average values were used to develop the synthetic pore-water recipe present in Section 3.

Also listed in Table 9 are pH values measured on extracted pore water. Despite obvious opportunities for pH alteration due to CO_2 exchange during sample collection, extraction, and analysis, these pH values were the best available at the time of Phase-1 planning. Thus, Phase-1 tracer mixtures were pH-adjusted to a value of 8.4 ± 0.1. During Phase-2 installation, attempts were made to measure pH in situ by inserting pH paper into boreholes for a few days. Results were mixed, but seemed to indicate lower in-situ pH values than those measured in the laboratory (consistent with

Table 9. Chemical Composition of Busted Butte Pore Water with J-13 Groundwater for Comparison.

	Concentrations (mg/L)					
Constituent	**Sample 3B**	**Sample 3N**	**Sample 3Q**	**Sample 3U**	**Avg. 3N-3U**	**J-13 water**
Br	0.06	0.07	0.06	0.06	0.06	—
Ca	17.73	24.35	21.16	19.81	21.77	12.5
Ce	< 0.5	< 0.5	< 0.5	< 0.5	< 0.6	—
Cl	16.13	19.06	17.71	16.74	17.84	6.5
Co	< 1.0	< 1.0	< 1.0	< 1.0	< 1.1	—
F	2.36	1.82	1.85	1.41	1.69	0.53
Fe	< 0.1	< 0.1	< 0.1	< 0.1	< 0.2	< 0.05
HCO_3 (est.)	33.0	52.7	45.6	40.6	46.3	137.2
K	4.14	3.35	3.37	3.44	3.39	4.5
Li	0.11	0.11	0.10	< 0.1	0.10	< 0.1
Mg	3.20	4.13	3.64	3.19	3.66	2.1
Mn	< 0.5	< 0.5	< 0.5	< 0.5	< 0.6	< 0.01
Mo	< 1.0	< 1.0	< 1.0	< 1.0	< 1.1	—
Na	17.67	21.36	19.63	17.89	19.63	44.6
Ni	< 1.0	< 1.0	< 1.0	1.34	1.34	—
NO_3	22.76	26.48	22.62	20.99	23.36	1.3
PO_4	< 0.1	< 0.1	< 0.1	< 0.1	< 0.2	—
Re	< 1.0	< 1.0	< 1.0	< 1.0	< 1.1	—
Si	29.69	31.85	34.10	31.00	32.32	29.6
Sm	< 0.5	< 0.5	< 0.5	< 0.5	< 0.6	—
SO_4	31.29	33.63	31.36	30.08	31.69	18.6
Sr	0.37	0.49	0.42	0.38	0.43	—
TDS	178.5	219.4	201.6	186.9	203.6	257.4
pH	8.20	8.48	8.45	8.28	8.40	7.3–8.4
Gravimetric moisture content:	0.123	0.134	0.158	0.109	0.133	N/A

degassing of excess soil CO_2 before lab analysis). Accordingly, Phase-2 tracer mixtures were pH-adjusted to a value of 7.0 ± 0.1.

4.5. Tracer Evaluation

A large number of possible tracers were proposed in the Busted Butte initial planning. However, final determination of tracers and their concentrations was dependent on both rock and pore-water characteristics. Rock and pore-water samples became available in early 1998, and a set of fast-turnaround batch studies and geochemical modeling efforts were initiated.

4.5.1 Batch-sorption studies

Preliminary batch-sorption studies were conducted using proposed reactive tracers and two rock samples from the Main Adit at Busted Butte. Tracers tested included lithium, manganese, cobalt, nickel, molybdate, and perrhenate; rocks were samples of the Calico Hills (Tac) and Topopah Springs (Tptpv2) from Phase-1 Boreholes 4 and 7. Because of the need for rapid turnaround on these results, the sorption studies differed from standard YMP procedures in two important respects: pre-equilibration and equilibration times were shorter than normal and fewer concentration levels were studied. Therefore, these results must be considered preliminary, and more complete batch-sorption studies are planned for fiscal year 1999. The results of the preliminary sorption studies for lithium, manganese, cobalt, and nickel are presented in Table 10. The results indicate that the Tac sample sorbed the metals more strongly than the Tptpv2 sample and that, on both samples, the metals showed a consistent sequence of sorption: Li << Mn << Ni < Co. Based on these results, all four of these metals show significant sorption and may be useful reactive tracers in the field. Neither of the proposed pertechnetate analogues (molybdate and perrhenate) displayed any significant sorption and were therefore eliminated from further consideration in our testing.

Table 10. Preliminary Measured Sorption Coefficients.

Rock sample	Measured K_d (ml/g)			
	Li	Mn	Co	Ni
Tac	≤ 1	16	38	34
Tptpv1	≤ 1	6	14	13

4.6 Geochemical Modeling

To further determine the suitability of manganese, cobalt, and nickel as field tracers at Busted Butte, Arend Meijer (GCX, Inc.) performed a series of geochemical speciation and solubility calculations based on the measured pore-water chemistry. His report is attached as Appendix D.

4.7 Field Transport Results

4.7.1 Phase 1B

Collection pads obtained from Phase-1B Collection Boreholes 6 and 8 have been analyzed for bromide, fluorescein, and pyridone. These pads have been collected on a weekly basis from each of the collection boreholes since the initial injection on May 12, 1998. Selected pads were extracted by mixing with 40 ml deionized water for 12 hr. The extract was then filtered through a 0.2-μm polycarbonate filter membrane and analyzed by fluorometry, IC, ICP/AES, and HPLC, as shown in Table 11. The polycarbonate membrane was analyzed by epifluorescent microscopy for the presence of microspheres. Approximate detection limits for these techniques are provided below (Table 11).

Tracer "breakthrough" has been detected in Collection Borehole 6 for the 10-ml/hr injection-rate experiment in Phase 1B (Figs. 17 and 18). As expected, fluorescein and bromide, both conservative tracers, showed similar breakthrough patterns. In both cases, first significant breakthrough was measured on June 16, 1998, five weeks after injection commenced. First breakthrough was detected on the pad at the 130-cm location in Borehole 6,

Table 11. Analytical Methods and Detection Limits for Phase 1.

Analyte	Method	Detection limit (ppm)	Initial concentration (ppm)	Maximum dilution factor
Br	IC	0.01	460.04	46,000
Li	ICP/AES	0.1	39.96	400
DFBA	HPLC	0.005	100	20,000
PFBA	HPLC	0.005	100	20,000
Fluorescein	Fluorimeter	0.001	500	500,000
Pyridone	Fluorimeter	0.001	100	100,000
Microspheres	Epifluorescent microscopy	??	107–108 per ml	??

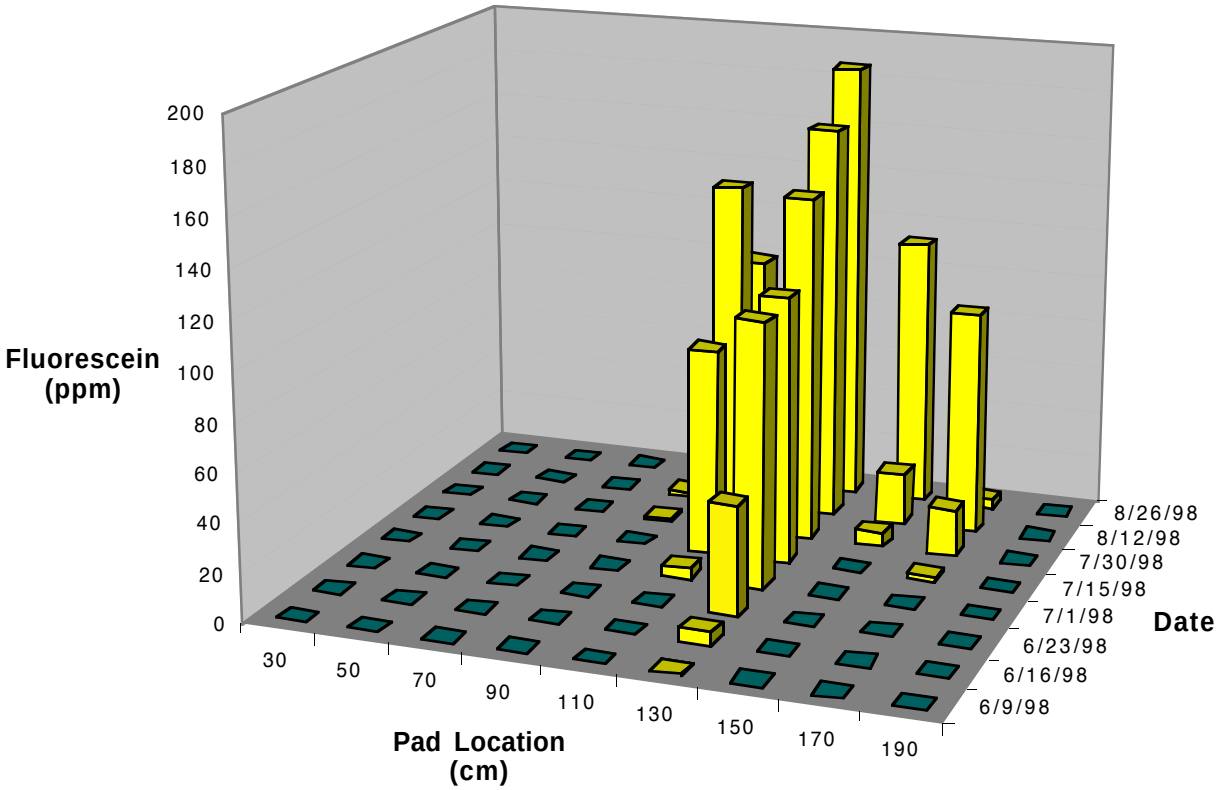

Figure 17. Fluorescein Breakthrough. The plot shows fluorescein dye "breakthrough" concentration (ppm) as a function both of distance into Borehole 6, or pad location (cm), and of the date the sample was collected. Note that the injection from Borehole 5 was initiated on May 12, 1998, at the 130-cm position at an injection rate of 10 ml/hr. The distance between the injection and collection boreholes is approximately 28 cm.

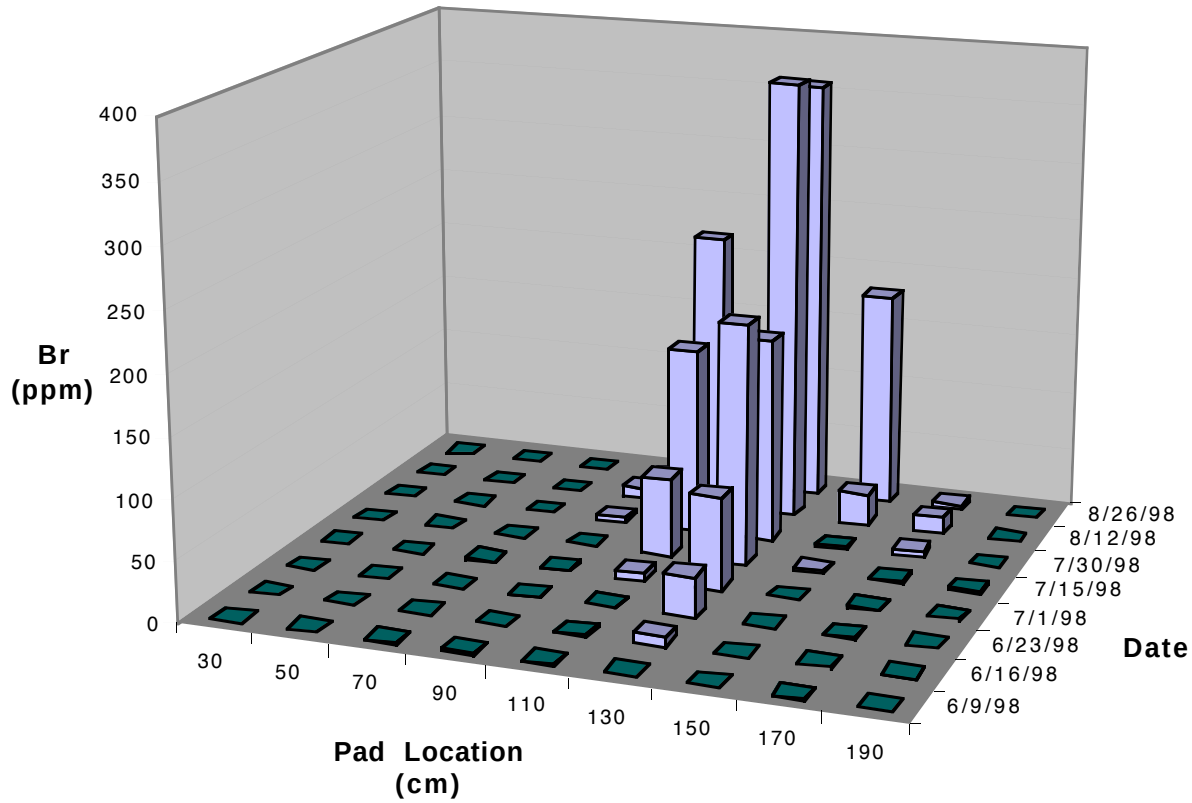

Figure 18. Bromide Breakthrough. The plot shows bromide "breakthrough" concentration (ppm) as a function both of distance into Borehole 6, or pad location (cm), and of the date the sample was collected. The conditions are the same as for Fig. 17.

directly beneath the 10-ml/hr injection point in Borehole 5. Two weeks later (July 1, 1998), both fluorescein and bromide breakthroughs were noted at the 110-cm pad; by August 12, 1998, the conservative tracer front had also reached the 90-, 150-, and 170-cm locations. No lithium breakthrough has been detected (through August 26, 1998) in Phase-1B pads; FBA and microsphere analyses are not yet complete. Complete data analysis awaits the completion of these chemical analyses.

Note that the pad located 130 cm into the borehole corresponds to the intersection of that borehole with a subvertical joint linking the injection hole (Borehole 5) to the collection hole (Borehole 6) located approximately 28 cm below. This observation is currently being modeled for the second submission of Phase-2 predictions due in February 1998.

4.8 Modeling Studies: Implications for Performance Assessment

The UZ transport test is designed to provide information suitable for assessing the validity of flow-and-transport models used in the site-characterization and performance-assessment programs for Yucca Mountain. This milestone is an update of the experimental and modeling work performed to date for the UZTT. Critical evaluation and iterative improvement of the flow-and-transport conceptual and numerical models awaits the collection of data, which is currently in progress. The first step in this process is reported in this milestone, namely the blind predictions of flow-and-transport behavior for both the Phase-1 and Phase-2 experiments.

Although flow-and-transport field data collected to date are limited, observations of the available data collected so far, and the modeling of these data, lead to several key conclusions of relevance to performance assessment. We summarize these conclusions below, categorizing them with respect to the particular field or modeling activity in this report.

1. *Laboratory measurements*: the collection of unsaturated hydrologic property data using the UFA provides data of particular relevance to flow-and-transport models because they are direct measurements under unsaturated conditions rather than indirect, model-derived parameters. Future laboratory data for the UZ rocks should be collected under unsaturated conditions to confirm the large existing database of hydrologic parameters. The Monte Carlo analyses (Section 6) indicate that the nature of the correlations between parameters such as permeability and the van Genuchten α parameter have a strong impact on the predictability of the flow-and-transport system. Therefore, a full suite of measurements of hydrologic and transport parameters should be made on each rock sample to constrain models and develop correlations.

2. *Phase-1A and -1B model results*: In addition to the point just made, the modeling analyses for Phase 1A indicate that strong capillary forces in the rock matrix of the Tac unit are likely to modulate fracture flow from overlying units, thereby dampening pulses of infiltrating water and providing a large degree of contact between radionuclides and the rock matrix. Several modeling approaches, from deterministic to Monte Carlo and stochastic models, were used to simulate the Phase-1A experiments (Sections 6 and 7). All yielded similar qualitative results. From this outcome, we conclude tentatively that the deterministic modeling approach taken at the site scale may be adequate. The parameterizations used in performing these calculations must be evaluated after data from the UZTT are available.

   A particularly interesting observation from the Phase-1B experiment is that, even when injection occurs immediately adjacent to a fracture, water appears to be imbibed quickly into the surrounding matrix. The transport times observed immediately below the injection point were on the order of 30 days, whereas pure fracture flow would have resulted in travel times of minutes to hours at this flow rate. Site-scale models must be evaluated in light of this observation. Models that predict significant fracture flow at percolation rates low enough for the matrix to transmit the flow may be inconsistent with the Phase-1B experiment.

3. *Phase-2 modeling*: Because there are not yet field-test results from this part of the test, it is difficult to draw conclusions relevant to the evaluation of models. Significant uncertainties uncovered by the modeling include the adequacy of continuum models in nonwelded units of high matrix permeability and the nature of the transition from fracture flow to matrix flow at contacts between hydrogeologic units. These are exactly the issues being studied within the UZTT. Therefore, we anticipate preliminary answers to these important questions in the next few months, after the first nine months of test data have been collected and analyzed.

5. TOMOGRAPHIC STUDIES

5.1 Ground-Penetrating Radar Tomography

(This section is from Kenneth H. Williams and John E. Peterson, Earth Science Division, Lawrence Berkeley National Laboratory.)

5.1.1 Experimental objective

The objective of the borehole radar data acquisition is to monitor the tracer injection of the Busted Butte UZTT and to investigate the nature of fluid migration through the Calico Hills member of the Yucca Mountain lithologic sequence. The data presented in this report include the pre-injection baseline measurements as well as several measurements made after the start of tracer injection. Subsequent measurements are to be made as determined by tracer breakthrough in an attempt to monitor the tracer distribution over time.

5.1.2 Background

The borehole radar method is one in which modified ground-penetrating radar antennas are lowered into the ground and high-frequency electromagnetic signals are transmitted through subsurface material to a receiving antenna. The electrical properties of the subsurface material influence the properties of the transmitted electromagnetic signal. In particular, the dielectric permittivity of the rock has a strong influence on the propagation of the signal and whether it travels at a high or low velocity or whether it is highly attenuated or not. Moisture content and chemical composition have such an effect. The high dielectric permittivity of water—in contrast to drier rock—typically results in greatly reduced signal velocities and increased signal attenuation. Changing chemical compositions may also alter the bulk dielectric permittivity of the rock. Because such changes in signal character are what are to be measured over the course of the Busted Butte UZTT, any increase in background moisture content or chemical composition resulting from the tracer injection should result in changes in the received radar wave velocity and amplitude. The transmitted signals may be represented as multiple ray paths crossing through the zone of interest. If sufficient ray paths are recorded, a tomographic image may be obtained through computer processing. The information extracted from such data includes the following: a) the transit time, which depends on the wave velocity, and b) the amplitude, which depends on the wave attenuation. This information, in the form of a processed tomogram, offers a high-resolution approach to monitoring the changes occurring in the rock over the duration of the tracer-injection experiment.

5.1.3 Equipment description

All radar data were acquired using the Sensors and Software pulseEKKO 100 ground-penetrating radar system equipped with 200-MHz center-frequency borehole antennas. The pulseEKKO system consists of six basic components, including a pair of identical antennas, a transmitter electronics unit, a receiver electronics unit, a control console, and a personal computer acting as a recording system and data storage unit.

5.1.4 Component specifications

Antenna Specifications: The pulseEKKO 100 antennas are resistively damped dipolar antennas. The antenna radiation patterns are the pattern of a half-wavelength dipole. Each antenna pair is designed to have a bandwidth-to-center-frequency ratio of one. The borehole antennas used in the Drift Scale Test have a center frequency of 200 MHz.

Transmitter Electronics Specifications: The pulseEKKO system used in the Drift Scale Test consisted of a transmitter having a peak voltage of 400 V with a rise time of 2.5 ns. The transmitter is powered by 12 V and emits a pulse on command from the control console. The power actually radiated from the system is very dependent on the subsurface conditions. The 400-V transmitter used here delivers a peak power of 1.6 kW into a 50-ohm load. Only a small fraction of the available power is actually transformed into a radiated electromagnetic signal because the antennas are damped and are very inefficient radiators.

Receiver Electronics Specifications: The receiver electronics digitize the voltage at the receiver antenna connector to 16-bit resolution. The receiver design is such that it acquires the received waveform with very high fidelity. The receiver electronics clip the incoming voltage at a 50-mV level, and the receiver noise level is nominally around 200 μV per stack. The present receiver resolution for a single bit, after analog to digital conversion, is 1.5 μV.

Control Console: The control console provides the overall management of the transmitter and receiver operation. The control console is a microprocessor-controlled unit that communicates with both the transmitter and receiver electronics and the external PC. The PC passes the system-configuration information and the acquisition parameters to the control console, which then manages all of the hardware functions of the pulseEKKO radar system.

5.1.5 Operating principles

The operating principles are as follows: a) the user defines the time window, sampling interval, and number of pulses to be stacked via the PC user interface; b) the user selects the acquisition mode; c) the PC configures the pulseEKKO console through the PC's standard RS232 port, and the console takes over control of data acquisition; d) the pulseEKKO console commands the transmitter to fire, and the transmitter generates a high-voltage pulse, which is shaped by the transmitting antenna into a radiated pulse; e) the console advises the receiver electronics to digitize the signal from the receiving antenna, the receiver digitizes the ambient electric field present at the receiving antenna after the band-limiting characteristics of the antenna transfer function, and the digital number representing the voltage at the time of acquisition is transferred to the control console; f) steps d and e are repeated until the desired waveform length and stack count are achieved; g) the console transmits the stacked waveform to the PC; and h) the PC stores the data and displays the radar trace.

5.1.6 Survey methodology

The borehole radar technique used is a crosshole radar-profiling method in which the transmitter and receiver antennas are located in separate boreholes and data are collected with the antennas at various vertical offsets. Data are collected using two acquisition modes. The first is a zero-offset profile (ZOP) in which the transmitting and receiving antennas are fixed such that there is no vertical offset between them. The second is a multiple-offset profile (MOP) in which the receiving antenna remains at a fixed location while the transmitting antenna moves incrementally in the second borehole. It is a series of multiple-offset profiles that are to used to acquire the ray paths necessary for subsequent tomographic processing.

The first-order results derived from the radar data are travel times and the resulting velocities. To determine accurate travel times between the transmitter and receiver antennas, it is vital to know the precise time at which the transmitter fires (known as time zero). The procedure used to determine time zero for the surveys consists of taking four direct air-wave measurements (the signal from transmitting antenna to receiving antenna in air) with the antennas held at a separation of 2.0 m. After the time-zero data are collected, the antennas are immediately moved into the boreholes and a ZOP data set is collected. In the case of the Busted Butte UZTT, the antennas are moved down the length of the boreholes within a set of PVC liners designed to protect the borehole walls from the damage of repeated radar measurements. The ZOP data set concludes with another set of four measurements in air at 2.0-m separation. Following this procedure, the MOP data sets are collected with the locations determined before the start of the survey. The transmitter and receiver intervals are every 0.125 m. As in all MOP gathers, the receiving antenna remains at a fixed location (1 m, 1.125 m, 1.25 m, etc.) while the transmitting antenna occupies each of its possible locations along the length of the borehole (e.g., 0 to 8.25 m at 0.125-m spacing). In this manner, all MOP gathers are collected and sorted as receiver gathers with filenames

corresponding to the well pair being surveyed and the fixed receiver location (e.g., MOP14000—an MOP gather collected for well pair #1 at a receiver location 4.000 m below the wall surface). In this manner, each of the necessary ray paths are collected and recorded for the subsequent tomographic processing. Following MOP acquisition, a final ZOP data set is collected as described above. This final step is done in an attempt to estimate any time-zero drift that may have occurred during the course of the survey. By comparing the two ZOP data sets along with the identical data included in the MOP data set, any time-zero drift may be compensated for and corrected.

5.1.7 Results of Busted Butte UZTT radar data acquisition

The radar data were acquired in eight of the Phase-2 collection boreholes orthogonal to the direction of the Phase-2 injection boreholes. Additionally, two of the Phase-2 injection boreholes were used to acquire data after the holes were affected by grout infiltration resulting from nearby ERT borehole grouting. The ten boreholes include the following: 9, 11, 13, 15, 16, 46, 47, and 48 (all Phase-2 collection); 19 and 22 (Phase-2 injection). As mentioned above, radar data are acquired in the 2-D planes defined by two boreholes, commonly referred to as well pairs. The well pairs acquired in support of the Busted Butte UZTT are the following: 15-13, 48-46, 47-11, 46-9, 46-16, and 22-19. The decision to acquire data in these particular well pairs was made based on their relative proximity to the injection boreholes. Data from both the upper horizontal Well Pair 15-13 and the vertical Well Pair 46-16 are acquired to monitor tracer injection associated with the upper injection Boreholes 18, 20, 21, and 23. Data from the lower horizontal Well Pairs 46-9, 47-11, and 48-46 are acquired to monitor tracer injection associated with the lower injection Boreholes 24, 25, 26, and 27. The vertical Well Pair 46-16 may also be used to image any tracer injection associated with the lower injection boreholes and the progress of the tracer beneath the horizontal Well Pair 15-13.

Thus far, the data collected have only been processed for travel times, and the resulting velocity tomograms are all that are completed. Also, two of the well pairs differ slightly in the acquisition method used between the baseline and the post-injection survey. These Well Pairs are 46-16 and 46-9. Data for Well Pair 46-16 was collected at a higher frequency (200 MHz) during the post-injection survey to better match the data collected in all of the other well pairs. Higher frequencies generally result in data of higher resolution (approximately 10.0 cm for 200 MHz), so the highest-frequency antennas should be used if at all possible. Data were not originally acquired in Well Pair 46-9 because it was believed that Well Pair 48-46 provided sufficient coverage in the area of the lower injection boreholes. Initial processing of the baseline data suggested, however, that mapped faults along the Main Adit were being imaged or were possibly affecting the tomography results of Well Pairs 46-16 and 48-46. Therefore, it was decided to acquire data in Well Pair 46-9 to better constrain the impact of the fault system.

Of the data processed so far, several of the well-pair images deserve particular attention. These Well Pairs are 48-46, 46-9, 46-16, and 22-19. The large horizontal surface defined by the 48-46 and 46-9 Well Pairs shows an area of very low velocity in the vicinity of the injection boreholes that differs dramatically from the data acquired before injection began (Figs. 19 and 20). Again, low velocities are likely the result of elevated moisture content or changing chemical composition. Therefore, these low velocities are possibly the result of the injected tracer moving through the plane of the well pairs. The close proximity of several of the injection boreholes to the collection boreholes (10.0 cm), however, might be the cause of the low-velocity zones. That is, the low-velocity zone may be due to the nature of the injection assemblies and any metallic or other velocity-affecting materials being present in such close proximity to the radar well pairs. Subsequent measurements in these well pairs should reconcile the problem because the injection assemblies will remain static while the

injected tracer will continue to pass through and be distributed throughout the well pairs. Differencing tomography (i.e., the subtraction of one set of radar measurements from another) will result in only those areas of tracer being imaged, as the tracer is all that will be changing over the duration of the experiment.

Similarly, the Well Pair 46-16 suggests areas of variable velocity and the possible presence of tracer (Fig. 21). The image is plotted with the injection and ERT boreholes shown as black dots intersecting the well pair. Particularly in the area of the lower injection boreholes (nearest Borehole 46), low velocities are found directly beneath the boreholes. Again, this may represent either the tracer or the injection assemblies, with subsequent data differencing needed to be done to remove the influence of the assemblies. Additionally, a rather striking feature exists between the two boreholes that resembles a low-velocity zone with high angle dip. This feature was also present in the baseline data acquired using the lower-resolution 100-MHz antennas. It may be the result of an elevated moisture content along the highly permeable fault zone mapped along the face of the Main Adit, thus explaining the lower velocities. The apparent strike of the fault would bring it into intersection with Well Pair 46-16 at roughly the observed location of the low-velocity zone. If this zone does represent the fault, then future data acquisition may be able to illuminate the tracer transport properties of the fault zone versus those of the matrix.

Finally, Well Pair 22-19 is notable due to the possible imaging of the pathway taken by the grout moving from an ERT borehole to the planned injection Borehole 22. The grout was apparently injected under sufficient pressure and at sufficient volume to travel from one borehole to another, likely along a fracture or similar fast pathway. The properties of the grout and their impact on radar wave propagation are similar in effect to those of the tracer.

Any zones of low or anomalous velocity are potential evidence of the presence of grout. Such a zone is clearly present in Well Pair 22-19 (Fig. 22). The point of grout injection between injection Boreholes 20 and 21 is shown as a low velocity (i.e., elevated water content) region in the tomogram. This low-velocity zone appears to connect with Borehole 22 and is present laterally 2.50 m down

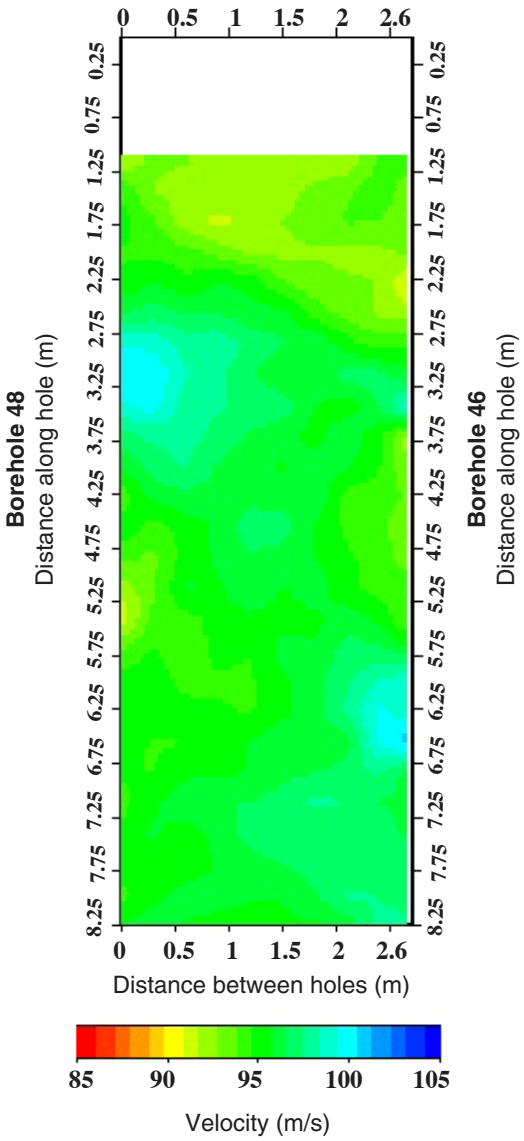

Figure 19. GPR Baseline Image for Pair 48-46. The image above from ground-penetrating radar measurements is for a horizontal section with the top of the figure corresponding to the right rib of the Main Adit. The measurements were taken June 10, 1998, before Phase-2 injection began.

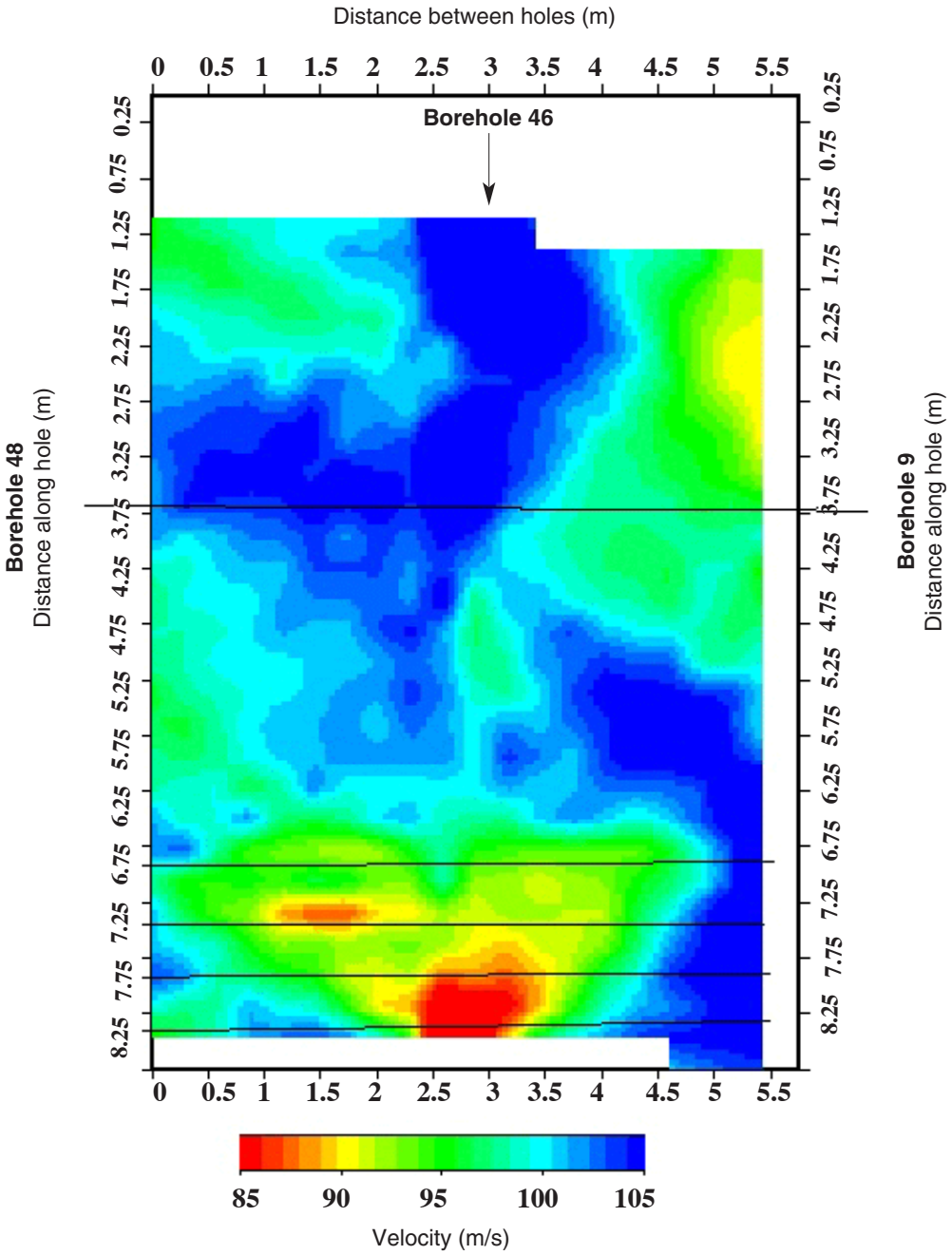

Figure 20. GPR Image of Pairs 48-46-9. The left axis of the ground-penetrating radar image above represents the trace of Borehole 48, the right axis represents the trace of Borehole 9, and Borehole 46 is between this pair at the 3-m position. The plot is a horizontal section taken September 1, 1998, a month after Phase-2B injection had started. The top of the figure corresponds to the right rib of the Main Adit, and the four horizontal lines represent the trace of Phase-2B injection holes. The left half of the figure (Pair 48-46) shows dramatic changes from the baseline image of Fig. 19 with an area of very low velocity (red) at the bottom of the figure in the vicinity of the injection boreholes. This low-velocity area may well be a result of injected tracer moving through the plane of the well pairs.

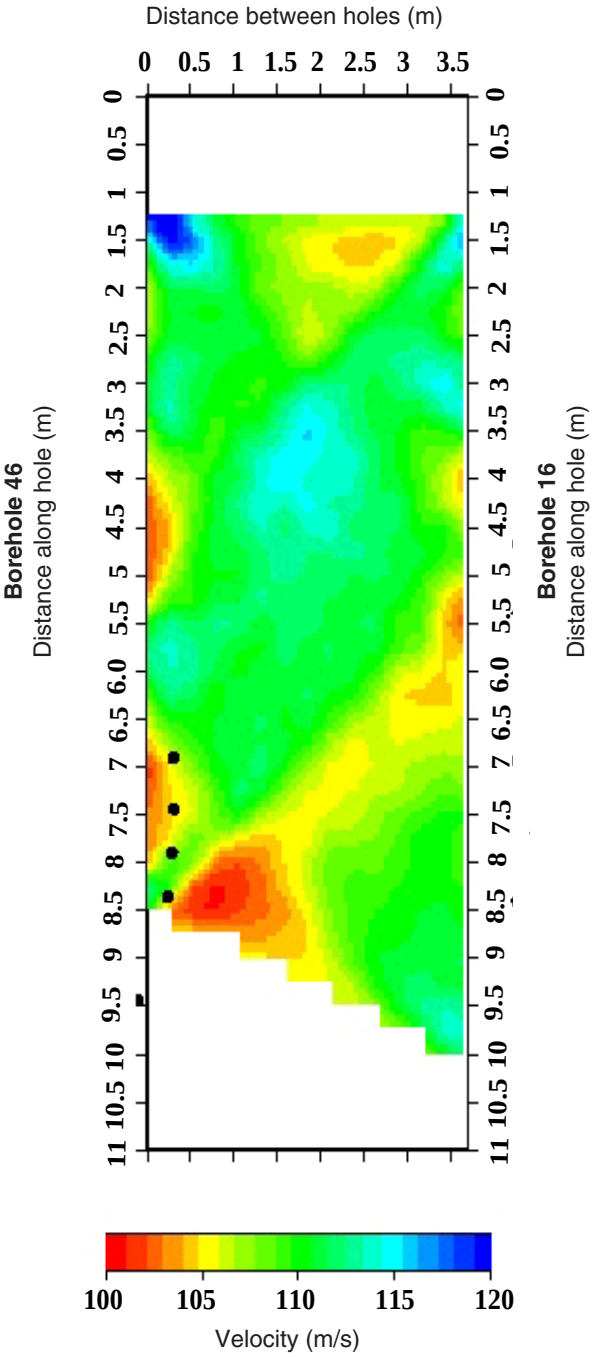

Figure 21. GPR Image of Pair 46-16. This image is a vertical section with the top representing the right rib of the Main Adit. The four dots on the left side of the image represent the intersection of the Phase-2B injection holes. The eight dots to the right outside of the image represent the intersection with injection holes from Phases 2A and 2C and ERT Holes 3 and 5. The image was taken September 1, 1998.

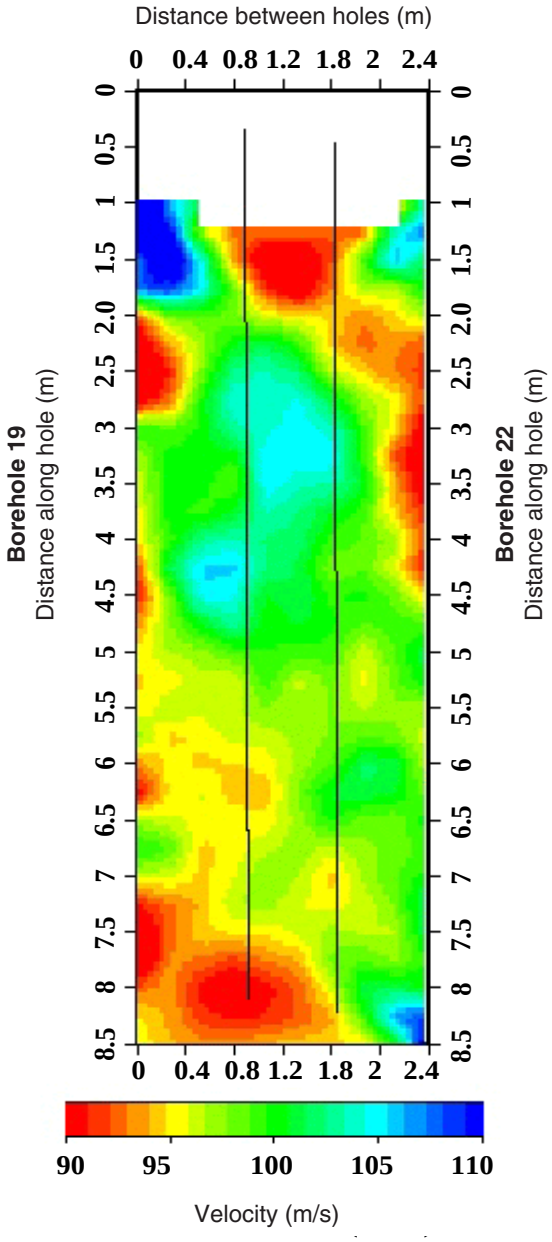

Figure 22. GPR Image of Pair 22-19. This image is a horizontal section with the top of the figure representing the left rib of the Test Adit. The vertical lines in the image represent, from left to right, the trace of Phase-2C Injection Holes 20 and 21. The low-velocity region (red) at the top that slants diagonally to the 2.5-m position of Borehole 22 may be evidence of grout injected into an ERT borehole under pressure that has moved along a fault. Other low-velocity regions in both Figs. 21 and 22 may be evidence of tracer movement along faults (with no grout present).

the length of Borehole 22. Based on the grout-injection history, this scenario appears to be the one experienced by the personnel present at the time. Another low-velocity zone in the area near the bottom of injection Borehole 19 should also be noted. This zone, if located spatially with respect to Well Pair 46-16, nearly intersects the low-velocity zone imaged in the tomogram of Well Pair 46-16. It, too, may be another representation of the elevated moisture content along the fault zone and may have nothing to do with the ERT grouting infiltration.

5.1.8 Conclusions

The radar data collected thus far in support of the Busted Butte UZTT suggest that the method is an appropriate one for investigating subsurface velocity anomalies that may be related to tracer injection. Such anomalies are the result of changes in the dielectric permittivity or chemical composition of the rock mass. As noted above, such changes are most likely the result of both the injected tracer or the downhole assemblies (injection and ERT assemblies). Although the data presented above describe areas of unusually low velocity, subsequent radar data acquisition should remove the effects of the downhole assemblies and result in the singular imaging of the tracer front. This effort, combined with the ongoing processing of the radar-wave amplitude data, should allow for the most accurate imaging of the injected tracer to date.

5.2 Electrical-Resistance Tomography

(This section is from Michael Buettner, William Daily, and Abe Ramirez, Lawrence Livermore National Laboratory.)

5.2.1 Experimental objective

The objective of this work is to provide 3-D ERT images of the movement of a tracer through the test block at the UZTT at Busted Butte. ERT was chosen as an appropriate technology based on its success at many other locations, including the Drift Scale Test at Yucca Mountain. This report describes the results obtained during four separate data collections starting in July and ending in early September 1998.

5.2.2 Description of the electrical-resistance tomography (ERT) method

ERT is a new geophysical imaging technique that can be used to map subsurface liquids as flow occurs during natural or man-induced processes and to map geologic structure. Man-induced processes, for example, tank leaks and clean-up processes such as steam injection, can create changes in a rock's electrical properties that are readily measured. ERT is a technique for reconstruction of subsurface electrical resistivity. The result of such a reconstruction is a 2- or 3-D map of the electrical resistivity distribution underground made from a series of voltage and current measurements from buried electrodes. The ERT approach we follow here relies on detection and mapping of the changes in electrical resistivity associated with the movement of a tracer through the test block at the UZTT site.

ERT surveys are performed using a number of electrodes in boreholes and at the rock surface to image the resistivity distribution between two boreholes. Using an automatic data-collection and switching system, we collect a few hundred electrical-resistance measurements. The data are then processed to produce electrical-resistivity tomographs using state-of-the-art data-inversion algorithms. We use these measurements to calculate tomographs that show the spatial distribution of the subsurface resistivities.

5.2.3 Description of 2-D algorithms

Finite-element iterative algorithm: This algorithm involves solving both the forward and inverse problems. The forward and inverse algorithms used in this work are described in detail by LaBrecque et al. (1996, pp. 538–548); we summarize them below. The solution to the forward problem uses the finite-element method (FEM) to compute the potential electrical response of a 2-D earth to a 3-D source. To avoid the difficulty of numerically solving a 3-D problem, Poisson's equation is

formulated in the wave-number domain using the Fourier transformation in the strike (y) direction. The governing equation is:

$$\frac{\partial}{\partial x}\left(\sigma\frac{\partial V}{\partial x}\right) + \frac{\partial}{\partial z}\left(\sigma\frac{\partial V}{\partial z}\right) - \lambda^2\sigma V = -I\delta(x)\delta(z)\,, \qquad (1)$$

where V is the potential in the Fourier transform domain, σ is the conductivity, λ is the Fourier-transform variable, I is the source current, and $\delta(x)$ and $\delta(z)$ are delta functions (Hohmann 1988). Our 2-D FEM algorithm is based on the theory described by Huebner and Thornton (1982), and our implementation of it follows that described by Wannamaker et al. (1987) for modeling 2-D magnetotelluric data.

Using the FEM, we can calculate the potentials for a discrete number of transform variables at the nodes of a mesh of quadrilateral elements. We can then transform the potentials back into the Cartesian domain using the method described by LaBrecque (1989). The boundary conditions are assumed to be Neumann (zero potential gradient and no vertical current flow) at the ground-air interface and Dirichlet (potential set to zero) along the other three boundaries.

The inverse algorithm iteratively finds the maximum value of the stabilization parameter α_s to minimize the objective function for the stabilization parameter:

$$Y(\mathbf{P}) = \chi^2(\mathbf{P}) + \alpha_s W(\mathbf{P})\,, \qquad (2)$$

where $\mathbf{P}$ is the vector of unknown parameters, $W(\mathbf{P})$ is the roughness operator (Tikhonov and Arsenin 1977), and χ^2 is the chi-squared statistic. Minimizing this function yields a value of $\chi^2(\mathbf{P})$ equal to an a-priori value, $\chi^2_{\text{a-priori}}$, which in our work, is assumed to equal the number of data points. The inverted parameters are the natural logarithms of the conductivities of pixels, where each pixel contains the elements of a rectangular region of a FEM mesh. The chi-squared statistic is given by:

$$\chi^2 = [\mathbf{D} - \mathbf{F}(\mathbf{P})]^{\mathsf{T}} W^{-1} [\mathbf{D} - \mathbf{F}(\mathbf{P})]\,, \qquad (3)$$

where $\mathbf{D}$ is the vector of known data values, $\mathbf{F}(\mathbf{P})$ is the forward solution, T signifies transpose, and W is the data covariance matrix.

The roughness operator stabilizes and removes ambiguity in the resistivity inversion by minimizing the model roughness, which is referred to as "smoothest inversion." The roughness operator $W(\mathbf{P})$ is given by:

$$W(\mathbf{P}) = \mathbf{P}^{\mathsf{T}}\mathbf{R}(\mathbf{P})\,, \qquad (4)$$

where, here, $\mathbf{R}$ is the roughness matrix, a numerical approximation to the 2-D Laplacian operator (Sasaki 1992, pp. 453–463).

At the ith iteration, our algorithm begins by approximating the forward solution by a first-order Taylor's series of the form:

$$\mathbf{F}(\mathbf{P}) = \mathbf{F}(\mathbf{P}_i) + \mathbf{A}(\mathbf{P} - \mathbf{P}_i)\,, \qquad (5)$$

where $\mathbf{F}(\mathbf{P})$ is the forward solution, $\mathbf{A}$ is the sensitivity matrix, and $\mathbf{P}_i$ is the vector of estimated parameters at the ith iteration.

Using a root-finding algorithm, we estimate α_s for this linearized system. We then use a modified Marquardt method iteration (Bard 1974, pp. 111–113) to find the parameters that minimize the objective function (Eqn. 2) for the estimated value of α_s. Iteration is repeated until the changes in α_s and χ^2 from one iteration to the next are suitably small.

Single-pass image reconstruction: The computational demands and potential convergence failure of a formal inverse solution such as that above has prompted the development of a number of image-reconstruction algorithms that are purely qualitative. We adopt here a version of one such algorithm, that of Kotre (1989, pp. 275–281), which

computes a "gray scale" associated with each element j =1, 2, ... m according to a simple matrix-vector product:

$$\mathbf{P}_j = \sum_{i=1}^{n} S_{i,j} \ln(\mathbf{T}_i'/\mathbf{T}_i) \quad j = 1, 2, \ldots m\,, \qquad (6)$$

where n is the number of independent measurements, $\mathbf{T}_i$ and $\mathbf{T}_i'$ are the ith-measured boundary transfer resistances before and after a change in resistivity within the region, and $S_{i,j}$ is a sensitivity coefficient for element j and independent measurement i derived in the same manner as the smoothness algorithm in the previous section.

The sensitivity matrix is computed on a finite-element mesh with uniform resistivity. Because no inverse matrices are required, the algorithm is computationally efficient and very fast as only one matrix vector product is required for each image.

5.2.4 Description of the 3-D imaging algorithm

Our 3-D inversion algorithm requires a forward solution, which can numerically solve the potential equation:

$$\frac{\partial}{\partial x}\left(\sigma\frac{\partial V}{\partial x}\right) + \frac{\partial}{\partial y}\left(\sigma\frac{\partial V}{\partial y}\right) + \frac{\partial}{\partial z}\left(\sigma\frac{\partial V}{\partial z}\right) = I(x,y,z)\,, \qquad (7)$$

where V is the scalar electrical potential and $I(x,y,z)$ is the distribution of electrical current sources and sinks. We use the FEM with rectangular, hexahedral elements (Pridmore et al. 1981, pp. 1009–1024) to convert the differential equation (Eqn. 1) into a system of linear equations. This system of equations is then solved iteratively using the diagonally weighted preconditioned-conjugate-gradient method (Pini and Gambolati 1990, pp. 147–153). The forward-modeling algorithm is a modified version of one written by Qin (1995). The boundary conditions are assumed to be Neumann (zero potential gradient, no vertical current flow) at the ground-air interface and Dirichlet (potential set to zero) along the other five boundaries.

Three-dimensional inversion is by nature strongly underdetermined, and so, inverse solutions that consider only the fitting of the forward model to field data are nonunique. Therefore, we implemented a regularized solution (Tikhonov and Arsenin 1977) that jointly minimizes the misfit of the forward model to the field data and stabilizes the inverted value of the parameters. To find the optimal value of the parameter vector $\mathbf{P}$, our algorithm finds the maximum value of α_s, the stabilization parameter, for which minimizing:

$$Y(\mathbf{P}) = \chi^2(\mathbf{P}) + \alpha_s \mathbf{P}^{\mathsf{T}} \underline{\mathbf{R}} \mathbf{P}\,, \qquad (8)$$

gives

$$\chi^2(\mathbf{P}) = \chi^2_{\text{a-priori}}\,. \qquad (9)$$

In Eqn. 8, we have chosen to use $\underline{\mathbf{R}}$, the solution roughness, as the stabilizing functional. This parameter is approximated by:

$$\underline{\mathbf{R}} = \underline{\mathbf{x}}^{\mathsf{T}}\underline{\mathbf{x}} + \underline{\mathbf{y}}^{\mathsf{T}}\underline{\mathbf{y}} + \underline{\mathbf{z}}^{\mathsf{T}}\underline{\mathbf{z}}\,, \qquad (10)$$

where $\underline{\mathbf{x}}$, $\underline{\mathbf{y}}$, and $\underline{\mathbf{z}}$ are the first-order difference operators in the x, y, and z directions. Also in Eqn. 9, $\chi^2_{\text{a-priori}}$ is equal to the number of data points, and χ^2 is given by:

$$\chi^2 = (\mathbf{D} - \mathbf{F}(\mathbf{P}))^{\mathsf{T}} \underline{\mathbf{W}} (\mathbf{D} - \mathbf{F}(\mathbf{P}))\,, \qquad (11)$$

where $\mathbf{D}$ is the vector of known data values, $\mathbf{F}(\mathbf{P})$ is the forward solution and $\underline{\mathbf{W}}$ is a data weight matrix. The diagonal elements of $\underline{\mathbf{W}}$ are the reciprocals of the data variances, and the nondiagonal elements are zero. This assumes noncorrelated data errors.

The parameters $\mathbf{P}$ are the natural logarithms of the conductivity of the FEM elements. In the foreground (the part of the FEM mesh between the boreholes and near the boreholes), each parameter corresponds to a single finite element. In the background (the region away from the boreholes), we lump several finite elements together into a single parameter.

The nonlinear inversion is carried out iteratively as:

$$\mathbf{P}_{k+1} = \mathbf{P}_k + \Delta\mathbf{P}_k \,, \tag{12}$$

where $\mathbf{P}_k$ is the vector of parameters from the previous iteration and $\Delta\mathbf{P}_k$ is the parameter change vector. The $\Delta\mathbf{P}_k$ vector is found by solving the linear problem:

$$\Delta\mathbf{P}_k = (\underline{\mathbf{A}}_k^{\mathsf{T}}\mathbf{W}\underline{\mathbf{A}}_k + \alpha_s\underline{\mathbf{R}})^{-1}(\underline{\mathbf{W}}\Delta\mathbf{D}_k - \alpha_s\mathbf{R}\mathbf{P}_k) \,, \tag{13}$$

where $\underline{\mathbf{A}}_k$ is the sensitivity matrix and $\Delta\mathbf{D}_k = \mathbf{F}(\mathbf{P}) - \mathbf{D}$. The elements of the sensitivity matrix, $A_{i,j}$, are:

$$A_{i,j} = \frac{\partial F_i(\mathbf{P}_k)}{\partial p_j} \,, \tag{14}$$

where p_j is the jth element of $\mathbf{P}_k$ and $F_i(\mathbf{P}_k)$ is the forward solution for the ith data point. Solving Eqn. 13 exactly is not practical because the system is very large (50,000 by 50,000), full, and ill-conditioned. Instead, we use the conjugate-gradient method described by Mackie and Madden (1993, pp. 215–229) to give a stable, approximate solution to this linear system. The details will not be repeated here, but note that the solution does not require the calculation of the full sensitivity matrix; it requires only the calculation of the sensitivity matrix and its transpose multiplied by a vector.

Our routine differs from that of Mackie and Madden in three ways. First, we use a method similar to that described by Rodi (1976, pp. 483–506) to calculate $\underline{\mathbf{A}}^{\mathsf{T}}\mathbf{u}$ and $\underline{\mathbf{A}}\mathbf{v}$, where $\mathbf{u}$ and $\mathbf{v}$ are vectors. Because we calculate a forward model for every electrode, this method does not require any additional forward solutions during the conjugate gradient iterations. Second, we use more conjugate gradient iterations than Mackie and Madden (1993, pp. 215–229). For the magnetotelluric inverse problem, Mackie and Madden found that the nonlinear inversion routine converged well with three conjugate gradient iterations. We usually require between 10 and 40 conjugate gradient iterations to achieve adequate convergence. Third, we use smoothness instead of comparison with an a-priori model to stabilize the inverse solution.

We have found that choosing the correct value of α_s is critical for both achieving rapid convergence of the nonlinear inversion and for finding a good final parameter estimate. With our method, a new value of α_s is estimated at the end of each nonlinear iteration. The estimate uses the assumption that the relation between χ^2 and α_s can be approximated by the rational function:

$$\chi^2 \cong \frac{b\alpha_s}{\alpha_s + a} \,. \tag{15}$$

The constant a is estimated from the values of α_s and χ^2 of the previous iteration. If the misfit is χ_k^2 and the desired misfit is χ^2_{target}, then the new estimate of α_s, $\alpha_{s_{k+1}}$, is:

$$\alpha_{s_{k+1}} = \frac{\frac{b}{\chi_k^2} - 1}{\frac{b}{\chi^2_{\text{target}}} - 1}\,\alpha_{s_k} \,. \tag{16}$$

The value of χ^2_{target} is chosen as the larger of $\chi^2_{\text{a-priori}}$ and $0.5\chi_k^2$.

Although the approach is simplistic, it usually converges to the correct value of χ^2 in 10 to 20 iterations.

5.2.5 ERT data-collection system

As shown in the block diagram of Fig. 23, the data-collection system is composed of three main parts: a transmitter, a receiver, and a laptop computer to control the system and archive the data. Without going into a great deal of detail, the action of the system can be briefly described as follows.

The computer sets the switches in the MX-30 multiplexer according to a predefined schedule so as to connect the transmitter to a particular electrode pair and the receiver channels in the GDP-32

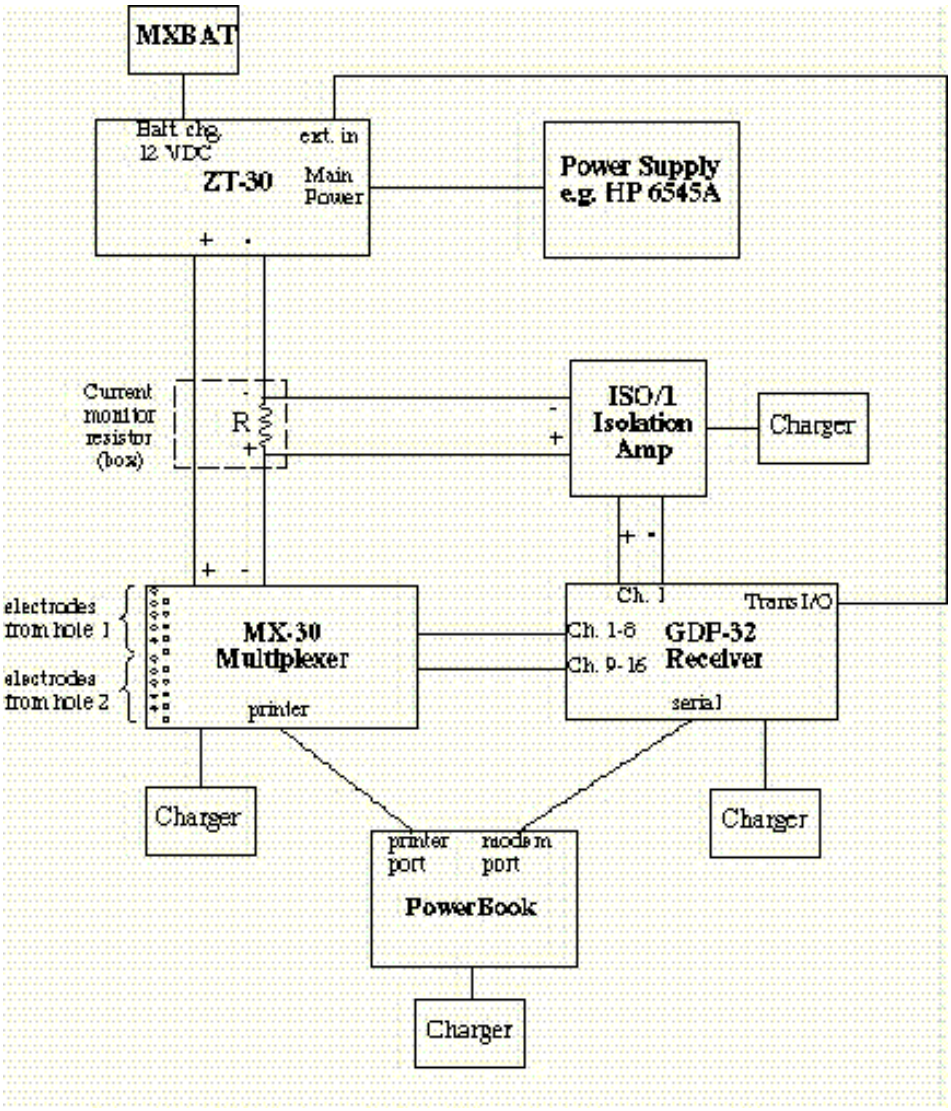

Figure 23. ERT Data-collection System. This block diagram illustrates the ERT data-collection system used at Busted Butte.

receiver to other sets of electrode pairs. The GDP-32 tells the ZT-30 to apply current to the transmitter pair and measures the resulting potentials at the other pairs. The data are then sent back to the computer and stored. A new transmitter pair is selected according to the schedule, and the process begins again until all the combinations in the schedule have been used.

5.2.6 Results from the data collections of July to early September

ERT data were collected four times: July 2, July 14, August 19, and September 9, 1998. The idea was to do comparisons between the baseline condition on July 2 and data collected at later times. We present comparisons between July 2 and August 19 and between July 2 and September 9 because the data from July 14 were of questionable quality.

Sixty ERT electrodes were installed in the test block as shown in Fig. 24. The electrodes were placed in six drilled holes, ERT-1 though ERT-6, and two surface arrays (upper and lower). Holes ERT-3, 4, 5, and 6 and the surface arrays were

drilled perpendicular to and from the instrumentation alcove. Holes ERT-1 and 2 were drilled from the main drift. The electrodes were grouped into Boreholes 1 through 4 as shown in Fig. 25. As is evident, each borehole is L-shaped and contains 15 electrodes. For example, Borehole 1 is composed of the 8 electrodes in Hole ERT-3 along with the 7 electrodes in the upper-surface array.

The ERT data are collected between borehole pairs, that is, between Boreholes 1 and 2 (upper horizontal plane), 3 and 4 (lower horizontal plane), 1 and 3 (left vertical plane), 2 and 4 (right vertical plane), 1 and 3 (diagonal), and finally, 2 and 4 (diagonal) for a total of six data sets. The total number of data values collected is 2430. These 2430 values provide the 3-D sampling of the test block resistivity, and the 3-D inversion algorithm operates on these data to produce a reconstruction of the 3-D resistivity distribution, a 3-D ERT image, of the block.

Although one could look at absolute ERT images or comparison images, we find it most useful to look at comparison images when changes are taking place over time. The results presented here consider difference images that compare the resistivity of the block on August 19 and September 9 to July 2. Because the water injected during Phase 2 of the UZTT experiment was approximately eight times more conductive than the pore water, we look for resistivity decreases in the images.

5.2.7 Absolute ERT images of the block

Figure 26 shows an absolute image of the baseline condition of July 2 (top) and the difference between August 19 and July 2 (bottom). The baseline image shows a layered structure consistent with the lithology in the rear half of the block—that is, a high-resistivity layer over most of the middle of the block, Tptpv1, with a lower-resistivity region, Tptpv2, at the top, and a low-resistivity region, Tac, at the bottom. The image also shows

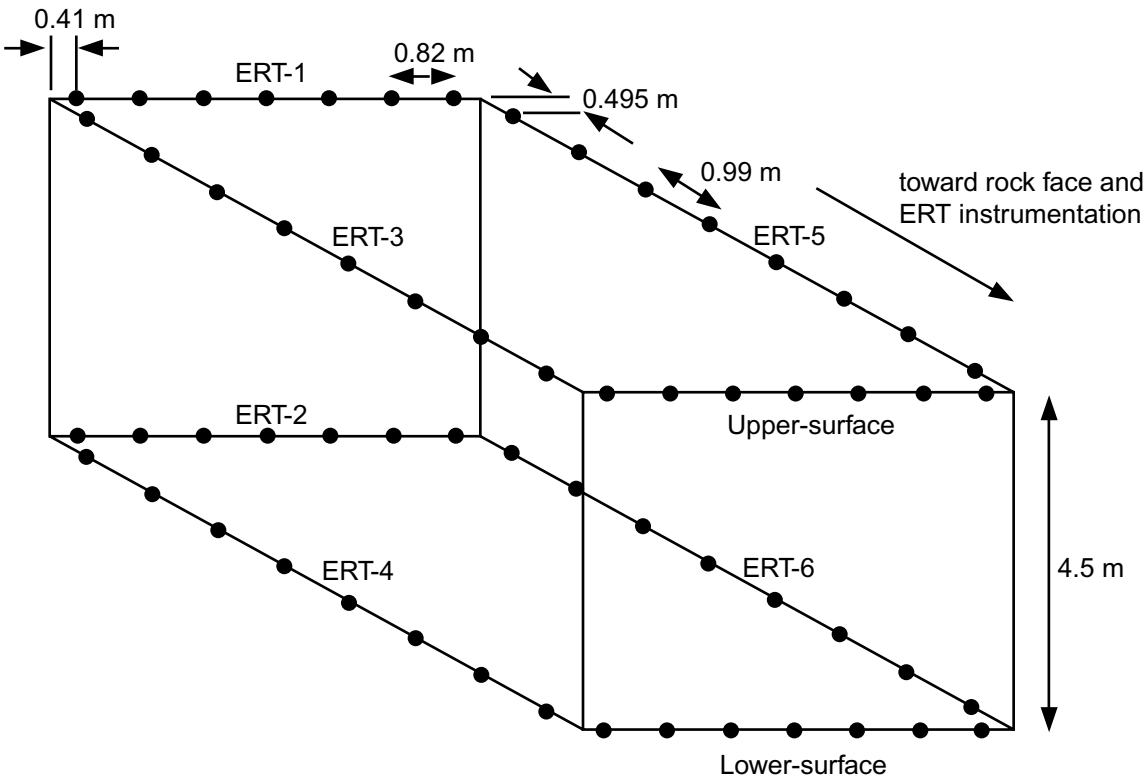

Figure 24. ERT Layout. This diagram gives the layout of drilled holes, ERT electrode locations, and spacing in the UZTT test block at Busted Butte.

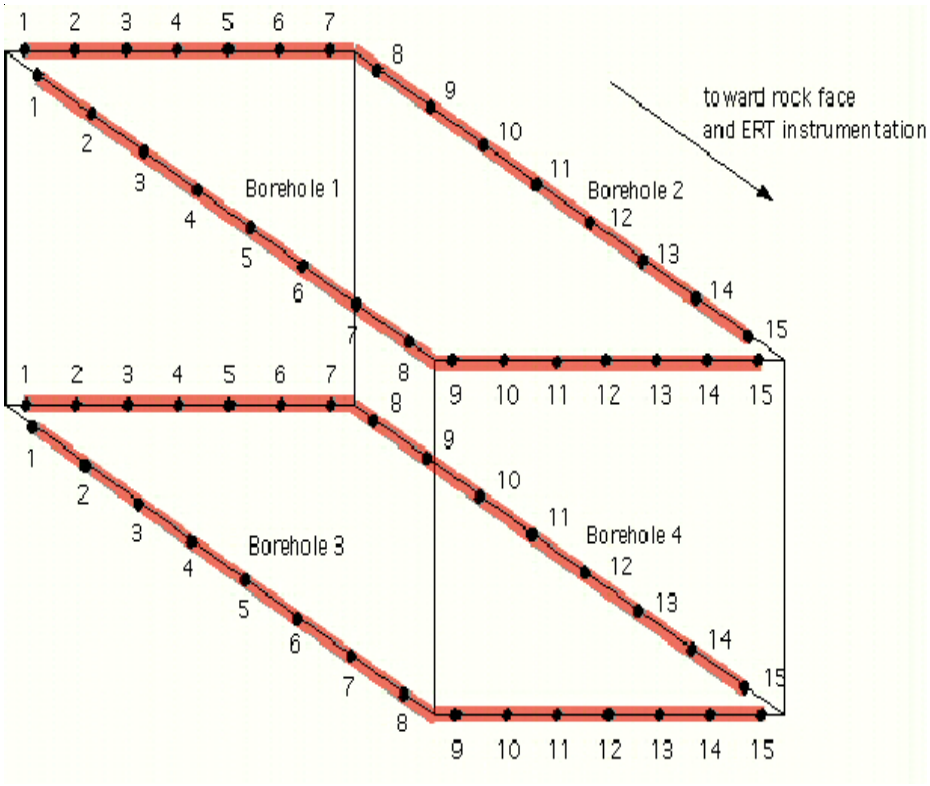

Figure 25. ERT Electrode Assignments. This diagram gives the layout of the ERT boreholes and electrode assignments in the UZTT test block.

an anomalously low resistivity region in the front half of the block, particularly near the bottom.

5.2.8 Difference ERT images of the block

The difference image of Fig. 26 shows regions of resistivity decrease near Injection Holes 18, 20, and 21, as one would expect from the injection of conductive water. One can also see a resistivity decrease that is very pronounced in the slice 2.66 m from the front of the block, which could be associated with water moving downward in the block. The region of the block between 1.33 and 4.0 m, which contains this slice, also appears to be a low-resistivity region in the absolute image.

The September 9–July 2 difference (Fig. 27) also shows regions of resistivity decrease near Injection Holes 18, 20, and 21. The effect is even stronger in the 5.33-m slice. Moreover, the effect of water moving down into the block seems to be more pronounced in the 1.33-m and 4.0-m slices compared to August 19.

5.2.9 Conclusions

The ERT baseline images show a resistivity structure that is consistent with the known lithology in the rear part of the block. There appears to be a low-resistivity region in the front half of the block, particularly near the bottom. This is not well understood and should be confirmed, if possible, by other means.

The difference images from August 19 and September 9 show clear and consistent resistivity decreases in the region near Holes 18, 20, and 21 that can be associated with the injection of conductive water. This effect appears to be stronger on September 9 in the 5.33-m slice. The images show very little effect in the region around the other injection holes—23 and 24 through 27—where far less water was injected.

In addition, the difference images from August 19 and September 9 show resistivity decreases that could be interpreted as water moving down into the block between the 1.33-m and 4.0-m slices. This is the same region that has an anomalously low resistivity in the baseline image.

These results should be considered preliminary and subject to change based on new information, such as the borehole radar data obtained by LBNL and, perhaps, neutron data.

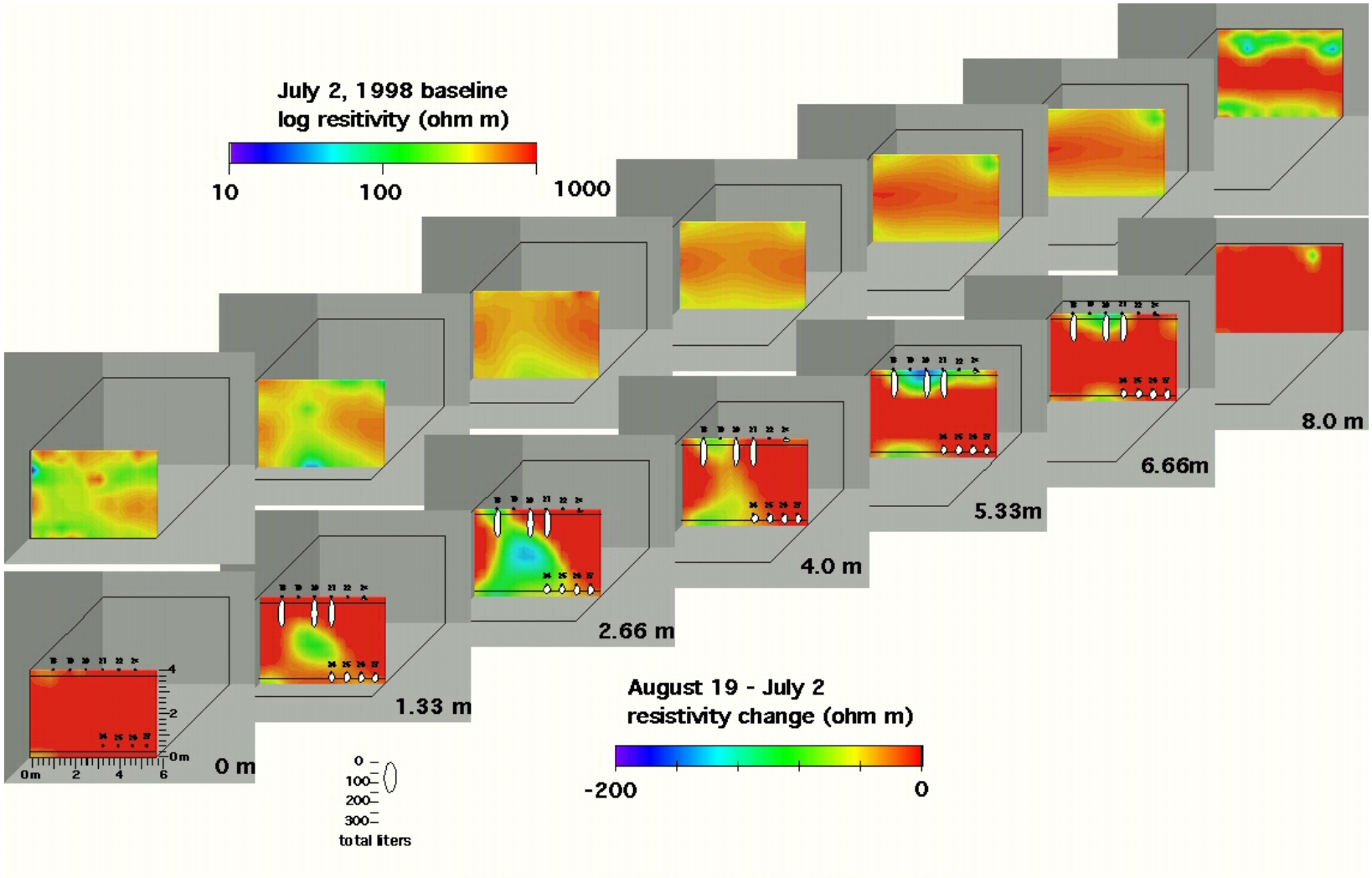

Figure 26. ERT Images of Test Block Viewed From Test Alcove: Baseline and August Differences. The diagram shows vertical slices through the block at 0, 1.33, 2.66, 4.0, 5.33, 6.66, and 8.0 m. The top series is an absolute image (baseline, July 2), and the bottom series consists of the August 19–July 2 difference images.

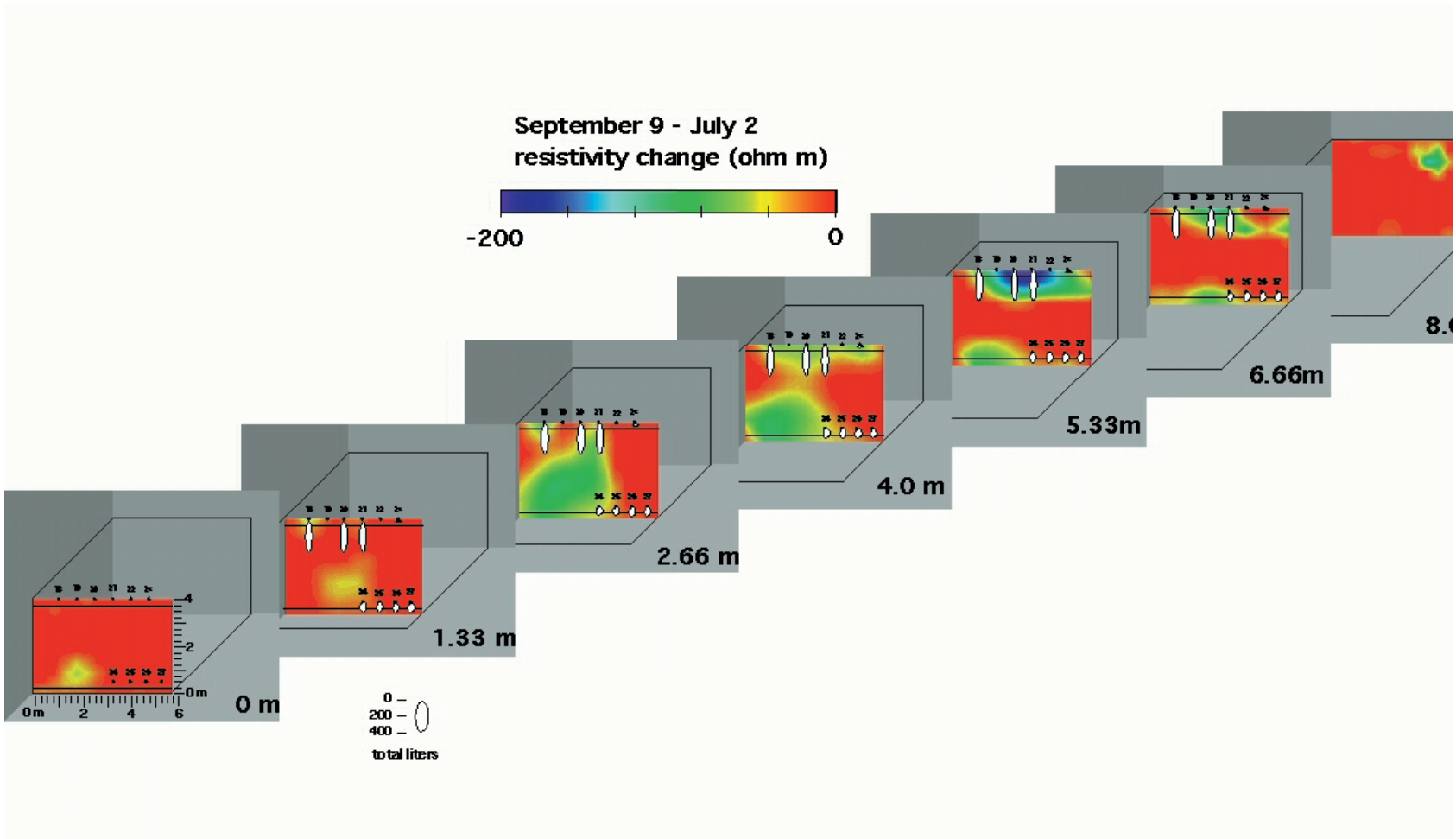

Figure 27. ERT Images of Test Block Viewed From Test Alcove: September Differences. The diagram shows vertical slices through the block at 0, 1.33, 2.66, 4.0, 5.33, 6.66, and 8.0 m that represent September 9–July 2 difference images.

6. PHASE-1A PREDICTIONS

6.1 Deterministic Model

The purpose of the UZTT at Busted Butte is to obtain new information about flow-and-transport behavior and to apply that information toward improving computational models used to predict flow and transport in the vadose zone. The field experiments at Busted Butte are being run to examine flow in unfractured, fractured, and composite systems. These experiments have been carefully designed to provide specific information that can be used both for database improvement and modeling improvement. Data collected through the UZTT will test the accuracy and value of data currently in the database and will improve it in the future. Improved data and increased experimental information about the site will improve computational models of the various flow-and-transport processes occurring in the system. The accuracy of current concepts for UZ flow and transport, and the iterative improvement of the model through incorporation of new data, can then be shown through increased accuracy of the model. As more data become available, we should be able to demonstrate the validity of refined flow-and-transport models, as well as the worth of the data-collection exercise at Busted Butte. At the end of the testing and modeling period, the Project should have a model that describes the flow-and transport-behavior at the site. In addition, refinements to the radionuclide transport model of the potential repository site should follow. This cyclic process of prediction, measurement, and model refinement will result in increased confidence in the unsaturated-zone model.

This document constitutes a preliminary blind prediction on the behavior of Phase 1A of the UZTT. The blind prediction is intended to test the current modeling concepts and tools available to the integrated site-scale model and their abstractions. This prediction uses parameters from the available Yucca Mountain hydrologic database, as well as initial laboratory values on samples taken from the Busted Butte site. As more data become available from the UZTT, they will be incorporated into refined versions of the models employed in these preliminary predictions.

The numerical experiments presented here were set up to determine the ability of numerical models to predict actual field response of flow and transport in porous media. The simulations are not intended to be a one-time prediction but, rather, are intended to provide insight into the quality and extent of the information needed to accurately represent a physical system and to identify physical processes that are not currently adequately represented in numerical models.

The computer code FEHM (Zyvoloski et al. 1995, 69 pp.) is used in the development of the predictions presented in this paper. FEHM is a multidimensional, multiphase, unsaturated and saturated, transient, finite-element code. FEHM is the code used by the Project for radionuclide migration predictions. Therefore, it was the obvious choice for predictions of the UZTT results. At this site, detailed geologic and hydrologic property distributions in three dimensions are not available at present, and the Calico Hills unit (Tac) in question is not fractured, so we began with a homogeneous, isotropic description of the porous media. However, three-dimensional effects may very well become apparent during the test, and we expect that more site data will also become available. Therefore, the model is fully three dimensional from the outset to allow us to capture any of these effects and to anticipate the three-dimensional property database that will be built for the test block.

In this simulation of Phase 1A, the focus is on the injection of a conservative tracer into the vitric Tac unit via a single injection point in a 10-cm diameter borehole. In this document, we make numerically based blind predictions of the tracer distribution for Phase 1A. These predictions are made prior to the beginning of any measurements at the site. Thus, the accuracy of our understanding of the system and the representation of the computa-

tional model can be tested.

This model for Phase 1A assumes a homogeneous, unfractured rock matrix. A 0.05-m-radius borehole is in the center of the computational domain. The tracer solution is injected through a polypropylene pad located 0.75 m down the length of the borehole. The base prediction is made using data measured on Busted Butte samples, with information about the injection pad provided from SEA, the contracted field-implementation team.

The simulations here are made assuming a 6-month (180-day) duration for Phase-1A testing. This corresponds to a mineback and auger schedule for Phase 1A of October 2, 1998. Measurements of the tracer concentrations from collected samples are to be conducted after that date. After auger samples are collected and analyzed and mineback completed, the numerical predictions will be compared against the measured values, and the accuracy of the model configuration will be addressed.

Using the experimental injection rate of 10 ml/hr, after 180 days, the model predicts tracer transport distances as shown in the Table 12. (In all the simulations discussed in this section, the tracer was injected at a concentration of "one," and cited concentration values are relative to this initial value.)

The predicted distribution of the tracer is generally uniform in all directions, that is, a spherical distribution. Changes in saturation from the background (in-situ) level are generally small. Table 13 shows the saturation at different distances from the injection point at 180 days for the base-case simulation. Note that the initial background saturation for this simulation is 0.35, based on measured moisture contents of 14.0 ± 2.5% and a porosity of approximately 0.5.

Table 12. Predicted Transport Distances for a Given Concentration.

Relative concentration	Distance traveled (m)
0.01	0.85
0.1	0.67
0.25	0.56
0.50	0.45

Table 13. Simulation Results at 180 Days.

Distance from injection point	Saturation, *S*, at 180 days
0.125	0.402
0.25	0.381
0.50	0.366
1.00	0.357

Additional simulations were run to assess the effect of variability of the hydrogeologic parameters used in the modeling. In the event that the predictions from the base simulation do not agree with field measurements, these sensitivity analyses will be used to identify potential discrepancies between the model and the actual field site.

6.1.1 Model configuration and parameter set

The simulations of the Phase-1A field experiment were run in a model system that approximates the field configuration as closely as possible. The model system was a single borehole with a diameter of 0.10 m embedded in a matrix of tuff in the Tac unit. The domain size for the simulations is 6 m × 6 m × 1.5 m. The borehole extended the full 1.5-m length of the z direction, and gravity acts in the $-x$ direction. The system configuration is shown in Fig. 12. Both 2-D and 3-D simulations of the system were run. The 2-D system was a vertical plane, an x-y slice through the injection point at 0.75 m.

The model attempted to capture the experimental setup as closely as possible, including accurately capturing the actual configuration of the injection pad. The injection pad resided inside the borehole,

centered at (0.0, 0.05, 0.75). The pad was a 0.05-m by 0.05-m polypropylene pad, with material parameters shown at the bottom of Table 14a. Injection occurred at a single point in the center of the pad, consistent with the actual physical injection system. For Phase 1A, the injection point is located on the side of the borehole, 90° off vertical, as shown in Fig. 12.

The boundary conditions for the simulation were no flow for the lateral sides ($y = \pm 3$ m) and the front face of the borehole ($z = 0$ m). The exposed face of the rock in the field ($z = 0$) has been sealed to minimize evaporative losses resulting from the experimental tunnel. The top and bottom faces ($x = \pm 3$ m) of the model, as well as the back side ($z = 1.5$ m), were held at a fixed capillary pressure. Capillary pressures were chosen to match measured in-situ saturation and capillary-pressure conditions. The use of capillary-pressure boundary conditions provides the most accurate means of capturing the real saturation distribution of the system. Although for a homogeneous rock matrix, capillary pressure can readily be converted to a constant saturation boundary, in a heterogeneous system, the saturation may vary drastically around the boundary, though the capillary pressure is relatively constant. In the vadose zone, the capillary pressure provides a much better representation of the steady-state condition of the system, and measured in-situ saturations can be much better captured by a model.

As mentioned previously, the purpose of the simulations was both as scoping calculations for Phase-1A and future injection tests and for assessing the viability of current models. In the simulations, the influence of a number of model parameters were assessed that can, at best, be only approximately known. These parameters include rock permeability, relative permeability, porosity, and in-situ conditions (saturation). For these simulations, the constitutive relationships (relative permeability versus saturation and capillary pressure versus saturation) are characterized using the van Genuchten curve fit (van Genuchten 1980, pp. 892–898). The van Genuchten method fits the data points of permeability versus saturation measured in the laboratory to a two-parameter function. The two parameters are typically denoted as α and n. The α parameter represents the air entry pressure and is given here in units of 1/m. The n parameter controls the slope of the capillary-pressure–saturation curve and is nondimensional.

Tables 14a and b, respectively, list the different parameter combinations that were run in 2-D and 3-D representations of Phase 1A. The "base case" represents our current best knowledge of the properties and conditions of the system. Using available data, a range for each parameter was simulated. The response of the system to various rates of injection of the tracer fluid was also assessed. Injection rates simulated were 1, 10, and 50 ml/hr. These injection rates were chosen to span the range of rates being considered for the various UZTT phases.

6.1.2 Modeling results

6.1.2.1 Overview of simulations

The large 3-D system size required relatively long simulation times. In an effort to minimize computer time and use the time most effectively, we started by running 2-D simulations. These simulations were used primarily as scoping calculations to identify the important simulations to run in three dimensions. As will be seen from the numerical results, the 2-D simulations showed shorter travel distances for the tracer than did the same simulation in 3-D. The differences in tracer movement between 2-D and 3-D simulations at the same effective injection rate are primarily due to the effective volume of injection. The 2-D system is implicitly 1 m in depth, resulting in a lower effective point-injection rate. Therefore, all quantitative predictions are made using values from the 3-D simulations; however, the 2-D simulations can be used to identify the relative response of one set of conditions versus another. Our results indicate that trends in the 2-D simulations mirror those in the 3-D simulations.

A series of 2-D simulations (Table 14a) were run to identify the relative importance of different parameters and injection scenarios. Figure 28, a graph of concentration versus distance from the borehole center, indicates that this system is relatively insensitive to many of the parameters but is quite sensitive to some. Three-dimensional simulations were chosen from the parameter sets to which the system was most sensitive. Six parameter combinations were chosen, which are listed as the first six

Table 14a. Hydrologic Parameters Used for the 2-D Simulations.

The simulation-variable column shows the parameter being varied (tested) in the simulation, including *k*, the intrinsic permeability (value under saturated conditions). The variables α and *n* are the van Genuchten function parameters taken from laboratory measurements.

Simulation variable	Porosity, *P*	Permeability (m^2)	α (1/m)	*n*	Saturation, *S* (in situ)	Inj. rate, *I* (ml/hr)
Base case	0.30	1.3×10^{-12}	0.82	1.31	0.30	10
$k = 0.1 \cdot k_{base}$	0.30	1.3×10^{-12}	0.82	1.31	0.30	10
$k = 10 \cdot k_{base}$	0.30	1.3×10^{-12}	0.82	1.31	0.30	10
$P = 0.20$	0.20	1.3×10^{-12}	0.82	1.31	0.30	10
$P = 0.40$	0.40	1.3×10^{-12}	0.82	1.31	0.30	10
α low, *n* low	0.30	1.3×10^{-12}	0.60	1.20	0.30	10
α high, *n* low	0.30	1.3×10^{-12}	1.20	1.20	0.30	10
α low, *n* high	0.30	1.3×10^{-12}	0.60	1.80	0.30	10
α high, *n* high	0.30	1.3×10^{-12}	1.20	1.80	0.30	10
In situ, $S = 0.2$	0.30	1.3×10^{-12}	0.82	1.31	0.20	10
In situ, $S = 0.4$	0.30	1.3×10^{-12}	0.82	1.31	0.40	10
In situ, $S = 0.5$	0.30	1.3×10^{-12}	0.82	1.31	0.50	10
In situ, $S = 0.6$	0.30	1.3×10^{-12}	0.82	1.31	0.60	10
In situ, $S = 0.7$	0.30	1.3×10^{-12}	0.82	1.31	0.70	10
In situ, $S = 0.8$	0.30	1.3×10^{-12}	0.82	1.31	0.80	10
In situ, $S = 0.9$	0.30	1.3×10^{-12}	0.82	1.31	0.90	10
In situ, $S = 0.2$, $I = 1$	0.30	1.3×10^{-12}	0.82	1.31	0.20	1
In situ, $S = 0.3$, $I = 1$	0.30	1.3×10^{-12}	0.82	1.31	0.30	1
In situ, $S = 0.4$, $I = 1$	0.30	1.3×10^{-12}	0.82	1.31	0.40	1
In situ, $S = 0.5$, $I = 1$	0.30	1.3×10^{-12}	0.82	1.31	0.50	1
In situ, $S = 0.6$, $I = 1$	0.30	1.3×10^{-12}	0.82	1.31	0.60	1
In situ, $S = 0.7$, $I = 1$	0.30	1.3×10^{-12}	0.82	1.31	0.70	1
In situ, $S = 0.8$, $I = 1$	0.30	1.3×10^{-12}	0.82	1.31	0.80	1
In situ, $S = 0.9$, $I = 1$	0.30	1.3×10^{-12}	0.82	1.31	0.90	1
In situ $S = 0.3$, $I = 50$	0.30	1.3×10^{-12}	0.82	1.31	0.30	50
In situ $S = 0.9$, $I = 50$	0.30	1.3×10^{-12}	0.82	1.31	0.90	50
Polypropylene pad	0.85	2.2×10^{-11}	17.0	1.12	N/A	N/A

N/A—not applicable

rows in Table 14b. From these simulations, both spatial and temporal concentration profiles will be presented. Although time-history concentration profiles are presented here, for this prediction, the concentration distribution at 180 days after injection is of most interest, as this is the time when the overcoring will begin.

The most influential parameter, based on Fig. 28, is the value of the van Genuchten power *n*. The values of both van Genuchten parameters, α and *n*, for the base case were taken from laboratory measurements made on cores from the Busted Butte site. Available data for the Tac unit were also collected from other sources (Flint 1998, pp. 1–64; Bodvarsson 1997, Table 6.5.4-1) to try to capture the uncertainty of these parameters. From these data, we chose high and low values of α and *n* and tested the range of responses for the combinations of those values. The value of *n* strongly controls the relative influence of capillary forces and gravity forces. Increasing *n* decreases the capillary forces, resulting in more gravity-driven flow.

Another parameter that clearly influenced the tracer transport was the porosity. Although flow is only slightly affected by even relatively large changes in porosity, transport is more strongly affected. Porosity affects transport because pore velocity is the bulk velocity of the fluid divided by the porosity. Two-dimensional and 3-D simulations were run with porosity increased and decreased by 10 to 15%. The higher porosity did not substantially change the transport, but the lower porosity made an observable difference.

A third factor affecting tracer transport was, not surprisingly, the injection rate. Prior to starting Phase 1A, simulations were run using different injection rates to help select a rate for Phase 1A

Table 14b. Hydrologic Parameters Used for the 3-D Simulations.

The simulation-variable column shows the parameter being varied (tested) in the simulation, including *k*, the intrinsic permeability (value under saturated conditions). The variables α and *n* are the van Genuchten function parameters taken from laboratory measurements.

Simulation variable	Porosity, *P*	Permeability (m^2)	α (1/m)	*n*	Saturation, *S* (in situ)	Inj. rate, *I* (ml/hr)
Base case	0.35	1.3×10^{-12}	0.82	1.31	0.35	10
$k = 0.1 \cdot k_{base}$	0.35	1.3×10^{-12}	0.82	1.31	0.35	10
$P = 0.20$	0.20	1.3×10^{-12}	0.82	1.31	0.35	10
α high, *n* low	0.35	1.3×10^{-12}	1.20	1.20	0.35	10
α high, *n* high	0.35	1.3×10^{-12}	1.20	1.80	0.35	10
In situ, $S = 0.2$	0.35	1.3×10^{-12}	0.82	1.31	0.20	10
In situ, $S = 0.6$	0.35	1.3×10^{-12}	0.82	1.31	0.60	10
In situ, $S = 0.9$	0.35	1.3×10^{-12}	0.82	1.31	0.90	10
In situ, $S = 0.2$, $I = 1$	0.35	1.3×10^{-12}	0.82	1.31	0.20	1
In situ $S = 0.35$, $I = 1$	0.35	1.3×10^{-12}	0.82	1.31	0.35	1
In situ $S = 0.6$, $I = 1$	0.35	1.3×10^{-12}	0.82	1.31	0.60	1
In situ $S = 0.9$, $I = 1$	0.35	1.3×10^{-12}	0.82	1.31	0.90	1
In situ $S = 0.2$, $I = 50$	0.35	1.3×10^{-12}	0.82	1.31	0.20	50
In situ $S = 0.35$, $I = 50$	0.35	1.3×10^{-12}	0.82	1.31	0.35	50

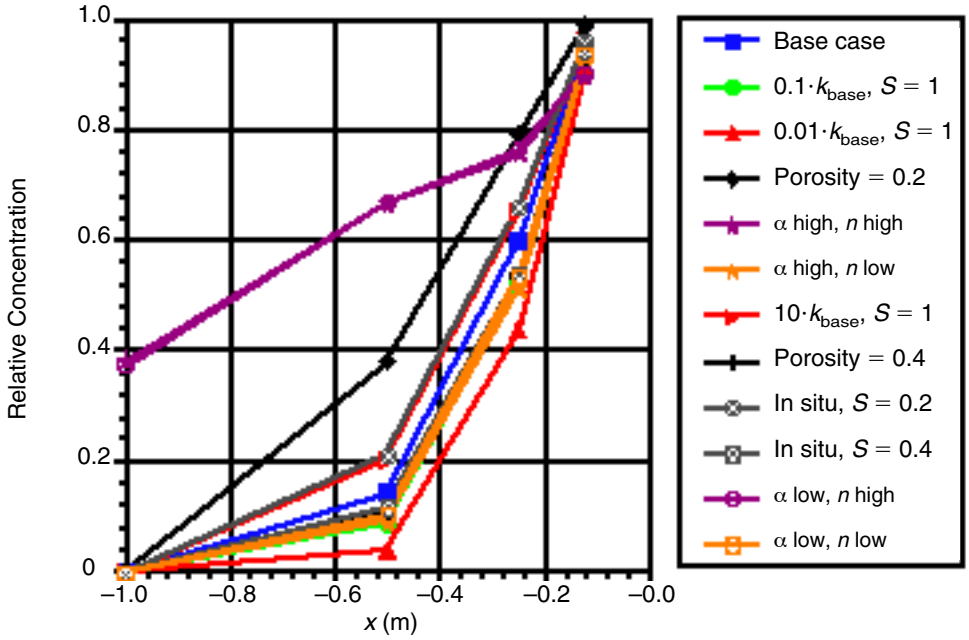

Figure 28. 2-D Sensitivity Runs. The plots give concentration as a function of vertical distance from the injection point, *x*, for different 2-D sensitivity runs. The base case represents our current best knowledge of the properties and conditions of the system.

that would allow the tracer to move sufficiently far to produce readily measurable distributions but not so far that the tracer could not be fully recovered. Testing multiple injection rates is also intended to help select injection rates for Phase 2. An injection rate of 10 ml/hr was chosen for Phase 1A. Therefore, the discussion here will focus on simulation results using 10 ml/hr. Results with other injection rates are presented later, for completeness. These other injection scenarios are also useful for making predictions for Phase 2.

6.1.2.2 Discussion of simulations

Base case. The base-case parameters were taken from values measured in core samples taken from the UZTT site itself. These parameters are given as the first row of Tables 14a and 14b. These simulations mark our best guess prediction of the water and tracer distribution in Phase 1A.

Measurements from core samples suggested in-situ saturations in the range of 20 to 40%. In the simulations, an initial capillary pressure of 5.6 Mpa corresponds to a saturation of 20%, 0.55 Mpa corresponds to 35%, and 0.07 Mpa corresponds to 60%. Comparing locally measured values and values reported for the Tac unit, the in-situ saturation of approximately 35% most closely represented "reality."

The saturation of the system changed only slightly over the 180-day period for the base case. After 180 days, at a distance of 0.125 m below the injection point, the saturation had increased by only 5%, whereas at a distance of 1 m it had increased by only a fraction of a percent (0.7%). The tracer distributes relatively evenly in all directions, centered at the injection point. Some asymmetry is introduced, however, by the presence of the borehole and by injecting 90 degrees off vertical. Water and tracer has to move around the borehole to flow out in the negative horizontal direction where there is no impedance in the positive horizontal direction. Thus, flow and transport will be somewhat nonsymmetric.

The relatively even distribution of tracer and the lack of increase in saturation near the borehole indicate that this system is dominated by capillary forces over gravitational forces. Gravitationally dominated flows have a much more asymmetric character. We see by these simulations that a 10-ml/hr injection rate should not introduce enough water to change the overall flow-and-transport processes that occur in the undisturbed system.

At 180 days, for the 2-D run, the approximate radius of the tracer at a relative concentration C of 0.01 is 0.75 m and at a C of 0.5 is 0.30 m. Concentrations of 0.01 and 0.5 for the 3-D simulation are, respectively, 0.85 m and 0.45 m. Figure 29 plots the concentration as a function of distance from the borehole center at 180 days for the 2-D and 3-D systems. In the 3-D simulation, at a distance of 0.125 m, the concentration is almost 1 (0.96), whereas at 1 m the concentration has fallen to 2×10^{-4}.

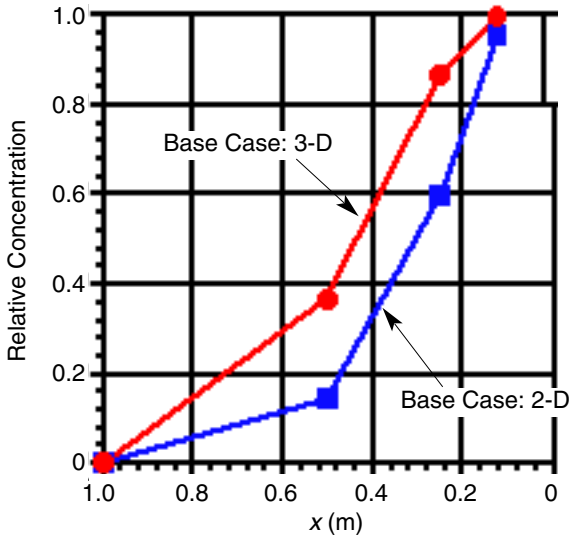

Figure 29. Tracer Concentration Versus Distance for 2-D and 3-D Simulations. The graph shows relative tracer concentration as a function of vertical distance from the injection point, and though the shapes of the curves are similar, the 2-D system lags the 3-D system by a concentration of approximately 0.20.

Figure 30 plots the time history of concentration at a vertical distance of 0.125 m, 0.25 m, and 0.5 m below the center of the borehole for the 3-D simulation. Figure 30 shows that, at 180 days and a distance of 0.125 m, the tracer concentration has almost reached a value of 1.0, whereas at 0.5 m, the concentration is still increasing rapidly.

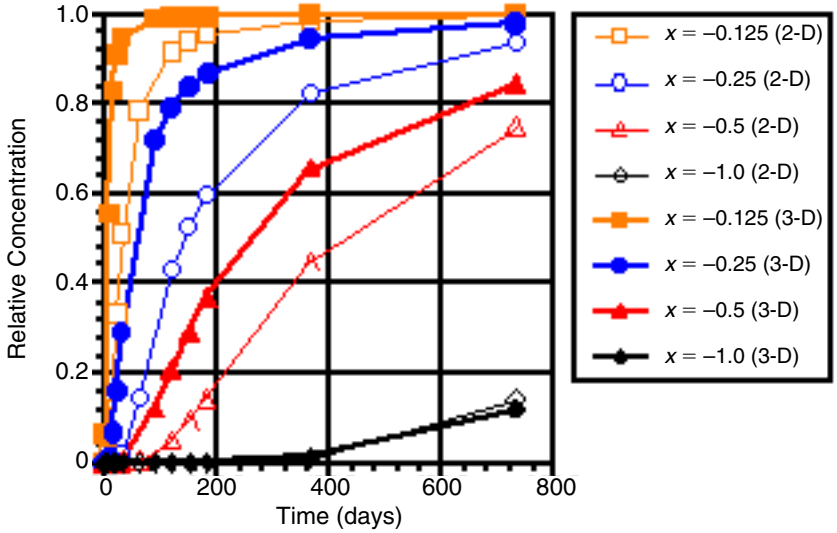

Figure 30. Time Profiles of Tracer Concentrations for 2-D and 3-D Simulations. The graph shows plots of relative tracer concentration as a function of time for different distances, *x,* from the injection point. The hollow symbols represent 2-D simulations, and the solid symbols represent 3-D simulations.

Sensitivity analyses. The accuracy of these numerical simulations will not be known until site measurements are made. It is known that our knowledge of the actual hydrologic and material properties contains some uncertainty. Furthermore, these properties will also vary somewhat within the hydrogeologic units, as reflected in variations

in measured values from different cores. Using stochastic methods, these uncertainties can be incorporated directly into the calculations. Such predictions will be presented in later sections. Within this deterministic modeling approach, we have attempted to account for and understand the influence of such uncertainty by assessing the sensitivity of the simulation to various system parameters. Figures 31 to 34 compare the results of these simulations. Figure 31 shows the effect of water injection on matrix saturation with time for the different sensitivity runs. Figure 32 plots concentration against distance from the borehole that the measurement was made for the first six 3-D simulations in Table 14b. Figure 33 shows the same information plotted as concentration versus time with each graph plotting a different distance from the borehole. Figure 34 compares the values of concentration versus time for 3-D simulations against those for 2-D.

If the predictions of the base-case simulation do not match the measurements made in the field, it will be possible to use this series of simulations to identify parameter values that may be in error. From this knowledge, it will be possible to modify the model to improve accuracy.

Figure 31 shows that saturation for the Phase-1A model system is not really affected by any of the simulation scenarios. Further, the saturation is not particularly sensitive to many of the parameters. Not surprisingly, the biggest changes are observed for conditions that increase the relative influence of gravity forces over the otherwise prevailing viscous forces. Both a higher α and the much higher injection rate produce relatively rapid and apparent increases in saturation. Otherwise, little change in saturation is observed.

At 180 days, Fig. 32 demonstrates that, based on measurements at a distance of 0.125 m from the borehole, it is not really possible to tell how well the system characteristics have been captured. At 0.125 m, there is negligible difference in concentrations among the different simulations. At a distance of 0.5 m, however, variations in system characteristics result in a 60% range of concentrations. Figure 32 shows that a system with an order-of-magnitude lower intrinsic permeability, k, is indistinguishable from one with a value of van Genuchten power n that is at the low end of reported values. Both of these cases are very similar to the base case as well. This fact indicates that transport in this system is not particularly sensitive to the values of k or α; errors in these values are not expected to demonstrably influence the accuracy of predictions in this system.

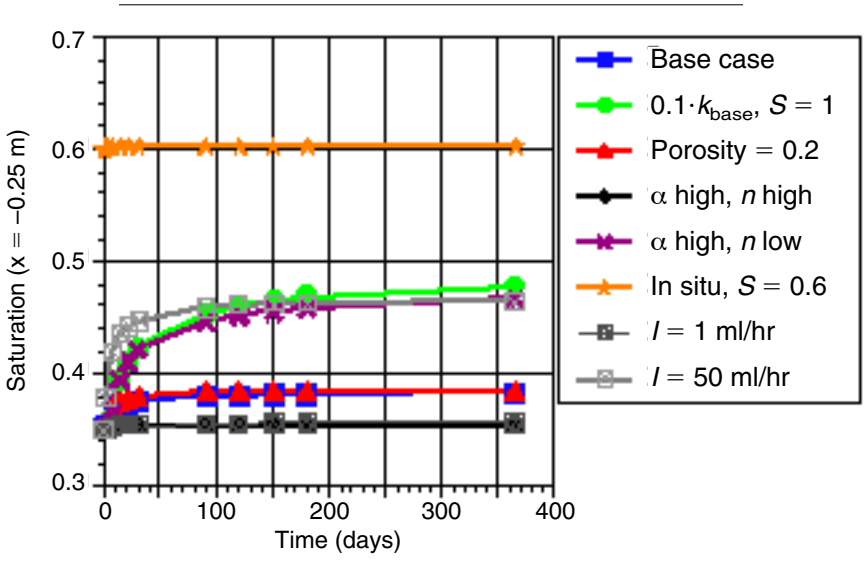

Figure 31. Effect of Water Injection on Matrix Saturation. The graph shows changes in saturation through time at a distance of 0.25 m from the injection point. Note that in most cases there is little change in saturation over a year.

If the reported porosity is in error by as much as 15% (0.20 instead of 0.35), tracer concentration at 0.5 m and 180 days is expected to be 0.58, which is a differ-

ence of 25% from the base value. By 365 days, as seen in Fig. 33, the difference in concentration has decreased somewhat but is still a substantial 10%. At shorter distances from the injection point, the low-porosity system is very close to the fastest transport system—one with high van Genuchten n—and leads the base prediction by 10% concentration.

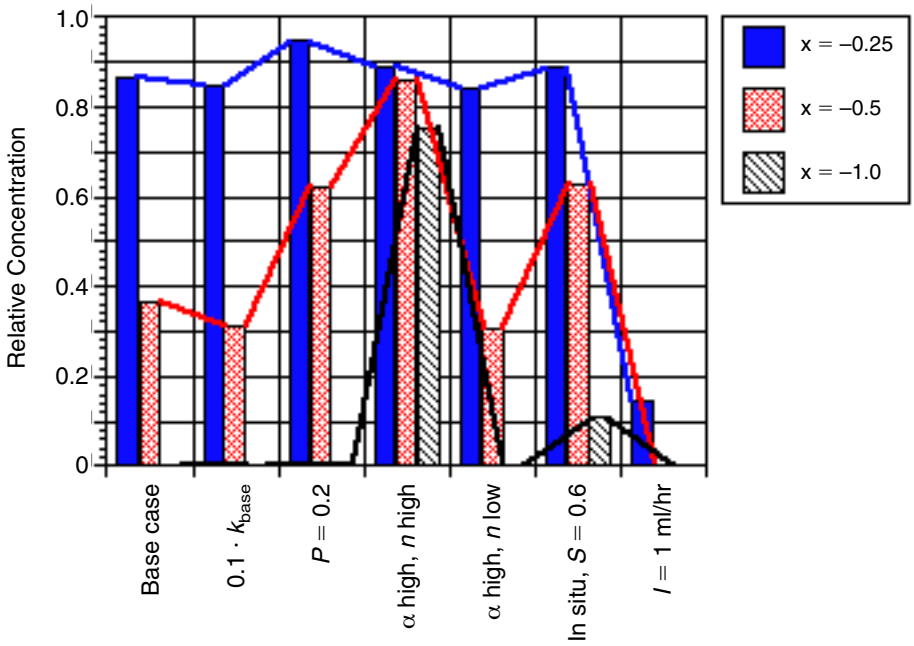

Figure 32. Tracer Concentration for Different Sensitivity Runs. The graph shows differences in concentration for different sensitivity runs at three distances from injection. The sensitivity to the system parameters is not captured at the smallest distances but is apparent at a distance of 0.5 m.

Flow in the simulation that starts with an in-situ saturation of 60%, instead of the estimated 35%, is actually dominated by gravity rather than capillarity. For this simulation, tracer is carried much farther down than in any of the lateral directions. At 180 days and a vertical distance of 0.5 m below the borehole, the concentration is 0.57 versus 0.11 laterally. The transport rate is substantially faster than the base case, as demonstrated by much higher concentrations at greater distances (Fig. 32). At a distance of 0.5 m below the borehole, decreased porosity and increased saturation are virtually indistinguishable but differ significantly in 3-D distribution. The lower-porosity transport is capillary driven, producing a relatively uniform tracer cloud, whereas the high-saturation system produces a highly elongated tracer profile. Note that saturation as high as 60% is not indicated by the reported capillary pressures measured in this system. The measured capillary pressures indicate an in-situ saturation in the vicinity of 25 to 35%.

The simulation results were most sensitive to the value of the van Genuchten parameter n. Reported values for this parameter ranged from 1.2 to 1.8, with the value from Busted Butte samples being 1.31. At a value of n = 1.8, transport was strongly gravity-dominated. The resulting concentration profiles were long vertically and thin laterally. This effect was much stronger than that observed for the high-saturation simulation. Concentration at a vertical distance of 0.5 m was 0.88 versus 0.04 at the same lateral distance. At a distance of 0.5 m, tracer concentration was 60% higher than the base case and 30% higher than the high-saturation case. Furthermore, by 180 days, this system had just about reached its steady-state distribution, whereas even at 365 days (Fig. 33), the other systems were continuing to change. If the actual value of n is significantly different from the measured value for the Busted Butte core, it should be recognizable by the distinct, long and thin, tracer distribution and by the high vertical concentrations.

The 2-D simulations (Fig. 28) indicated that the value of α appears to have little influence on the system as compared to n. As a result, 3-D simulations were only done for the two different variations in van Genuchten parameters presented.

2-D versus 3-D simulations. The 2-D and 3-D simulations followed very much the same trends in tracer distribution and concentrations in space and time. Figure 34 shows concentration as a function of time measured at a distance of 0.5 m vertically below the borehole center for both 2-D and 3-D simulations. The numerical difference in concentration between equivalent 2-D and 3-D systems remained relatively constant. Numerical differences were approximately 10 to 15% after approximately 90 simulation days. Concentration values between the 2-D runs and the 3-D runs were much closer at early times and began to converge at later times, as all concentrations approached 1.

6.1.3 Implications for UZTT Phase-2 design and analysis

These simulations also provide us with a tool to select injection rates for the Phase-2 experiment, as well as to help understand how the injection rates used will influence what is observed at different monitoring locations. For example, after 180 days at an injection rate of 10 ml/hr, concentrations had increased to greater than 0.20 within a radius of 0.4 m from the injection point but fell off rapidly beyond that and were below 1% beyond 0.9 m. Thus, a 2-m spacing between boreholes and injection points within boreholes would probably produce a system in which each injection location was distinct from every other.

Faster injection rates, such as 50 ml/hr, can be expected to strongly

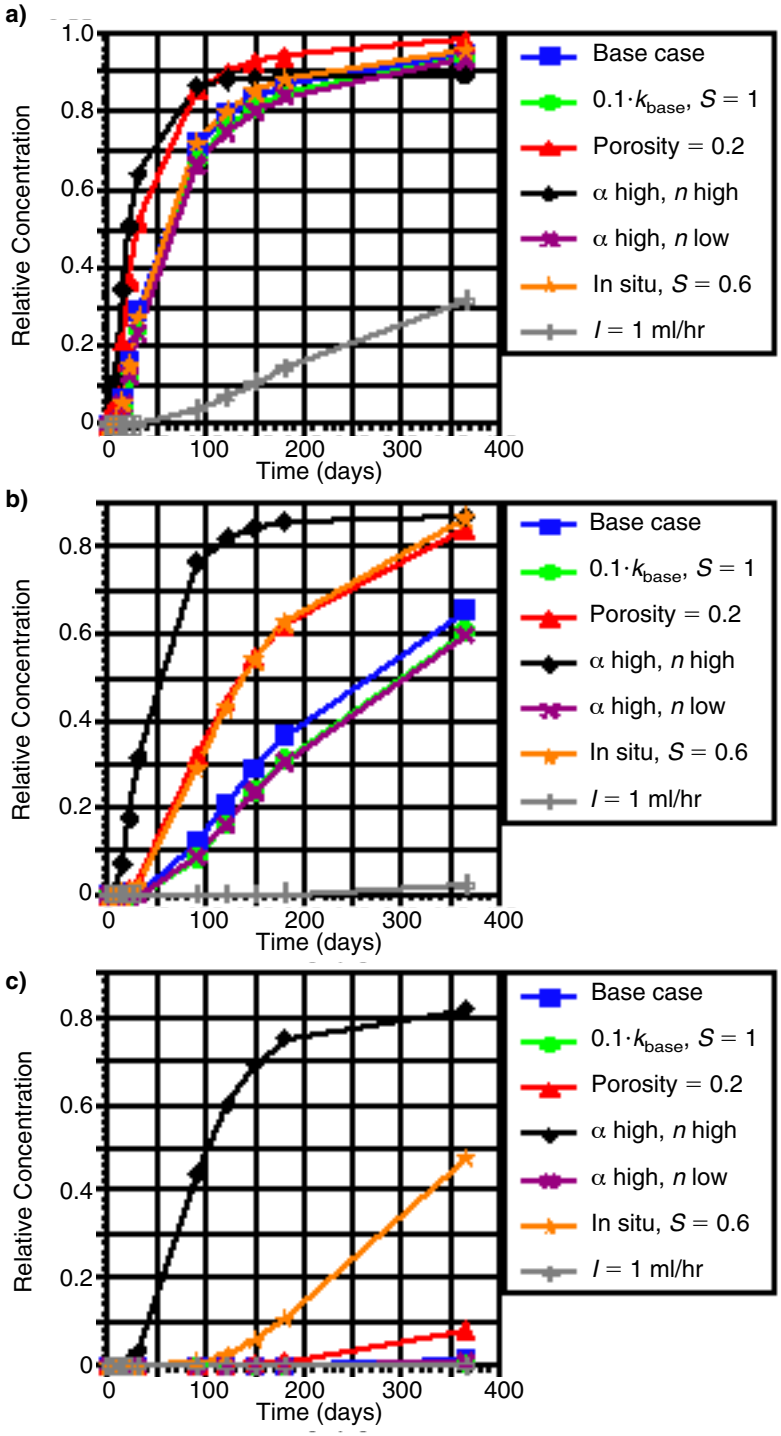

Figure 33. Concentration Versus Time at Various Distances From Injection. These plots show concentration changes as a function of time for distances from the injection point of a) 0.25 m, b) 0.5 m, and c) 1.0 m. Note that at a 1-m distance, there is, in most cases, little change in concentration after injecting tracer for one year.

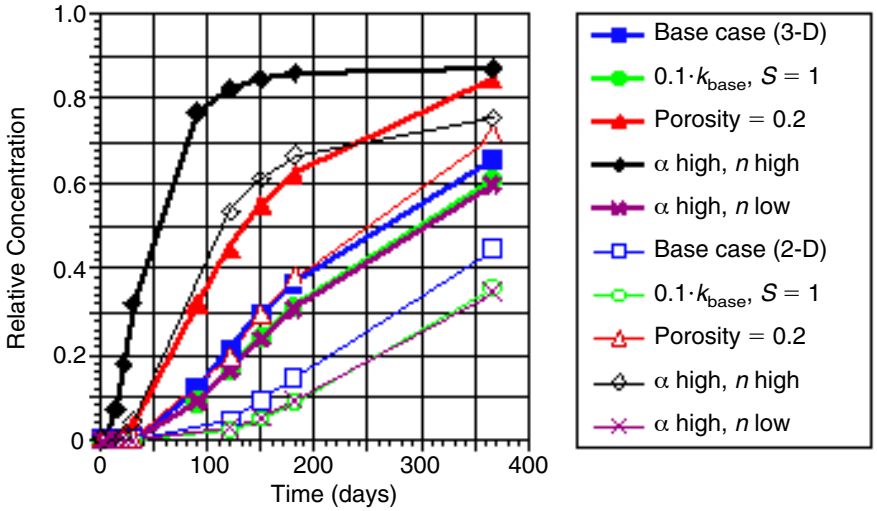

Figure 34. Differences in 2-D and 3-D Predicted Concentrations. These plots of concentration versus time show that differences between 2-D (open or nonbold points) and 3-D values (closed or bold points) are fairly consistent between different runs. The concentration is measured at a distance of 0.5 m vertically below the borehole center.

6.1.4 Summary

This document describes the results of the blind predictions of the Phase-1A injection test being run in the Tac unit at Busted Butte. For these preliminary predictions, we have assumed that the matrix is more or less homogeneous and is unfractured. Using these assumptions and the described system configuration, we can make a prediction of the expected tracer distribution after 5 months of injection, at which time, measurements at the field test will begin.

modify natural flow patterns, producing gravity-dominated flow. At this injection rate, concentrations 0.5 m from the injection point are predicted to rise to 0.80 in only 3 months. Thus, boreholes or injection points spaced 1 m apart are expected to start influencing each other very early in the experiment.

On the other hand, an injection rate of 1 ml/hr is seen to hardly influence the system at all. Even after 1 year, concentrations do not even rise to 0.05 at the 0.5-m distance. At such a low injection rate, it would take an extremely long time to analyze the system or identify important physical and chemical processes that are occurring. Further, at such slow rates of movement, it is very difficult to distinguish differences in tracer movement that might arise due to geochemical effects.

Using different tracers at various injection rates and injection separation distances can provide an opportunity to differentiate controlling processes and material features.

Based on the available information about Tac hydrologic properties and properties measured on samples taken from this site, we set up a baseline numerical simulation that ideally should reflect the actual system. From this simulation, we predict that a nonsorbing tracer will have traveled approximately 0.81 m (at a relative concentration of 0.01) over the 5-month injection period. We also expect that the tracer will travel as far in the horizontal direction as the vertical. This uniform spread of the tracer indicates that the Tac system is more strongly controlled by capillary forces than by gravitational forces.

There is a possibility, however, that the baseline prediction is not correct. Errors in our prediction may be caused by uncertainty in the value of many of the hydrologic and physical parameters. For each of these parameters, we analyzed the sensitivity of flow and transport. These analyses will allow us to identify what aspects of the model system might be in error if the baseline-case predictions do not match the observations in the field. If, for example, we find the tracer has traveled much farther than predicted and predominantly in the vertical direction, we know that gravitational

forces are dominating. This outcome could be the result of a much higher in-situ saturation or an error in the van Genuchten parameter α. If the tracer cloud has traveled farther than expected but has retained a rather symmetric shape, it is possible that our estimate of the matrix porosity is in error. There are many possibilities. If the field data do not match the baseline case, we have the alternative simulations that will help us identify potential differences in the actual material characteristics and the properties used in the simulations.

The similarity in the 2-D and 3-D trends suggests that if we were to correct the injection rate, a 2-D simulation might be sufficient for predicting flow and transport in this homogeneous system. This suggestion does not imply that a 2-D simulation is adequate for more complex geology, though. In fact, all of the above predictions are based on a homogeneous rock matrix. If the matrix is not homogeneous, these predictions may be in error.

6.2 STOCHASTIC MODEL.

6.2.1 Introduction

The purpose of this section is to document the use of stochastic predictions made for Phase 1A of the Busted Butte testing program. Phase 1A of the field test is located in the Calico Hills vitrified tuff at Busted Butte. At this time, there is a paucity of physical-properties information on the lithologies of that site, and the spatial variability of rock properties cannot be accurately depicted. Although this lack of information results in uncertainties for any flow-and-transport prediction, we attempt in this section to use stochastic predictions for the site using current YMP databases. We directly incorporate the input uncertainties from these databases into flow predictions through a recently developed stochastic model. This model requires that the first two statistical moments of rock properties be specified (i.e., saturated hydraulic conductivity and pore-size-distribution parameter α). The predictions represent the first two moments (expected value and standard deviation) of flow quantities, and these two moments are used to construct confidence intervals for the flow quantities. These flow moments serve as a basis for future stochastic predictions of tracer migration.

In the near future, field-test results of flow quantities, such as saturation, will be used to compare with the predicted confidence intervals of these same quantities. It is expected that the field-test results will fall within the predicted confidence intervals with a 95% probability. However, because the statistical and other input parameters are taken or estimated from the YMP databases, these parameters may or may not represent the rock properties at the test site, thereby introducing another level of uncertainty in the analyses. We have performed some sensitivity analyses on these parameters and found that the flow predictions are sensitive to the background saturation, the mean and variance of pore-size-distribution parameter α, the mean and variance of the logarithm of the saturated hydraulic conductivity, and the injection rate. This indicates that the refinement of these parameters is important.

6.2.2 Stochastic modeling

Although geologic media exhibit a high degree of spatial variability, rock properties, including fundamental parameters such as permeability and porosity, are usually observed only at a few locations due to the high cost associated with subsurface measurements. This combination of significant spatial heterogeneity with a relatively small number of observations leads to uncertainty about the values of material properties and, thus, to uncertainties in predicting flow and solute transport in such media. It has been recognized that the theory of stochastic processes provides a natural method for evaluating flow-and-transport uncertainties. In the last two decades, many stochastic theories have been developed to study the effects of spatial variability on flow and transport in both saturated (e.g., Gelhar and Axness 1983, pp. 161–180; Dagan 1984, pp. 151–177, 1989, pp. 157–259; Winter et al. 1984, pp. 411-424; Neuman et al. 1987, pp. 453–466; Graham and McLaughlin 1989, pp. 2331–2355; Rubin 1990, pp. 133–142; Zhang and Neuman

1995, pp. 39–51, 1996a, pp. 77–83, 1996b, pp. 2715–2723) and unsaturated zones (e.g., Yeh et al. 1985a, pp. 447–456, 1985b, pp. 457–464; Mantoglou and Gelhar 1987, pp. 37–46; Mantoglou 1992, pp. 251–267; Russo 1993, pp. 383–397, 1995a, pp. 139–145, 1995b, pp. 1647–1658; Harter and Yeh 1996a, pp. 1585–1595, 1996b, pp. 1597–1609; Zhang and Winter 1998, pp. 1091–1100; Zhang et al. 1998, pp. 1437–1447). In the unsaturated zone, the problem is complicated by the fact that the flow equations are nonlinear because unsaturated hydraulic conductivity depends on pressure head.

In many of these previous theories, there are a number of simplifying assumptions such as gravity-dominated flow (for steady-state cases) and slow-varying gradient (for transient flow). These assumptions restrict the applications of the existing theories. For example, the assumption of gravity-dominated flow excludes the presence of domain boundaries and the existence of a water table. In addition, a slow-varying gradient does not permit local injection or fast-varying recharge. Recently, Zhang (1998, pp. 1–26) developed a stochastic model for transient unsaturated flow in bounded domains free of the above mentioned assumptions. The model results are the first two moments of the flow quantities, which may be used to construct confidence intervals for these quantities. The confidence intervals are a measure of the uncertainty caused by incomplete knowledge of material heterogeneities.

6.2.3 Phase-1A modeling

For Phase-1A simulations, we directly incorporate the input uncertainties from YMP databases into flow predictions using the stochastic model of Zhang (1998, pp. 1–26). This model requires that the first two statistical moments for rock properties, such as saturated hydraulic conductivity and pore-size-distribution parameter α, be specified. Because the variabilities of porosity and residual water content are likely to be small compared to that of hydraulic conductivity, both of them are assumed to be know with certainty. To model unsaturated flow, the constitutive relationships between capillary pressure and unsaturated hydraulic conductivity and between capillary pressure and saturation must also be specified. Although the parameters characterizing these relationships are reported in the YMP databases (Schenker et al. 1995, pp. 1–165; Flint 1998, pp. 1–64), these are based on the van Genuchten model (van Genuchten 1980, pp. 892–898). Conversely, the current stochastic model of Zhang (1998, pp. 1–26) assumes the constitutive relationships to obey the Gardner-Russo model (Gardner 1958, pp. 228–232; Russo 1988, pp. 453–459). In this study, the Gardner-Russo parameter α is estimated from the reported van Genuchten parameters by matching the main features of the retention curves for these two models. The first row of Table 15 summarizes the relevant parameters that are taken or estimated from the YMP databases (Schenker et al. 1995, pp. 1–165; Flint 1998, pp. 1–64). No information is found with respect to the correlation lengths of the logarithm of the hydraulic conductivity and pore size distribution. The value of 20 cm is assumed for both of these parameters.

Baseline case. In the baseline case, the size domain is 200 cm by 200 cm with material properties specified in Table 15. The steady-state simulations are run with the following boundary conditions: specified flux at the top, a constant head of –488 cm at the bottom and no-flow boundaries at the sides. The specified flux is consistent with the constant head at the bottom such that at steady state ($t = 0$), the flow is gravity-dominated with a constant mean pressure head ($h = –488$ cm) and a constant saturation ($S = 30\%$) through the whole domain. Specifically, we assume the intial mean saturation to be 30% and then compute the initial mean head to be –488 cm using the gravity-dominated condition and the specified characteristic curves. However, the head standard deviation is not uniform in such a bounded domain. The head standard deviation is zero at the bottom boundary, increases with distance from there, and reaches its maximum at the top. Figure 35 shows the confidence intervals for the pressure head h and the sat-

uration S along horizontal (y) and vertical (z) lines passing through the injection point. The profiles are obtained by adding one standard deviation to the result and subtracting it from the mean quantity. This result corresponds to the 95% confidence intervals for the flow quantities. By comparing the vertical profiles for pressure head (Fig. 35b) and saturation (Fig. 35d), it is seen that, unlike the head standard deviation, the saturation standard deviation is not zero at the bottom boundary of constant head. This result happens because the uncertainty in saturation comes from the uncertainty in the soil parameter α, even though the head is specified with certainty there. The behaviors of these flow moments under steady-state conditions have been discussed in detail by Zhang and Winter (1998, pp. 1091–100).

An injection of rate $Q = 1$ ml/hr starts at time $t = 0$, and lasts for 150 days. The actual injection at the field test site is a point in 3-D, whereas the model is in 2-D. In the model, the injection is approximated by a line source of length L_3 perpendicular to the 2-D domain. Therefore, the injection rate is Q/L_3 in 2-D. In this baseline case, we assume $L_3 = 50$ cm. It should be realized that the 2-D representation is an approximation and the accuracy of this approximation highly depends on the choice of L_3, which is, in turn, a strong function of injection rate. The 2-D predictions should have the same general trend as the 3-D predictions.

Figure 36 shows the vertical and horizontal profiles of pressure head and saturation at 150 days. It is seen that the impact of injection is the increase of pressure head and saturation in the vicinity of injection. The effects seem to be even in all directions near the injection. This result is caused by the fact that the injection rate is overwhelmingly large compared to the background unsaturated hydraulic

Table 15. Case Descriptions.

Case	Description
1	$\langle f \rangle = -6.258$, $\sigma_f^2 = 2.459$, $\lambda_f = 20$ cm, $\langle \alpha \rangle = 0.01$ cm^{-1}, $\sigma_\alpha^2 = 9 \times 10^{-6}$ (cm^{-1})^2, $\lambda_\alpha = 20$ cm, $\phi = 0.5$, $L_1 = L_2 = 200$ cm, $L_3 = 50$ cm, $Q = 1$ ml/hr, $S_o = 30\%$
2	Same as in Case 1, except $\lambda_f = \lambda_\alpha = 30$ cm
3	Same as in Case 1, except $L_1 = L_2 = 400$ cm
4	Same as in Case 1, except $S_o = 20\%$
5	Same as in Case 1, except $S_o = 40\%$
6	Same as in Case 1, except $S_o = 60\%$
7	Same as in Case 1, except $\phi = 0.3$
8	Same as in Case 1, except $\langle f \rangle = -4.258$ and $L_1 = L_2 = 400$ cm
9	Same as in Case 1, except $\langle \alpha \rangle = 0.02$ cm^{-1}
10	Same as in Case 1, except $\sigma_\alpha^2 = 0$
11	Same as in Case 1, except $Q = 10$ ml/hr
12	Same as in Case 8, except $Q = 50$ ml/hr, $L_3 = 100$ cm
13	Same as in Case 1, except $\langle f \rangle = -4.258$ and $L_1 = L_2 = 400$ cm, and $Q = 10$ ml/hr
14	Same as in Case 13, except $Q = 50$ ml/hr and $L_3 = 100$ cm

Note: $f = \ln K_s$ is the log-transformed saturated hydraulic conductivity (for Case 1, the mean $\langle f \rangle$ and variance σ_f^2 are obtained with $\langle K_s \rangle = 6.552 \times 10^{-3}$ cm/hr and $\sigma_{K_s} = 2.143 \times 10^{-2}$ cm/hr), α is a parameter related to pore-size distribution, λ_f and λ_α are the respective correlation lengths of f and α, ϕ is porosity, L_1 and L_2 are the vertical and horizontal dimensions of the domain, L_3 is the length of the third dimension used to calculate the injection rate for 2-D simulation, S_o is the background saturation, and Q is the actual injection rate.

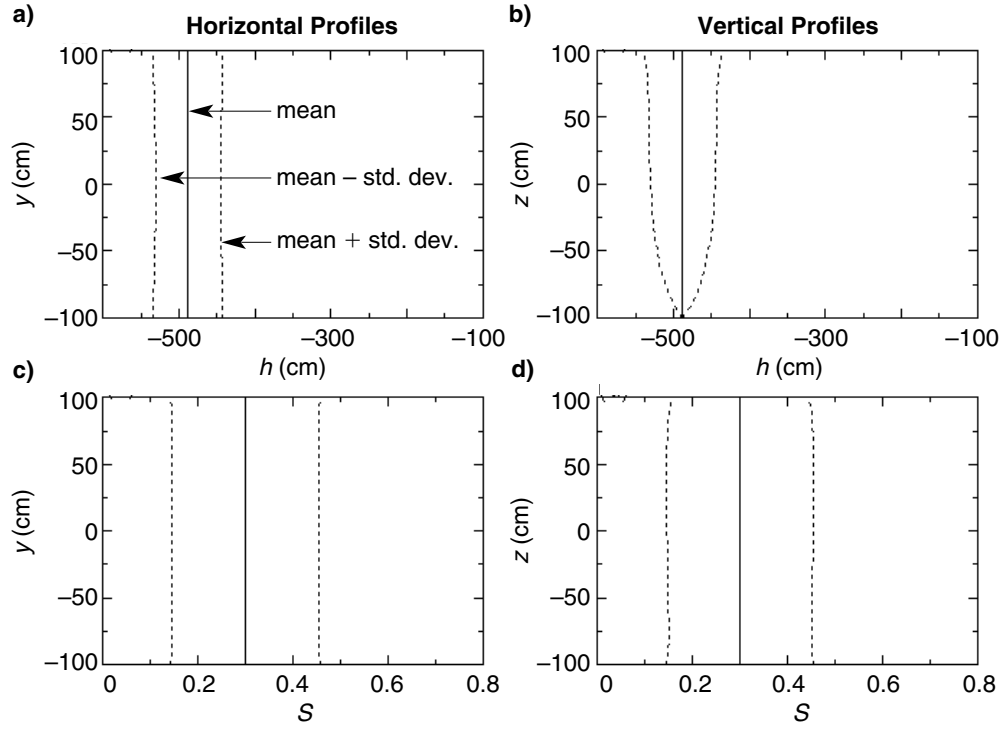

Figure 35. Steady-State Profiles. Horizontal and vertical profiles of pressure head *h* and saturation *S* under steady-state conditions.

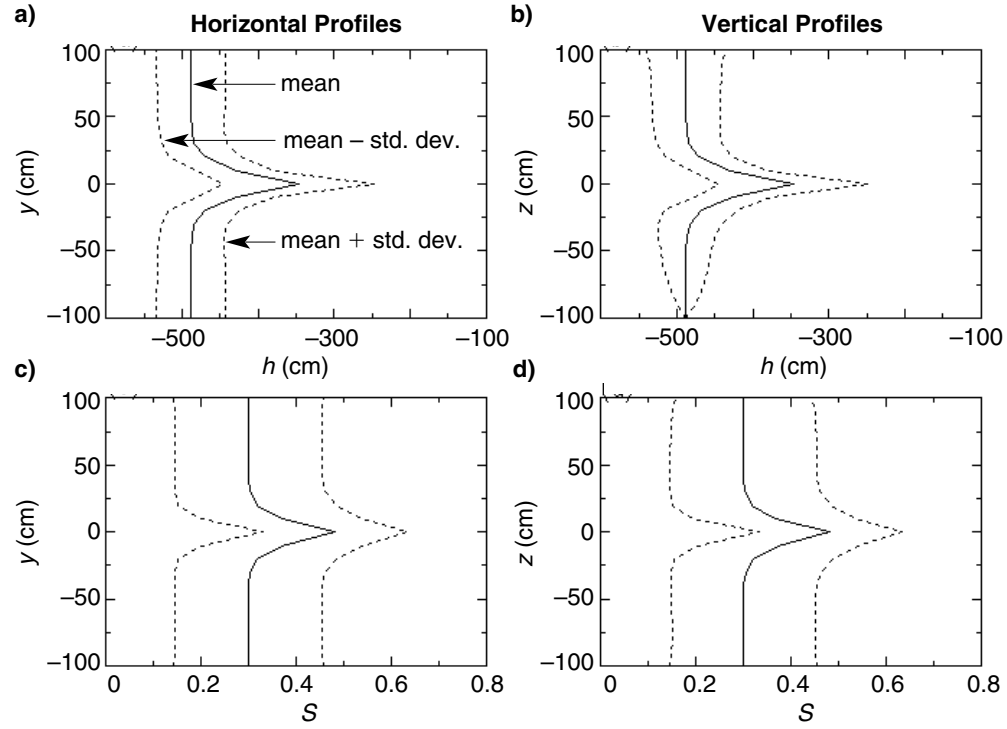

Figure 36. Case 1. Horizontal and vertical profiles of pressure head *h* and saturation *S* at 150 days after injection started.

conductivity. The approximate radius of noticeable pressure head and saturation changes is 40 cm.

Other flow quantities (e.g., flux and velocity) and their associated uncertainties can be given similarly. In principle, the concentration field and its associated uncertainty may be predicted based on this information. However, at this stage, there is no existing model for solute transport in a nonstationary, unsaturated flow field. Our ongoing related research may provide us with a model during Phase-2 prediction.

Sensitivity cases. Because the number of actual measurements at the site is too few to perform any statistical analysis, the statistical parameters are either taken or estimated from the relevant YMP databases. There is another level of uncertainty associated with inaccurate statistical and other parameters. We perform some sensitivity studies below using the stochastic model.

As mentioned before, there is no information regarding the correlation lengths of the log of the saturated hydraulic conductivity and the rock pore-size distribution parameter α. Case 2 investigates the effect of the correlation lengths by changing it from 20 cm to 30 cm. Figure 37 shows the corresponding profiles of pressure head and saturation. Comparison of Figs. 36 and 37 reveals that the prediction is insensitive to the correlation lengths.

In the base case, the domain size is $L_1 = 200$ cm by $L_2 = 200$ cm. However, the real domain is much larger than this. The size of the domain is expected to affect the standard deviations of flow quantities to some extent. In Case 3, we let $L_1 = 400$ cm and $L_2 = 400$ cm. It is seen from Fig. 38 that, in areas away from the boundaries, the confidence intervals are quite insensitive to the domain size.

Cases 4 to 6 investigate the effect of background saturation by changing the specified flux at the top and the constant head at the bottom. Figs. 39 to 41 show the cases for $S_o = 20\%$, 40%, and 60%, respectively. It is seen that the peak pressure head and saturation at the injection location decrease with the increase of the background saturation, but

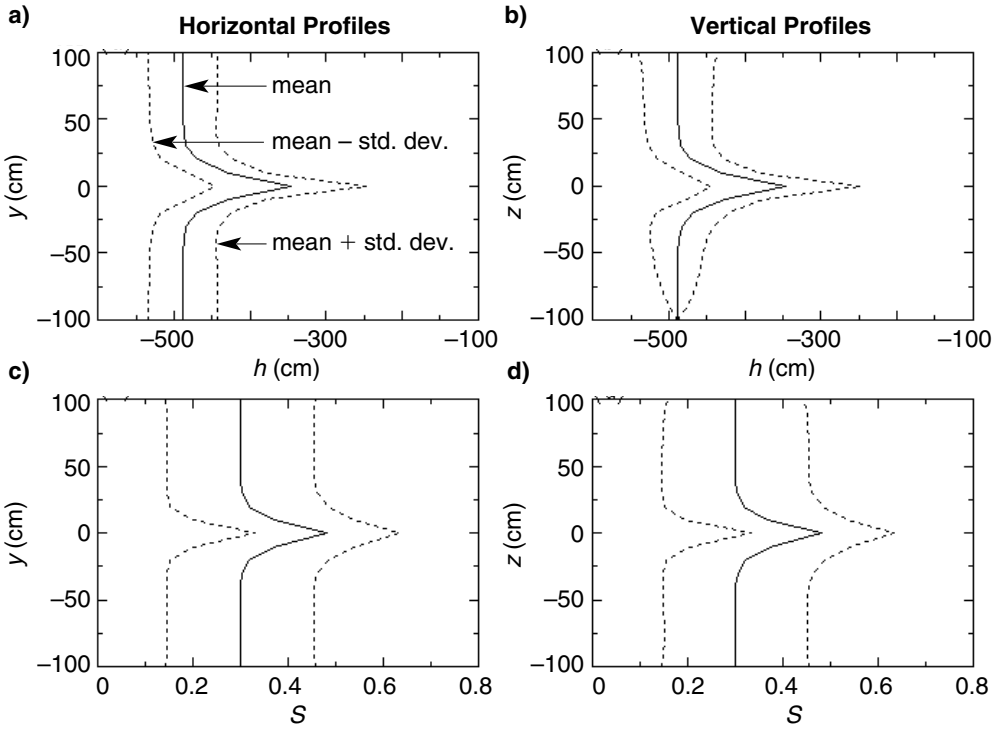

Figure 37. Case 2. The same as Case 1 in Fig. 36 but with $\lambda_f = \lambda_\alpha = 30$ cm.

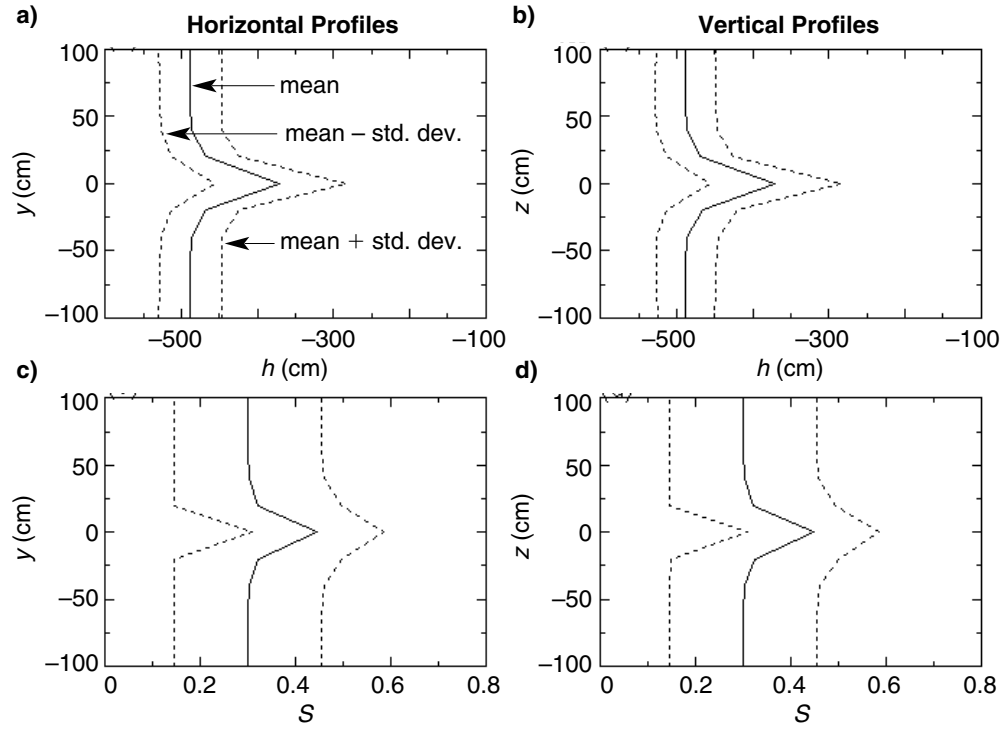

Figure 38. Case 3. The same as Case 1 in Fig. 36 but with $L_1 = L_2 = 400$ cm.

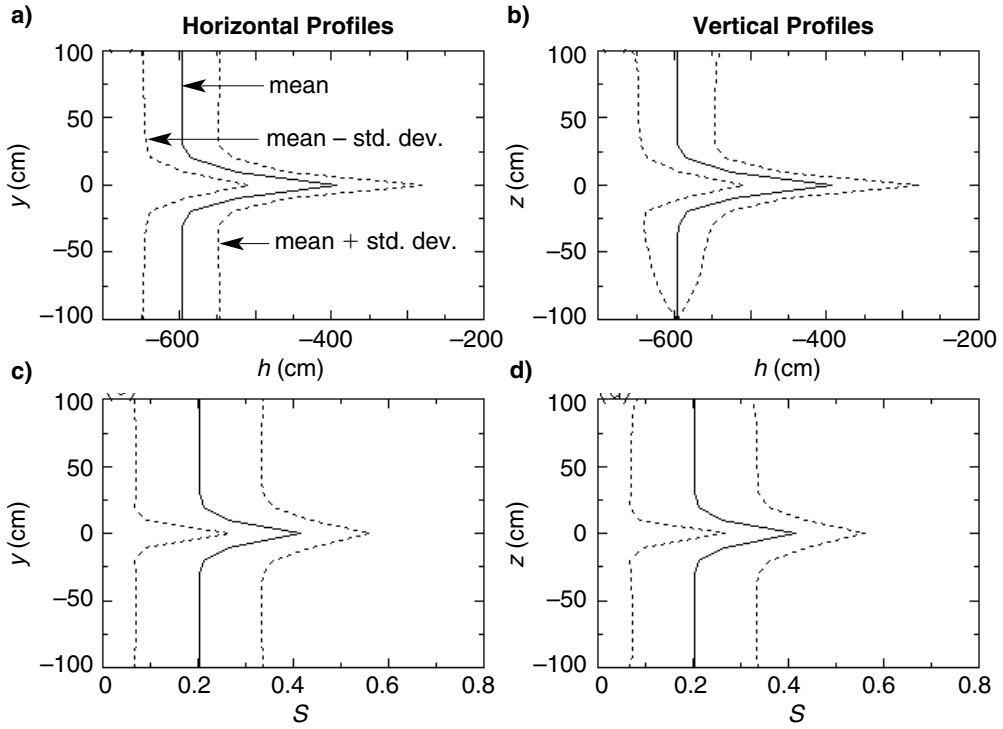

Figure 39. Case 4. The same as Case 1 in Fig. 36 but with $S_o = 20\%$.

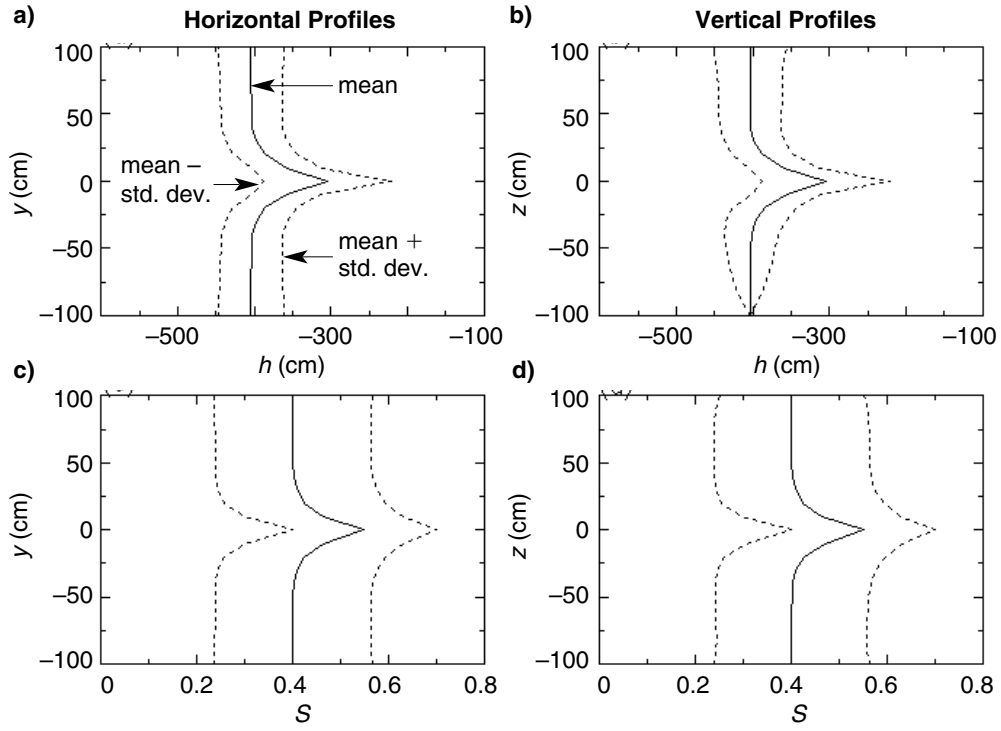

Figure 40. Case 5. The same as Case 1 in Fig. 36 but with S_o = 40%.

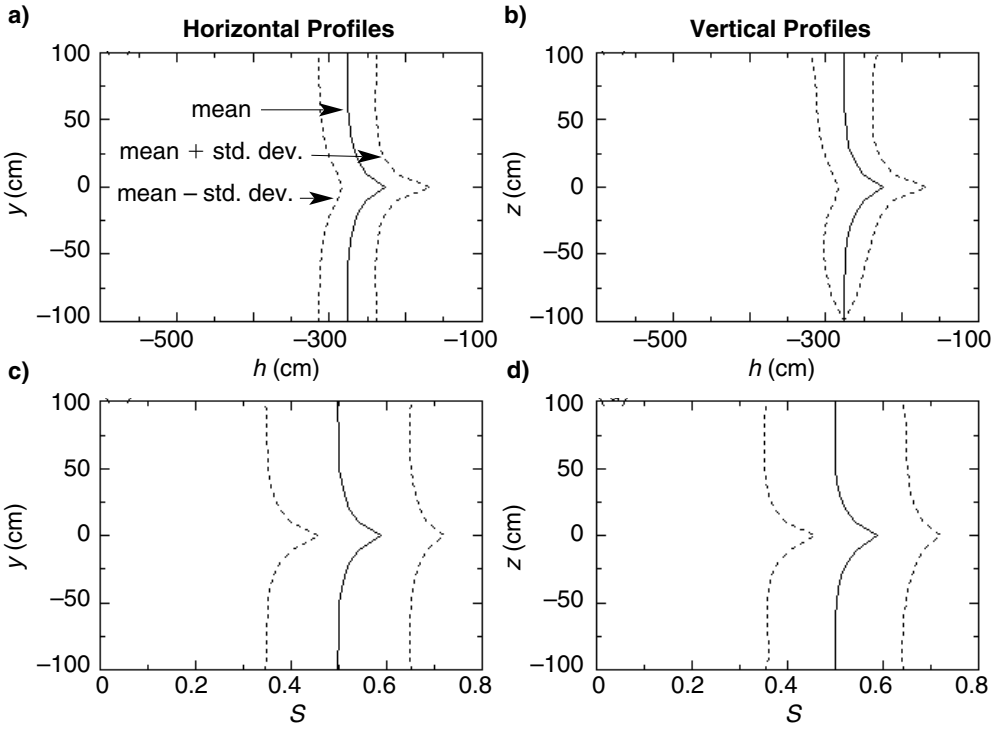

Figure 41. Case 6. The same as Case 1 in Fig. 36 but with S_o = 60%.

the impact radius increases with it. The width of confidence intervals for pressure head decreases with the increase of background saturation, whereas that for saturation profiles is quite insensitive to the background saturation.

In Case 7, the porosity is varied from $\phi = 0.5$ to 0.3 (Fig. 42). Comparison of Fig. 42 and Fig. 36 reveals that a lower porosity results in a slight increase in both the peak saturation and the radius of influence. However, the effect of porosity on solute transport is expected to be greater.

In Case 8, the mean of the log of the saturated hydraulic conductivity is increased from $\langle f \rangle = -6.258$ to -4.258 (where $f = \ln K$). As one should expect, a larger hydraulic conductivity renders a lower peak saturation and a larger radius of influence (Fig. 43). In this case, we have changed the size of the domain to 400 cm by 400 cm to accommodate the increase of saturation at large distance. In Case 9, the mean of α is varied from 0.01 to 0.02 while the variance of α is kept the same. It is seen that the mean head has increased significantly with a larger α for a given saturation (Fig. 44). The confidence intervals are qualitatively similar to those in Fig. 36, but the intervals are tighter in Fig. 45. This difference occurs because the variability in α is actually reduced by keeping the same variance but with an increased mean value. As expected, the prediction—in particular, the width of confidence intervals—is sensitive to the variabilities in saturated hydraulic conductivity and pore size distribution α. Case 10 shows the case in which the variability of α is zero. It is seen from Fig. 45 that the width of the confidence intervals is significantly reduced in the absence of variability in α. In this case, the uncertainties in the prediction are entirely caused by the variability in saturated hydraulic conductivity K_s. In the baseline case, the variability Cv in saturated hydraulic conductivity K_s is much larger than that in pore size distribution α ($Cv_\alpha = \sigma_\alpha / \langle \alpha \rangle = 0.3$, whereas $Cv_{K_s} = 3.27$). Therefore, it may be concluded that the results are much more sensitive to the variability in α than to that in K_s.

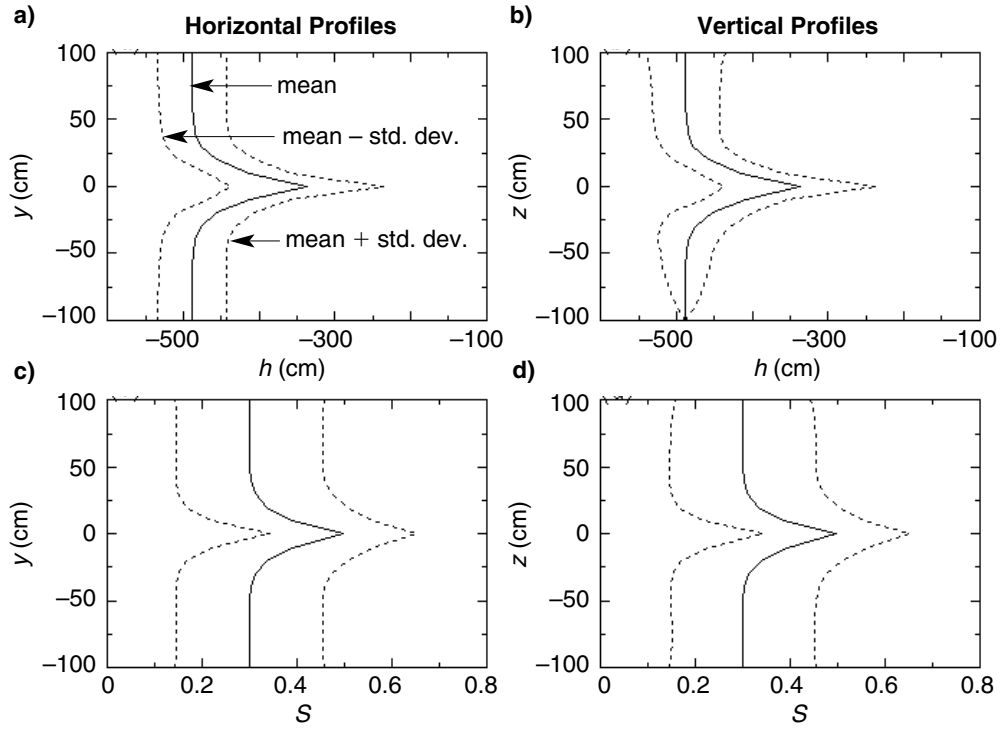

Figure 42. Case 7. The same as Case 1 in Fig. 36 but with $\phi = 0.3$.

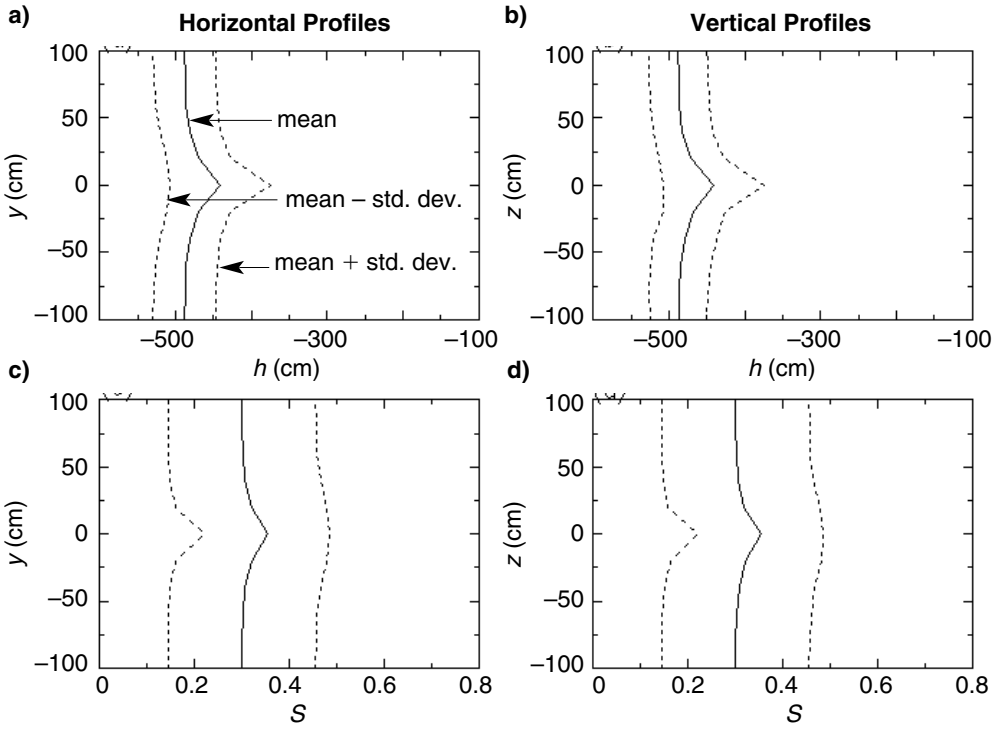

Figure 43. Case 8. The same as Case 1 in Fig. 36 but with $\langle f \rangle = -4.258$ and $L_1 = L_2 = 400$ cm.

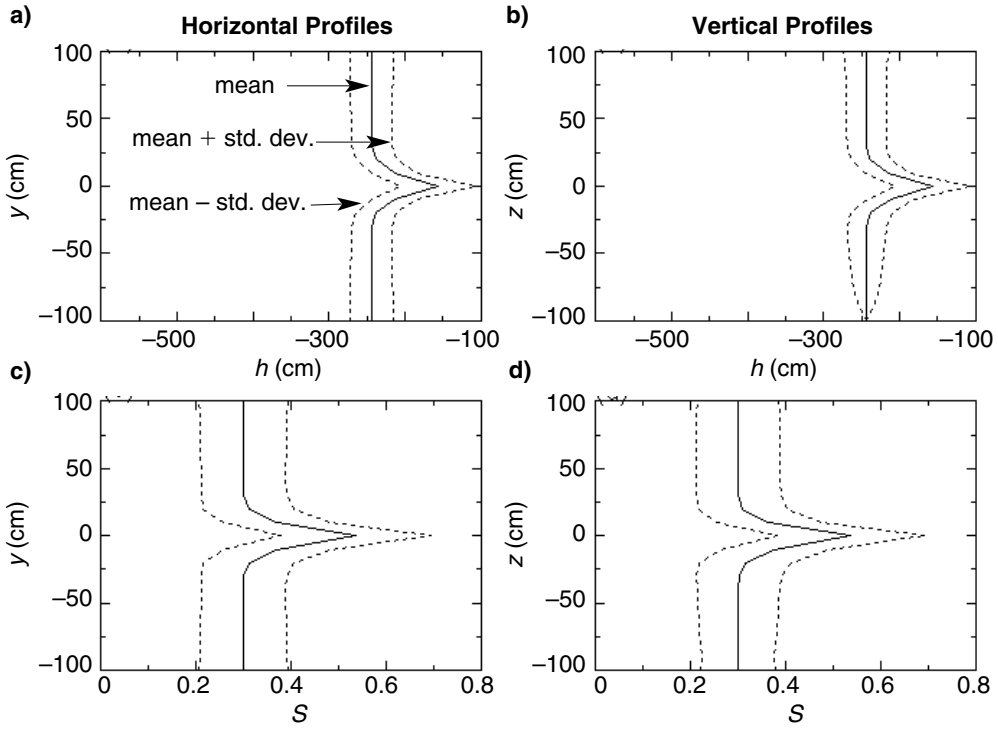

Figure 44. Case 9. The same as Case 1 in Fig. 36 but with $\langle \alpha \rangle = 0.02$ cm^{-1}.

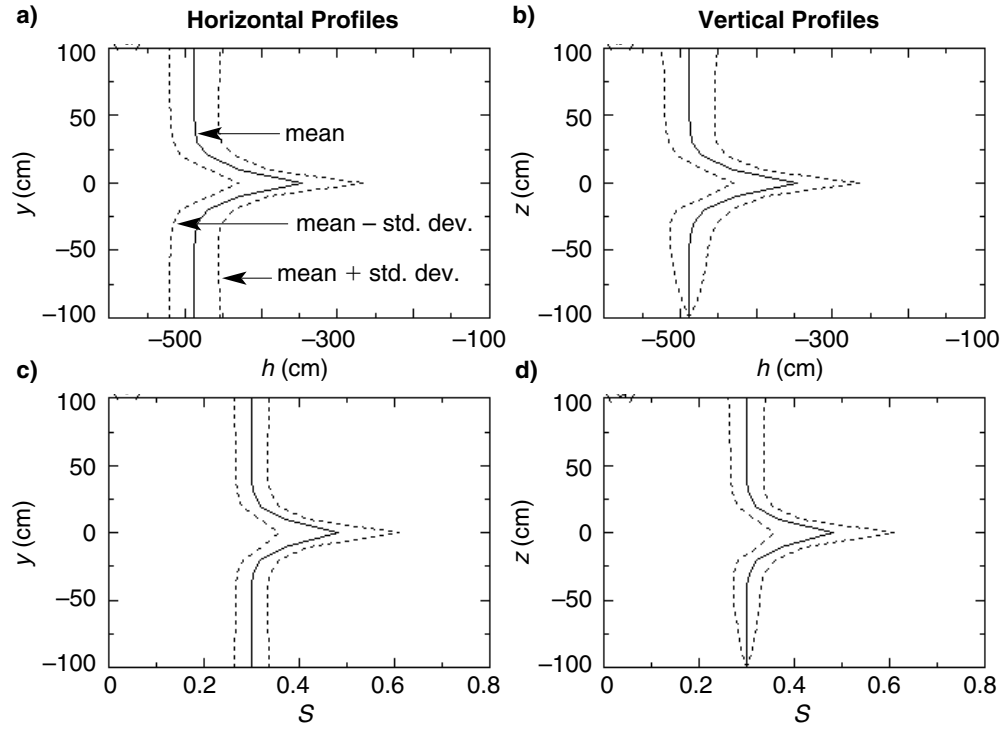

Figure 45. Case 10. The same as Case 1 in Fig. 36 but with $\sigma_\alpha = 0$.

As one should expect, the behaviors of pressure head and saturation profiles are very sensitive to the injection rate. In Case 11, the injection rate is $Q = 10$ ml/hr (Fig. 46). The peak saturation is much higher than that in Case 1 (Fig. 36), and the radius of influence is also larger. This difference is even clearer from Case 12 (Fig. 47), for which $Q = 50$ ml/hr.

In the last two cases, the mean saturated hydraulic conductivity $\langle K_s \rangle$ is taken to be 4.68 cm/hr. This value is based on some site-specific measurements and is three orders of magnitude larger than the value found in the YMP databases mentioned earlier. As for sensitivity runs, we take this value as the mean and $Cv_{K_s} = \sigma_{K_s}/\langle K_s \rangle = 3.27$, as in the baseline case. Equivalently, we have $\langle f \rangle = 0.314$ and $\sigma_f^2 = 2.459$. In Case 13, $Q = 10$ ml/hr and $L_3 = 50$ cm (Fig. 48); in Case 14, $Q = 50$ ml/hr and $L_3 = 100$ cm (Fig. 49). As found in Case 8 (Fig. 43), a larger hydraulic conductivity renders a lower peak saturation and a larger radius of influence. It is expected that the tracer travels significantly faster in these cases.

6.2.4. Summary

This section describes the results of the stochastic predictions of the Phase-1A injection test at Busted Butte. The UZTT was designed to validate and improve the YMP's flow-and-transport model for the unsaturated zone and to obtain new insight into flow-and-transport behavior at Yucca Mountain. The test is divided into three phases. Phase 1 serves as a scoping phase for Phases 2 and 3 and involves the injection of nonsorbing and sorbing tracers and microspheres into the Calico Hills vitric tuff in individual boreholes. Phase 1A started on April 2, 1998, and will last for approximately 180 days. At the end of the injection period, the results will be available after auger and mineback. The purpose of this modeling exercise is to provide blind predictions for the test based on some limited measurements of rock properties and available YMP databases.

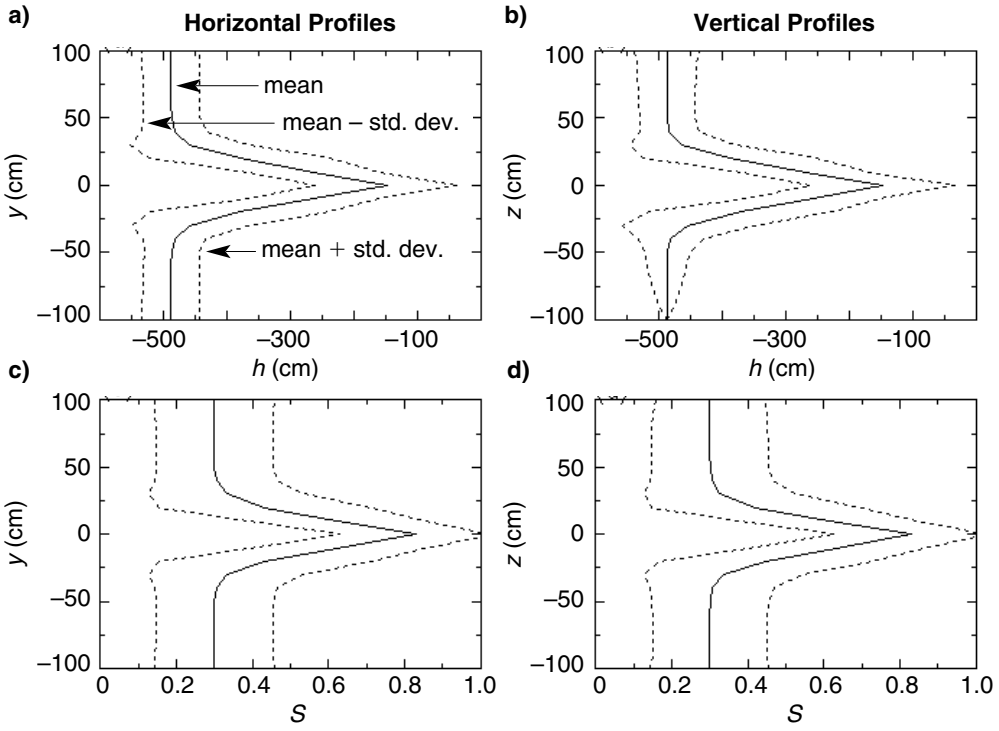

Figure 46. Case 11. The same as Case 1 in Fig. 36 but with $Q = 10$ ml/hr.

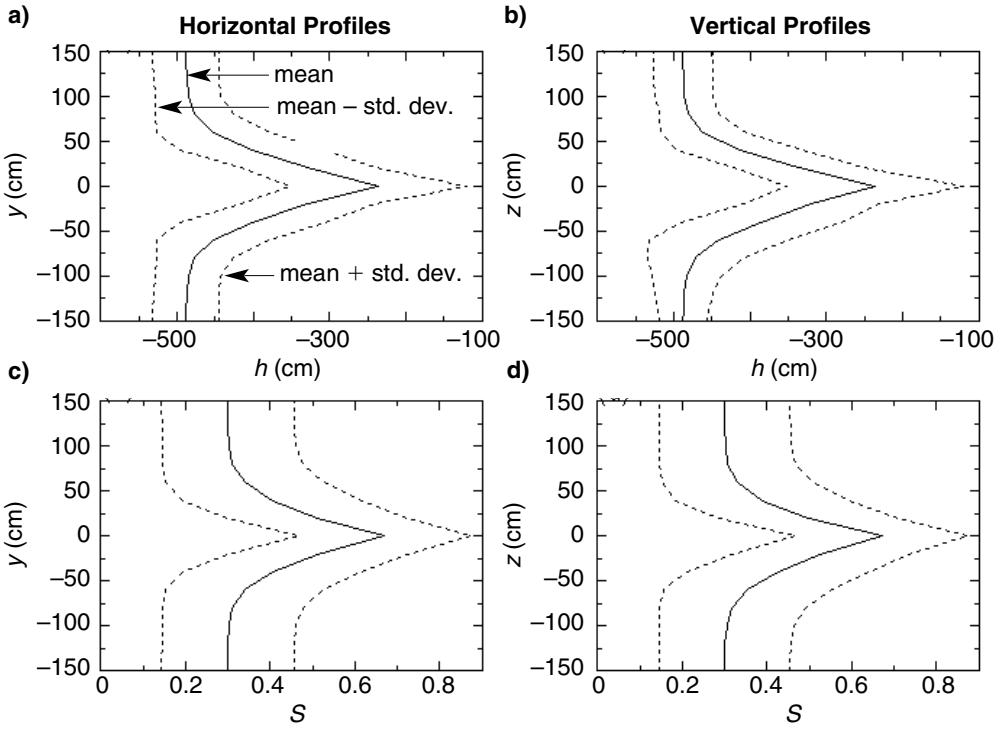

Figure 47. Case 12. The same as Case 8 in Fig. 43 but with $Q = 50$ ml/hr and $L_3 = 100$ cm.

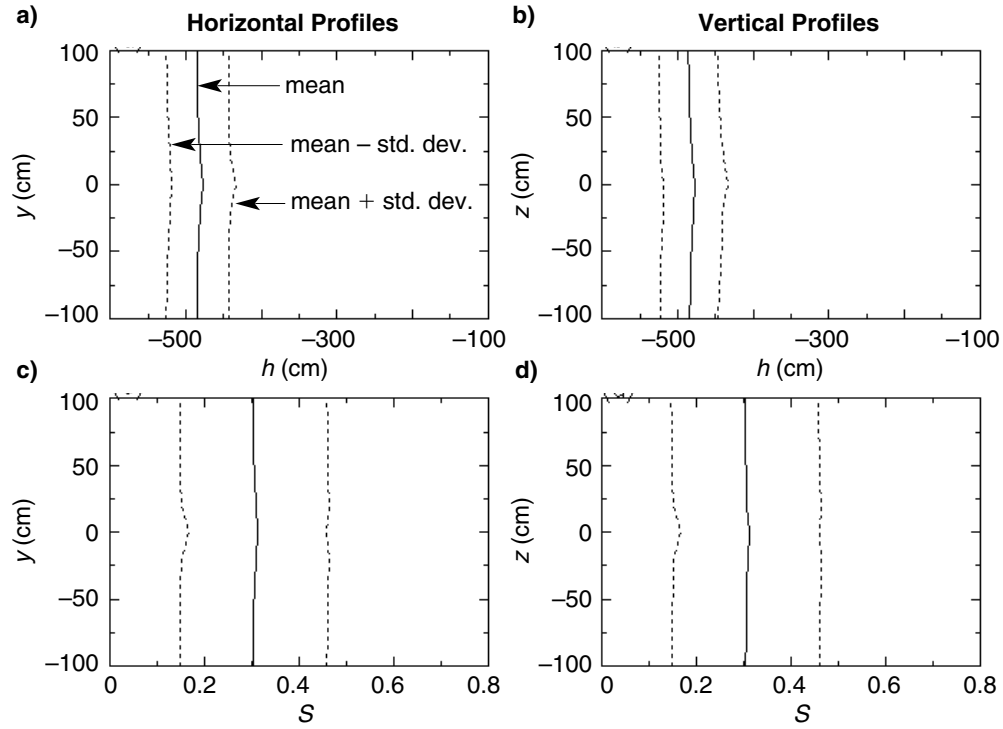

Figure 48. Case 13. The same as Case 1 in Fig. 36 but with $\langle f \rangle = 0.314$, $L_1 = L_2 = 400$ cm, and $Q = 10$ ml/hr.

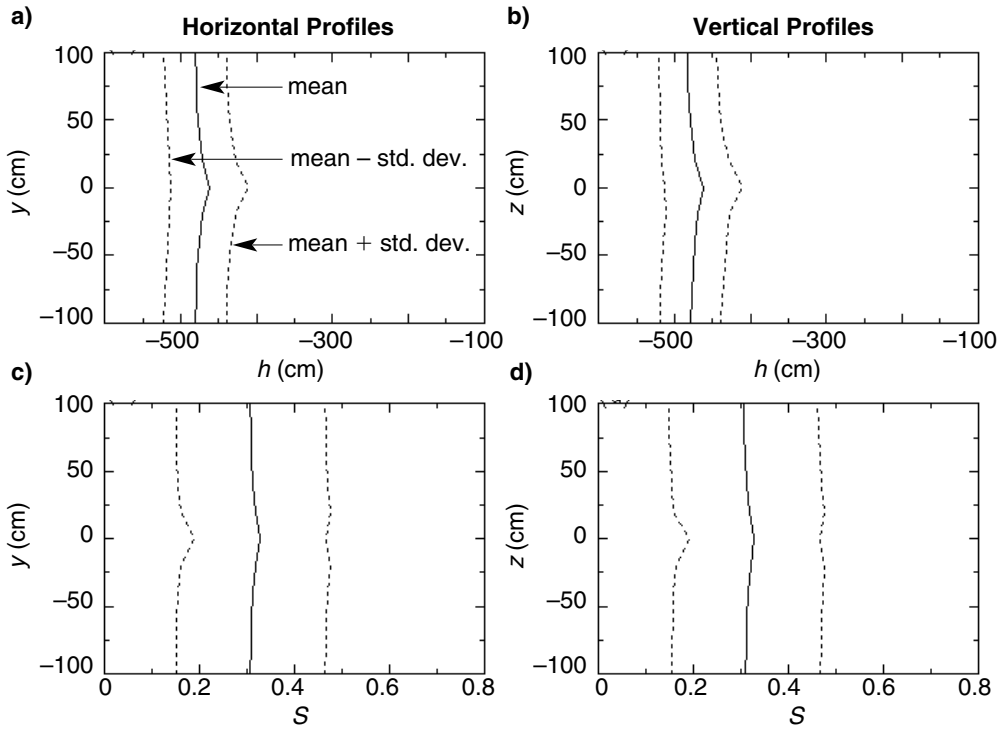

Figure 49. Case 14. The same as Case 13 in Fig. 48 but with $Q = 50$ ml/hr and $L_3 = 100$ cm.

The combination of inherent spatial variability in rock properties and insufficient measurements for these properties leads to uncertainties in the input parameters for any model and, thus, to uncertainties in flow-and-transport predictions. We incorporate these uncertainties directly into our flow predictions through a stochastic model. The results from this model are the first two moments (expected value and standard deviation) of flow quantities, and these two moments can be used to construct confidence intervals for the flow quantities. The statistical moments of flow quantities serve as a basis for future stochastic predictions of solute transport to be developed in fiscal year 1999.

Field test results of flow quantities, such as pressure head and saturation, if available, can be used to compare these values with the predicted confidence intervals of the same quantities (Case 1). It is expected that the field test results fall within the predicted confidence intervals with a 95% probability. However, statistical and other input parameters are taken or estimated from the YMP databases. These parameters may or may not represent the rock properties at the test site. Therefore, there is another level of uncertainty, and we have performed some sensitivity analyses regarding these parameters. It is found that the flow predictions are sensitive to the background saturation, the mean and variance of pore-size-distribution parameter α, the mean and variance of the log of the saturated hydraulic conductivity, and the injection rate. This sensitivity indicates that a refinement of these parameters is important.

6.3 Monte Carlo Flow-and-Transport Simulations.

6.3.1 Introduction.

To augment the results of the sensitivity analyses for the homogeneous-model calculations and the stochastic-model results, a series of Monte Carlo analyses were carried out in two dimensions. The goal of these simulations is to bracket the range of possible transport behavior that could arise due to variability in the hydrologic parameters. To accomplish this goal, a refined 2-D grid was generated (Fig. 50) for performing flow-and-transport calculations. As in the homogeneous simulations using FEHM, the top and bottom boundaries of the model are held at constant capillary pressure. A single realization of the model consists of two simulations: a background simulation (without fluid injection at the borehole) to establish a steady-state flow condition followed by a simulation in which fluid of unit concentration (arbitrary concentration units) is injected for 180 days, the duration of the Phase-1A experiments. To simulate a heterogeneous system, the model is populated with a distribution of permeability values with a given mean value and an assumed correlation length. Figure 51 shows a permeability distribution chosen at random from the Case-1 simulations (see Table 16 for a summary of the different cases treated in the Monte Carlo simulations; detailed discussion of the individual cases considered is described below). Contrasting permeability values within the region of rock in which fluid is injected is expected to affect the flow-and-transport behavior by providing preferential pathways for fluid migration through the rock.

6.3.2 Methodology

The Monte Carlo approach considers the results of all individual realizations to be equally likely outcomes of the behavior of the system. Therefore, once a metric is chosen for quantifying the behav-

Table 16. Summary of Monte Carlo Cases*

Case number	Correlation of α and permeability	Correlation length of heterogeneities (m)
1	None	0.2
2	Altman et al. 1996, pp. 34–36	0.2
3	Altman et al. 1996, pp. 34–36	0.1
4	Altman et al. 1996, pp. 34–36	0.5

*All cases assume $\ln(k_s) = 1.54$, where k_s is in cm/hr.

ior of the system, statistical properties of the behavior of the system can be established. In the present study, the movement of a conservative solute injected with the fluid is used because the post-test measurements will consist of a mine-back or selective drilling to collect rock and water samples and chemical analysis of tracer concentrations. The maximum penetration distance in all four directions away from the injection point are recorded for several different concentrations to establish the direction of movement of tracer. Then, for all 50 realizations in a given case, the mean value for these distances are recorded along with the standard deviation. The mean values establish the general location of the concentration front, whereas the standard deviation is a measure of the uncertainty in the predictions of concentration-front movement due to the heterogeneities of the rock mass.

6.3.3 Statistical results

One advantage of the Monte Carlo approach is that an individual realization can be examined in detail to understand the behavior of the system, after which, the multiple realizations can be used to quantify the uncertainty. We now examine (Fig. 52) the behavior of the flow-and-transport system for the permeability distribution shown in Fig. 51. The background saturation distribution shows little or no variability. This result is in contrast to the variability in predicted fluid saturation for the cases in which permeability and van Genuchten α are correlated.

For that type of heterogeneous field, the fluid saturation is a strong function of α. The left-hand figures of Fig. 52 show the movement of the saturation front into the rock mass for various times during the injection phase, and the right-hand figures are the concentrations of the conservative

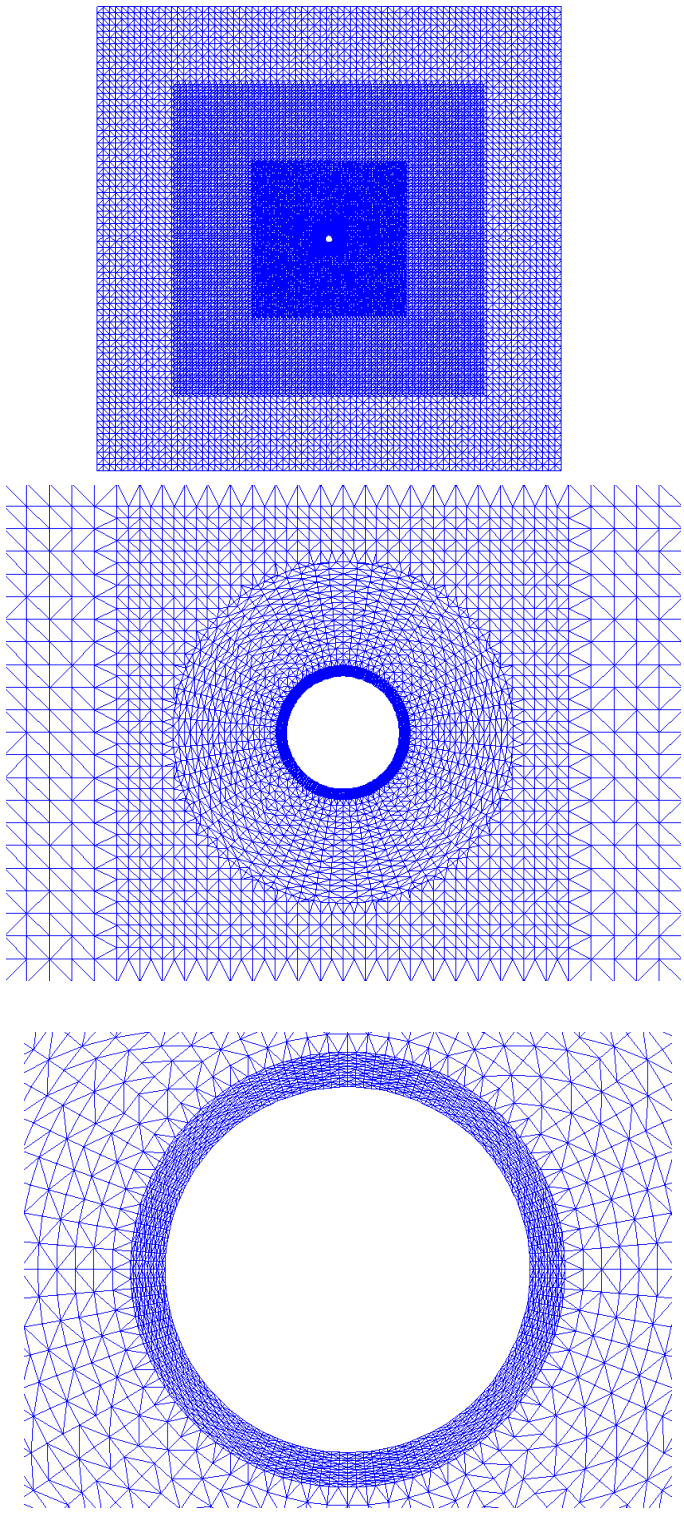

Figure 50. Finite-Element Grid Used in the Monte Carlo Simulations. Top: full view (6 m $\times$ 6 m); middle: intermediate close-up view (0.4 m $\times$ 0.5 m); bottom: close-up of borehole.

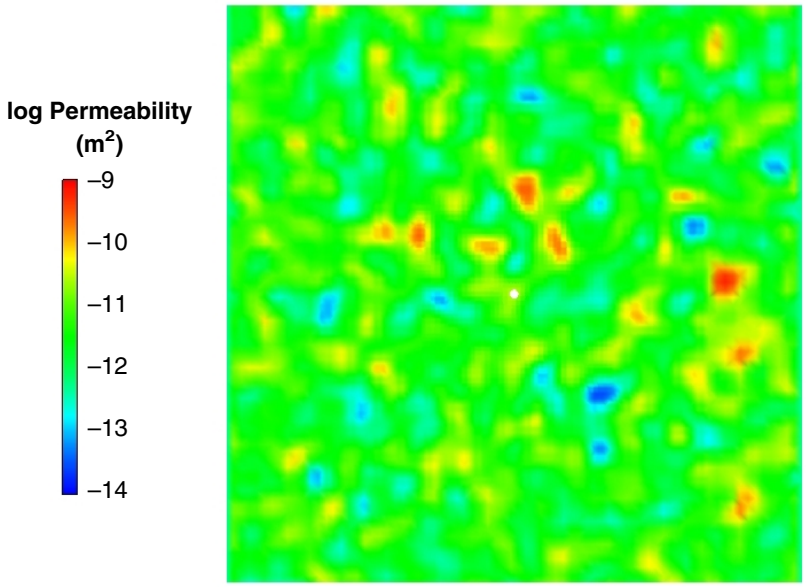

Figure 51. Permeability Distribution. This plot shows the permeability distribution for the Monte Carlo realization selected for discussion.

tracer for those same times. For this rock at this injection rate, there appears to be a relatively uniform migration of fluid and tracer away from the injection point in all directions, even upward. Under these conditions, the capillary-pressure driving forces are strong enough to pull water against the force of gravity. The presence of the borehole produces a "shadow effect" in which fluid must migrate around the borehole to reach the rock on the opposite side of the injection pad. Regarding the influence of heterogeneities, there is some tendency for fluid to be drawn preferentially into portions of the rock with higher capillary suction. The resulting saturation and concentration fronts exhibit an irregular pattern that tracks the heterogeneities. Nevertheless, the general patterns of movement of fluid and solute match fairly closely those of the homogeneous simulations.

We now examine the results of the statistical analyses of the Monte Carlo simulations. Table 17 shows the mean and standard-deviation values for the four cases summarized in Table 16. The *y* coordinate in the table represents the vertical direction, with negative values below the borehole injection point. The

Table 17. Statistical Results of Monte Carlo Simulations* (all values in m)

	***C* = 0.01**				***C* = 0.1**				***C* = 0.5**			
	x_{min}	x_{max}	y_{min}	y_{max}	x_{min}	x_{max}	y_{min}	y_{max}	x_{min}	x_{max}	y_{min}	y_{max}
Case 1												
Mean	–0.35	0.53	–0.45	0.42	–0.28	0.46	–0.37	0.35	–0.20	0.37	–0.29	0.27
Std. dev.	0.11	0.12	0.082	0.093	0.098	0.11	0.077	0.085	0.08	0.098	0.070	0.068
Case 2												
Mean	–0.30	0.47	–0.42	0.41	–0.23	0.41	–0.35	0.35	–0.16	0.33	–0.27	0.27
Std. dev.	0.019	0.014	0.015	0.012	0.016	0.013	0.013	0.013	0.010	0.012	0.011	0.013
Case 3												
Mean	–0.29	0.48	–0.41	0.41	–0.22	0.41	–0.35	0.35	–0.15	0.33	–0.27	0.27
Std. dev.	0.014	0.012	0.011	0.011	0.011	0.012	0.011	0.011	0.007	0.013	0.011	0.010
Case 4												
Mean	–0.28	0.49	–0.41	0.42	–0.22	0.42	–0.35	0.35	–0.15	0.34	–0.27	0.27
Std. dev.	0.027	0.024	0.022	0.024	0.022	0.020	0.019	0.018	0.015	0.017	0.018	0.017

*Results based on 50 realizations for each case

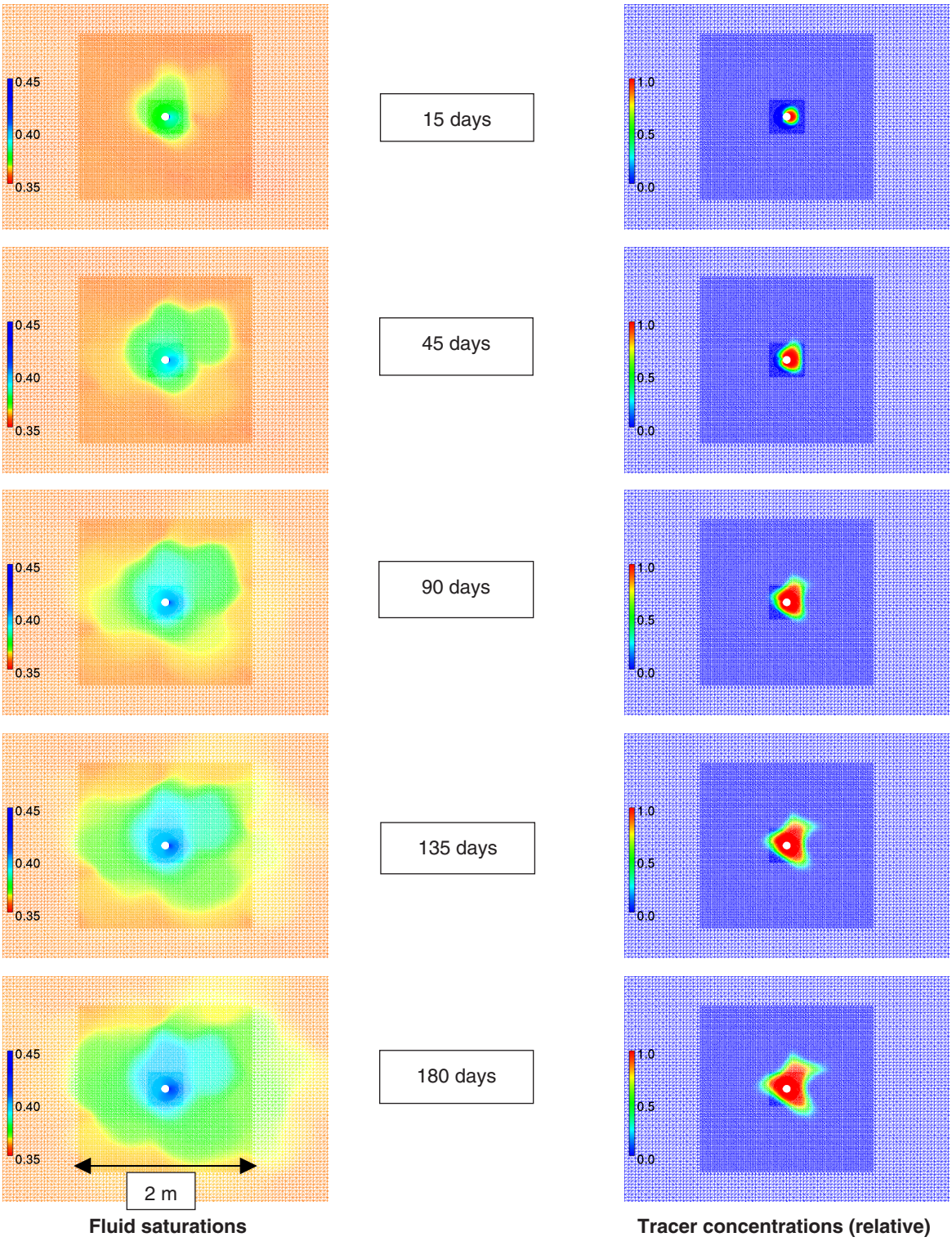

Figure 52. A Monte Carlo Simulation. These plots show fluid saturations and relative tracer concentrations during a Monte Carlo simulation as time increases from top to bottom. Note the restricted range of saturation values used (0.35 to 0.45).

x coordinate is laterally away from the borehole, with positive values located on the side on which the injection pad is located. We first focus on the results of Case 1, in which the permeability field is assumed to vary but the van Genuchten α value is constant. The mean values for the minimum and maximum *y* illustrate the degree to which the transport occurs uniformly in upward and downward directions. The Case-1 results show that capillary forces tend to pull water (and tracer) uniformly upward and downward with little or no tendency for downward migration due to gravity. The $C = 0.01$ isoconcentration value is meant to represent the migration of the front edge of the concentration plume; it travels approximately 40 to 45 cm in the upward, downward, and outward (positive *x*) directions, on average. The injection point is located at approximately $x = 5$ cm and $y = 0$. The travel distance for the $C = 0.5$ isoconcentration value is more indicative of bulk plume movement, rather than the leading edge. This front travels approximately 30 cm in the three directions. The x_{min} values suggest a slight asymmetry in plume migration. This asymmetry is caused by the "shadow effect" due to the presence of the borehole, as described above.

The borehole causes the plume to have more difficulty migrating in the negative *x* direction. The standard deviation values reflect the uncertainty in the predicted migration of the plume caused by the heterogeneous permeability distribution. For Case 1, the uncertainty in the $C = 0.01$ isoconcentration value is about 8 to 12 cm (depending on direction), whereas for the $C = 0.5$ value, the uncertainty ranges from about 7 to 10 cm. Therefore, for Case 1, the heterogeneous permeability field (with no variability in α) adds considerable uncertainty to the predictions.

A comparison of Cases 1 and 2 illustrates the influence of imposing a correlation of permeability and α on the uncertainty of the predictions. The mean values for the spreading of the plume in all directions are very similar for the two cases, but the uncertainty due to heterogeneity is much smaller when α is assumed to be correlated with permeability (Case 2). The correlation imposes a larger α for lower permeability, resulting in a larger capillary suction for regions of the rock with lower permeability. This result counteracts the tendency for fluid to travel preferentially through higher permeability rock, as in Case 1. Therefore, the spreading of tracer in Case 2 is more uniform, and the standard deviation values are consequently smaller. A series of hydrologic measurements on samples collected at the site will help to evaluate which of the situations is more likely for the Calico Hills tuffs.

Finally, the influence of correlation length on plume spreading can be examined by comparing Cases 2, 3, and 4, which assumed correlation lengths of 0.2 m, 0.1 m, and 0.5 m, respectively. The mean behavior of the plumes is very insensitive to the correlation length. Regarding the uncertainty in plume prediction (as measured by the standard deviation), there is a trend toward larger uncertainty as the correlation length increases, as expected. Nevertheless, the uncertainty for these cases is much smaller than the correlation length itself. This result is caused by the assumed correlation of permeability and α for each of these cases, which, as just discussed, largely negates the distribution of permeability values. Therefore, the largest uncertainty in these simulations appears to be the nature of the correlation (or lack thereof) of different hydrologic properties. Permeability and the van Genuchten α parameter were correlated in these simulations. Altman et al. (1996, pp. 34–36) also propose correlations between permeability and porosity for Yucca Mountain tuffs. Therefore, the most important data that could be collected to further constrain these predictions are hydrologic property measurements on a much larger set of samples from the test block. A full suite of property measurements (porosity, permeability, and unsaturated hydrologic parameters) on samples collected from known locations in the block would be useful to set correlations between parameters and assign correlation lengths for future simulations.

6.3.4 Summary

Critical evaluation and iterative improvement of

the flow-and-transport conceptual and numerical models awaits the collection of data, which is currently in progress. Although flow-and-transport field data collected to date are limited, observations of the available data collected so far, and the modeling of these data, lead to several key conclusions of relevance to performance assessment.

The modeling analyses for Phase 1A indicate that strong capillary forces in the rock matrix of the Tac unit are likely to modulate fracture flow from overlying units, thereby dampening pulses of infiltrating water and providing a large degree of contact between radionuclides and the rock matrix. Several modeling approaches, from deterministic to Monte Carlo to stochastic models, were used to simulate the Phase-1A experiments. All yielded similar qualitative results. From these results, we conclude tentatively that the deterministic modeling approach taken at the site scale may be adequate. The parameterizations used in performing these calculations must be evaluated after data from the UZTT are available.

A particularly interesting observation from the Phase-1B experiment is that, even when injection occurs immediately adjacent to a fracture, water appears to be imbibed quickly into the surrounding matrix. The transport times observed immediately below the injection point were on the order of 30 days, whereas pure fracture flow would have resulted in travel times of minutes to hours at this flow rate. Site-scale models must be evaluated in light of this observation. Models that predict significant fracture flow at percolation rates low enough for the matrix to transmit the flow may be inconsistent with the Phase-1B experiment.

7. INITIAL PHASE-2 MODEL PREDICTIONS

7.1 Introduction

The predictions discussed here were first presented to the YMP M&O as a white paper on July 15, 1997, eight days prior to the commencement of Phase-2 injections. This work constitutes the first "blind" prediction on the behavior of the Phase-2 block of the Busted Butte transport test prior to injection. These predictions are intended to test the current modeling concepts and tools available to the integrated site-scale model and the validity of the abstractions of that model for performance assessment. The predictions use parameters from currently available Yucca Mountain hydrologic and geochemical databases. At this stage, no model calibration has been performed, as Busted Butte test results are not yet available. As data become available from the various phases of the UZTT, we will incorporate them into refined versions of the model. The new information will be used to make improved predictions. All simulation results presented in this paper have been data-logged into the M&O/YMP file system to guarantee that all predictions herein precede the injection of Phase-2 tracers.

The YMP-qualified computer code FEHM used in the site-scale UZ flow-and-transport model and its abstractions for performance assessment is also used in the development of the 3-D model presented in this paper. Specifically, this code is used by the Project for radionuclide migration predictions using the "calibrated" site-scale flow solutions (Bodvarsson et al. 1997, Table 6.5.4-1) and, therefore, is ideal for predictions of the UZTT results. Although detailed geologic and hydrologic property distributions in three dimensions are not available at present, we anticipate that during the course of the testing, these data will become available. Three-dimensional effects will probably become important as data specific to the test block become available for the Phase-2 block. The model is, therefore, being developed in three dimensions at the outset to capture these effects and to anticipate the three-dimensional property database that will be collected for the test block.

In this chapter, we predict conservative and reactive tracer breakthrough times for each of the sampling boreholes for up to one year from the present, the planned input time of the test results into the TSPA-LA.

7.2. Model Description

The Phase-2 test block at Busted Butte encompasses, from top to bottom, the lower section of the Topopah Springs vitrophyre (Tptpv2) and the hydrologic Calico Hills unit (Tptpv1 and Tac) (Fig. 53). The first step in constructing a 3-D finite-element model of the Phase-2 test is to build a finite-element mesh using the coordinates of the injection and collection boreholes. The file used in this work contains the surveyed local coordinates of the boreholes and the layered stratigraphy at the site.

Figure 53 shows the AUTOCAD 3-D representation of the Phase-2 block with the boreholes represented as colored lines. The block is approximately 7 m high $\times$ 10 m deep $\times$ 10 m wide and contains twenty-eight boreholes ranging from 7.5 m to 10.0 m in length. The eight injection boreholes (shown in red) all originate in the left rib of the Test Alcove (located in front of the figure). These boreholes are subparallel, distributed along two horizontal planes, and are perpendicular to the twelve collection boreholes (dark blue) coming from the right rib of the Main Adit (to the left of the vertical *y*-*z* plane). The other boreholes (light blue) are dedicated to ERT and GPR-T.

For the purposes of modeling, we chose the model domain to extend from +2 to +14 m in the *x*-direction, +60 to +72 m in the *y*-direction, and –8.2845 to +2.5015 m in the *z*-direction. These coordinates are consistent with the surveyed local coordinates and the stratigraphy of the block. Figure 54 shows a top view of the finite-element grid with the borehole locations.

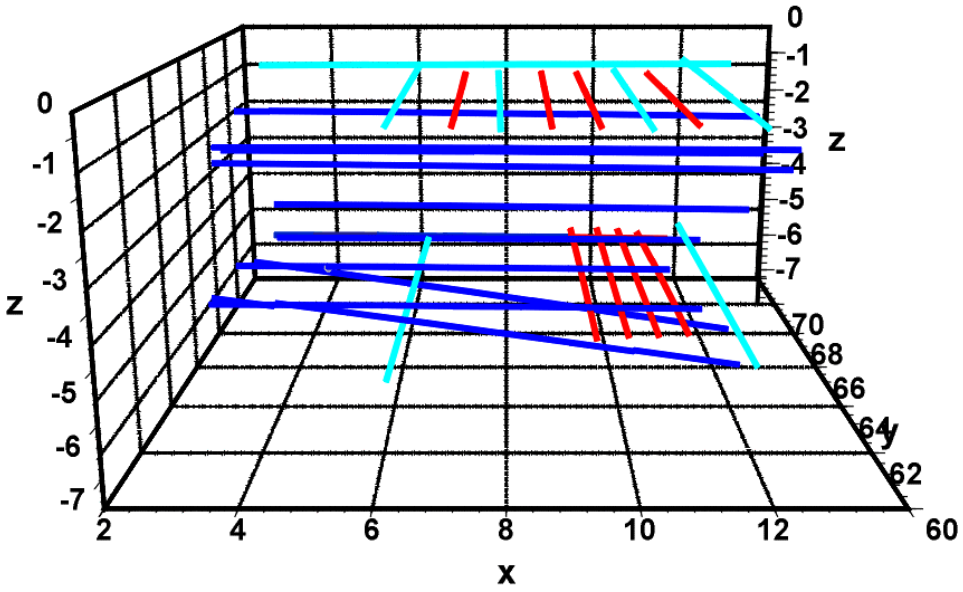

Figure 53. Three-Dimensional View of the Injection and Collection Boreholes. The red lines represent injection boreholes, the dark blue lines collection boreholes, and the light blue lines are devoted to tomography (ERT and GPR-T). In this view, the Test Alcove is located in front of the figure, and the Main Adit is to the left of the figure (beyond the $x = 2$ plane).

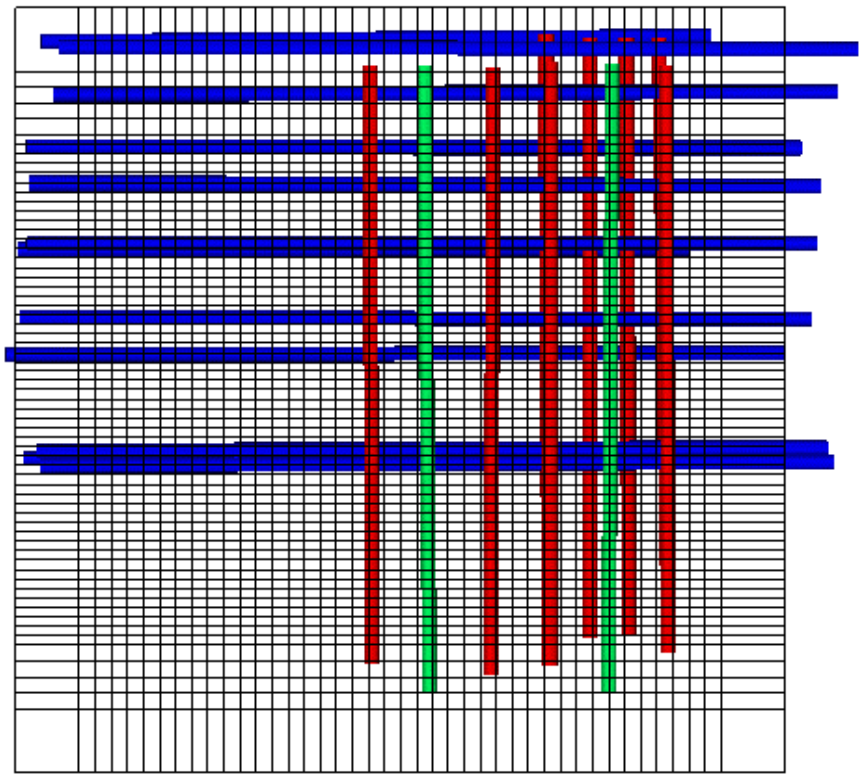

Figure 54. Top View of Finite-Element Grid and the Injection and Collection Boreholes. As in Fig. 53, injection boreholes are depicted as red lines, collection boreholes as blue.

In general, the mesh was refined at locations between the injection and collection boreholes to accurately capture the migration of the tracers and heterogeneities at scales smaller than the layer thickness. In the *x*-direction, we chose a grid spacing of 0.25 m at locations close to the boreholes. In both the *x*- and *y*-directions, we chose a coarse mesh spacing at the block boundaries, because no transport is expected at these locations. In the *y*-direction, we chose a mesh spacing of 0.125 m at locations close to boreholes. A slightly finer grid spacing was used in the *y*-direction than the *x*-direction to accurately capture the location of the injection points, which are spaced 0.61 m apart in the *y*-direction (10 injection points per injection borehole). In the *z*-direction, we represent the stratigraphy with six distinct layers: 5 layers to represent the hydrologic Calico Hills unit (Tac: 3 layers; Tptpv1: 2 layers), and 1 layer to represent Tptpv2. The discretization in the *z*-direction is dependent on the particular layer because some layers are thicker than others. The discretization ranged from 0.15 to 0.25 m. The entire model is comprised of 128,570 nodes. Figures 55 and 56 show views of the grid from the Test Alcove and the Main Adit, respectively. Once the mesh was constructed, the next step was to assign properties to the model. Table 18 contains the property sets used in the different layers.

For this preliminary investigation, layers 1 through 3 were lumped together as one Calico Hills unit (Tac), layers 4 to 5 were assigned Tptpv1 properties, and layer 6 was assigned Tptpv2 properties. As additional data become available, layers 1 through 3 and 4 through 5 will all be treated as distinct layers. Porosity values were obtained from a few samples from the Busted Butte site (Appendix C). Permeabilities and van Genuchten relative-permeability parameters for the matrix were obtained from Flint et. al (1998, p. 44, Table 7). We chose this study because it represents the existing YMP database for the unsaturated zone and contained sufficient samples to generate statistics on the variability of key parameters, such as matrix permeability and matrix van Genuchten parameters. Ideally, a database of fracture properties for the Busted Butte site would be used, but these data are not yet available. Instead, fracture van Genuchten parameters were taken from the "calibrated" flow model of Bodvarsson et al. (1997, Table 6.5.4-1). These data were obtained by fitting field data at the site scale. Although there is a great amount of uncertainty in fracture properties, we consider this data set to be a reasonable representation of YMP material properties applicable to Busted Butte.

For this preliminary investigation, and in view of the absence of data on fracture-matrix interactions

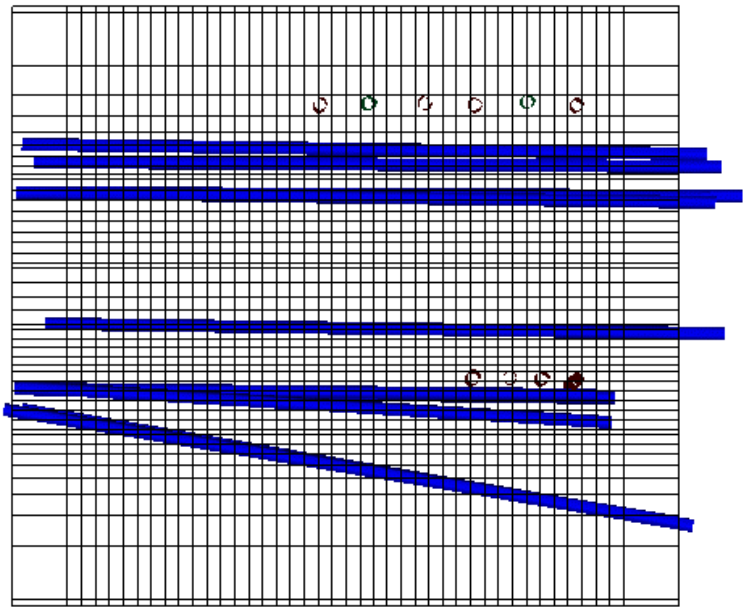

Figure 55. The Finite-Element Grid as Seen From the Test Alcove. The blue colored lines represent collection boreholes. Because the injection boreholes originate in the Test Alcove, they are perpendicular to the plane of the figure and are depicted as circles.

in the Calico Hills, we have used the equivalent-continuum model (ECM) to model Phase 2. As we refine our predictions, isotropic and anisotropic dual-permeability models and stochastic models will be used in addition to the ECM, if necessary. The ECM was also used in scoping calculations done during design of the test and is currently being used to understand both Phases 1A and 1B.

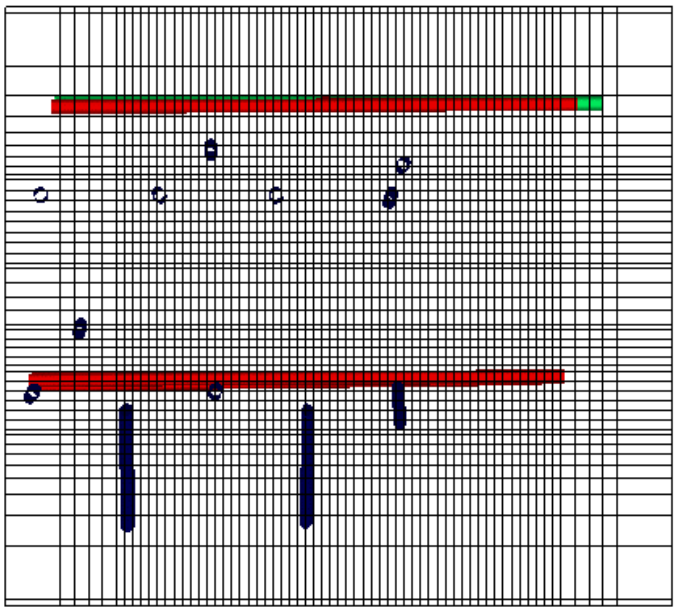

Figure 56. The Finite-Element Grid as Seen From the Main Adit. The horizontal red lines represent the location of injection boreholes, which are perpendicular to the collection boreholes (blue). The collection boreholes originate in the Main Adit, but several are plunging down and, thus, show up as blue lines rather than circles. The green line represents one of the tomography boreholes.

Tracer breakthrough has occurred in the 10ml/hr injection system of Phase 1B (Borehole #6). Specifically, tracer was detected at the pad 35 days after injection. This result means the time of breakthrough occurred between 28 and 35 days in relation to the collection-pad schedule. To compare model predictions with test breakthrough times as defined by the appearance of fluorescein tracer on a collection pad, the concentration of the tracer must be known. For example, if we define the time of breakthrough to be when the normalized concentration reaches 0.5, then for Tptpv2, the ECM predicts a breakthrough at 47 days for a distance traveled by the tracer of 28 cm (Fig. 57). At a normalized concentration of 0.3, the model predicts breakthrough at 31 days for the same distance, which is close to the observed breakthrough time for Borehole #6.

Table 18. Property Sets for the Phase-2 Test.
Here, α and n are the van Genuchten parameters, K is permeability, ϕ is volume fraction, and θ is porosity. The subscript m signifies matrix material and the subscript f signifies fracture material.

Busted Butte Layer	Matrix Material (Flint 1998, p. 44, Table 7)				Fracture Material (Bodvarsson et al. 1997, Table 6.5.4-1)					Appendix C
	Layer	α_m (1/m)	n_m	K_m (m^2)	Layer	α_f (1/m)	n_f	K_f (m^2)	ϕ_f	θ
Tac1	CHv	3.5	1.19	5×10^{-12}	CH1v	11.52	3.0	2.43×10^{-9}	7.14×10^{-5}	0.5
Tac2	CHv	3.5	1.19	5×10^{-12}	CH1v	11.52	3.0	2.43×10^{-9}	7.14×10^{-5}	0.5
Tac3	CHv	3.5	1.19	5×10^{-12}	CH1v	11.52	3.0	2.43×10^{-9}	7.14×10^{-5}	0.5
Tptpv1	BT1	0.56	1.31	1×10^{-13}	CH1v	11.52	3.0	2.43×10^{-9}	7.14×10^{-5}	0.5
Tptpv1	BT1	0.56	1.31	1×10^{-13}	CH1v	11.52	3.0	2.43×10^{-9}	7.14×10^{-5}	0.5
Tptpv2	PV2	2.2	1.25	1×10^{-16}	TSW2	0.91	2.92	6.6×10^{-9}	1.29×10^{-4}	0.25

In the future, as data become available, we will be able to use Phase-1 results to improve on the current predictions of Phase 2. However, for the first phase of predictive modeling and in the absence of appropriate data, we simply use the database listed in Table 18 with no attempt at calibration. The background flow conditions are obtained by setting a capillary pressure at the top and bottom boundaries and allowing the block to equilibrate to a steady-state saturation profile. A capillary pressure of 200 m of water was chosen, which is within the range of capillary-pressure measurements at Yucca Mountain (Altman et al. 1996, p. 38, Fig. 3-12). The capillary pressure was set so that a saturation of about 0.35 to 0.45 was obtained in the block. Moisture measurements and preliminary porosity data from test-block lithologies indicate that these saturation values are reasonable. Once the background conditions are set, the next step is to begin pumping and injecting tracer.

Three different pumping rates are to be used in Phase 2: a) 1 ml/hr (1 upper borehole), b) 10 ml/hr (4 lower boreholes), and c) 50 ml/hr (3 upper boreholes). The 1-ml/hr rate is equivalent to an infiltration rate of approximately 30 mm/yr, which is well within the range of infiltration rates at Yucca Mountain. The predictions we have made (given below) show that, during a 1-yr test, the 1-ml/hr pumping rate is not expected to transport any tracer to the sampling wells. Injection Borehole 23 will be the only one that pumps at 1 ml/hr. The 10-ml/hr injection rate is equivalent to an infiltration rate of approximately 380 mm/yr, which is slightly higher than the highest anticipated infiltration that will occur at Yucca Mountain. The lower Injection Boreholes 24, 25, 26, and 27 will operate at 10 ml/hr. Finally, 50 ml/hr is equivalent to an approximate infiltration rate of 1550 mm/yr. This infiltration rate is far higher than what is expected at Yucca Mountain even under wetter future climate scenarios. The purpose of the 50-ml/hr rate is to obtain enough separation in travel times between the conservative and reactive tracers so as to be visible and distinct in the field test. Boreholes 18, 20, and 21 will pump continuously at 50 ml/hr.

7.3 Predictions

The predictions below are borehole specific and can, therefore, be used to compare directly to test-block results. Table 19 shows the distance between the closest sampling point and the injection planes. Tables 20 through 28 predict the tracer break-

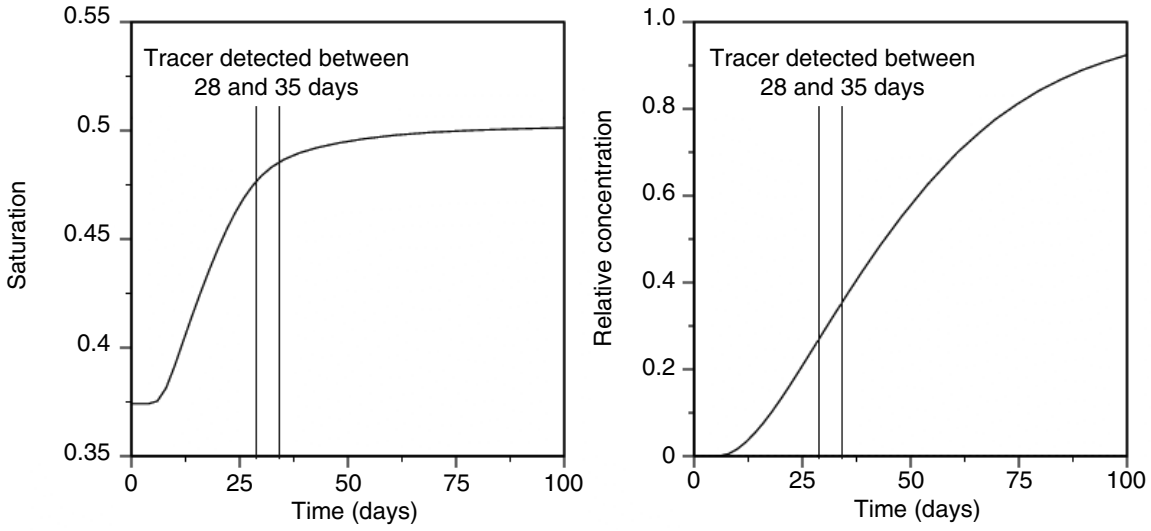

Figure 57. Using ECM and Tptpv2 Properties to Predict Phase 1B. The plots show the conservative breakthrough of tracer at a point 28 cm from the injection pad: a) saturation breakthrough, b) concentration breakthrough. (Refer to M&O/YMP file: inject.trc, generated on July 8, 1998.)

Table 19. Closest Sampling Point to the Injection Planes Within Each Collection Borehole.

Collection borehole	Distance from top injection plane (m)	Collection borehole	Distance from bottom injection plane (m)
16	0.61	46	0.175
17	0.80	48	0.175
14	1.17	9	0.175
15	1.17	10	0.59 (above plane)
13	1.17		
12	1.17		

throughs at each of these locations.

For all predictions, we use three criteria for tracer-breakthrough times: a) a 5% concentration limit, b) a 50% concentration limit, and c) the concentration after 1 year from the time of injection (the time of submittal of results for TSPA-LA). Note that we will assume that the concentration of tracer in the injection fluid is unity. Also, note that tracers are continuously injected for the duration of the test.

A diffusion coefficient of 1×10^{-11} m^2/s was used for all tracers. Longitudinal and transverse dispersivities were zeroed out for this preliminary set of calculations. However, as with any finite-element model, some numerical dispersion is present. Due to the fine mesh spacing and small time steps taken in these simulations, numerical dispersion is not expected to play a significant role in these simulations. A bulk-rock density of 2580 kg/m^3 was used for all layers. This parameter only affects the reactive-tracer breakthrough times. As more data become available, all of these parameters will be adjusted. However, we feel that the values chosen are reasonable representations of Yucca Mountain properties, given the existing database.

Conservative tracers. We first predict the travel times for fluorescein, a conservative tracer. We assume uniform properties for porosity, permeability, and van Genuchten model parameters within each of the six layers of the test block. In the last part of this report, we will briefly examine the effect of heterogeneous property distributions. Figure 58 depicts a concentration plume for fluorescein after 1 yr.

Table 20. Fluorescein from Upper Injection Boreholes.
(Refer to M&O/YMP file: cons.trc, generated July 9, 1998.)

Borehole	5% breakthrough concentration	50% breakthrough concentration	Normalized concentration at 1 yr
16	27 days	68 days	1.0
17	48 days	118 days	1.0
14	118 days	238 days	0.87
15	103 days	218 days	0.90
13	103 days	218 days	0.90
12	212 days	$>$ 1 yr	0.46
Remaining collection boreholes	$>$ 1 yr	$>$ 1 yr	0.0

Tables 20 and 21 show the predicted breakthrough times of tracer for the upper and lower collection sampling points, respectively. As expected, sampling locations closer to the injection planes exhibit tracer breakthrough times that are earlier than those from more distant locations. As discussed in the next

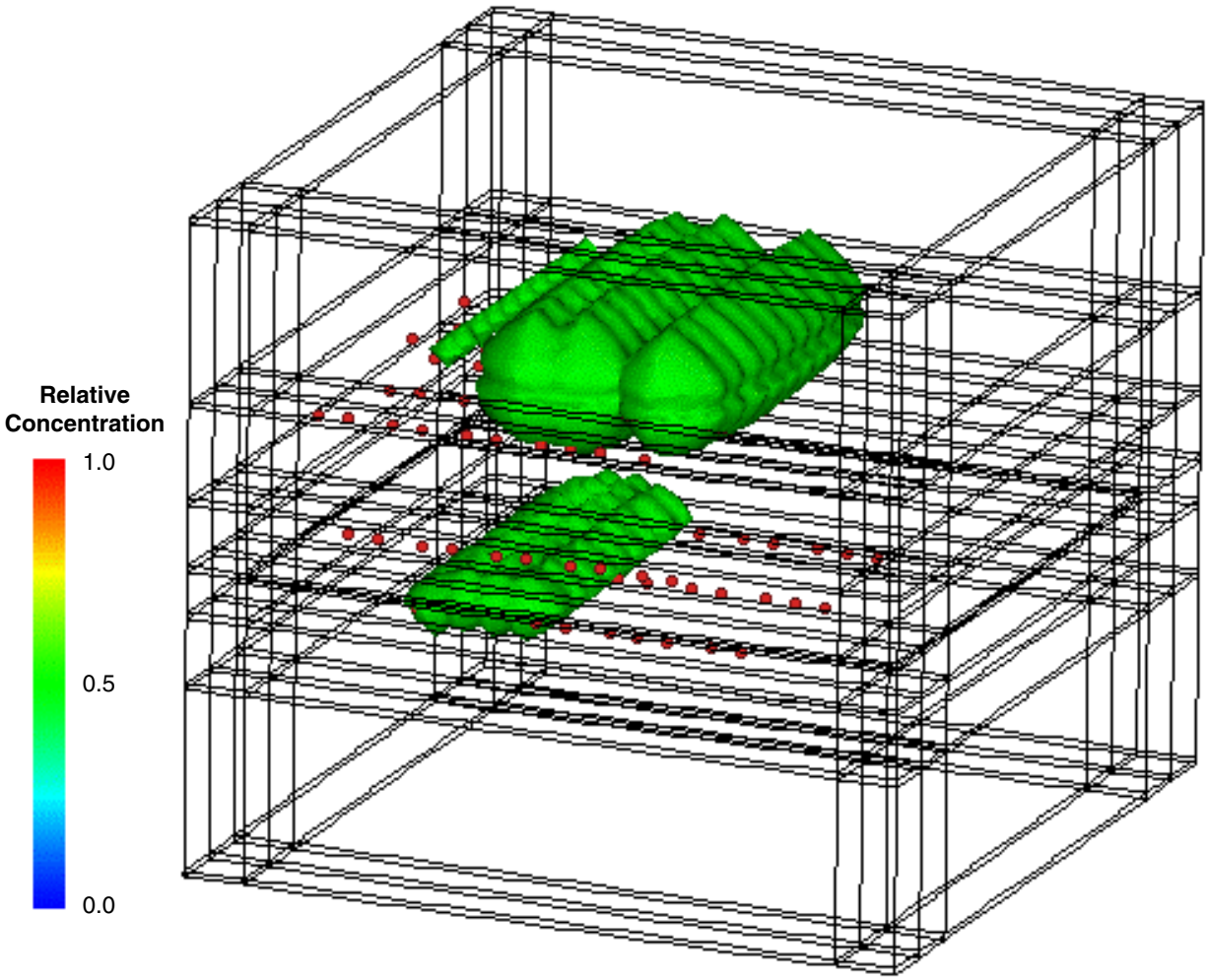

Figure 58. A Conservative-Tracer Concentration Plume. The figure depicts the concentration plume after 1 yr of conservative-tracer injection. The green isosurface represents a normalized concentration of 0.5; the red dots represent the sampling points along the collection boreholes. (Refer to M&O/YMP file: inject.10004_con_node, generated on July 13, 1998.)

Table 21. Fluorescein from Lower Injection Boreholes.
(Refer to M&O/YMP file: cons.trc, generated July 9, 1998.)

Borehole	5% breakthrough concentration	50% breakthrough concentration	Normalized concentration at 1 yr
46	4 days	30 days	1.0
48	20 days	91 days	0.98
9	53 days	166 days	0.91
10	171 days	> 1 yr	0.37

section, for simulations involving heterogeneous property distributions, this result may be modified due to preferential flow paths. The results indicate that we expect tracer breakthrough at several sampling locations within the first year and some are

expected within the first month. Conservative-tracer breakthroughs could occur at earlier times than predicted by the ECM model if the model assumptions are erroneous. Fracture flow through Tptpv2, for example, could result in faster travel times. Even so, an additional year of operation may be required to achieve transport distances on the order of the entire length of the block.

Nonconservative tracers. Table 22 shows the distribution coefficients, K_d, for the reactive, nonconservative tracers determined by parallel laboratory studies and used in Phase 2 for the various units. The measurements are preliminary but provide a starting point for the modeling effort. Travel times for reactive tracers are extremely sensitive to these distribution coefficients and errors in these parameters strongly bias the results. One major deficiency in the preliminary measurements is that these results do not include reversible sorption and equilibrium may not have been achieved when obtaining the distribution coefficients.

The next set of tables shows the predicted breakthroughs for the three reactive tracers: lithium Tables 23 and 24), manganese (Tables 25 and 26), and nickel or cobalt (Tables 27 and 28). The data indicate that lithium does not sorb in Tptpv2 but mildly sorbs in Tac and Tptpv1. Although lithium sorption in Tac is mild when compared to manganese and nickel or cobalt, the sorption has a large effect on travel times over the time scale of interest. The lithium only breaks through at locations that are extremely close to the injection boreholes (i.e., Boreholes 16, 17, 46, 48 and 9).

Manganese is predicted to sorb much more strongly than lithium. For this reason, manganese is only expected to breakthrough at Boreholes 46 and 48 within a one-year time span. Cobalt or nickel sorbs even more strongly than manganese and is not expected to breakthrough at any of the boreholes during the time of the test.

There are many caveats that could strongly affect the predicted travel times of the reactive tracers. First, the model is extremely sensitive to the values of K_d and the current K_d measurements are uncertain at this time. A simple K_d may not be sufficient to model sorption of these tracers due to chemical heterogeneities and nonlinear reactions. More rigorous reactive transport models will be used in the future to check the linear K_d assumption. Finally, these immobile reactive tracers may sorb onto colloids, thereby enhancing their mobility.

Table 22. Retardation of Reactive Tracers.

Tracer	K_d (cc/g)	
	Tptpv1, Tac	Tptpv2
Lithium	1.0	0.0
Manganese	15.6	6.5
Nickel/cobalt	34.0	13.0

Table 23. Lithium from Upper Injection Boreholes.
(Refer to M&O/YMP file: chem.trc, generated on July 13, 1998.)

Borehole	5% breakthrough concentration	50% breakthrough concentration	Normalized concentration at 1 yr
16	52 days	193 days	0.79
17	257 days	> 1 yr	0.12
14	> 1 yr	> 1 yr	0.0
15	> 1 yr	> 1 yr	0.02
13	> 1 yr	> 1 yr	0.0
12	> 1 yr	> 1 yr	0.0
Remaining collection boreholes	> 1 yr	> 1 yr	0.0

Table 24. Lithium from Lower Injection Boreholes.
(Refer to M&O/YMP file: chem.trc, generated on July 13, 1998.)

Borehole	5% breakthrough concentration	50% breakthrough concentration	Normalized concentration at 1 yr
46	28 days	267 days	0.62
48	63 days	327 days	0.55
9	242 days	> 1 yr	0.12
10	> 1 yr	> 1 yr	0.0

Table 25. Manganese from Upper Injection Boreholes.
(Refer to M&O/YMP file: chem.trc, generated on July 13, 1998.)

Borehole	5% breakthrough concentration	50% breakthrough concentration	Normalized concentration at 1 yr
16	> 1 yr	> 1 yr	0.0
17	> 1 yr	> 1 yr	0.0
14	> 1 yr	> 1 yr	0.0
15	> 1 yr	> 1 yr	0.0
13	> 1 yr	> 1 yr	0.0
12	> 1 yr	> 1 yr	0.0
Remaining collection boreholes	> 1 yr	> 1 yr	0.0

Table 26. Manganese from Lower Injection Boreholes.
(Refer to M&O/YMP file: chem.trc, generated on July 13, 1998.)

Borehole number	5% breakthrough concentration	50% breakthrough concentration	Normalized concentration at 1 yr
46	277 days	> 1 yr	0.06
48	328 days	> 1 yr	0.06
9	> 1 yr	> 1 yr	0.0
10	> 1 yr	> 1 yr	0.0

Heterogeneous system. A major assumption of the above modeling results is that properties are homogeneous within a layer. In this section, we explore the effects of the heterogeneity of properties within the layers. In these simulations, permeability values are distributed within each layer. We assume that the mean of the permeability is the same as the permeability values used in the homogeneous simulations. In each layer, we assume a log-normal distribution of permeability with a ln(k) variance of 2.0 and a correlation length of 1 m in the x, y, and z directions. In the Calico Hills and Tptpv1 units, the van Genuchten parameter α_m has been shown to be correlated to matrix permeability (Altman et. al. 1996, p. 36, Fig. 3-10). We use this correlation to distribute α_m throughout the hydrologic Calico Hills or Tac and Tptpv1 units.

Figure 59 shows the background saturation profile and the saturation profile after one year of continuous injection. The saturation profile shows that the 50-ml/hr boreholes have a strong effect on the saturation profile. This effect is for two reasons, including the obvious reason that 50 ml/hr is the high injection rate. The second reason is that the 50-ml/hr boreholes inject into the lower section Topopah Springs Basal Vitrophyre (Tptpv2), which has a much lower matrix permeability than the

hydrologic Calico Hills (Tac and Tptpv1). The 10-ml/hr injections in the Tac unit do not have a large effect on the saturation profile. The simulations indicate that capillary action is an important process around the 10-ml/hr injections, which is mostly due to the high matrix permeabilities in this unit.

Table 27. Nickel or Cobalt from Upper Injection Boreholes.
(Refer to M&O/YMP file: chem.trc, generated on July 13, 1998.)

Borehole	5% breakthrough concentration	50% breakthrough concentration	Normalized concentration at 1 yr
16	$>$ 1 yr	$>$ 1 yr	0.0
17	$>$ 1 yr	$>$ 1 yr	0.0
14	$>$ 1 yr	$>$ 1 yr	0.0
15	$>$ 1 yr	$>$ 1 yr	0.0
13	$>$ 1 yr	$>$ 1 yr	0.0
12	$>$ 1 yr	$>$ 1 yr	0.0
Remaining collection boreholes	$>$ 1 yr	$>$ 1 yr	0.0

Table 28. Nickel or Cobalt from Lower Injection Boreholes.
(Refer to M&O/YMP file: chem.trc generated on 7/13/98)

Borehole	5% breakthrough concentration	50% breakthrough concentration	Normalized concentration at 1 yr
46	$>$ 1 yr	$>$ 1 yr	0.0
48	$>$ 1 yr	$>$ 1 yr	0.0
9	$>$ 1 yr	$>$ 1 yr	0.0
10	$>$ 1 yr	$>$ 1 yr	0.0

Tables 29 and 30 show the breakthrough times for two realizations. As expected, heterogeneities do add some fluctuations in the trends observed previously; however, many of the trends still hold. Many more realizations are required to gauge the spread or uncertainty in the travel times. The methodology for performing these Monte Carlo simulations now exists, and the next step will be to run many more realizations.

7.4 Conclusions

This chapter constitutes a preliminary "blind" prediction of the behavior of the Phase-2 block of the UZTT at Busted Butte. The prediction is intended to test the current modeling concepts and tools available to the integrated site-scale model and their abstractions for performance assessment. This prediction uses parameters from the available Yucca Mountain hydrologic and geochemical databases. No calibrations have been performed using information from Busted Butte. As more data become available from the UZTT, they will be incorporated into refined versions of the models employed in these preliminary predictions and documented.

Modeling results for fluorescein, a conservative tracer, indicate that we expect tracer breakthrough at several sampling locations within the first year of testing. For some sampling locations, tracer breakthrough is predicted for travel times of less than a month. Tracer breakthroughs could be even quicker than predicted if the ECM assumption does not hold. Fracture flow through the Topopah Springs formation (Tptpv2) could result in faster travel times. The fracture parameters for the van Genuchten model are not known to a high degree of accuracy. Sensitivity analyses on these parameters will be performed to determine how sensitive travel times are to these fracture parameters. Another

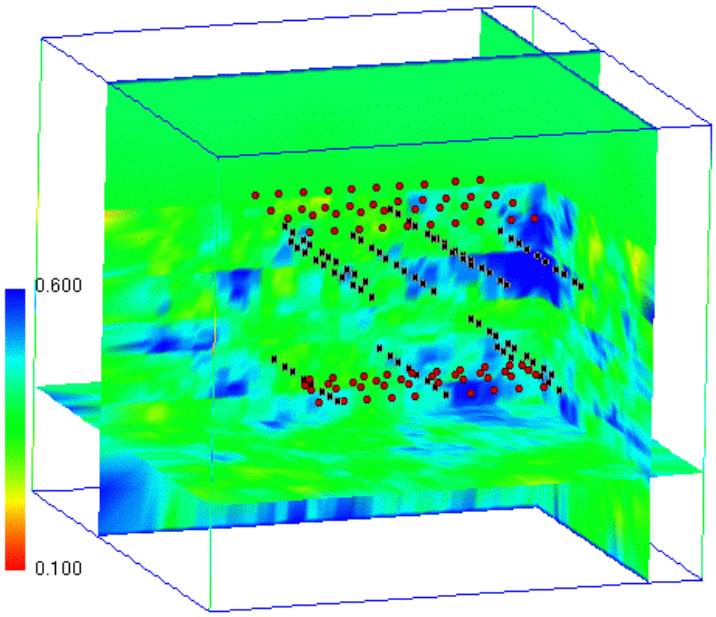

a) Background saturation

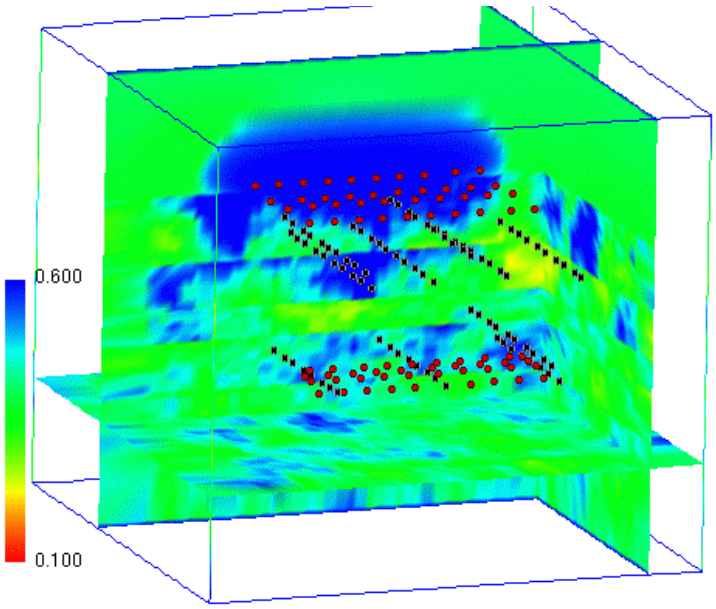

b) Saturation profile after 1 yr of injection

Figure 59. Saturation Profiles. These saturation profiles are from 10 to 60% of the heterogeneous Realization 1: a) background saturation and b) saturation profile after 1 yr of injection. In the figure, injection points are red dots and collection points are blue dots. (Refer to M&O/YMP files: bg.10002_sca_node.inp, generated on July 15, 1998, and inject.10002_sca_node.inp, generated on July 15, 1998.)

caveat in these modeling results is the effect of physical heterogeneities within each layer. Small-scale heterogeneities could result in preferential flow paths, which results in faster flow paths in some parts of the block and slow flow paths in other parts of the block. In the future, Monte Carlo simulations and more elegant stochastic techniques will be employed to attempt to capture the uncertainty in the travel times.

More uncertainty exists in the predicted travel times of the reactive tracers when compared with the conservative-tracer predictions. The strongly sorbing tracers manganese and cobalt (or nickel) are not expected to breakthrough within the first year of testing. Even weakly sorbing lithium only reaches a few collection boreholes. Therefore, an additional year of operation may be required to achieve transport distances that reach more sampling points. At this stage, it is important to note that the model is extremely sensitive to the values of K_d used, which are preliminary. In addition, a linear-K_d model may not be sufficient to model sorption of these tracers due to chemical heterogeneities and nonlinear reactions. More rigorous reactive transport models will be used in the future to check the linear-K_d assumption. Finally, these immobile reactive tracers may sorb onto colloids, thereby enhancing their mobility.

Table 29. Fluorescein from Upper Injection Boreholes with Physical Heterogeneities.
(Refer to M&O/YMP files: real1.trc, generated July 13, 1998, and real2.trc, generated July 12, 1998.)

	5% breakthrough concentration		50% breakthrough concentration		Normalized concentration at 1 yr	
Borehole	**Realiz. 1**	**Realiz. 2**	**Realiz. 1**	**Realiz. 2**	**Realiz. 1**	**Realiz. 2**
16	28 days	36 days	70 days	106 days	1.0	0.96
17	70 days	60 days	238 days	161 days	0.7	0.91
14	173 days	170 days	$>$ 1 yr	$>$ 1 yr	0.35	0.38
15	126 days	126 days	278 days	267 days	0.72	0.76
13	118 days	142 days	247 days	347 days	0.80	0.54
12	222 days	247 days	$>$ 1 yr	$>$ 1 yr	0.42	0.29
Remaining collection boreholes	$>$ 1 yr		$>$ 1 yr	$>$ 1 yr	0.0	0.0

Table 30. Fluorescein from Lower Injection Boreholes with Physical Heterogeneities.
(Refer to M&O/YMP files: real1.trc, generated July 13, 1998, and real2.trc, generated July 12, 1998.)

	5% breakthrough concentration		50% breakthrough concentration		Normalized concentration at 1 yr	
Borehole	**Realiz. 1**	**Realiz. 2**	**Realiz. 1**	**Realiz. 2**	**Realiz. 1**	**Realiz. 2**
46	4 days	4 days	37 days	32 days	1.0	1.0
48	24 days	22 days	106 days	96 days	0.97	0.98
9	52 days	47 days	156 days	$>$ 1 yr	0.94	0.94
10	197 days	202 days	$>$ 1 yr	$>$ 1 yr	0.28	0.26

8. FISCAL YEAR 1999 ACTIVITIES

8.1 Fiscal Year 1999 Workscope

The results from the Busted Butte test will be incorporated into the site-scale transport process model for analysis and model validation for TSPA-LA abstractions of that model. The following represents the YMP statement of work for FY99 for the Busted Butte test as of September 1998:

Conduct UZTT at Busted Butte and assess the validity of key model assumptions important to performance assessment used in the large-scale, UZ site transport process model and probabilistic UZ transport calculations for license application. The principal assumptions of the process model to be tested include but are not restricted to:

1) The migration of colloids in fractured and unfractured Calico Hills rocks under unsaturated conditions to calibrate the UZ colloid model being developed.

2) The field validation of laboratory sorption and transport measurements of the key radionuclides (Pu, Tc, Np, and Am).

3) The effects of heterogeneities in Calico Hills rocks (e.g., fractures and permeability contrasts) on solute migration under unsaturated and partially saturated conditions using a stochastic approach.

4) The validation of the 3-D equivalent-continuum/dual-permeability/discrete-fault representations of the site-scale UZ flow and transport model.

5) The scaling of laboratory, field, and site scales.

6) The updating of scoping calculations, predictive modeling exercises, and model calibration for Phase-2 tests with the results from Phase-1 tests.

7) The laboratory testing with real radionuclides to compare with the analog tracers used in the field.

8) The calibration of the radionuclide transport model for surface-complexation and ion-exchange results from the field tracer tests.

9) The development of structured and unstructured modeling grids for the Phase-2 test block.

This work scope involves four level-4 deliverables and one level-3:

Deliverable ID: SP3492M4.
Deliverable Title: Submit new predictions on field test.
Baseline Due Date: February 12, 1999.
Description: 1998 Phase-1 and -2 predictions of reactive and nonreactive tracer transport at Busted Butte contained in milestone SPU85M4 will be updated with new laboratory and field data.
Criteria Statement: This deliverable is complete when three copies of the draft deliverable and associated documentation are submitted to the NEPO for review and acceptance in accordance with Steps 4.5 and 4.6 in “Interim Direction for Document Development” (interoffice correspondence LV.NEPO.PP.LRH.07/98-083). Acceptance of the deliverable occurs when the technical review conducted by NEPO has been satisfactorily concluded, the final (concurrence) version of the deliverable has been signed by the NEPO Technical Lead, and the approved deliverable has been submitted to Document Control for controlled distribution in accordance with Steps 4.10 through 6.1 in “Interim Direction for Document Development.” Transmittal of the controlled version of the deliverable to the author constitutes notification of acceptance.

Deliverable ID: SP3494M4
Deliverable Title: Submit UZ Transport Data Feed to PA Model
Baseline Due Date: February 12, 1999
Description: Submit to the technical database (TDB) all relevant field and laboratory data collected from October 1998 through January 1999. This deliverable is complete when the technical lead has verified submittal to the TDB.

Deliverable ID: SP33L6M4
Deliverable Title: Draft LA UZ Transport Testing Status
Baseline Due Date: July 15, 1999
Description: This status report will detail the combined results of Test Phases 1 and 2 as well as associated construction activities. The report will also assess the applicability of laboratory data to site transport predictions and present all relevant field and laboratory results and their incorporation into transport model simulations. The report will also document QA procedures used in the testing program. These results will address the migration of colloids in fractured and unfractured Calico Hills rocks under unsaturated conditions, the field validation of laboratory sorption measurements, and the effects of heterogeneities in Calico Hills rocks (e.g., fractures and permeability contrasts) on solute migration under unsaturated and partially saturated conditions. Recommendations for performance-confirmation testing will be presented.
Criteria Statement: This deliverable is complete when three copies of the draft deliverable and associated documentation are submitted to the NEPO for review and acceptance in accordance with Steps 4.5 and 4.6 in "Interim Direction for Document Development" (interoffice correspondence LV.NEPO.PP.LRH.07/98-083). Acceptance of the deliverable occurs when the technical review conducted by NEPO has been satisfactorily concluded, the final (concurrence) version of the deliverable has been signed by the NEPO Technical Lead, and the approved deliverable has been submitted to Document Control for controlled distribution in accordance with Steps 4.10 through 6.1 in "Interim Direction for Document Development." Transmittal of the controlled version of the deliverable to the author constitutes notification of acceptance.

Deliverable ID: SP3497M4
Deliverable Title: Submit UZ Transport Data Feed 2 to PA Model
Baseline Due Date: June 15, 1999
Description: Submit to the TDB all relevant field and laboratory data collected from February 1999 through May 1999. This deliverable is complete when the technical lead has verified submittal to the TDB.

Deliverable ID: SPU87M3
Deliverable Title: Submit UZ Transport Test Status Report
Baseline Due Date: September 30, 1999.
Criteria Statement: The status report will detail the combined results of Test Phases 1 and 2 as well as associated construction activities. The report will also assess the applicability of laboratory data to site transport predictions and present all relevant field and laboratory results and their incorporation into transport model simulations. The report will also document QA procedures used in the testing program. These results will provide a direct feed into the TSPA transport-model level-2 deliverable by addressing, specifically, results associated with the migration of colloids in fractured and unfractured Calico Hills rocks under unsaturated conditions, the field validation of laboratory sorption measurements, and the effects of heterogeneities in Calico Hills rocks (e.g., fractures and permeability contrasts) on solute migration under unsaturated and partially saturated conditions. Recommendations for performance-confirmation testing will be presented. This deliverable will be prepared in accordance with OCRWM-approved quality-assur-

ance procedures implementing requirements of the QARD. Qualified (Q) and non-Q data used and cited in this deliverable will be appropriately noted and clearly identified. Every effort will be made to assure that Q data are used in this deliverable as specified in Supplement III, Section 2.5, Data Usage, of the current revision of the QARD. Technical data contained within the deliverable and not already incorporated in the Geographic Nodal Information Study and Evaluation System (GENISES) will be submitted, if appropriate, for incorporation into GENISES in accordance with YAP-SIII.3Q. Verification of technical data submittal compliance will be demonstrated by including as part of the deliverable: 1) a copy of the Technical Data Information Form generated identifying the data in the Automated Technical Data Tracking System and 2) a copy of the transmittal letter attached to the technical data transmittal to the GENISES Administrator. Record accession numbers and Automated Data Tracking numbers will be included, as appropriate, for all data used and/or cited in this deliverable.

8.2 Construction

Construction activities for fiscal year 1999 will be principally associated with the recovery of Phase-1 test samples and test-characterization activities. The work, involving Phase 1A and Phase 1B, will be associated with mineback, augering, and overcoring activities. Phase-1A mineback is due to begin in early October 1998. Phase-1B mineback and/or overcoring is due to begin in mid to late October 1998. No construction actvities are planned for Phase 2.

Some construction activities may involve the recovery of a 1 m^3 block of CHn material for use in bench testing by AECL. This activity will involve drilling and mineback activities in late October and early November 1998.

8.3 Predictive Modeling

Several new predictions are scheduled for the Phase-2 test block in fiscal year 1999 based on updated hydrologic, mineralogic, and transport databases from Phase-1 testing. These calculations will involve sensitivity analyses and stochastic and Monte Carlo simulations of flow and transport for the Busted Butte Phase-2 test block. These predictions are to be submitted as Level-4 milestones in February, June, and September of 1999.

8.4 Laboratory Studies

Core samples recovered from the fiscal year 1998 boreholes and fiscal year 1999 mineback, auger, and overcoring activities will be tested in the laboratory to determine hydrologic, geochemical, and mineralogic properties of the test block. These laboratory tests will allow the use of scoping calculations in planning the test (e.g., borehole configuration and injection sequences and volumes). The mineralogical characterization of the block will serve to link the Busted Butte test results to process model predictions at and near the potential repository system at Yucca Mountain. The hydrologic characterization will involve the determination of the hydrologic properties of the test block and scaling of the nonlinear dependence of those properties with fluid injection or percolation rates. The geochemical laboratory work will aim to establish the relation between the actual radionuclides expected in the repository inventory and the analogs used in the field tests.

8.4.1 Mineralogy/petrology

Further characterization of the Busted Butte core samples used in sorption and hydrologic laboratory characterization studies is expected in fiscal year 1999. This work will help interpret the results and assess the role of mineralogical heterogeneities on the physical and transport properties of the Calico Hills UZ barrier. All samples analyses will be “Q” and entered into the YMP database by June 1999.

8.4.2 Hydrology

Up to 75 samples from the Busted Butte test area are to be characterized by the U.S. Geological Survey (USGS) (L. Flint) using the UFA and other methodologies. All samples will be "Q" and entered into the YMP database by June 1999. This large number of samples will allow for true stochastic modeling and analysis of Phase-2 tests, to be incorporated into our overall understanding of flow and transport in the UZ for TSPA-LA. Splits of these samples will be used in Min/Pet and transport laboratory experiments to complete the YMP database on UZ properties.

8.4.3 Geochemistry and transport

We will study the migration of radionuclides and nonradioactive analogs to waste elements through tuff samples under a variety of conditions in the laboratory. The experiments are intended to investigate the effects of kinetics, dispersion, diffusion, and speciation on the transport of radionuclides, which could alter the level of detail required to model repository performance. The experiments to be performed range in complexity from crushed tuff, in which the tuff is nearly identical in composition and physical form to tuff samples used in batch-sorption experiments and hydrodynamic dispersion is minimal, to fractured tuff columns, in which the transport is affected by channeling, matrix diffusion, and the processes affecting transport in the crushed tuff columns. In addition, we hope to collaborate on bench tests on radionuclide transport through a 1-m^3 tuff block to be recovered in the fall of fiscal year 1999 from the Phase-1A test area at Busted Butte.

8.5 Tomographic Techniques

As in fiscal year 1998, tomographic techniques will be used in fiscal year 1999 to ascertain the state of saturation and the degree of heterogeneity of the Phase-2 test block. Neutron logging will be combined with GPR and ERT to cross-calibrate the techniques and solidify the geophysical results. A report on the tomographic results will be included in the June 1999 milestone.

9. REFERENCES

Altman, S.J., B.W. Arnold, C.K. Ho, S.A. McKenna, R.W. Barnard, G.E. Barr, and R.E. Eaton. 1996. Flow calculations for Yucca Mountain groundwater travel time (GWTT-95). Sandia National Laboratories technical report SAND96-0819. (YMP TIC # 226629)

Bard, Y. 1974. *Nonlinear Parameter Estimation*, pp. 111–113. New York, NY: Academic Press.

Bodvarsson G.S., T.M. Barndurraga, and Y.S. Wu, editors. 1997. The site-scale unsaturated-zone model of Yucca Mountain, Nevada, for the viability assessment. Lawrence Berkeley National Laboratory technical report LBNL-40378.

Bussod, G.Y., B.A. Robinson, D.T. Vaniman, D.E. Broxton, and H.S. Viswanathan. 1997. UZ transport test plan: Demonstration of the applicability of laboratory data to repository transport calculations: Field-scale experiments to study radionuclide transport at Yucca Mountain. Los Alamos National Laboratory technical report YMP Milestone SP343TM4.

Bussod, G.Y., B.A. Robinson, A.V. Wolfsberg, C.W. Gable, and H.S. Viswanathan. 1998. An integrated UZ flow and transport model for Yucca Mountain, Nevada, U.S.A. In *Synthesis and Proceedings from the GEOTRAP II NEA Project Workshop on Modeling the Effects of Spatial Variability on Radionuclide Migration, Paris, France, June 9–11, 1997*, pp. 165–192.

Carey, J.W., S.J. Chipera, D.T. Vaniman, and D.L. Bish. 1998. Three-dimensional mineralogic model of Yucca Mountain, Nevada, Rev. 2.0. Los Alamos National Laboratory report on Yucca Mountain milestone SP32B1M4.

Dagan, G. 1984. Solute transport in heterogeneous porous formations. *Journal of Fluid Mechanics* 145: 151–177. (YMP RIS # NNA.19930215.0048)

Dagan, G. 1989. *Flow and Transport in Porous Formations*. New York, NY: Springer-Verlag. (YMP TIC # 234219)

Flint, L. 1998. Characterization of hydrogeologic units using matrix properties, Yucca Mountain, Nevada. U.S. Geological Survey water-resources investigations report 97-4243, 64 pp. (YMP TIC # 236515 and RIS # MOL.19980429.0512)

Flint, A.L, J.A. Hevesi, and L.E. Flint. 1996. Conceptual and numerical models of infiltration for the Yucca Mountain Area, Nevada. U.S. Geological Survey water-resources investigations report YMP Milestone 3GUI623M. (YMP RIS # MOL.19970409.0087)

Gardner, W.R. 1958. Some steady-state solutions of unsaturated moisture flow equations with application to evaporation from a water table. *Soil Science* 85: 228–232. (YMP TIC # 240150)

Gelhar, L.W., and C.L. Axness. 1983. Three-dimensional stochastic analysis of macrodispersion in aquifers. *Water Resources Research* 19(1): 161–180. (YMP TIC # 222815)

Graham, W., and D. McLaughlin. 1989. Stochastic analysis of nonstationary subsurface solute transport: 2. Conditional moments. *Water Resources Research* 25(11): 2331–2355. (YMP TIC # 239451)

Harter, Th., and T.-C.J. Yeh. 1996a. Stochastic analysis of solute transport in heterogeneous, variably saturated soils. *Water Resources Research* 32(6): 1585–1595.

Harter, Th., and T.-C.J. Yeh. 1996b. Conditional stochastic analysis of solute transport in heterogeneous, variably saturated soils. *Water Resources Research* 32(6): 1597–1609.

Hohmann, G.W. 1988. Numerical modeling for electromagnetic methods in geophysics. In *Electromagnetic Methods in Geophysics*,

Nabighian, M.N., editor. Tulsa, OK: Society of Exploration Geophysics.

Huebner, K.H., and E.A. Thornton. 1982. *The Finite Element Method for Engineers*. New York, NY: John Wiley and Sons. (YMP TIC # 209778)

Kotre, C.J. 1989. A sensitivity coefficient method for the reconstruction of electrical impedance tomograms. *Clinical Physics and Physiological Measurement* 10: 275–281.

Krier, D., P. Longmire, R.H. Gilkison, and H.J. Turin. 1997. Geologic, geohydrologic, and geochemical data summary of MDAG, TA-54. Los Alamos National Laboratory document LA-UR-95-2696.

LaBrecque, D.J. 1989. Cross-borehole resistivity modeling and model fitting. Ph.D. thesis, University of Utah, Salt Lake City, UT.

LaBrecque, D.J., M. Milleto, W. Daily, A. Ramirez, and E. Owen. 1996. The effects of noise on Occam's inversion of resistivity tomography data. *Geophysics* 61(2): 538–548.

Mackie R.L., and T.R. Madden. 1993. Three-dimensional magnetotelluric inversion using conjugate gradients. *Geophysical Journal International* 115: 215–229.

Mantoglou, A. 1992. A theoretical approach for modeling unsaturated flow in spatially variable soils: Effective flow models in finite domains and nonstationarity. *Water Resources Research* 28(1): 251–267.

Mantoglou, A., and L.W. Gelhar. 1987. Stochastic modeling of large-scale transient unsaturated flow systems. *Water Resources Research* 23(1): 37–46. (YMP TIC # 223510)

Neuman, S.P., C.L. Winter, and C.M. Newman. 1987. Stochastic theory of field-scale Fickian dispersion in anisotropic porous media. *Water Resources Research* 23(3): 453–466. (YMP TIC # 225294)

Pini, G., and G. Gambolati. 1990. Is a simple diagonal scaling the best preconditioner for conjugate gradients on supercomputers? *Advances in Water Resources* 13: 147–153.

Pridmore, D.F., G.W. Hohmann, S.H. Ward, and W.R. Sill. 1981. An investigations of finite-element modeling for electical and electromagnetic data in three dimensions. *Geophysics* 46: 1009–1024. (YMP TIC # 239438)

Qin, J. 1995. Three-dimensional DC resistivity forward and inversion by finite-element method. Ph.D. dissertation, University of Arizona, Tucson, AZ.

Rodi, W.L. 1976. A technique for improving the accuracy of finite-element solutions for magnetotelluric data. *Geophysics Journal of the Royal Astronomical Society* 44: 483–506.

Rubin, Y. 1990. Stochastic modeling of macrodispersion in heterogeneous media. *Water Resources Research* 26(1): 133–142.

Russo, D. 1988. Determining soil hydraulic properties by parameter estimation: On the selection of a model for the hydraulic properties. *Water Resources Research* 24: 453–459.

Russo, D. 1993. Stochastic modeling of macrodispersion for solute transport in a heterogeneous unsaturated porous formation. *Water Resources Research* 29: 383–397.

Russo, D. 1995a. On the velocity covariance and transport modeling in heterogeneous anisotropic porous formations: 2. Unsaturated flow. *Water Resources Research* 31: 139–145.

Russo, D. 1995b. Stochastic analysis of the velocity covariance and the displacement covariance tensors in partially saturated heterogeneous

anisotropic porous formations. *Water Resources Research* 31: 1647–1658.

Sasaki, Y. 1992. Resolution of resistivity tomography inferred from numerical simulation. *Geophysical Prospecting* 40: 453–463.

Schenker, A.R., D.C. Guerin, T.H. Robey, C.A. Rautman, and R.W. Barnard. 1995. Stochastic hydrogeologic units and hydrogeologic properties development for total-system performance assessments. Sandia National Laboratories report SAND94-0244 (September). (YMP TIC # 236084)

Scott, R.B., and J. Bonk. 1984. Preliminary geologic map of Yucca Mountain, Nye County, Nevada, with geologic sections (1:12,000). U.S. Geological Survey open-file report 84-494, 9 pp. plus 1:24,000 map. (YMP TIC # 203162)

Soll, W.E. 1998. Busted Butte field experiment: Phase 1, a blind prediction: Deterministic model. Los Alamos National Laboratory white paper.

Sub Terra, Inc. 1998. Design report for the UZ Transport Test, Busted Butte Test Facility. Project Number: 97-35, July 20, 1998, for TRW Environmental Safety Systems. Las Vegas, NV: TRW Environmental Safety Systems.

Tikhonov, A.N., and V.Y. Arsenin. 1977. *Solutions of Ill-posed Problems*, J. Fritz, editor. New York, NY: John Wiley and Sons.

van Genuchten, M.T. 1980. A closed-form equation for predicting the hydraulic conductivity of unsaturated soils. *Soil Science Society of America Journal* 44: 892–898. (YMP TIC # 217327)

Wannamaker, P.E., J.A. Stodt, and L. Rijo. 1987. PW2D finite-element program for solution of magnetotelluric responses of two-dimensional Earth resistivity structure. University of Utah Research Institute, Earth Science Laboratory report ESL-158 (DOE/SAN/12196-13).

Winter, C.L., C.M. Newman, and S.P. Neuman. 1984. A perturbation expansion for diffusion in a random velocity field. *SIAM Journal on Applied Mathematics* 44(2): 411–424.

Yeh, T.-C., L.W. Gelhar, and A.L. Gutjahr. 1985a. Stochastic analysis of unsaturated flow in heterogeneous soils: 1. Statistically isotropic media. *Water Resources Research* 21: 447–456. (YMP TIC # 216857)

Yeh, T.-C., L.W. Gelhar, and A.L. Gutjahr. 1985b. Stochastic analysis of unsaturated flow in heterogeneous soils: 2. Statistically anisotropic media with variable α. *Water Resources Research* 21: 457–464. (YMP TIC # 239649)

Zhang, D. 1998. Nonstationary stochastic analysis of transient unsaturated flow in randomly heterogeneous media. *Water Resources Research*, under review.

Zhang, D.X., and S.P. Neuman. 1995. Eulerian-Lagrangian analysis of transport conditioned on hydraulic data: 1. Analytical-numerical approach. *Water Resources Research* 31(1): 39–51.

Zhang, D.X., and S.P. Neuman. 1996a. Head and velocity covariances under quasi-steady-state flow and their effects on advective transport. *Water Resources Research* 32(1): 77–83.

Zhang, D.X., and S.P. Neuman. 1996b. Effect of local dispersion on solute transport in randomly heterogeneous media. *Water Resources Research* 32(9): 2715–2723.

Zhang, D.X., and C.L. Winter. 1998. Nonstationary stochastic analysis of steady-state flow through variably saturated, heterogeneous media. *Water Resources Research* 34(5): 1091–1100.

Zhang, D.X., T.C. Wallstrom, and C.L. Winter. 1998. Stochastic analysis of steady-state unsaturated flow in heterogeneous media: Comparison of

the Brooks-Corey and Gardner-Russo models. *Water Resources Research* 34(6): 1437–1449.

Zyvoloski, G.A., B.A. Robinson, Z.V. Dash, and L.L. Trease. 1995. Models and methods summary for the FEHMN application. Los Alamos National Laboratory report LA-UR-94-3787, Rev. 1. (YMP TIC # 222337)

APPENDIX A: CHRONOLOGY OF FISCAL YEAR 1998 ACTIVITIES

To initiate field activities for the unsaturated-zone transport test (UZTT) at Busted Butte, a number of documents and steps needed to be completed and approved, including permits, safety evaluations and construction, design, and scientific requirements. The chronology of events leading to the initiation of testing is as follows:

Permits and Safety Analyses:

1. The YMP Land Access/Environmental Compliance Request Transmittal. Submitted and signed by DOE on September 29, 1997, as required by YAP-30.2.

2. The YMP Field Operations Permit. Completed and signed on October 29, 1997.

3. The Determination of Importance Evaluation (DIE) for the UZTT at Busted Butte. Conducted and included in the DIE for ESF Subsurface Testing Activities, October 29, 1997.

4. A Medical Needs Analysis for the UZTT at Busted Butte for road improvements and highwall/pad construction. Completed on October 31, 1997.

5. The Transmittal of Design and Test Related Information (TD&TRI) for Design and Construction at Busted Butte. Sent to the Registered Professional Engineer who is doing the construction configuration on November 4, 1997. The TD&TRI was provided by the Principal Investigator to the TCO on November 3, 1997.

6. Partial Approval of Land Access and Environmental Compliance for Busted Butte. Obtained from DOE on November 6, 1997, for road improvements only.

7. Job Safety Analyses (2) associated with testing. Completed on November 10, 1997.

8. Erionite survey and analyses conducted at Busted Butte by Los Alamos scientists. Documented in a position paper entitled "Survey of potential erionite horizons at the Busted Butte UZ Transport Test locality," dated November 12, 1997.

9. A Preliminary Hazard Analysis addressing safety aspects of the Busted Butte project. Completed on November 13, 1997.

10. Land Access and Environmental Compliance for Pad Construction and Excavation at Busted Butte Drift. Approval obtained from DOE on November 21, 1997.

11. Application to permit use of tracers in Phase 1 of the UZTT at Busted Butte. Submitted to M&O Environmental on November 21, 1997.

12. Application to permit use of tracers in Phases 2 and 3. Submitted December 29, 1998.

13. GET Training Class. Completed January 29, 1998.

14. GUT Training Class. Completed February 6, 1998.

15. Phase-1 tracer usage. Approval received on March 3, 1998.

16. Application to permit use of tracers in Phase 2. Resubmitted on May 4, 1998.

17. Phase-2 tracer usage. Approval received on June 11, 1998.

18. Modification of permit application for increased mass of tracers. Submitted on July 13, 1998.

19. Modified Phase-2 tracer usage. Approval received on August 13, 1998.

Construction and Test Installation Activities:

1. Gate 25-4P. Relocated through DOE NVO Security and the FOC on November 5, 1997, to allow access to the Busted Butte site.

2. Access Road. Started on November 7, 1997.

3. Highwall/Pad Construction Configuration. Completed by a Registered Professional Engineer, Chris Breeds, on November 14, 1997.

4. Access Road. Completed on November 14, 1997.

5. Highwall/Pad Construction. Started on November 24, 1997, including the rimrock impact-hazard barrier wall and pad.

6. Highwall/Pad Construction. Completed on December 18, 1998.

7. Underground excavation. Started on December 18, 1998, including portal and excavation of Main Adit.

8. Main Adit, 75 m in length. Completed on January 21, 1998.

9. Test Alcove, 19 m in length. Completed on January 30, 1998.

10. Test borehole surveys. Started February 4, 1998.

11. Test borehole coring. Completed on March 19, 1998, including six ERT holes, 16 injection boreholes, and twelve collection boreholes.

12. Inventory of Q samples from test boreholes by SMF. Completed March 19, 1998.

13. Phase-1A instrument installation. Completed April 2, 1998.

14. Phase-1B instrument installation. Completed May 12, 1998.

15. Short surface ERT hole coring and electrode installation. Completed June 8, 1998.

16. Phase-2A instrument installation. Completed July 23, 1998.

17. Phase-2B instrument installation. Completed July 30, 1998.

18. Phase-2C instrument installation. Completed August 5, 1998.

Test Implementation and Scientific Activities

1. Busted Butte reconnaissance GPS mapping and sample collection. October, 8, 1997.

2. Quantitative XRD sample analyses of samples for erionite presence. Completed October 20, 1997.

3. Collection of additional potential erionite samples. October 28, 1998.

4. Busted Butte GPS mapping and sample collection. November 6–7, 1997.

5. Position Paper on "Survey of potential erionite horizons at the Busted Butte UZ Transport Test locality." Submitted November 12, 1997.

6. Submission of Phase-1 tracer permit application to TCO. November 14, 1997.

7. Preliminary 10′ geologic base map of Busted Butte. Completed November 17, 1997.

8. Quantitative XRD sample analyses results. Completed November 19, 1997.

9. Field Work Package FWP-ESF-97-002, Rev. 0, entitled "UZ Transport Test at Busted Butte." Controlled on November 19, 1997.

10. Phase-1 Tracer permit application to M&O. Submitted November 21, 1997.

11. Busted Butte GPS mapping and sample collection. Completed November 25, 1997.

12. Samples for laboratory hydrologic characterization. Submitted December 8, 1997.

13. Pad/highwall construction field overview. December 11–12, 1997.

14. Portal/Main Adit construction field overview. Completed December 23, 1997.

15. Phase-2 tracer permit application to M&O. Submitted December 23, 1997.

16. EQ3/6-MinTech preliminary model results for analog tracers. Completed December 24, 1997.

17. Results from UFA laboratory hydrology tests. Completed January 13, 1998.

18. GEOMESH of Phase-1 injection borehole. Completed January 13, 1998.

19. Preliminary Burec fracture map of Main Adit. Completed January 28, 1998.

20. Preliminary model simulation results for injection-system design. Completed January 28, 1998.

21. Phase-1 borehole siting. Completed January 30, 1998.

22. Water-chemistry sample collection. Completed January 30, 1998.

23. Preliminary Burec fracture map of Test Alcove. Completed February 6, 1998.

24. Test-design scoping calculations. Completed February 18, 1998.

25. Water-extraction analyses. Completed February 23, 1998.

26. Air-permeability testing. Completed March 4, 1998.

27. Phase-2 collection-borehole siting. Completed March 11, 1998.

28. Phase-1 borehole surveys. Completed March 13, 1998.

29. Phase-1 borehole video logging. Completed March 19, 1998.

30. Phase-1 borehole neutron logging. Completed March 25, 1998.

31. Stratigraphic mapping of test-block Main Adit and Test Alcove faces. Completed March 27, 1998.

32. Laboratory transport experiments. Initiated March 30, 1998.

33. Phase-1A injection. Started on April 2, 1998.

34. Phase-2 injection-borehole surveys. Completed April 15, 1998.

35. Sequential installation of Phase-1B injection systems. Completed April 20, 1998.

36. GPR survey of Phase-1B boreholes. Completed April 20, 1998.

37. Phase-2 GPR measurements, boreholes 48–46. Completed August 25, 1998.

38. Phase-2 injection-borehole video logging. Completed April 22, 1998.

39. Phase-2 injection-borehole neutron logging. Completed April 29, 1998.

40. Phase-1B injection. Started on May 12, 1998.

41. Phase-2 collection-borehole surveys. Completed May 19, 1998.

42. Phase-2 collection-borehole video logging. Completed May 27, 1998.

43. Phase-2 collection-borehole neutron logging. Completed June 6, 1998.

44. Baseline GPR on Phase-2 collection holes. Completed June 11, 1998.

45. Phase-2 ERT cross-hole tomography installation. Completed June 12, 1998.

46. Phase-1B initial tracer breakthrough. Observed on June 16, 1998.

47. Phase-2 GPR measurements, Boreholes 19–22. Completed June 20, 1998

48. Phase-2 ERT baseline measurements. Completed on July 2, 1998.

49. Initial Phase-2 predictive simulations. Submitted to M&O July 15, 1998.

50. Baseline GPR on Phase-2 Injection Holes 19 and 22. Completed July 20, 1998.

51. Phase-2A injection-system installation. Completed July 22, 1998.

52. Phase-2A injection. Started July 23, 1998.

53. Phase-2 collection-system installation. Completed July 29, 1998.

54. Phase-2B injection-system installation. Completed July 30, 1998.

55. Phase-2B injection. Started July 30, 1998.

56. Phase-2C injection-system installation. Completed August 4, 1998.

57. Phase-2C injection. Started August 5, 1998.

58. Phase-2B initial tracer breakthrough. Observed August 6, 1998.

59. Phase-2 GPR measurements, Boreholes 48–46. Completed August 25, 1998.

60. Phase-2 injection of reactive ionic tracers. Started September 2, 1998.

61. Phase-2 GPR measurements, Boreholes 46–9, 46–16, 15–13. Completed September 2, 1998.

APPENDIX B: DATALOGGERS CONTROL INFORMATION

This appendix presents additional information about the Campbell Scientific dataloggers.

System Checks

The following system checks are performed by the datalogger:

- Low pressure in either the membrane-injection or the membrane-sampling manifolds. The code sets a flag for the user if a low pressure is measured.

- Low battery voltage. The code sets a flag for the user if low voltage is measured, as well as suspends data collection so that all remaining power is used to save stored data.

- Continuous cycling of any of the injection pumps. If a problem is detected, the datalogger will suspend injection of the tracer fluid. Flags will be set to alert the user if any of the pulse counters have detected a problem.

- Incompatibility between the user-defined output interval and the injection intervals. The desire is to have the relative saturation at the injection points be measured directly after an injection has taken place. Thus, the pump-injection rates and the output interval must be compatible. If they are not, the code sets a flag.

Datalogger Control Panel and Setup

Figure B-1 shows a sketch of the instrumentation control panel with the Campbell scientific 23X datalogger. The moisture sensors are connected to six Campbell Scientific AM416 Relay Multiplexers (for a total of 192 single-ended input channels). The load cells and pressure transducers are connected to a seventh multiplexer. The multiplexers are controlled via the control ports on the 23X (all 8 ports are used). An HMP35C relative-humidity/temperature probe is the only sensor connected directly to the front panel of the 23X. The number of times the banks of syringe pumps cycle are counted via three pulse ports on the 23X. The remaining pulse port is used to measure the output of the anemometer (wind speed in the ventilation ducts). The syringe pumps are controlled via the two continuous analog output (CAO) ports. The CAO ports are used to activate relays on the relay card. The first CAO port activates a bank of 8 relays (this CAO port will control the injection of the 1- and 10-ml/hr pumps). The second CAO port activates the remaining 4 relays (to control injection of the 50-ml/hr pumps). Of the four excitation channels on the 23X, two are used to control the AM416 relay multiplexers. The remaining two are used to excite the HMP35C relative-humidity/temperature probe.

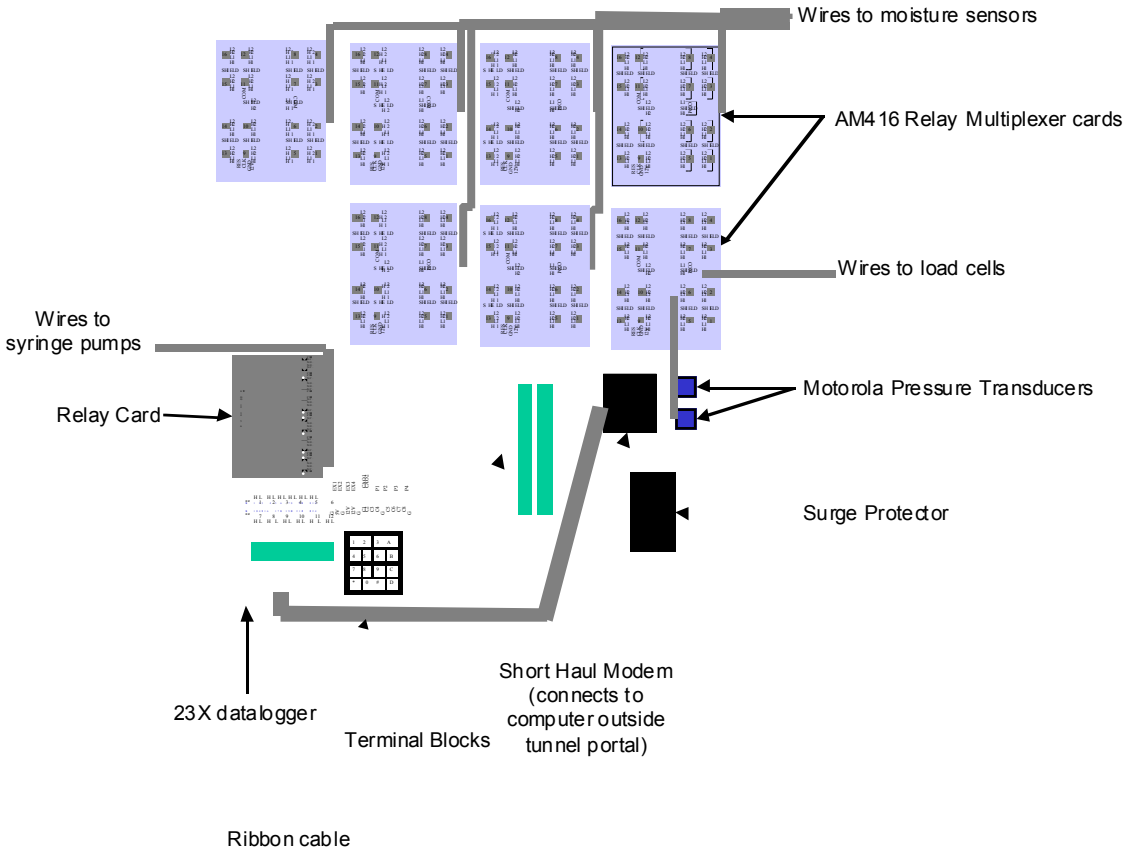

Figure B-1. Datalogger Control. The above schematic summarizes the setup of the control panel and 23X datalogger for the Phase-2 test.

APPENDIX C:
REPORT ON HYDROLOGIC PROPERTIES OF BUSTED BUTTE SAMPLES

UFA Ventures, Inc.

UFA Ventures, Inc.
2000 Logston Boulevard
Richland, Washington 99352
james@ufa.owt.com
(509) 375-3268
FAX 375-4838
http://ufa.owt.com

2/4/98

Gilles Bussod
Wendy Soll
MS F665
Los Alamos National Laboratory
Los Alamos, NM 87545
FAX (505) 665-8737

January Monthly Report

Enclosed are data for six samples, 4 whole rock cores and two recomposites from shavings. All cores were very friable and behaved similarly overall. The seventh core, a non-friable denser, less permeable core is presently being run. All cores were run using the UFA Method for unsaturated hydraulic conductivity, $K(\theta)$, and matric potential, $\psi(\theta)$, or water retention. The first step upon receipt of the cores was to pot them in epoxy resin to the correct diameter and rough cut the ends to the correct length. They were then vacuum-saturated in a vacuum desiccator, and the saturated water content and hydraulic conductivity was measured using a traditional Falling Head method. A synthetic generic vadose zone water was used that closely approximates J-13 well water. However, the composition of the water is not important with respect to $K(\theta)$ or $\psi(\theta)$ unless the field composition drastically differs from this water, e.g., brines or distilled water. All water contents are measured by weight at each step in the process to determine the volumetric water content, θ. Then the sample is put into the UFA to determine $K(\theta)$. The first unsaturated point is taken at low rotation speed and high water flux. Again, after steady-state is reached (in hours), the sample is weighed to determine the water content. Then the flux is decreased and/or the rotation speed is increased to desaturate the sample in a step-wise fashion, weighing the sample at the end of each step. This $K(\theta)$ curve measurement takes about 5 days. After the last $K(\theta)$ point is obtained, the sample is resaturated and the $\psi(\theta)$ run is started at 300 rpm (0.04 bar equivalent) with no flux into the sample. The sample drains until equilibrium is reached, then weighed for θ, and then put back on at the next higher speed, up to 10,000 rpm (up to 47 bar equivalent). This takes about 11 days. The attached data gives the $K(\theta)$ and $\psi(\theta)$ results, both as tables and as graphs. The shape of the curves reflect texture and structure with respect to pore size and distribution. Recompositing cores SPC 7049 and SPC 7048 did affect the behavior noticeably by altering the average pore size and distribution.

SPC 7050 vertical was a whole rock core having a dry bulk density of 1.57 and a total porosity of 51%. The saturated K was 3.85×10^{-4} cm/s.

SPC 7049 vertical was a whole rock core having a dry bulk density of 1.4 g/cm^3 and a total porosity of 64%. The saturated K was 5.61×10^{-4} cm/s. A disaggregated portion of the

core was also run as a recomposite core. The density and the porosity were extremely different, 1.03 g/cm^3 and 45%, but the saturated K was very close, 3 x 10^{-4} cm/s. The residual water contents were also very different in both the $K(\theta)$ and $\psi(\theta)$ relationships, with the recomposite having lower water contents by at least 10% of the total volume. In general, recomposition tended to average the pore sizes, remove the largest and smallest pores and made the curves look like a better sorted material, especially in $\psi(\theta)$. Therefore, the internal structure of this unit is critical to the transport properties in the field.

SPC 7048 vertical was a whole rock core having a dry bulk density of 1.08 g/cm^3 and a total porosity of almost 50%. The saturated K was 1.13 x 10^{-3} cm/s. SPC 7048 horizontal was a whole rock subcore of the same unit having a dry bulk density of 1.14 g/cm^3 and a total porosity of almost 56%. The saturated K was almost identical to the vertical core, 2.51 x 10^{-3} cm/s. The shape of the $K(\theta)$ curve suggests better pore size sorting in the horizontal direction, consistent with the emplacement mode of the rock. The residual water contents were slightly higher in the horizontal core. A disaggregated portion of the core was also run as a recomposite and its behavior was similar to the vertical whole rock core, although there was significantly less structure to the $K(\theta)$ curve. The density and the porosity were close to the vertical core, 1.02 g/cm^3 and 48%, and the saturated K was slightly lower, 8 x 10^{-4} cm/s. The residual water contents were significantly lower in both the $K(\theta)$ and $\psi(\theta)$ relationships, with the recomposite having lower water contents by about 5% of the total volume. Therefore, the internal structure of this unit is not so critical to the transport properties in the field, and the anisotropy is also not very important.

It should be noted that the total porosity is generally quite variable in tuffs, and the same unit can have significant differences only a foot away, and the results for these cores are very consistent with this.

UFA VENTURES/NESTT Client Report

Client/PO#:	LANL/JAKE TURIN				
Client ID:	SPC 7047 vertical		Lab ID:	97-0068	
Time Collected:	unknown		Time Received:	12:00	
Date Collected:	1//7/97		Date Received:	12/10/97	
Receipt Condition:	GOOD				
Run type:	WHOLE ROCK			RockCoreCalcw/F,G,H,&M v2.0.1	
Dry bulk density (g/cm^3):	2.04				
Initial Water Content	By weight %:	3.84%			
	By vol %:	7.86%			

NOTE: The initial water content value was taken at time of receipt at our lab and may or may not reflect the actual field value.

Hydraulic Conductivity Results

Vol moisture content%	K Value (cm/s)	Comments
8.75%	4.03E-09	Gravity Feed Value
8.66%	3.90E-10	

Moisture Potential Results

Vol moisture content%	Matric Pressure (Bar)	Comments
9.55%	0.04	
9.52%	0.17	
9.47%	0.30	
9.41%	0.46	
9.32%	0.67	
9.20%	1.04	
9.04%	1.50	
8.84%	2.04	
8.21%	4.17	
7.84%	7.41	
7.50%	11.58	
7.06%	16.67	
6.71%	22.69	
6.36%	29.64	
6.14%	37.51	
5.95%	46.31	

Comments/Observations:

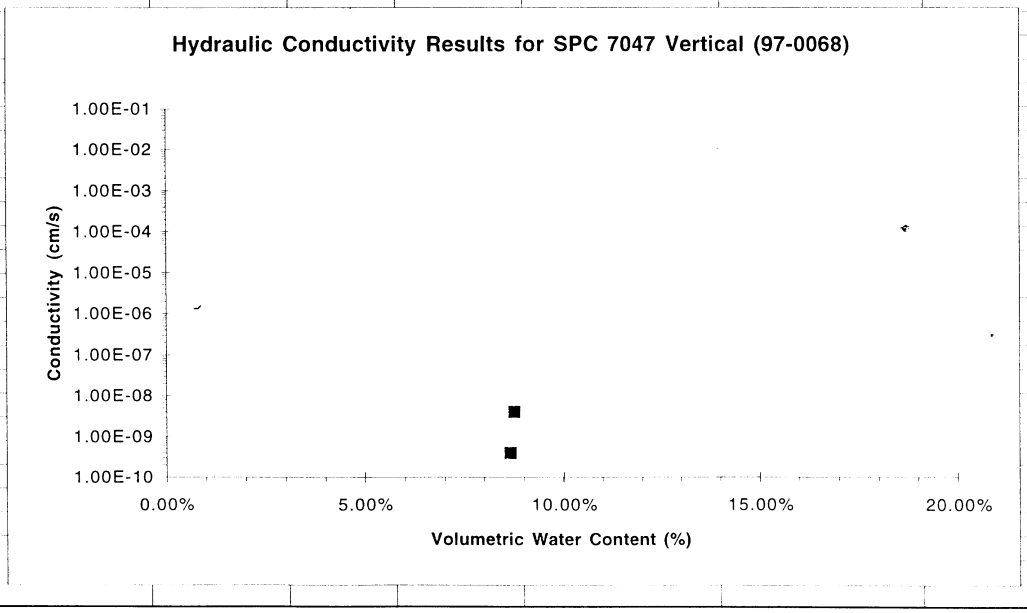

RockCoreCalcw/F,G,H,&M v2.0.3

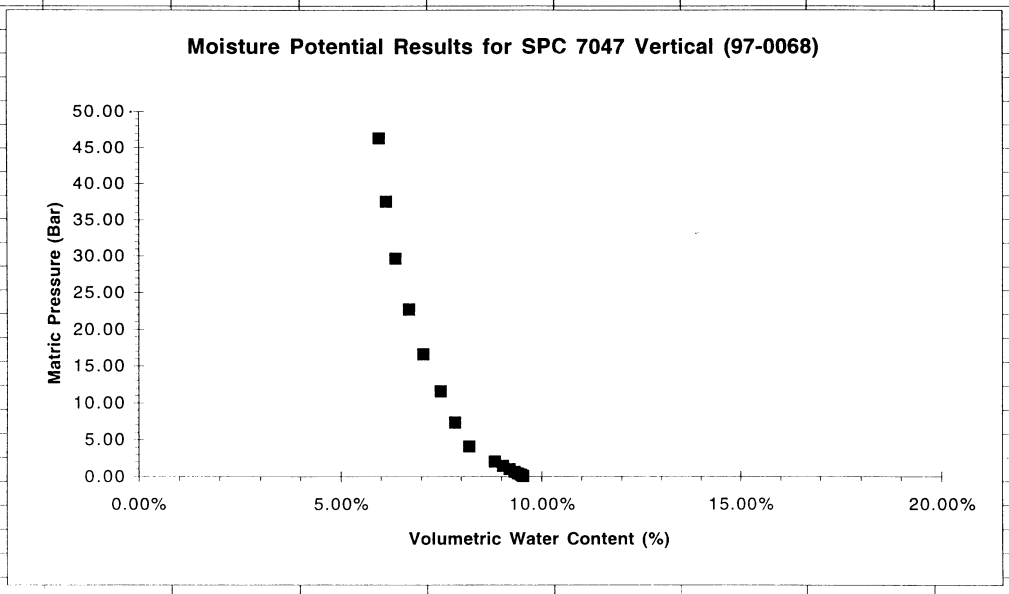

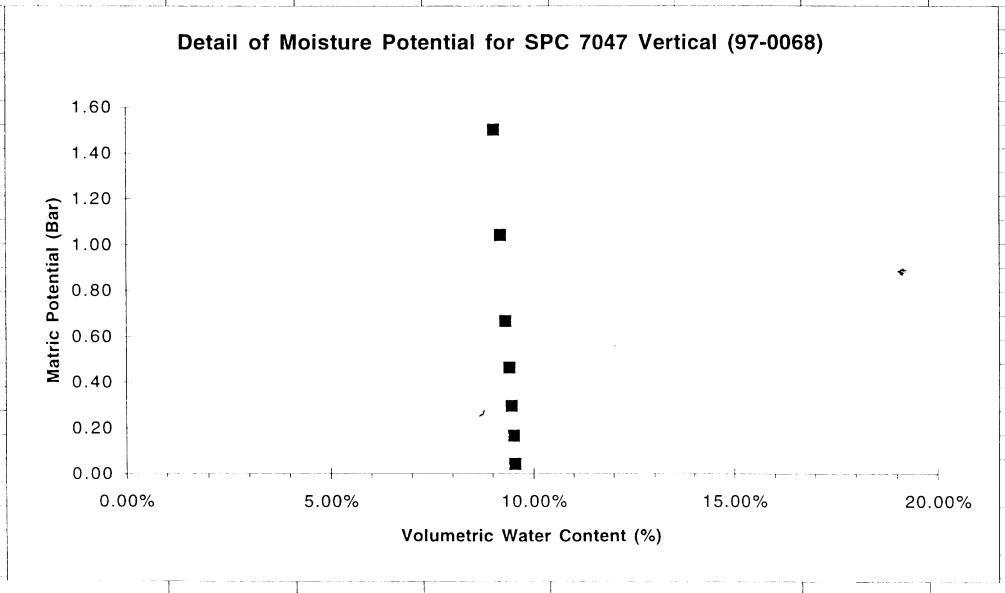

UFA VENTURES/NESTT Client Report

Client/PO#:	LANL/JAKE TURIN				
Client ID:	SPC 7048 vertical		Lab ID:	97-0069	
Time Collected:	unknown		Time Received:	12:00	
Date Collected:	1//7/97		Date Received:	12/10/97	
Receipt Condition:	GOOD				
Run type:	WHOLE ROCK			RockCoreCalcw/F,G,H,&M v2.0.1	
Dry bulk density (g/cm^3):	1.08				
Initial Water Content	By weight %:	2.75%			
	By vol %:	2.98%			

NOTE: The initial water content value was taken at time of receipt at our lab and may or may not reflect the actual field value.

Hydraulic Conductivity Results			**Moisture Potential Results**		
Vol moisture content%	K Value (cm/s)	Comments	Vol moisture content%	Matric Pressure (Bar)	Comments
49.51%	1.13E-03	Falling Head Value	49.05%	0.04	
47.89%	2.07E-04		40.37%	0.17	
46.44%	5.17E-05		32.26%	0.30	
38.13%	1.86E-05		28.44%	0.47	
34.75%	8.27E-06		25.99%	0.67	
31.44%	3.72E-06		23.46%	1.05	
30.90%	1.40E-06		21.96%	1.51	
30.15%	4.65E-07		20.68%	2.05	
26.37%	9.31E-08		19.25%	2.91	
24.52%	3.52E-08		17.34%	4.19	
21.63%	6.00E-09		16.11%	7.45	
20.03%	4.74E-10		15.32%	11.64	
			12.98%	22.82	
			12.63%	29.80	
Comments/Observations:	bottom end of sample fell apart at the higher tensions		11.90%	37.72	
	during the matric potential measurements		11.36%	46.57	

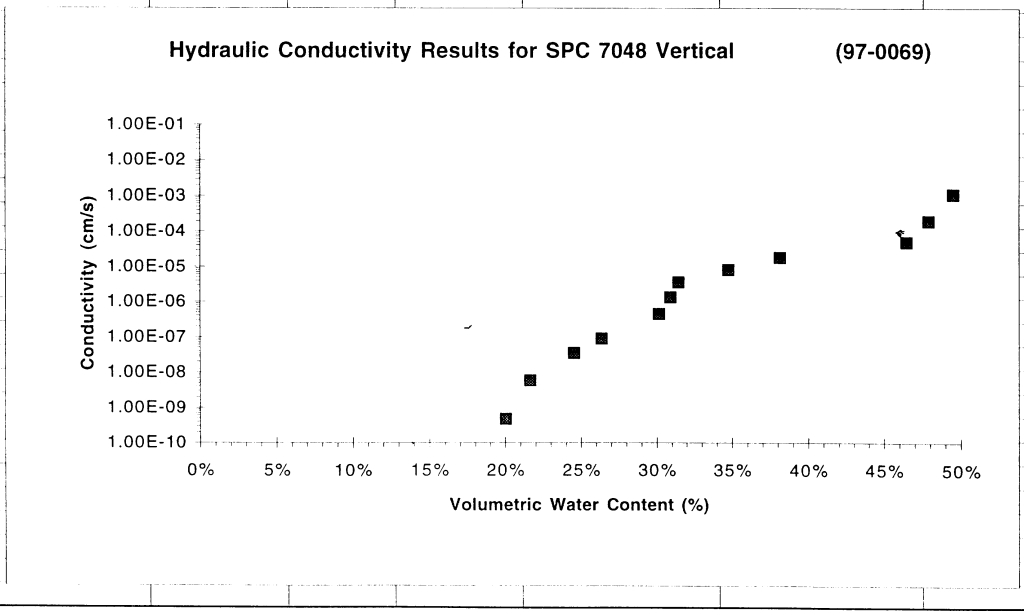

RockCoreCalcw/F,G,H,&M v2.0.3

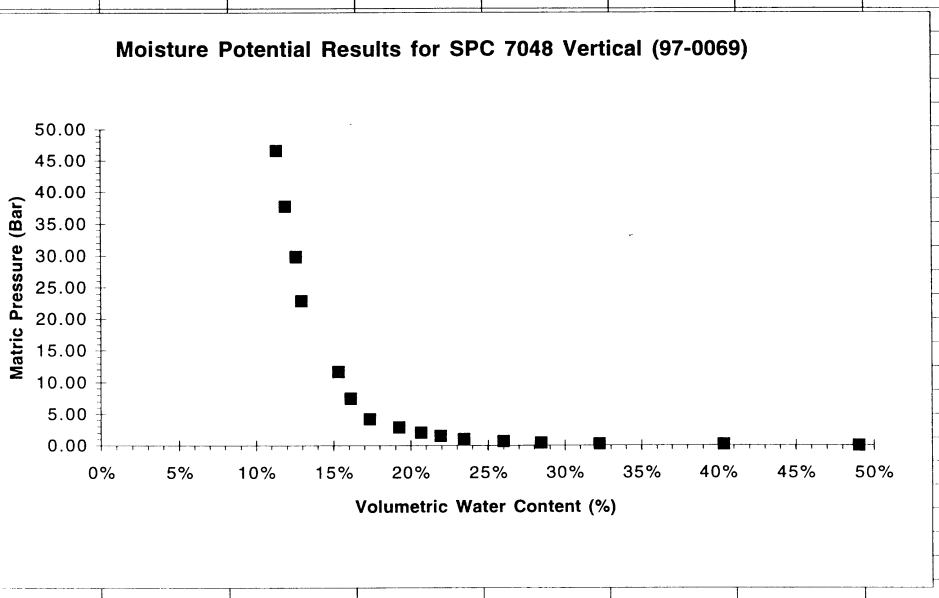

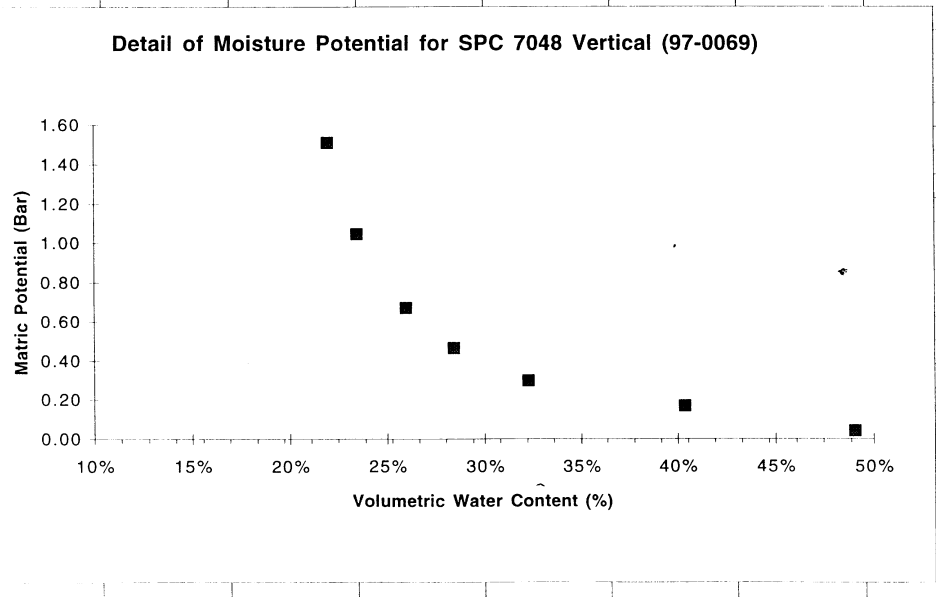

UFA VENTURES/NESTT Client Report

Client/PO#:	LANL/JAKE TURIN				
Client ID:	SPC 7048 horizontal		Lab ID:	97-0070	
Time Collected:	unknown		Time Received:	12:00	
Date Collected:	11/7/97		Date Received:	12/10/97	
Receipt Condition:	GOOD				
Run type:	WHOLE ROCK			RockCoreCalcw/F,G,H,&M v2.0.1	
Dry bulk density (g/cm^3):	1.14				
Initial Water Content	By weight %:	1.24%			
	By vol %:	1.41%			

NOTE: The initial water content value was taken at time of receipt at our lab and may or may not reflect the actual field value.

Hydraulic Conductivity Results			**Moisture Potential Results**		
Vol moisture content%	K Value (cm/s)	Comments	Vol moisture content%	Matric Pressure (Bar)	Comments
56.13%	2.51E-03	Falling Head Value	54.80%	0.03	
55.45%	2.87E-04		43.90%	0.12	
53.10%	7.17E-05		38.08%	0.21	
41.65%	2.58E-05		34.40%	0.33	
37.70%	1.15E-05		31.50%	0.48	
34.58%	5.16E-06		28.48%	0.75	
33.25%	1.93E-06		26.45%	1.08	
31.38%	6.45E-07		24.70%	1.47	
29.35%	1.29E-07		23.18%	2.09	
28.55%	4.88E-08		21.70%	3.01	
24.40%	8.32E-09		19.90%	5.35	
23.20%	6.57E-10		18.80%	6.77	
			17.13%	12.03	
			15.75%	16.37	
Comments/Observations:			14.65%	27.06	
			13.90%	33.41	

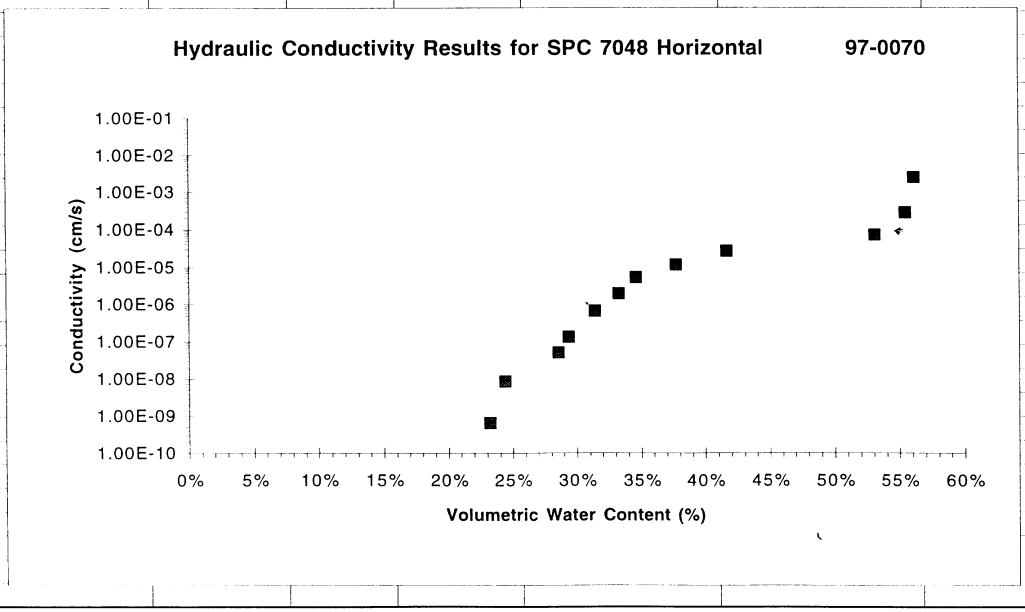

RockCoreCalcw/F,G,H,&M v2.0.3

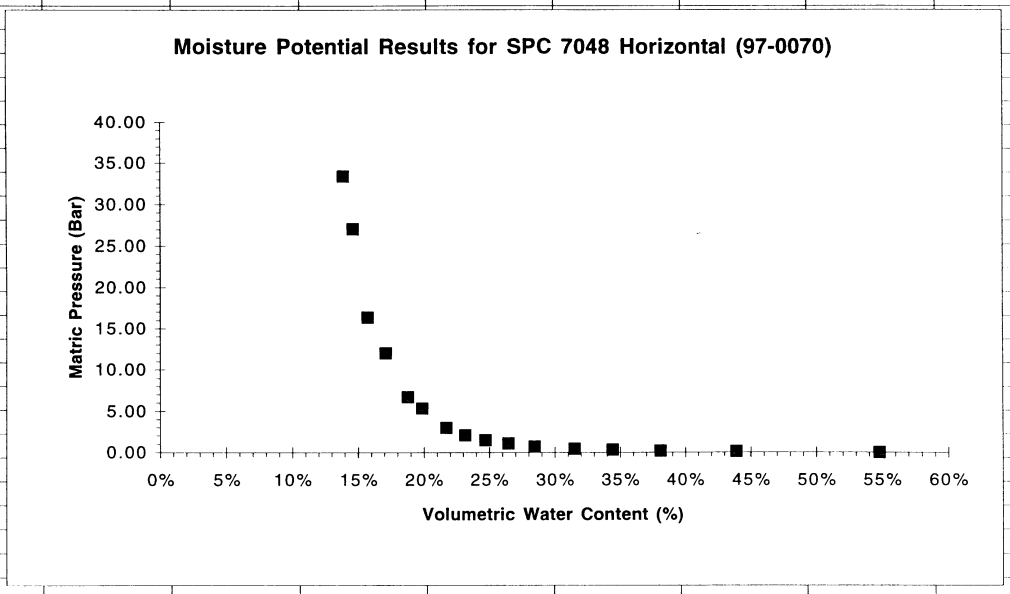

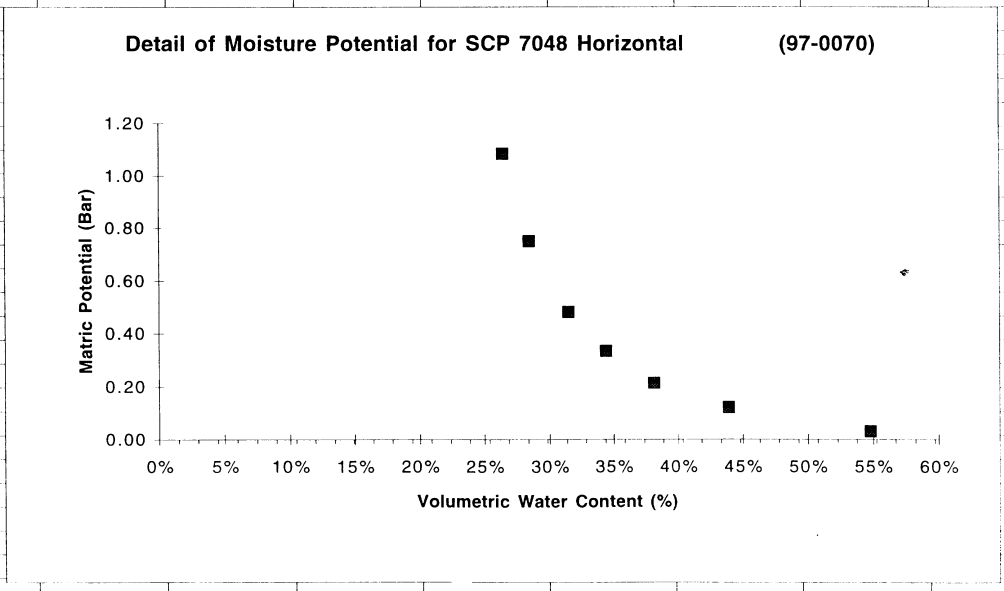

UFA VENTURES/NESTT Client Report

Client/PO#:	LANL/JAKE TURIN		
Client ID:	SPC7048 shavings	Lab ID:	97-0071
Time Collected:	unknown	Time Received:	12:00
Date Collected:	11/7/97	Date Received:	12/10/97
Receipt Condition:	GOOD		
Run type:	RECOMPOSITE		
Dry bulk density (g/cm^3):	1.02		

Hydraulic Conductivity Results

Vol moisture content%	K Value (cm/s)	Comments
48.00%	8.03E-04	Falling Head Value
42.19%	1.00E-04	
40.78%	2.50E-05	
36.39%	9.00E-06	
31.66%	4.00E-06	
28.62%	1.80E-06	
26.70%	6.75E-07	
25.01%	2.25E-07	
22.48%	4.50E-08	
20.65%	1.70E-08	
18.36%	3.40E-09	
15.99%	2.33E-10	

Comments/Observations:

Moisture Potential Results

Vol moisture content%	Matric Pressure (Bar)	Comments
48.00%	0.04	
45.61%	0.17	
40.32%	0.30	
28.51%	0.46	
21.77%	0.67	
20.34%	1.04	
18.99%	1.50	
17.62%	2.04	
16.47%	2.89	
15.20%	4.17	
14.15%	5.67	
13.35%	7.41	
12.47%	11.58	
11.63%	16.67	
10.88%	22.69	
10.17%	29.64	
9.55%	37.51	
8.93%	46.31	

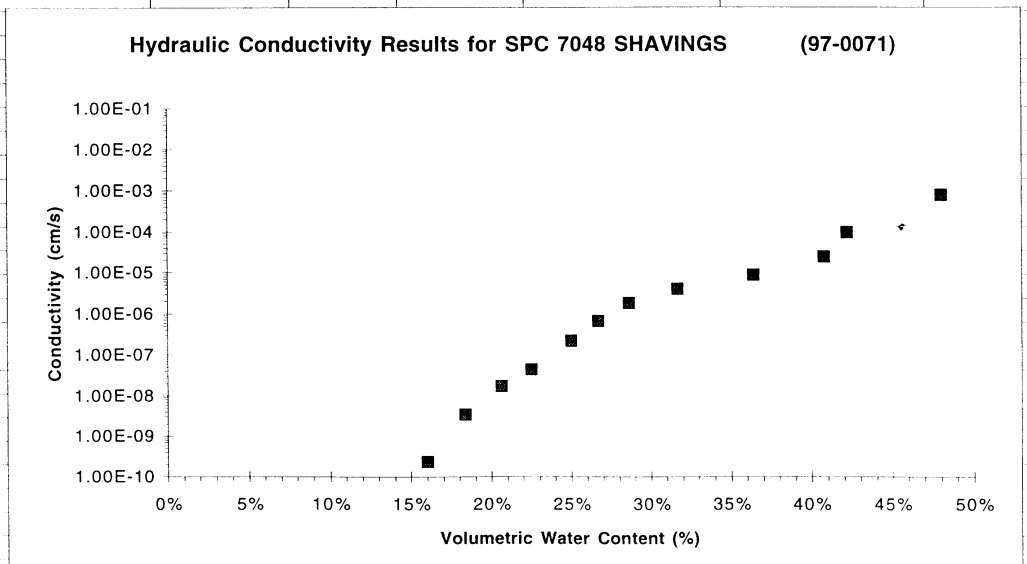

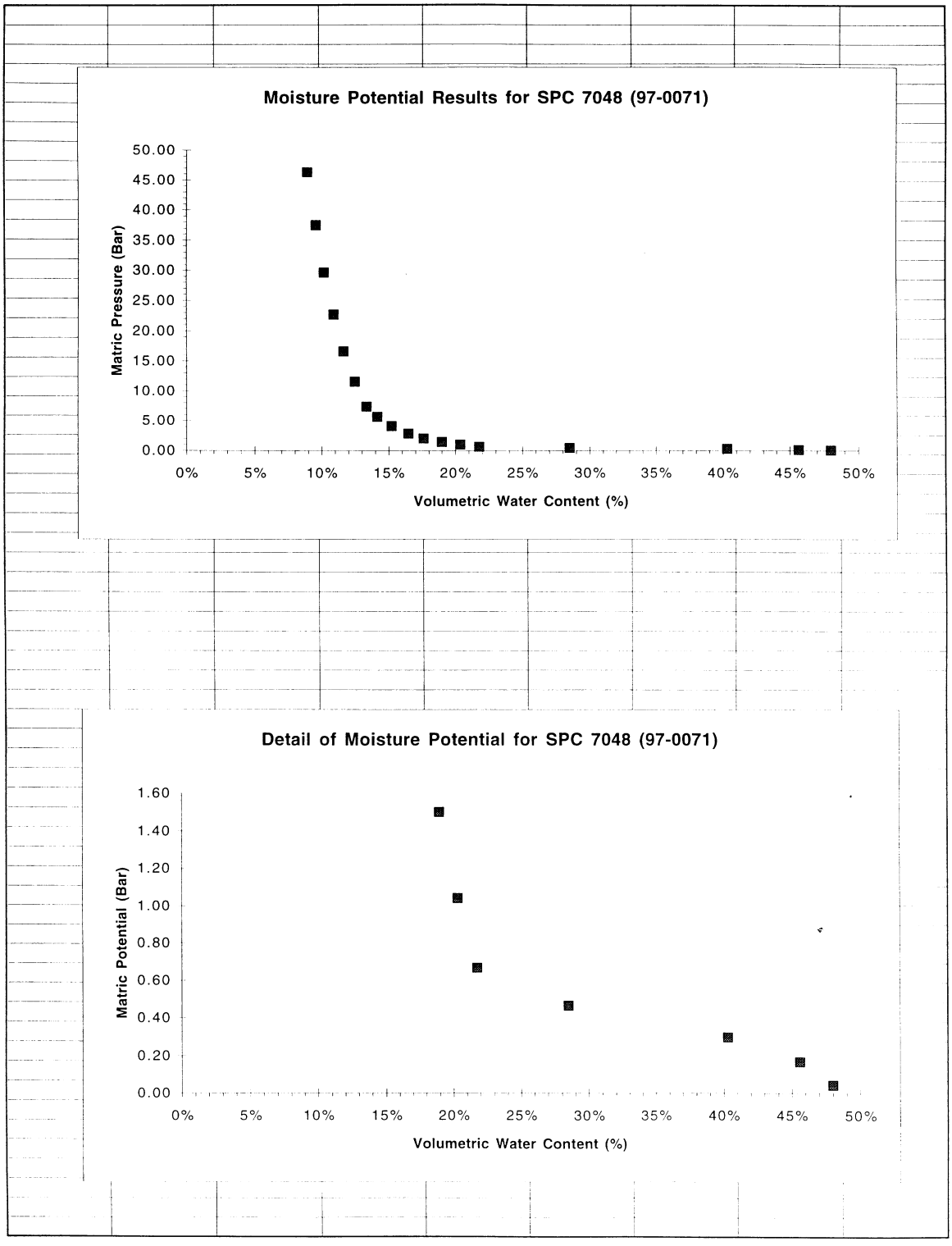
Moisture Potential Results for SPC 7048 (97-0071)
Matric Pressure (Bar)
50.00
45.00
40.00
35.00
30.00
25.00
20.00
15.00
10.00
5.00
0.00
0%
5%
10%
15%
20%
25%
30%
35%
40%
45%
50%
Volumetric Water Content (%)
Detail of Moisture Potential for SPC 7048 (97-0071)
Matric Potential (Bar)
1.60
1.40
1.20
1.00
0.80
0.60
0.40
0.20
0.00
0%
5%
10%
15%
20%
25%
30%
35%
40%
45%
50%
Volumetric Water Content (%)

UFA VENTURES/NESTT Client Report

Client/PO#:	LANL/JAKE TURIN				
Client ID:	SPC 7049 Vertical		Lab ID:	97-0072	
Time Collected:	unknown		Time Received:	12:00	
Date Collected:	1//7/97		Date Received:	12/10/97	
Receipt Condition:	GOOD				
Run type:	WHOLE ROCK			RockCoreCalcw/F,G,H,&M v2.0.1	
Dry bulk density (g/cm^3):	1.40				
Initial Water Content	By weight %:	3.39%			
	By vol %:	4.73%			

NOTE: The initial water content value was taken at time of receipt at our lab and may or may not reflect the actual field value.

Hydraulic Conductivity Results			**Moisture Potential Results**		
Vol moisture content%	K Value (cm/s)	Comments	Vol moisture content%	Matric Pressure (Bar)	Comments
63.97%	5.61E-04	Falling Head Value	59.56%	0.03	
60.78%	7.55E-05		55.21%	0.12	
53.27%	2.72E-05		47.28%	0.22	
50.56%	1.21E-05		42.14%	0.34	
44.69%	5.44E-06		38.95%	0.49	
42.72%	2.04E-06		35.33%	0.77	
39.89%	6.80E-07		33.08%	1.11	
36.36%	1.36E-07		31.44%	1.51	
34.63%	5.14E-08		29.98%	2.14	
29.73%	8.91E-09		28.61%	3.09	
28.24%	8.12E-10		26.85%	5.49	
			25.84%	6.94	
			24.32%	12.35	
Comments/Observations:			23.26%	16.80	
			22.16%	21.95	
			21.37%	27.78	
			20.55%	34.29	

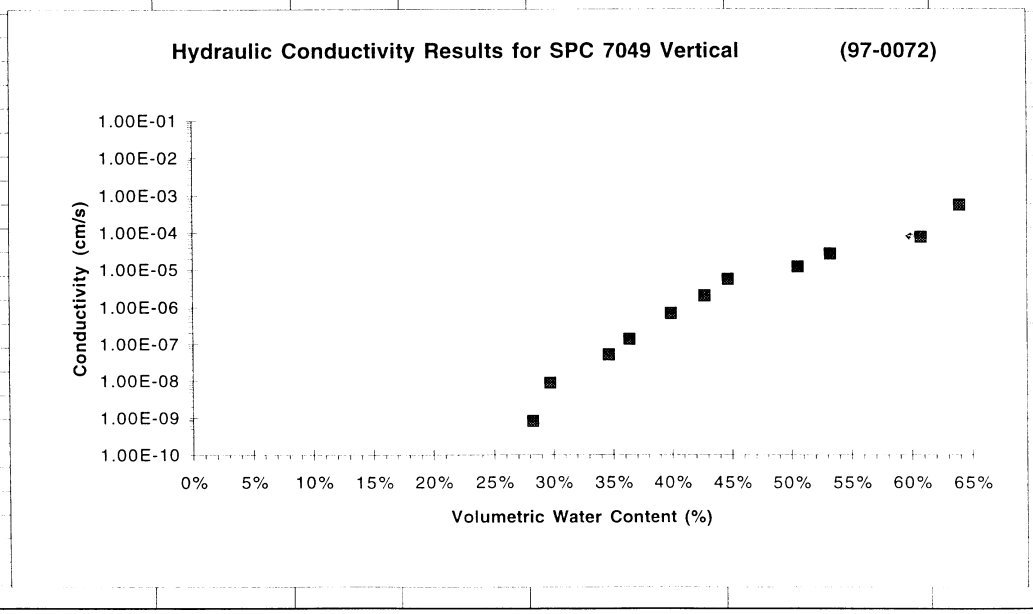

RockCoreCalcw/F,G,H,&M v2.0.3

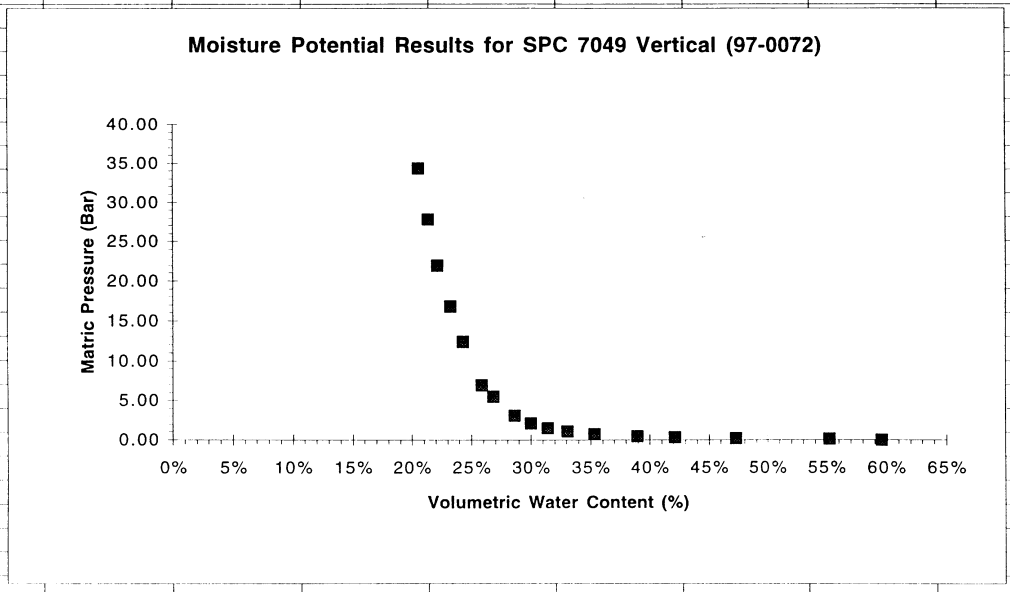

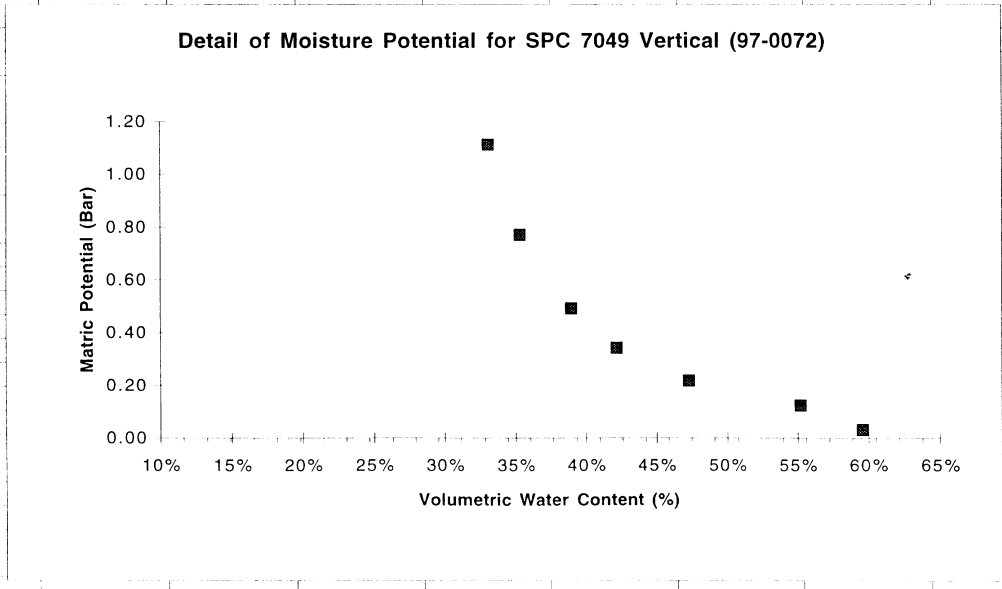

UFA VENTURES/NESTT Client Report

Client/PO#:	LANL/JAKE TURIN				
Client ID:	SPC7049 shavings		Lab ID:	97-0073	
Time Collected:	unknown		Time Received:	12:00	
Date Collected:	11/7/97		Date Received:	12/10/97	
Receipt Condition:	GOOD				
Run type:	RECOMPOSITE				
Dry bulk density (g/cm^3):	1.03				
Initial Water Content	By weight %:	note: water content done only on the intact cores			
	By vol %:				

NOTE: The initial water content value was taken at time of receipt at our lab and may or may not reflect the actual field value.

Hydraulic Conductivity Results			**Moisture Potential Results**		
Vol moisture content%	K Value (cm/s)	Comments	Vol moisture content%	Matric Pressure (Bar)	Comments
44.99%	3.00E-04	Falling Head Value	44.99%	0.04	
40.84%	2.50E-05		42.39%	0.17	
36.11%	9.00E-06		26.48%	0.30	
30.56%	4.00E-06		22.90%	0.46	
27.79%	1.80E-06		20.45%	0.67	
24.37%	6.75E-07		18.57%	1.04	
23.39%	2.25E-07		17.76%	1.50	
20.47%	4.50E-08		16.49%	2.04	
18.83%	1.70E-08		15.54%	2.89	
16.92%	3.40E-09		14.40%	4.17	
14.71%	2.33E-10		13.48%	5.67	
			12.82%	7.41	
			12.04%	11.58	
Comments/Observations:			11.30%	16.67	
			10.63%	22.69	
			10.02%	29.64	
			9.46%	37.51	
			8.92%	46.31	

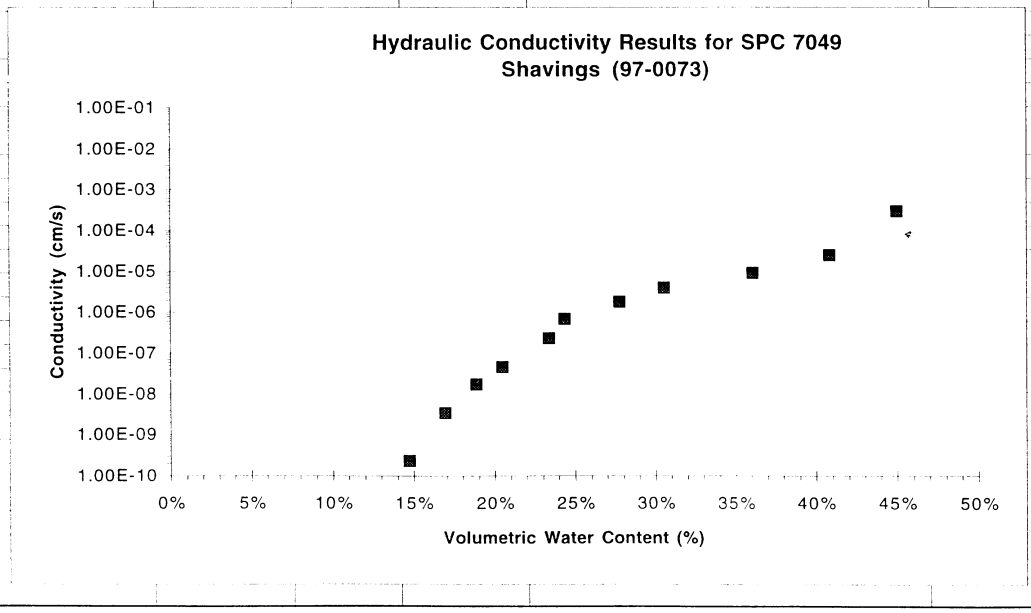

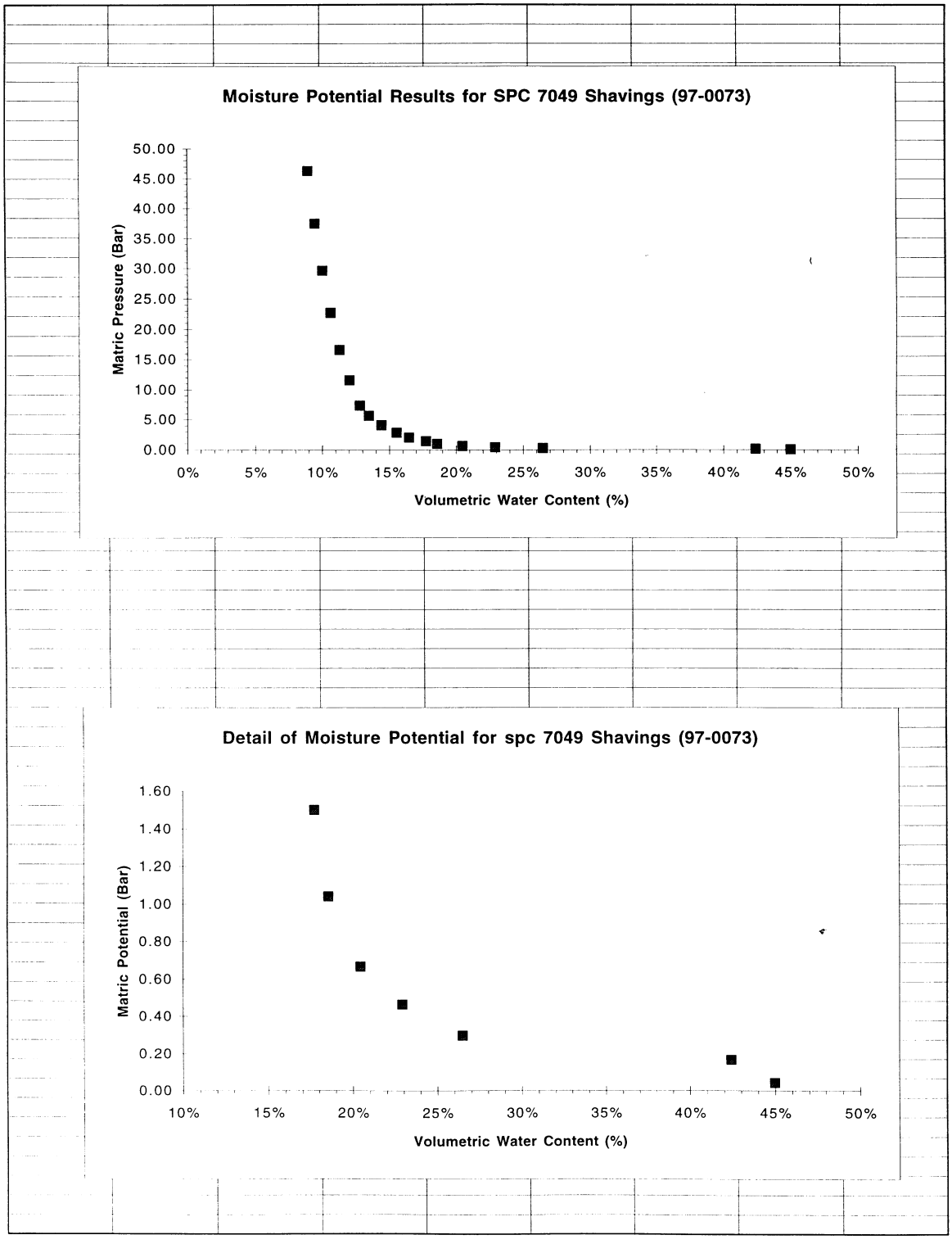
Moisture Potential Results for SPC 7049 Shavings (97-0073)
Matric Pressure (Bar)
50.00
45.00
40.00
35.00
30.00
25.00
20.00
15.00
10.00
5.00
0.00
0%
5%
10%
15%
20%
25%
30%
35%
40%
45%
50%
Volumetric Water Content (%)
Detail of Moisture Potential for spc 7049 Shavings (97-0073)
Matric Potential (Bar)
1.60
1.40
1.20
1.00
0.80
0.60
0.40
0.20
0.00
10%
15%
20%
25%
30%
35%
40%
45%
50%
Volumetric Water Content (%)

UFA VENTURES/NESTT Client Report

Client/PO#:	LANL/JAKE TURIN				
Client ID:	SPC 7050 Vertical		Lab ID:	97-0074	
Time Collected:	unknown		Time Received:	12:00	
Date Collected:	1//7/97		Date Received:	12/10/97	
Receipt Condition:	GOOD				
Run type:	WHOLE ROCK			RockCoreCalcw/F,G,H,&M v2.0.1	
Dry bulk density (g/cm^3):	1.57				
Initial Water Content	By weight %:	1.26%			
	By vol %:	1.97%			

NOTE: The initial water content value was taken at time of receipt at our lab and may or may not reflect the actual field value.

Hydraulic Conductivity Results			Moisture Potential Results		
Vol moisture content%	K Value (cm/s)	Comments	Vol moisture content%	Matric Pressure (Bar)	Comments
50.89%	3.85E-04	Falling Head Value	46.19%	0.03	
50.40%	7.51E-05		44.82%	0.11	
41.97%	2.70E-05		37.40%	0.19	
39.07%	1.20E-05		32.04%	0.29	
35.11%	5.41E-06		28.48%	0.42	
32.44%	2.03E-06		24.89%	0.66	
29.01%	6.76E-07		22.60%	0.95	
27.83%	1.35E-07		21.26%	1.29	
24.50%	5.11E-08		19.89%	1.83	
21.82%	8.87E-09		18.62%	2.63	
18.68%	8.08E-10		17.93%	3.58	
			17.18%	4.68	
			16.56%	7.31	
Comments/Observations:			15.91%	10.53	
			15.35%	14.33	
			14.89%	18.71	
			14.47%	23.68	
			14.05%	29.24	

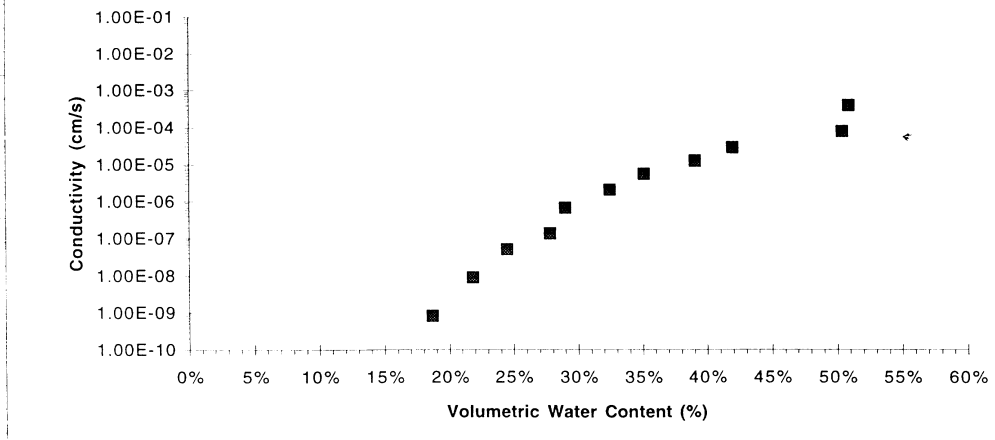

RockCoreCalcw/F,G,H,&M v2.0.3

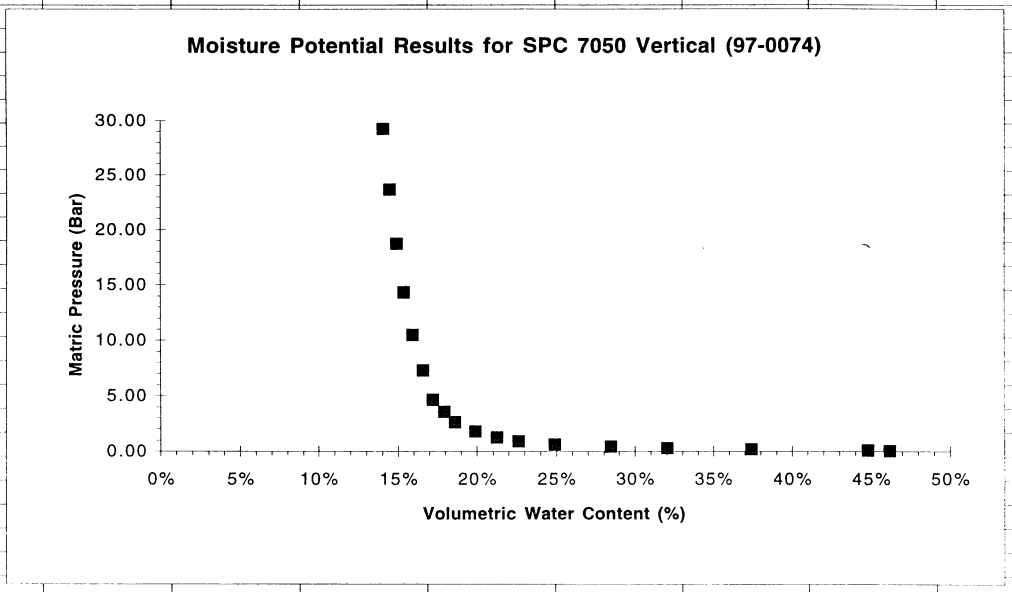

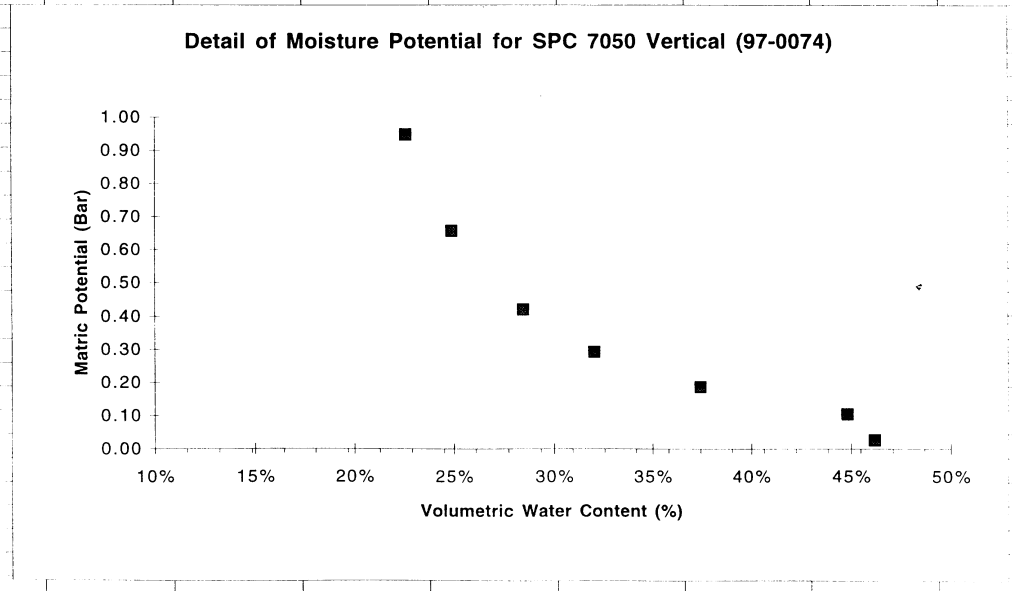

APPENDIX D.
SOLUBILITIES OF NICKEL, COBALT, AND MANGANESE COMPOUNDS IN BUSTED BUTTE WATERS

Arend Meijer
GCX Inc.
P.O. Box 82427
Albuquerque, NM 87108
(505) 256-3769
email: eltjo@aol.com

The reactive-tracer test requires an injection water that is spiked with the reactive-tracer metals. A bulk-water composition has been formulated to simulate the composition of pore water in the Calico Hills Tuff present within the Busted Butte Adit. The reactive-tracer metals are added to this water as soluble chloride compounds. A critical question is how much of each of the metals can be added to this water composition without causing the precipitation of a compound containing the reactive tracers. This appendix attempts to address this question.

To calculate how much of a given metal can be added to a Busted Butte pore-water composition, the possible compounds containing this metal that could precipitate from the pore-water composition must be identified. Once these compounds have been identified, calculations must be carried out to identify the least soluble of these compounds. The thermochemical calculations to be carried out require thermodynamic data (i.e., the free energy of formation ΔG_f^o and the equilibrium constant) for each of the compounds of interest. With the appropriate thermodynamic data, the calculations can readily be carried out with a code such as EQ3NR (Wolery 1992). These codes allow calculation of the degree to which the tracer solution is over or undersaturated with the compounds of interest under equilibrium conditions. Because precipitation is generally a nonequilibrium process, kinetic considerations must be included in the evaluation of possible precipitation reactions.

Identification of the metal compounds that could control the solubility of the reactive tracer in the Busted Butte pore water is an imperfect process because of the incompleteness of the database on such compounds. Although many compounds containing the metals of interest (nickel, cobalt, and manganese) have been identified in various natural settings, these settings do not necessarily duplicate the chemical conditions at the Busted Butte site. For the metals nickel (Ni) and cobalt (Co), perhaps the most pertinent information relates to the localities where ore deposits of these metals are found. Information on the secondary phases formed in the zone of weathering at these localities is of particular significance. For the metal manganese (Mn), the secondary phases identified within the vadose zone in Yucca Mountain (Carlos 1993) can be used as a database.

In nickel deposits, the secondary nickel minerals most commonly identified include pimelite, nepouite, falcondoite, and nickel-bearing smectites (Manceau et al. 1985, pp. 367–387). These minerals generally form solid solutions with magnesium (Mg) end-member compositions kerolite, lizardite, sepiolite, and stevensite, respectively. Pimelite as the nickel analog of kerolite has a theoretical composition $Ni_3Si_4O_{10}(OH)_2 \cdot 4H_2O$. Kerolite is defined as a hydrous magnesium silicate "with a talc-like structure and composition but with additional water and a highly disordered and non-swelling stacking of layers" (Brindley et al. 1979). The nickel analog of talc is called willemseite with a theoretical composition $Ni_3Si_4O_{10}(OH)_2$.

Nepouite as the nickel analog of lizardite has a theoretical composition $Ni_3Si_2O_5(OH)_4$. Falcondoite as the nickel analog of sepiolite has a theoretical composition of $Ni_4Si_6O_{15}(OH)_2 \cdot 6H_2O$. The nickel-bearing smectites have not been reliably characterized to date but would likely have compositions analogous to stevensite such as $(Mg,Ni)_3Si_4O_{10}(OH)_2 \cdot nH_2O$.

Less information is available on the secondary cobalt minerals formed in the zone of weathering. According to Lindgren (1933), asbolite is commonly found as a (meta)stable cobalt phase in the zone of oxidation. Chukhrov et al. (1982) renamed this phase Co-Ni asbolan and determined that it was a "mixed phase" composed of layers of MnO_2 intermixed with layers of $Ni(OH)_2$ and CoOOH. Note that the cobalt in this phase is in the +3 oxidation state (Manceau et al. 1987). The oxidation of Co^{2+} to Co^{3+} in asbolan is likely due to its incorporation into a MnO_2 phase (Burns 1976).

Thermodynamic data are available for manganese and various divalent cobalt oxides in the EQ3 database DATA0.com. The data for manganese oxides should be adequate to evaluate the saturation state for this metal in Busted Butte pore-water compositions. Under oxidizing conditions, the solubility of manganese will largely determine the solubility of cobalt. The EQ3 DATA0.com database has a cobalt-spinel phase (Co_3O_4), which will have to represent the Co^{3+} "phase" in asbolan. Under less-oxidizing conditions, other cobalt oxides may control the solubility of this metal. The EQ3 DATA0.com database contains data for various divalent cobalt oxides that will represent cobalt solubility under these conditions.

For nickel, the situation is more problematic because thermodynamic data are not available for the hydrous nickel silicates that likely would control the solubility of this metal in the Busted Butte pore waters. The approach taken for the derivation of estimated thermodynamic properties for these phases was as follows. Free energy-of-formation values were assembled for compounds for which data were available for both the magnesium and nickel end members. These data are shown in Table D-1. The average difference between the magnesium and nickel end-member free energies

Table D-1. Thermodynamic Data for Ni and Mg Compounds*

Compound	ΔG_f°(Mg) (kJ)	ΔG_f°(Ni) (kJ)	Difference (Mg – Ni) (kJ)
MeO	–569.384	–211.59	–357.787
$Me(OH)_2$	–835.319	–447.200	–388.12
$MeCO_3$	–1027.833	–612.50	–415.33
Me_2SiO_4	–2051.325	–1317.123	(739.581/2) = –369.79
MeF_2	–1071.051	–604.100	–466.95
$MeSO_4$	–1170.60	–759.70	–410.90
$MeSO_4 \cdot 6H_2O$	–2631.389	–2224.61	–406.78
$MeSO_4 \cdot 7H_2O$	–2869.914	–2461.83	–408.08
$MeCl_2 \cdot 2H_2O$	–1118.00	–760.100	–357.90
$MeCl_2 \cdot 4H_2O$	–1623.29	–1234.90	–388.39
$MeCl_2 \cdot 6H_2O$	–2114.581	–1713.19	–401.39
			Average = –397.40

*From EQ3 Data0.com datafile.

was found to be –397.40 kJ/mole Mg. This difference, corrected to the appropriate molar magnesium numbers, was added to the values available for the magnesium end members of the minerals of interest (i.e., lizardite, talc, and sepiolite). For lizardite, thermodynamic data for its polymorph chrysotile was used. The resulting values are shown in Table D-2.

The estimated values for the free energy of formation and equilibrium constants for the nickel end members were entered into the EQ3 datafile DATA0.com. Input files for EQ3 runs were generated based on the Busted Butte pore-water compositions spiked with the metals of interest as given in Table D-3. The results of EQ3 runs with these water compositions at a pH value of 7.00, 25°C, and an oxidation potential Eh of 803 mV are tabulated in Table D-4. The Eh value of 803 mV was used because that is the Eh to be expected for water in equilibrium with atmospheric oxygen levels (i.e., 6–7 mg/L dissolved oxygen). Note that only the phases that were supersaturated in the water compositions are listed in Table D-4.

In addition to being supersaturated with several silica phases, the spiked Busted Butte water composition is also saturated with various nickel, manganese, and cobalt phases. For nickel, there are apparently only two supersaturated phases: Ni-talc and Ni-olivine. Because Ni-talc is representative of the phases formed in weathering environments, it is the most likely to control Ni solubility in this water. However, because the saturation index is only 1.24, slow nucleation and precipitation kinetics will likely keep the nickel in solution.

Only two cobalt phases show supersaturation in the Busted Butte water composition: cobalt olivine and cobalt spinel. These phases show somewhat higher saturation indices than the nickel phases. However, they are unlikely to precipitate from this water for the same reasons as those given for the nickel phases. Note that cobalt oxide, hydroxide, and carbonate (sphaerocobaltite) are not supersaturated in this water composition. If cobalt were to

Table D-3. Spiked Busted Butte Pore-water Compositions.

Constituent	Concentration (mg/L)
Si	31.7
Ca	19.81
Mg	3.19
Na	17.89
K	3.44
Ni	2.5
Co	2.5
Mn	2.8
Cl	16.74
SO_4	30.08
NO_3	21.02
F	1.41
HCO_3	33.0
Eh	803 (mV)

Table D-2. Estimated Thermodynamic Data for Ni Phases.

Compound	ΔG_f^o(Mg) (kJ)*	Estimated ΔG_f^o(Ni) (kJ)
$Me_3Si_4O_{10}(OH)_2$ (talc-willemseite ≈ kerolite-pimelite)	–5523.667	–4331.466
$Me_3Si_2O_5(OH)_4$ (chrysotile-nepouite)	–4037.020	–2844.820
$Me_4Si_6O_{15}(OH)_2 \cdot 6H_2O$ (sepiolite-falcondoite)	–9251.627	–7662.03

*From EQ3 Data0.com datafile.

precipitate from this water, it would most likely be as a coprecipitate with manganese.

The manganese phases are oversaturated to much higher levels than either nickel or cobalt phases. For example, birnessite shows a saturation index of 53.8. At these levels of oversaturation, tetravalent manganese oxides would be expected to precipitate from the water composition. However, two factors argue for a slow precipitation rate. First, the oxidation reaction by which the divalent manganese added to the water is converted to tetravalent manganese is kinetically very slow and could take from hundreds of days to years in the Busted Butte water composition (Eary and Schramke 1990). Second, the nucleation and precipitation of tetravalent manganese oxides will likely also be slow (Hem 1963). Therefore, it likely will take longer than several hundred days before the spiked Busted Butte water would precipitate manganese.

Table D-4. Results of EQ3 Runs: Summary of Pure Mineral Saturation States.
(Minerals with affinities less than –10 kcal are not listed.)

Mineral	log *Q*/*K*	Affinity (kcal)	State*
Birnessite	53.792	73.387	ssatd
Bixbyite	10.102	13.782	ssatd
Bunsenite	–2.967	–4.048	
Calcite	–1.652	–2.253	
Chalcedony	0.752	1.025	ssatd
Chrysotile	–7.099	–9.685	
$Co(OH)_2$	–5.553	–7.576	
Co_2SiO_4	3.837	5.235	ssatd
$CoFe_2O_4$	–2.402	–3.277	
CoO	–6.808	–9.288	
Cristobalite(α)	0.472	0.644	ssatd
Cristobalite(β)	0.029	0.039	satd
Falcondoite	–2.593	–3.537	
Hausmannite	8.553	11.669	ssatd
Manganite	4.733	6.457	ssatd
$Mn(OH)_2$(am)	–5.734	–7.823	
$Mn(OH)_3$	–1.773	–2.419	
$MnHPO_4$	–0.881	–1.202	
MnO_2(g)	7.642	10.425	ssatd
Ni-chrysotile	–2.796	–3.814	
Ni-talc	1.239	1.691	ssatd
$Ni(OH)_2$	–3.244	–4.425	
Ni_2SiO_4	1.691	2.308	ssatd
$NiCO_3$	–4.385	–5.983	
$NiSO_4 \cdot 6H_2O(\alpha)$	–6.130	–8.363	
Pyrolusite	9.159	12.496	ssatd
Quartz	1.023	1.395	ssatd
Rhodochrosite	–0.609	–0.831	
Rhodonite	–3.130	–4.271	
SiO_2(am)	–0.263	–0.359	satd
Sphaerocobaltite	–3.398	–4.636	
Spinel-Co	1.904	2.598	ssatd
Talc	–3.065	–4.181	
Tephroite	–6.902	–9.417	
Todorokite	46.689	63.697	ssatd
Tridymite	0.851	1.161	ssatd

*satd = saturated; ssatd = supersaturated

APPENDIX D REFERENCES

Brindley, G.W., D.L. Bish, and H-M. Wan. 1979. Composition, structures, and properties of nickel-containing minerals in the kerolite-pimelite series. *American Mineralogist* 64: 615–625.

Burns, R.G. 1976. The uptake of cobalt into ferromanganese nodules, soils, and synthetic manganese (IV) oxides. *Geochimica et Cosmochimica Acta* 40: 95–102.

Carlos, B.A., S.J. Chipera, D.L. Bish, and S.J. Craven. 1993. Fracture-lining manganese oxide minerals in silicic tuff, Yucca Mountain, Nevada, USA. *Chemical Geology* 107: 47–69. (Yucca Mountain Project TIC # 20862)

Chukhrov, F.V., A.I. Gorshkov, V.A. Drits, A.I. Sivtov, and Ye.S. Rudnitskaya. 1982. Crystallographic nature of Co-Ni asbolan. *AN SSSR Izvestiya, Sr. Geol*. 6: 73–81 (Trans. *Internat. Geol. Rev*. 24: 598–604).

Eary, L.E., and J.A. Schramke. 1990. Rates of inorganic oxidation reactions involving dissolved oxygen. In *Chemical Modeling of Aqueous Systems II: American Chemical Society Symposium Series 416*, D.C. Melchior and R.L. Bassett, editors, pp. 379–396. Washington, D.C.: American Chemical Society.

Hem, J.D. 1963. Chemical equilibria and rates of manganese oxidation. U.S. Geological Survey water-supply paper 1667-A.

Lindgren, W. 1933. *Mineral Deposits*. New York, NY: McGraw-Hill Book Co., Inc.

Manceau, A., G. Calas, and A. Decarreau. 1985. Nickel-bearing clay minerals: I. Optical spectroscopic study of nickel crystal chemistry. *Clay Minerals* 20: 367–387.

Manceau, A., S. Llorce, and G. Calas. 1987. Crystal chemistry of cobalt and nickel in lithiophorite and asbolane from New Caledonia. *Geochimica et Cosmochimica Acta* 51: 105–113.

Wolery, T.J. 1992. EQ3NR, a computer program for geochemical aqueous-speciation–solubility calculations: Theoretical manual, user's guide, and related documentations (version 7.0). Lawrence Livermore National Laboratory report UCRL-MA-110662 PT III.

Los Alamos
NATIONAL LABORATORY
Los Alamos, New Mexico 87545